Technische Universität München

TUM School of Life Sciences

Establishment and characterization of human *Engrailed1*-knockout iPSC models in the context of Parkinson's Disease pathophysiology

Sina Hembach

Vollständiger Abdruck der von der TUM School of Life Sciences der Technischen Universität München zur Erlangung des akademischen Grades einer

Doktorin der Naturwissenschaften (Dr. rer. nat.)

genehmigten Dissertation.

Vorsitzender:

Prof. Dr. Kay H. Schneitz

Prüfer*innen der Dissertation:

1. Prof. Dr. Wolfgang Wurst
2. Prof. Angelika Schnieke, Ph.D.

Die Dissertation wurde am 05.06.2023 bei der Technischen Universität München eingereicht und durch die TUM School of Life Sciences am 25.10.2023 angenommen.

Abstract

A key pathological feature of Parkinson's Disease (PD) is the progressive degeneration of dopaminergic neurons (DANs) in the substantia nigra pars compacta. Genetics as well as acquired factors like exposure to pesticides or toxins can be responsible for the development of PD. The great heterogeneity of PD with regard to etiology and clinical phenotypes requires different models to analyze the various aspects underlying the pathophysiology of the disease. Although genetic as well as neurotoxic animal models have been generated and analyzed in depth, none of the existing models is able to recapitulate all features of PD and the pathophysiology is still not clear. The transcription factor Engrailed1 (EN1) is crucial for the development and survival of the DANs and has a neuroprotective effect in a PD MPTP mouse model, where it has been associated with enhanced translation of two complex I subunits. Hence, En1 is linked to signaling pathways that are associated with the survival of DANs and thus implicated in PD. *En1* knockout mice were generated to study the pathology of PD and crucial survival pathways for therapeutic intervention. Heterozygous *En1* mice represent one of few models that show slow degeneration of dopaminergic neurons. However, even in mice the background affects the severity of the phenotype and a human cellular model carrying *EN1* knockout is still missing.

Therefore, human induced pluripotent stem cell (hiPSC) lines harboring an *EN1* knockout were generated. The CRISPR/Cas9 technology was used to induce insertions/deletions in Exon 1 of *EN1* resulting in premature termination of translation. The re-clonalized *EN1* -/- hiPSCs were controlled for a normal karyotype, pluripotency, and normal colony morphology. Following quality control, the *EN1* knockout cells were successfully differentiated into neuronal progenitor cells (NPCs) with midbrain identity. A transcriptome analysis revealed pathways connected to established En1 functions, indicating that EN1 role is conserved also in the human models. Interestingly, alterations in mitochondrial pathways were not detected as shown by comparative transcriptome analysis. With NPCs being an early developmental state, the expression of *EN1* was probably too low. DANs, which stably express *EN1*, exhibited a deficit in glycolysis, whereas mitochondrial function was unperturbed in contrast to findings in $En1^{+/-}$ mouse models. Enhancing the effect of the *EN1* knockout in NPCs by Wnt stimulation confirmed the suggested bottleneck in glycolysis, in transcriptome data and results of mitochondrial and glycolytic stress tests of Wnt stimulated WT and *EN1* -/- NPCs. Investigation of the transcriptome for the effect of the Wnt stimulation on the individual genotypes revealed that Wnt only demasked the glycolysis deficit in *EN1* -/- NPCs. Therefore, EN1 might either be protective of the Wnt induced changes or EN1 is crucial in conveying the protective effect of the Wnt signaling. In contrast to unstimulated NPCs, Wnt stimulated NPCs also showed reduced mitochondrial functionality. As genes associated with mitochondrial function were not detected in the transcriptome data one might hypothesize that different targets are control by EN1's function as transcription factor versus its function as regulator of translation.

In conclusion, the human *EN1* -/- models revealed that most of the functional networks EN1 is involved in are conserved in the human models. However, the human models indicated a glycolytic deficiency, rather than mitochondrial dysfunction for the first time in connection with EN1. Glycolytic dysfunction might therefore be an early molecular alteration that could contribute to the neurodegenerative phenotype that has been described for genetic *En1* knockout mouse models.

Zusammenfassung

Ein wesentliches pathologisches Merkmal der Parkinson-Krankheit (PD) ist die fortschreitende Degeneration der dopaminergen Neuronen (DAN) in der Substantia nigra pars compacta. Sowohl genetische als auch erworbene Faktoren können für die Entstehung von Morbus Parkinson verantwortlich sein. Genetische als und neurotoxische Tiermodelle sind nicht in der Lage, alle Merkmale von Morbus Parkinson zu rekapitulieren und die Pathophysiologie ist noch immer unklar. Der Transkriptionsfaktor Engrailed1 (EN1) ist entscheidend für die Entwicklung und das Überleben der DANs und zeigte eine neuroprotektive Wirkung in einem Parkinson MPTP-Mausmodell, die mit der verstärkten Translation von zwei Komplex-I-Untereinheiten in Verbindung gebracht wurde. En1 ist somit assoziiert mit Signalwegen die essenziell sind für das Überleben von DANs. Um die Pathologie der Parkinson-Krankheit und entscheidende protektive Signalwege für therapeutische Interventionen zu analysieren, wurden *En1*-Knockout (ko) Mäuse erzeugt. Heterozygote *En1* Mäuse sind eines der wenigen Modelle, die eine langsame Degeneration von DANs aufweisen. Allerdings ist der genetische Hintergrund entscheidend für die Ausprägung des Phänotyps und ein humanes zelluläres Model, eines *EN1*-ko in wurde bisher noch nicht untersucht.

Deshalb wurden humane induzierte pluripotente Stammzellen (hiPSC) mit einen *EN1*-ko erzeugt. CRISPR/Cas9 wurde verwendet um Insertionen/Deletionen in *EN1* Exon 1 zu induzieren, die zu einem vorzeitigen Abbruch der Translation führen. Die reklonalisierten *EN1* -/- hiPSCs wurden bezüglich ihres Karyotyps, Pluripotenz und Koloniemorphologie überprüft und erfolgreich in neuronale Vorläuferzellen (NPCs) differenziert. Die Transkriptomanalyse identifizierte Signalwege, die mit bekannten En1-Funktionen assoziiert sind und implizierte eine konservierte Funktion von EN1. Interessanterweise lieferte eine vergleichende Transkriptomanalyse keinen Hinweise auf Veränderungen in mitochondrialen Funktionen. Dies war wahrscheinlich zurückzuführen auf das frühe Entwicklungsstadium der NPCs mit einer zu geringen Expression von *EN1*. DANs, die *EN1* stabil exprimieren, wiesen ein Defizit in der Glykolyse auf, während die mitochondriale Funktion im Gegensatz zu den Ergebnissen des *En1*$^{+/-}$ Mausmodells nicht verändert war. Die Analyse von NPCs mit einer durch Wnt-Stimulation erhöhten *EN1* Expression, bestätigte ein Defizit in der Glykolyse von *EN1*-ko's. Dies wurde sowohl im Transkriptom als auch via mitochondrialen und glykolytischen Stresstest nachgewiesen. Die Wnt-Stimulation demaskierte das Glykolysedefizit nur bei *EN1* -/- NPCs im Transkriptom. Dies deutet darauf hin, dass EN1 die Zelle entweder vor Wnt-induzierten Veränderungen schützt oder, dass EN1 entscheidend ist für die Vermittlung der schützenden Wirkung von Wnt. Wnt-stimulierte NPCs zeigten auch eine reduzierte mitochondriale Funktion. Da im Transkriptom keine mitochondrialen Gene identifiziert wurden, könnte dies darauf hindeuten, dass EN1 in seiner Funktion als Transkriptionsfaktor andere zelluläre Signalwege reguliert als in seiner Funktion als Regulator der Translation.

Zusammenfassend zeigen die humane *EN1* -/- Modelle, dass die funktionalen Netzwerke in die EN1 eingebunden ist in den humanen Modellen konserviert sind. Dennoch wurde in diesen humanen Modellen zum ersten Mal ein glykolytisches Defizit anstelle einer mitochondrialen Dysfunktion im Zusammenhang mit EN1 festgestellt. Eine dysfunktionale Glycolyse könnte daher als eine frühe molekulare Veränderung zu dem neurodegenerativen Phänotyp beitragen der für das genetische *En1* knockout Mausmodell beschrieben wurde.

Contents

1 Introduction

Today our world faces many challenges. The crisis, however, we tend to forget because it is not constantly covered by the news, is our aging society which represents an enormous challenge to the health and social systems (*1*). In 2019, the World Health Organization already listed Alzheimer's disease and other dementias as the 2nd most common cause of death in high-income countries (*2*). Neurodegenerative diseases, like Alzheimer's Disease and Parkinson's Disease, significantly increase with age, with an ever-rising number of people suffering from still incurable neurodegenerative diseases due to the demographic development. Although having been described as early as 1817 in the western societies, the etiology of Parkinson's Disease remains elusive (*3*). The progressive nature of PD and limited treatment options represents an enormous burden for the patient, their relatives, and friends and eventually our society. It is therefore of the greatest importance to tackle the challenges of the very complex field of neurodegenerative diseases and focus on understanding its etiology to develop efficient therapies and hopefully cures.

1.1 Parkinson' Disease

1.1.1 Epidemiology

The clinical picture of Parkinson's Disease (PD) has already been described in ancient India and was treated methodically (*4*). Centuries later in 1817, the surgeon James Parkinson described similar observations in his famous publication "An essay on the shaking palsy" (*5*). The symptoms were later refined by Jean Martin Charcot who also named the disease after James Parkinson. Today, it is the second most common neurodegenerative disease after Alzheimer disease with an incidence of 5-35 cases per 100,000 individuals yearly depending on the demographics. Age is by far the greatest risk factor for PD. Below the age of 50 the incidence is quite low but increases 5-10-fold thereafter and rises to > 3 % at the age of 85. The number of people with PD is expected to double between 2005 and 2030 as a result of our aging society (*3, 6*). Interestingly, ethnicity seems to be a risk factor for PD and the prevalence is higher in countries of the Western World compared to Asian, African or Arabic countries. Lifestyle, diet and exposure to environmental factors can partially explain these ethnic and geographical differences (reviewed in (*3*) and (*7*)). Another risk factor for PD is gender, with men being affected twice as often as women. It has been suggested that the higher estrogen levels in women might have a protective effect (*8*) but the difference can also be due to the exposure to different environmental factors. This highlights more than ever the need to understand the pathology and develop new therapies and ideally cures for PD.

1.1.2 Symptoms

The three cardinal motor symptoms, bradykinesia (slowness of movement), rest tremor, and rigidity are used for clinical diagnosis. Patients usually present with unilateral motor symptoms and this asymmetry remains while the disease progresses (*3, 7*).
In addition to the well-known motor symptoms, most patients also suffer from non-motor symptoms like olfactory dysfunction, cognitive impairment, autonomic dysfunction, sleep disorders and pain. These non-motor symptoms often occur before the onset of the characteristic motor symptoms. This phase is called the prodromal or pre-motor phase, which can start long

before first motor symptoms appear. For example, it has been shown that up to 12-14 years can pass from the occurrence of rapid eye movement sleep disorder to the appearance of motor symptoms (*9*). With progression of the disease, the prevalence of non-motor-symptoms increases which represent a major burden for the patients. Of patients surviving more than 20 years with the disease, 83 % suffer from dementia, 74 % from hallucinations and 71 % from urinary incontinence (*10*).
With progression of the disease the motor symptoms also become worse, and late-stage patients often present with postural instability, freezing of gait, dysphagia and speech dysfunction. These severe symptoms result in doubling of the mortality rate after 10 years of disease progression emphasizing the need for early diagnosis and new therapeutic options (*11*).

1.1.3 Etiology

Genetics as well as acquired factors like exposure to pesticides or toxins can be responsible for the development of PD. Accordingly, PD is classified into two different forms, namely familial PD (fPD) and sporadic PD (sPD), which is caused by an unknown combination of risk factors. Sporadic PD is the most common form and only 15 % of patients present with a family history of PD and 5-10 % suffer from monogenic PD (*12*).

1.1.3.1 Sporadic Parkinson's Disease

A disease is described as sporadic when it occurs irregularly and infrequently with no known cause. The majority of PD patients suffer from sPD. Today, it is believed that sPD has a multifactorial etiology where environmental factors, genetic predisposition and also lifestyle contribute to PD pathogenesis (*13*).
A recent genome-wide association study (GWAS) identified 90 independent PD risk variants in 78 genomic loci that explain 16-36 % of the heritable risk of PD depending on the prevalence (*14*). Nevertheless, the gene-environmental interplay is crucial and environmental risk factors are of high importance. Following the initial discovery that 1-methyl-4-phenyl-1,2,3,6-tetrahydropyridine (MPTP) the prodrug for the neurotoxin 1-methyl-4-phenylpyridinium (MPP+) can cause PD (*15*), numerous other toxins, pesticides and solvents were linked to PD. The pesticides paraquat and rotenone have a similar structure as MPP+ and interfere with complex I of the respiratory chain leading to excessive generation of reactive oxygen species (*16*). Considering this, it is not surprising that rural living, consumption of well water in these regions, and agricultural occupancy are associated with a higher risk for PD, simply due to higher exposure to pesticides (*17*) (*18*). Interestingly, environmental factors that are associated with a lower risk of developing PD have been identified as well. For example, smokers have half the risk of developing PD compared to nonsmokers, with a dose-dependent effect (*19*). This effect is most likely mediated by nicotine although the molecular mechanism remains elusive. In addition, caffeine consumption, including coffee and tea drinking is also associated with a reduced risk of PD. Men with a high coffee consumption have a 60 % reduced risk of PD compared to non-drinkers. In women, however, this effect is less clear (*20*). Besides dietary influences, there is also evidence that physical activity is protective against PD. Studies showed the higher the activity the lower the risk of developing PD, with up to 40 % reduced risk in the group that participated in frequent moderate to vigorous activities (*21*).
Epidemiological studies have shown that environmental stimuli and lifestyle have an important impact on the etiology of PD. As these factors present a target for prevention and disease

modification, they are a highly interesting area of research. However, the interaction with genetic variants still needs to be unraveled.

1.1.3.2 Familial Parkinson's disease

The first gene that was identified to be causative for PD was *SNCA* which encodes for α-synuclein. However, it became clear in the following years that additional genes are also involved in the etiology of PD making it a genetically heterogeneous disorder. Today, 19 genes are known to cause monogenic PD (**Table 1)** and about 90 genetic loci have been identified as risk factors (*12, 14*).
Monogenic PD can be inherited in an autosomal dominant or an autosomal recessive manner. Mutations in the β-glucocerebrosidase gene *GBA* and *LRRK2* are the most common causes of autosomal dominant PD but mutations in *SNCA*, which is the major component of Lewy Bodies are the most studied genetic factors of PD so far. The genes that have been extensively studied in terms of autosomal-recessive PD include *PRKN*, *PINK1*, and *DJ-1*. In contrast to autosomal dominant cases, a recessive inheritance is often linked with an early onset of PD under the age of 50. The clinical presentation between these forms is similar, however, the most common cause for autosomal recessive as well as early onset PD is *PRKN (22)*. Mutations in *PRKN* account for more than 50 % of familial cases with autosomal recessive PD and are the most common cause of a juvenile (< 20) onset (*23*).
Depending on the causative gene, the etiology, pathogenesis, age of onset, and clinical progression can be highly variable. Even patients harboring the same mutation can present differently, which adds to the complexity of the disease. Genes that are associated with PD and their corresponding phenotypic characteristics are summarized in **Table 1**.

Table 1 | **Monogenic forms of PD.** AD: autosomal dominant; AR: autosomal recessive; ID: intellectual disability. Table modified from (*12, 22, 24*)

Symbol	Gene	Inheritance	Disease Onset	Incidence of adult PD	Phenotypic features
PARK1/4	*SNCA*	AD	early-onset	rare	Onset age may be <50 years Cognitive & psychiatric features more likely
PARK2	*PRKN*	AR	early-onset	1 % (4.6%-10.5% of early-onset adult PD)	Slow progression Mild non-motor manifestations
PARK3		AD	late-onset	rare	
PARK5	*UCHL1*	AD	early-onset/ late-onset	rare	
PARK6	*PINK1*	AR	early-onset	Rare (3.7 % of early-onset)	Phenotype similar to PRKN Non-motor manifestations more common
PARK7	*DJ1*	AR	early-onset	Rare	Phenotype similar to PRKN ID &/or seizures occasionally
PARK8	*LRRK2*	AD	late-onset	1-2 %	Classic manifestations with less non-motor involvement Variable penetrance dependent on age, variant & ethnicity
PARK9	*ATP13A2*	AR	juvenile-onset	rare	Wide variability; Triad of spasticity, supranuclear gaze palsy & dementia Also referred to as Kufor-Rakeb syndrome or juvenile-onset atypical PD
PARK10		Risk factor	late-onset	rare	
PARK11		AD	late-onset	rare	
PARK12		Risk factor	late-onset	rare	

PARK13	*HTRA2*	AD or risk factor	early-onset	rare	
PARK14	*PLA2G6*	AR	early-onset	rare	
PARK15	*FBXO7*	AR	juvenile-onset	rare	Juvenile or early-onset, rapidly progressive, may have corticospinal signs Early-onset parkinsonism with bradykinesia in some families
PARK16		Risk factor	early-onset	rare	
PARK17	*VPS35*	AD	late-onset	rare	Classic PD with tremor Fewer non-motor manifestations
PARK18	*EIF4G1*	AD	late-onset	rare	
PARK19	*DNAJC6*	AR	juvenile-onset	rare	2 subtypes identified: Slowly progressing, levodopa-responsive parkinsonism; onset in 3rd-4th decade Rare juvenile-onset with rapid disease progression; atypical features of hyperreflexia, seizures & intellectual disability
PARK20	*SYNJ1*	AR	juvenile-onset	rare	Variants in the SAC1-like domain cause juvenile-onset dystonia with dyskinesia 1 family with early-onset PD reported
PARK21	*TMEM230*	AD	late-onset	rare	
PARK22	*CHCHD2*	AD	late-onset	rare	
PARK23	*VPS13C*	AR	early-onset	rare	Early-onset PD with very rapid progression; truncating variants cause severe disease
	GBA	AD	late-onset	3-7 %	Onset age may be <50 years; Associated with dementia and Lewy bodies Higher likelihood of cognitive impairment, atypical motor findings & severe progression

The findings that mutations in specific genes can cause or enhance the risk for PD provided the opportunity to use genetically modified model organisms. Animal models have contributed majorly to the understanding of the molecular pathogenesis and the development of candidate therapies. However, animal models have drawbacks, and no model completely recapitulates the pathogenesis of PD (see 1.1.5). In addition, the translational aspect is also a major concern, enhancing the need for human models to unravel the molecular pathogenesis of PD.

1.1.4 Pathophysiology

Although clinical symptoms are quite heterogeneous, two major neuropathologies are required for the definite diagnosis of PD, the loss of dopaminergic neurons (DAN) in the substantia nigra pars compacta (SNpc) and, although not present in all cases, the intracellular accumulation of α-synuclein the major component of Lewy bodies (*3*). The degeneration of the DANs is slow but progressive and responsible for the well-known motor symptoms of PD. However, motor symptoms occur only when already 40-60% of the DANs are lost due to the resulting dopamine deficiency in the primary projection area, the dorsal putamen of the striatum (*25*). The substantia nigra (SN) and the striatum belong to the basal ganglia, a group of subcortical nuclei that are primarily responsible for motor control but also regulate emotions and behavior. The basal ganglia integrate input from different cortical (limbic, associative and motor regions) but also thalamic areas that are processed onto fewer output neurons which project to the thalamus and back to the cortex. This suggests a 'filter-like' function of the basal ganglia circuit (*26*). The basal ganglia are divided into input nuclei, consisting of the striatum and subthalamic nucleus (STN), output nuclei,

consisting of the globus pallidus internus (GPi) and the SN pars reticulata and intrinsic nuclei, made up of the globus pallidus externus (GPe), STN and the SNpc. The internal nuclei are crucial to relay input information to the output nuclei. Degeneration of DANs in the SNpc thus results in changes of the basal ganglia circuits. Dopamine has opposing effects on the γ-aminobutyric acid (GABA)ergic medium spiny neurons (MSN) of the indirect and direct pathway in the striatum (**Figure 1**). Reduced activation of the direct pathway MSNs and reduced inhibition of indirect pathway MSNs eventually cause increased activation of inhibitory GABAergic neurons in the basal ganglia output nuclei (GPe and SN pars reticulata) that project to the thalamus. Thus, motoric output is reduced leading to the PD-specific motor symptoms (*26*, *27*).

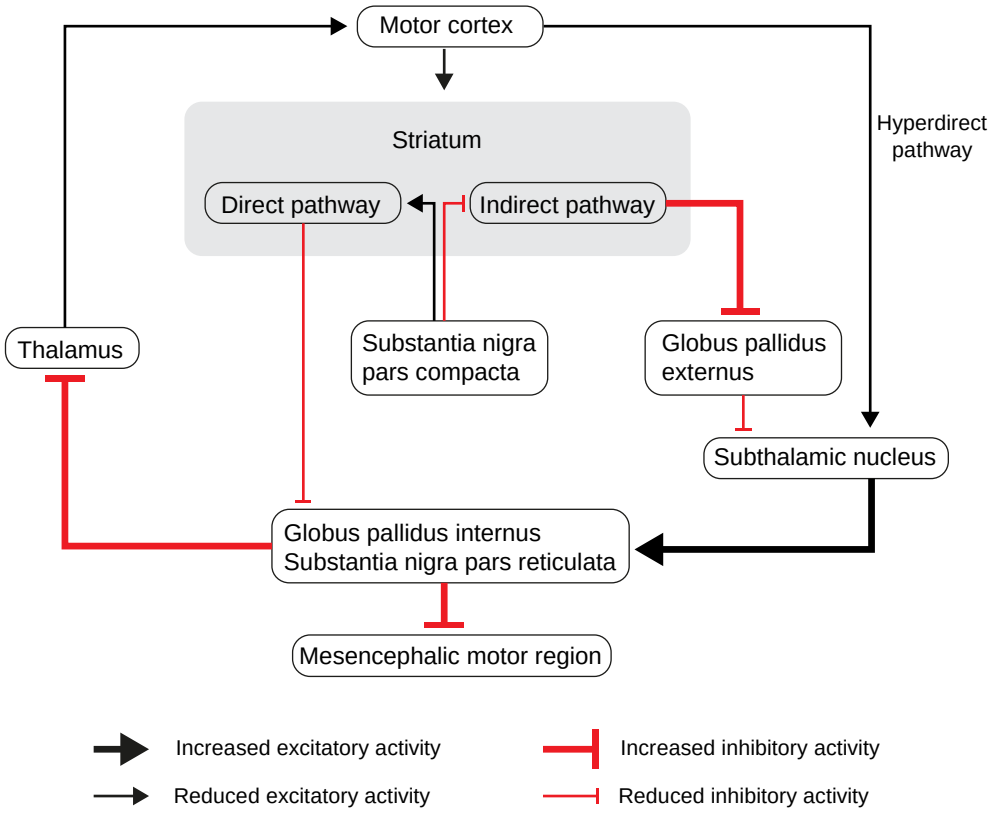

Figure 1: PD associated activity changes in the thalamo-cortical basal ganglia circuits. The loss of dopaminergic innervation in the striatum results in changes in the direct and indirect pathway output. Consequently, the globus pallidus internus and the substantia nigra pars reticulata strongly inhibit the thalamus resulting in reduced motor output. Figure adapted from (*3*).

However, the pathophysiology of PD cannot be fully explained by alterations in the firing rates of these neurons. More complex changes like abnormal neural synchronization and cortico-subcortical coupling in specific frequency bands are involved as well (*28*). In addition, neuronal loss has also been observed in other brain regions including the noradrenergic neurons of the locus ceruleus, cholinergic neurons in the pedunculopontine nucleus and the nucleus basalis of Meynert and the serotonergic neurons of the raphe nuclei. Degeneration within these regions most likely contribute to the non-motor symptoms of PD (*25*).

This observation is concordant with Lewy body (LB) pathology, the other neuropathological hallmark of PD, which is not restricted to the SNpc but can also be found in different areas of the central nervous system and in the peripheral nervous system. Lewy bodies are intracellular inclusions that mainly consist of aggregations of misfolded α-synuclein (*29*). These inclusions can

be localized in the cell body (Lewy bodies) but also in neuronal processes (Lewy neurites). LB pathology has been hypothesized to progress in a certain regional pattern from the peripheral nervous system to the central nervous system in a caudal to rostral direction. According to this spreading, Braak staging was introduced, which corresponds with and explains the clinical progression of PD. Braak stages 1 and 2, with LB pathology in the peripheral nervous system and olfactory system correspond with the onset of pre-motor symptoms, whereas motor symptoms appear in stage 3 when also the midbrain starts to be affected by LB pathology (*7, 30*). The spreading of LBs as proposed by Braak et al. is supported by recent evidence for a prion like propagation of α-synuclein (*31, 32*). As α-synuclein aggregates are found in most PD patients and mutations in *SNCA* cause monogenic PD, α-synuclein most likely plays an important role in the pathogenesis of PD. The function of soluble α-synuclein is not fully understood but it seems to be involved in vesicle trafficking and mitochondrial function (*33*). Aggregation of α-synuclein can be triggered by overproduction of the protein, mutations that facilitate its misfolding, or defects in pathways that are involved in its degradation (*3*). Nevertheless, not all PD patients have LB pathology (e.g. some patients with LRRK2 mutations) and LB have also been found in brains of individuals without PD (*34, 35*), which challenges the critical function of LBs in the pathogenesis of PD.

However, α-synuclein aggregates can be linked to neuroinflammation, another pathological hallmark of PD that contributes to PD pathogenesis but is most likely not the initial trigger (*36*). Neuroinflammation has been observed in post-mortem tissue, *in vivo* studies, and animal models. Furthermore.it has been shown that α-synuclein aggregates can induce the innate and adaptive immunity in PD (*37, 38*). Vice versa, neuroinflammation has also been shown to induce α-synuclein misfolding by oxidization and nitration (*39*) implying a vicious cycle. However, a solely pathogenic role of neuroinflammation is not true as recruited and activated microglia can also degrade extracellular α-synuclein. Furthermore, antibodies against α-synuclein have been developed as immunotherapies highlighting a supportive effect of the immune system (*40*).

The described neuropathological hallmarks are not restricted to the DANs of the SN, however specifically these neurons degenerate. Heritable forms of PD have provided great insights into the molecular pathways that are involved in the pathogenesis of both fPD and sPD, like α-synuclein proteostasis, mitochondrial dysfunction, and oxidative stress. Nevertheless, the reason for the selective vulnerability of the SNpc DANs to these stressors remains a key question. Considering the physiology of this neuronal subpopulation it seems to be a combination of different characteristics [reviewed in (*25, 35*)]. At first, DANs of the SNpc (in contrast to the ventral tegmental area (VTA)) are some of the most highly arborized neurons in the nervous system and therefore require an enormous amount of energy. Having such high energetic demands, there is little capacity for further energetic stress which makes them susceptible to mitochondrial oxidative stress (*35, 41*) Secondly, SNpc DANs are autonomous pace makers, which involves large oscillations of intracellular calcium (Ca^{2+}). Ca^{2+} also enters the mitochondria and stimulates oxidative phosphorylation (OXPHOS) and adenosine triphosphate (ATP) production to meet the energetic demands. However, this also promotes chronically high reactive oxygen species (ROS) production, which might become more severe with age when mitochondrial function declines (*42, 43*). Furthermore, the unstable nature of the neurotransmitter dopamine itself might be a culprit for the vulnerability of these neurons. Normally dopamine is contained inside synaptic vesicles, however when in the cytosol, dopamine spontaneously oxidizes to dopamine o-quinone and

aminochrome leading to the formation of highly reactive superoxide radicals in the process. This can be prevented by the enzymatic metabolization of dopamine by the monoamine oxidase. However, this is also accompanied by the formation of hydrogen peroxide, which is less reactive than other ROS but nevertheless elevates the oxidative stress levels (*44, 45*). Finally, the high iron content of SNpc DANs which accumulates with age in the SNpc (*46*) can also contribute to the formation of ROS via the Fenton reaction and can enhance the auto-oxidation of dopamine (*45*). Here, the biopigment neuromelanin, which consists amongst others of molecules involved in the catecholamine metabolism has a protective role in the redox homeostasis of DANs by sequestering redox-active iron and toxic chemicals. However, alterations in the neuromelanin composition and density have been associated with elevated ROS production and were observed in PD patients (*45*). Taken together, the high energetic burden of SNpc DANs places them at the edge of neurodegeneration, which can be linked to the affected molecular pathways. ROS and reactive nitrogen species can negatively affect a cell's ability to cope with proteostatic challenges and thus enhance α-synuclein aggregation (*47*). This can further exacerbate mitochondrial dysfunction by inducing complex I deficiency (*48*), leading to a vicious cycle of ROS generation and selective cell death of SNpc DANs promoted by their physiology and age.

1.1.5 Models of Parkinson's Disease

Pathology of PD can only be examined post-mortem in humans, thus there is a great need for experimental models to unravel the molecular mechanisms involved in the pathogenesis. The great heterogeneity of PD with regard to etiology and clinical phenotypes requires different models to analyze the various aspects underlying PD. Animal as well as cellular models have been used frequently and exhibit different advantages and limitations as discussed in the following paragraphs.

1.1.5.1 Animal models of PD

Rodents, non-human primates, and non-mammalian species have been used to model PD, however, most studies are performed in rodents which are easy to maintain and show a correlation between nigro-striatal dopaminergic degeneration and motor deficits that can be assessed in well-established behavioral tests (*49*). Similar to the etiology, there are mainly two approaches to model PD in animals: neurotoxic models and genetic models.

Neurotoxic models represent the classic PD models which try to reproduce the pathological and behavioral changes of PD by injection of pharmacological agents that result in the selective degeneration of nigrostriatal DANs. Thus, these agents modulate the pathology associated with environmental stimuli. The common neurotoxins that are used are MPTP, 6-hydroxydopamine (6-OHDA) as well as the pesticides rotenone and paraquat. Depending on the agents' ability to cross the blood-brain barrier (BBB), administration can either be systemically (MPTP, rotenone, paraquat) or locally (6-OHDA) (*50*). In general, all toxin-based models exhibit strong and rapid cell loss induced by inhibition of mitochondrial complex I and recapitulate motor symptoms and some behavioral changes (*51–53*). Dosing (MPTP, 6-OHDA) as well as the site of injection (6-OHDA) can slightly modulate the severity of cell loss and the corresponding phenotype (*52*). Nevertheless, the rapid cell loss also presents one of the weaknesses of neurotoxic animal models, as the slow degeneration of DANs in PD cannot be recapitulated. Another major drawback of neurotoxic animal models is missing LB pathology, except for pesticide models where intracellular

α-synuclein aggregates have been detected (*54*, *55*). The characteristics and limitations of the different neurotoxic animal models are summarized in **Table 2**.

Table 2: Neurotoxic PD models. MPTP: 1-methyl-4-phenyl-1,2,3,6-tetrahydropyridine; 6-OHDA: 6-hydroxydopamine; MFB: medial forebrain bundle; DA: dopamine; BBB: blood-brain barrier. Table modified from (*49*, *52*, *56*).

Toxin	Mechanism	Administration	Characteristics	Limitations
MPTP (neurotoxin)	Inhibition of complex I	systemical	Acute dose: - Rapid and strong dopaminergic neurodegeneration - Strong motor deficit - Decreased striatal DA levels Subacute/chronic dose: - Progressive model - No dopaminergic neurodegeneration - No motor deficit	- Acute damage of the DAergic system - No α-synuclein aggregates - Rats are resistant - Functional recovery in mice
6-OHDA (neurotoxin)	Inhibition of complex I and oxidative stress	local (striatum, MFP, SNpc)	Injection site-dependent lesion: - Rapid and strong dopaminergic neurodegeneration - Strong asymmetric motor deficits - Major behavioral deficits as seen in PD - Decreased striatal DA levels	- Acute damage of the DAergic system - No α-synuclein aggregates - Lack of BBB penetration - High mortality with bilateral injection
Rotenone (pesticide)	Inhibition of complex I	systemical	- α-synuclein aggregates - Moderate dopaminergic neurodegeneration - Some motor deficits - Behavioral impairment	- Low reproducibility - Acute toxicity
Paraquat (herbicide)	Oxidative stress	systemical	- α-synuclein aggregates - Some dopaminergic neurodegeneration	- Lack of striatal dopamine loss in some models - High doses of paraquat cause pulmonary fibrosis

Genetics is an important component in the pathogenesis of PD and animal monogenic PD models have been generated to study the effects of the affected proteins in PD pathogenesis. However, most of the animal models only reproduce some of the hallmarks of PD and fail to induce degeneration of DANs and associated motor symptoms (*49*, *56*). With *SNCA* being the first gene linked to PD, a lot of research has been focused on α-synuclein models. Transgenic models of the autosomal dominant missense mutations (A53T, A30P, and E46K), duplications, and triplications have been generated. Although neuronal α-synuclein inclusions have been found in some models, only few show degeneration of the dopaminergic nigrostriatal system (*57*, *58*). Thus, these mice are an interesting model to elucidate the function of α-synuclein. However, the relevance of this model for PD is limited. Viral vectors that induce overexpression of wildtype (WT) and mutated forms of *SNCA* as well as preformed fibrils have been used to induce pathology in adulthood. Both approaches can achieve progressive dopaminergic cell loss and motor deficits (*59*, *60*), however, both models are invasive, viral vectors might interfere with downstream experiments, and results and reproducibility could be another issue. Transgenic models of the other autosomal dominant PD gene *Lrrk2* have been unsuccessful in recapitulating PD hallmarks. Overexpression of G2019S *Lrrk2* leads to mild degeneration of SNpc DANs (20%) but alterations in locomotor activity or striatal dopamine level were not detected (*61*). Mutations in the genes causing autosomal recessive PD *Prkn*, *Pink1*, and *Dj1* are loss of function mutations. Therefore, knockout (ko) models have been generated. Some models have abnormalities in striatal dopamine levels or release and mitochondrial dysfunction, however, none of these models shows degeneration of DANs and motor

impairment (*49, 62*). The features and limitations of the genetic PD models are summarized in **Table 3**.
None of the existing animal models is able to replicate all pathological and phenotypical features of PD. Nevertheless, they significantly contributed to our understanding of the various molecular pathways that are involved in PD.

Table 3 | Genetic models of PD. DA: dopamine. Table modified from (*49, 56*).

PD model	Characteristics	Limitations	Use
SNCA transgenic rodents **Point mutations (A53T, A30P, E46K) and overexpression of α-synuclein**	- Widespread α-synuclein aggregation - Some motor deficits	- No significant DA neuron loss - May affect development	- Models familial mutations of SNCA - Study α-synuclein function/propagation and synucleinopathies
Viral transfection of α-synuclein	- α-synuclein aggregates - Moderate DA neurodegeneration - Moderate motor deficits	- Potential vector toxicity and interference of viral vector - Invasive	- Study α-synuclein function, propagation, and synucleinopathies - Potential preclinical use
α-synuclein preformed fibrils	- Widespread α-synuclein aggregation - Mild DA neurodegeneration - Some motor deficits in mice	- Slow/weak onset of pathology - Invasive	- Study α-synuclein function/propagation and synucleinopathies
LRRK2	- Little DA neurodegeneration - Most lack motor deficits	- No significant DA neuron degeneration - Lacking α-synuclein inclusions	- Useful for LRRK2 functional study - Therapeutic target and useful for LRRK2 targeted drug test
Parkin, PINK, DJ-1	- Some abnormalities in striatal DA level - Affects aggregation in α-synuclein models - Lack clear motor deficits	- No DA neurodegeneration - Lacking α-synuclein inclusions - Large number of identified mutations	- Study role of Parkin, PINK1, and DJ-1 - Used in combination with α-synuclein or MPTP models to study interaction

1.1.5.2 Cellular models of PD

Animal models provided great insights into the pathology of PD. However, there are also some limitations. First, modeling of sPD is very difficult as most transgenic models are based on familial mutations. In addition, although the physiology between humans and rodents is quite similar, there are some differences. For example, the metabolism of MPTP differs and there are species-specific differences in transcription factor binding sites which might have an influence on variable gene expression (*63, 64*). Lastly, studies of animal models are time-consuming, cost-intensive, and associated with ethical concerns (*65*). To avoid these limitations, cellular models have also been used, as they develop the pathology more quickly, are easier to genetically manipulate, are quick and cost effective, and suitable for large scale screens and molecular studies (*65*).
Cells lines that can be differentiated to show a dopaminergic phenotype like the Lund human mesencephalic (LUHMES) cells and the neuroblastoma cell line SH-SY5Y have been used in the past and still are used (*65, 66*). Aggregation of α-synuclein pathology can also be modeled *in vitro* by overexpression in HEK293 cells.
However, with the discovery of Takahashi and Yamanaka (*67*) new possibilities for human stem-cell based disease modelling arose. Human induced pluripotent stem cells (hiPSCs) enabled researchers to conduct experiments on patient-derived cells and thus also allowed modeling of sPD (*68*). In addition, genetically modified hiPSCs allow the investigation of genes causing fPD in a

human context. Protocols to differentiate hiPSCs into various cell types including DANs, microglia, and astrocytes have been developed. As cell-cell interactions might be crucial in PD, the ability to differentiate hiPSCs into organoids, 3D organ-like structures, offers another interesting possibility to study PD *in vitro*.
Therefore, hiPSCs are a great model to study the pathophysiology in a human genetic background, nevertheless, cellular models lack complete physiological connection and findings still need to be verified in animals.

1.2 Development and maintenance of midbrain dopaminergic neurons

The main neuropathological hallmark of PD is the degeneration of DANs in the SNpc. Understanding how this neuronal subpopulation, is specified, differentiated, and maintained holds promises for the generation of DANs for regenerative therapy as well as for the identification of neuroprotective factors. Midbrain DANs (mDANs) are located in three distinct nuclei, the SNpc (A9), the VTA (A10) and the retrorubral field (A8) (*69*).
During gastrulation, posterior-to-anterior cell migration is accompanied by the formation of the three germ layers, ectoderm, mesoderm, and endoderm. The expression of a set of inhibitors like *Dkk1, Nog* and *Lefty1* at the rostral end of the embryo suppresses posterior signals and leads to anterior-posterior pattering of the neural ectoderm and formation of the anterior neural tube (*70*). Two signaling centers are formed in the process, the isthmic organizer (IsO) which determines the mid-hindbrain boundary (MHB) and the floor plate (FP) which controls ventralization. Both, the IsO and the FP mediate various events including regional identity, specification, and proliferation of mDAN progenitors, as well as differentiation and survival of mDANs. These processes are mediated by the induction of a network of various transcription factors (**Figure 2**) (*69*). Formation of the IsO is a crucial patterning event and starts at E7.5 in mice through the coordinated expression of the transcription factors *Otx2* in the midbrain and *Gbx2* in the hindbrain (*71, 72*). Both transcription factors repress each other and control the expression of the morphogens *Wnt1* and *Fgf8* in the midbrain and hindbrain, respectively. Fgf8 but not Wnt1 is required for the induction of the IsO (*73*). The Fgf8 gradient secreted by the IsO subsequently specifies hindbrain identity (high concentration) and midbrain identity (lower concentrations) in the more anterior regions. Both events also require *Wnt1* expression (*74*). The second important patterning event of the neural tube is dorso-ventral patterning initiated by the morphogen *Shh*. Shh initially secreted by the notochord induces the expression of *Foxa2* and thus specifies the most ventral part of the neural plate, the FP. The FP eventually starts to secrete Shh and becomes a secondary ventral organizer. Depending on the Shh level, another set of transcription factors is activated leading to dorso-ventral patterning of the neural tube. Low levels of Shh in the dorsal region result in upregulation of *Nkx6-1* and *Otx2*, whereas high levels of SHH upregulate *Foxa2* which inhibits *Nkx2-2* expression in the midbrain FP (mFP) (*69*). mDAN progenitors are marked by the expression of *Foxa1/2* and *Otx2* which regulate the transcription factors *Lmx1a* and *Lmx1b*. Lmx1a is necessary for the specification of mDAN in the mFP and mediates the repression of basal plate fates via *Msx1* expression (*75*). Lmx1b is required for the differentiation of mDAN progenitors (*76*). The coordinated interplay of the *Shh-Foxa2* and the *Otx2-Wnt1-Lmx1a/b* networks is crucial for the specification of the mFP and the suppression of alternative fates.

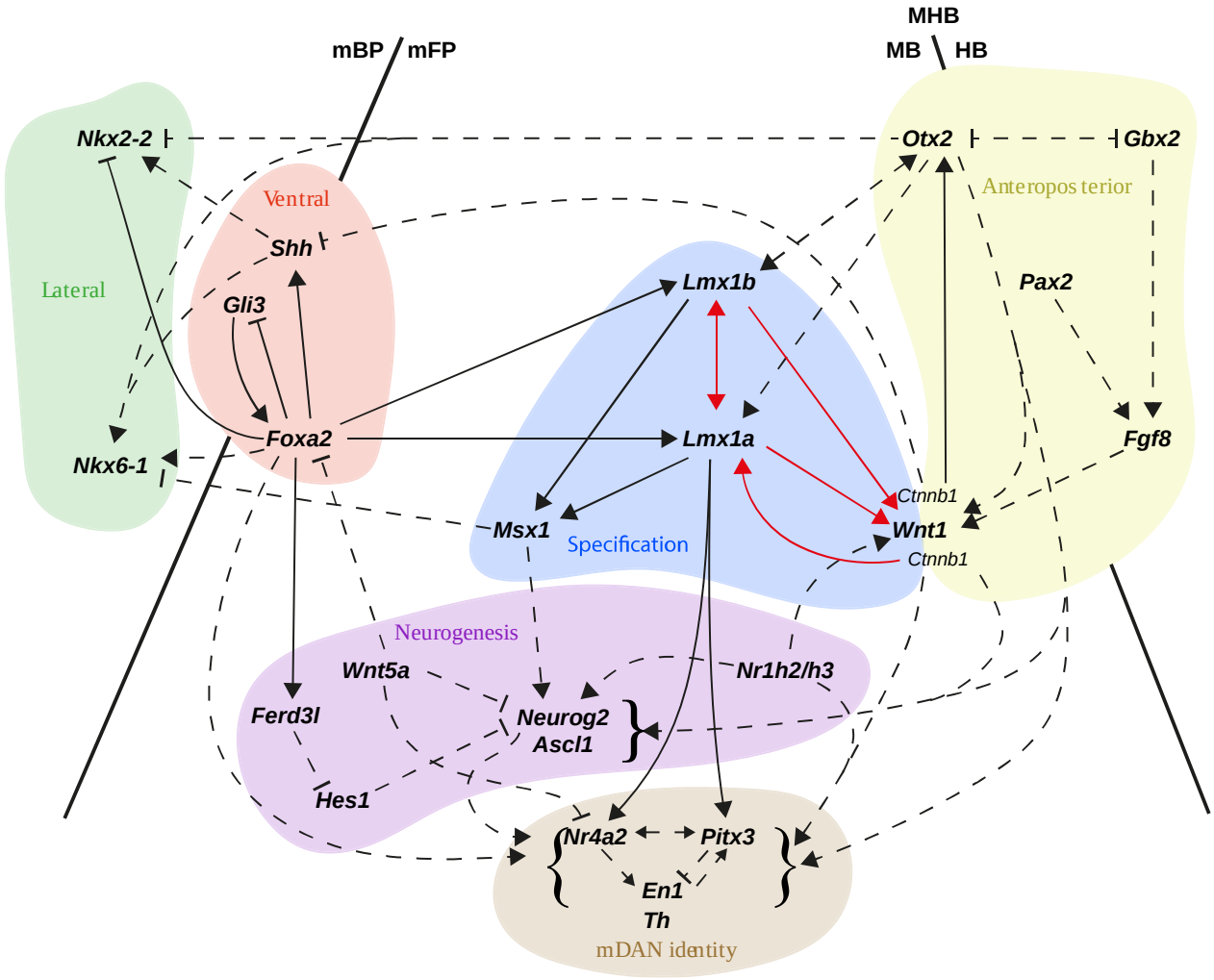

Figure 2: Genetic networks that control mDAN development. The Otx2-Gbx2-Wnt1 and the Shh-Foxa2 networks are responsible for anteroposterior (yellow) and dorso-ventral (red) patterning, respectively. They then also coordinately control the specification (blue), neurogenesis (purple) as well as differentiation and survival of mDANs (brown). Solid lines indicate direct interaction which were shown by chromatin immunoprecipitation. All other interactions are depicted by dashed lines. Arrowheads indicate activation and perpendicular lines indicate inhibition. mBP: midbrain basal plate; mFP: midbrain floor plate; MB: midbrain; HB: hindbrain; MHB: midbrain-hindbrain boundary. Figure adapted from (*69*).

During mDAN differentiation the cells migrate from the radial glia cell-containing ventricular zone through the intermediate zone towards the outer mantel zone, where postmitotic tyrosine hydroxylase (Th) positive cells appear. In rodents, the first mDANs emerge at day E10.5, whereas in humans mDAN neurogenesis begins 5 to 6 weeks post conception. The pro-neural genes *Ascl1* and *Ngn2* which are regulated by the *Shh-Foxa2* and *Otx2-Wnt1-Lmx1a/b* networks are expressed in the ventricular zone and control mDAN neurogenesis together with the morphogen Wnt5a. Differentiation of the postmitotic neuroblasts that migrate towards the mantel zone is mediated by the early genes *Foxa1/2*, *Otx2* and *Lmx1a/b* and the homeobox genes *En1/2* (see also1.3.2). The early genes induce the expression of late transcription factors like *Nurr1* and *Pitx3* which are involved in mDAN differentiation, survival, and the acquisition of the appropriate neurotrophic factors and neurotransmitter phenotype (*69*). Besides Lmx1a/b which directly regulates *Nurr1* and *Pitx3*, *Wnt1* is also important for the survival of mDANs and *Pitx3* expression (*77*). In addition to being crucial regulators of terminal mDAN differentiation, *Nurr1*, *Pitx3*, and *En1* which remain

expressed in adult mDANs are also required for their survival and maintenance. Insights into the mDAN differentiation process enabled the generation of this subpopulation from hiPSCs and embryonic stem cells for disease modeling. Furthermore, understanding the role and targets of the survival factors like En1 provide new opportunities for the development of possible therapies. Thus, in addition to the PD causing genes, transgenic mice harboring homozygous and heterozygous ko's of transcription factors *Nurr1*, and *En1* have also been investigated. Homozygous *Nurr1* and *En1* ko's fail to differentiate DANs or exhibit broad developmental defects, respectively and die shortly after birth (*78, 79*). However, mice heterozygous for *Nurr1* and *En1* show progressive degeneration of DANs accompanied by motor deficits and also behavioral changes in the case of *En1*+/- mice (*80, 81*). Hence, these mice recapitulate a PD-like phenotype, although α-synuclein aggregates are missing. Nevertheless, these results indicate that pathways downstream of the crucial DAN maintenance transcription factors like Nurr1 or En1 might be of importance regarding PD intervention and treatment.

1.3 Engrailed

Engrailed and its importance in development was first characterized in *Drosophila melanogaster* but has been investigated in many different organisms since. Two *engrailed* homologs, *engrailed1* (*En1*) and *engrailed2* (*En2*) exist in most vertebrate species including humans and mice (*82*).

1.3.1 Structure and properties of Engrailed

Engrailed genes belong to the homeobox gene family and encode homeodomain-containing transcription factors. Although the two homologs *En1* and *En2* only share 55 % of their amino acid identity, the biochemical function is quite similar. This can be explained by five distinct, yet highly conserved subregions in the Engrailed proteins, the *Engrailed* homology regions (EH) 1-5, which have been identified by sequence comparisons between species (*83, 84*). EH4 contains the approximately 60 amino acid long homeodomain which shows the highest level of conservation between species (*83*). The homeodomain contains three alpha helices which mediate binding to the DNA (*85*) and thus Engrailed's function as a transcriptional regulator. Engrailed mainly functions as passive transcriptional repressor by competing with specific activators for binding sites upstream of the basal promotor (*86, 87*) and also by competition with transcription factor II D (TFIID) for binding to the TATA box (*88*). All other subregions are important for interactions with other proteins. EH1 and EH5 are involved in Engrailed's function as an active transcriptional repressor. To execute this repression, EH1 requires binding to the co-repressor graucho (*89*). Engrailed can also bind to the other homeodomain-containing transcription factors PBX/extradenticle via the EH2 and EH3 subregions (*90*). Binding to PBX/extradenticle, has an impact on the affinity of Engrailed proteins to the DNA, can redirect them to different targets and controls whether Engrailed proteins function as transcriptional activator or repressor (*91, 92*). Furthermore, the affinity of Engrailed to the DNA can be modified by phosphorylation of a serine-rich site N-terminal to EH2 (*82*).

Although being a transcription factor, Engrailed proteins also regulate expression of target genes by modulating mRNA translation (*93, 94*). This process is mediated through the mammalian target of rapamycin (mTOR) pathway and binding to the eukaryotic translation initiation factor 4E (eIF4E). This has been observed at first for En2 in the guidance of retinal growth cones (*93*), but

seems to be a property of many homeodomain proteins (*95*). Engrailed proteins function as transcriptional and translational regulators which are normally localized in the nucleus. However, Engrailed proteins have also been detected in the cytoplasm associated with membrane vesicles. This led to the discovery of another interesting property of Engrailed. Around 5 % of intracellular Engrailed is secreted and internalized by other cells (*96–98*). Engrailed lacks a classical secretion signal but a small region between helix 2 and 3 in the homeodomain resembling a class of nuclear export signals is necessary for the nuclear export and secretion (*98*). Internalization is also mediated by a region in the homeodomain (helix 3) (*99*). This suggests an additional function of Engrailed as intercellular polypeptide messengers.

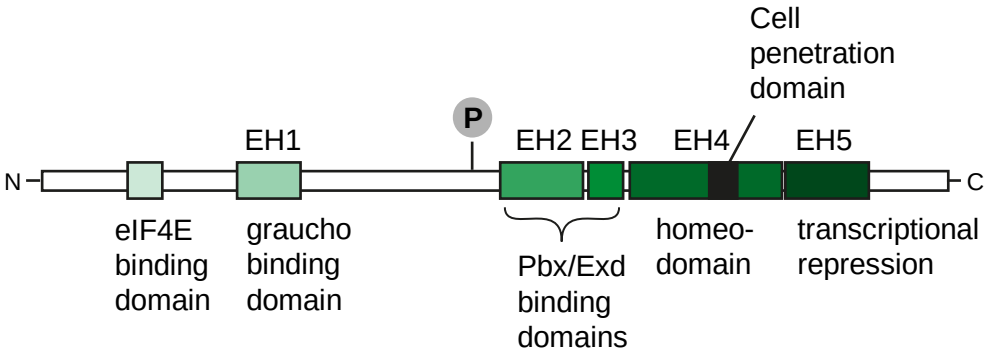

Figure 3: Engrailed homology (EH) regions and their function. The conserved domains of the *Engrailed* genes are depicted. EH4 contains the homeodomain, EH1 and EH5 mediated active and EH2 and EH3 passive repression of transcription. The eIF4E binding sites is responsible for the modulation of translation. Figure adapted from (*82*) (*100*).

1.3.2 Function of Engrailed in the development and maintenance of dopaminergic neurons

The transcription factors En1 and En2 are essential during the development and maintenance of mDANs. They are required for at least two distinct events during the development, the regionalization and the survival of post-mitotic mDANs (*101*).

Expression of *En1* and *En2* starts at around embryonic day (E) 8 (all data are referring to mouse development) in a region that will give rise to the mid-/hindbrain border. At this stage, Engrailed is involved in the maintenance of FGF8 expression, which is important for correct mid-/hindbrain patterning (*102*). *En1* null mice thus show amongst others an early mid/hindbrain deletion at E9.5 and die within 24 hours after birth (*79*). In contrast to this, *En2* null mice do not exhibit such a severe phenotype. These mice have a smaller cerebellum and postnatal alteration of cerebellar foliation (*103*). Replacing *En1* with *En2* in the *En1* locus, the severe phenotype of *En1* null mice could be rescued, showing that En1 and En2 are functionally redundant during early patterning events (*84*). The different phenotypes can be explained by a slightly different expression pattern during early embryogenesis. *En1* expression begins already at the one-somite stage, whereas *En2* expression is initiated at the five-somite stage and their expression overlaps only at the eight-somite stage (*84*, *104*). This lack of En1 in the beginning is therefore crucial for the phenotypic differences between the two *Engrailed* mutants.

Furthermore, the expression of *Engrailed* is essential for the survival of mDANs in a dose-dependent manner. Although exhibiting a strikingly different phenotype, both *En1* null mice and *En2* null mice have a normal distribution and packaging of DANs in the SN and VTA at postnatal day (P) 0. In double mutants, however, mDANs of the VTA and SN are completely absent at P0, indicating that En1 and En2 can compensate for each other. Interestingly they do so in a gene-dose

dependent manner. A single allele of *En1* on an *Engrailed* null background is sufficient to maintain a normal phenotype whereas one allele of *En2* is not. Despite being lost at day P0, DANs are induced and acquire their neurotransmitter phenotype in *Engrailed* null mutants (E11) but die by apoptosis soon thereafter (E14). This indicates that differentiation is independent of Engrailed but its expression in mDAN progenitors starting around E11 is crucial for mDAN survival in a dose-dependent and cell-autonomous manner (*105, 106*). Furthermore, both *En1* and *En2* remain expressed in adult DANs but similar to what has been observed during development, their expression pattern differs. *En1* is expressed throughout the SN and the VTA, whereas *En2* is only expressed by a subset of DANs (*105*).

The importance of En1 and En2 for the survival of DANs has also been strengthened by observations made in mice heterozygous for *En1*. Whereas *En1* null mice die at birth and exhibit an abnormal distribution of DANs in the ventral midbrain, animals heterozygous for *En1* show no DAN-specific phenotype at birth, but then experience degeneration of DANs (*80, 107*). Depending on the presence of En2 and the background of the mice, the timing of DAN degeneration and the affected populations are distinct. In *En1* heterozygous animals on an *En2* null background, the degeneration starts already 2 weeks after birth and DAN numbers continue to decrease until 3 months after birth (loss of 32 % of DA neurons). Here, the loss is selective for SN DANs (*107*). In contrast to that, *En1* heterozygous animals on an *En2* WT background experience DAN degeneration starting at about 8 weeks after birth and reaching a plateau at the age of 6 months (38 % of loss). In addition to the SN, DAN loss is also observed in the VTA, but to a lower extent. This decline could be rescued by injection of En2, confirming the role of Engrailed as a survival factor (*80*). Interestingly, the degeneration of DANs in *En2* WT animals was only observed on a Swiss genetic background but not on a C57/BL6 background, implying that despite the dose also other genetic variables are important for the protective function of the Engrailed proteins (*80, 107*).

1.3.3 Engrailed1 and its implications in Parkinson's Disease

There is increasing evidence that disruption of *En1* might be associated with PD. Some studies reported that *En1* polymorphisms are associated with an increased risk of PD, however, the studies were small and results from larger cohorts could not replicate these findings (*108*).

Nevertheless, the most striking connection has been observed in heterozygous *En1* knockout ($En1^{+/-}$) mouse models (see also 1.1.5.1 and 1.3.2.), which display a PD like phenotype. One of the main hallmarks of PD, the slowly progressive degeneration of DANs in the SNpc is recapitulated in this model (*80, 107*). Similar to what has been observed in PD patients, the DANs in the lateral ventral part of the SNpc preferentially die in $En1^{+/-}$ mice (*80*). Furthermore, signs of axonal degeneration and reduced striatal dopamine have been observed in these mice before any DANs are lost (*109*). Again, this is identical to the progressive retrograde degeneration of nigrostriatal neurons that is believed to occur in PD patients (*110*). Accompanying the pathological changes, $En1^{+/-}$ mice also exhibit impaired motor skills including abnormal spontaneous motor behavior and deficits in motor coordination as well as non-motor phenotypes like depressive and anhedonic-like behavior (*80*). The loss of DANs in $En1^{+/-}$ mice can be antagonized by infusion of biochemically equivalent En2 into the midbrain, thus supporting its role as a survival factor. The survival effect can at least partially be explained by suppression of the neurotrophin receptor $P75^{NTR}$ that induces cell death via repression of the Erk1/2 survival pathway. Furthermore, the dose of Engrailed determines the vulnerability of DANs to mitochondrial insults, one of the major pathogenic

pathways associated with PD (*111*). The connection of En1 to mitochondria has also been strengthened by the regulation of complex I. Although being a transcription factor, En1 can also regulate gene expression on a post-transcriptional level. Two interesting targets that are regulated by En1 are key subunits of the complex I of the respiratory chain (Ndufs1 and Ndufs3). Enhanced translation of these two subunits mediates the neuroprotective effect of En1 against MPTP in a toxin-based MPTP mouse model (*94*). Reduced levels of NADH:Ubiquinone oxidoreductase core subunit S1 (Ndufs1) and NADH:Ubiquinone oxidoreductase core subunit S3 (Ndufs3) in the SNpc of *En1*$^{+/-}$ mice further support the association of En1 and complex I. Besides the MPTP model, the neuroprotection was not only observed in the 6-OHDA toxin model which, like MPTP, also targets complex I but also extends to α-synuclein toxicity (*94*). Furthermore, following acute oxidative stress, Engrailed protects DANs from DNA damage, apoptosis and restores heterochromatin marks. Thus, besides mediating short-term survival by translational modification, Engrailed seems to act also as a transcriptional and epigenetic regulator to secure long-term survival of DANs (*112*). These results support the relevance of En1 as a survival factor and highlight the link between Engrailed and PD.

Defects in mitochondrial homeostasis and quality control are also associated with impaired mitochondrial function. During this process, damaged mitochondria or mitochondrial proteins are normally degraded by autophagy of mitochondria, a process called mitophagy. There is extensive evidence from familial PD as well as from post-mortem PD patients, that defective mitophagy and dysregulated autophagy are involved in the pathogenesis of PD (*113, 114*). Interestingly, signs of decreased autophagy have also been observed in *En1*$^{+/-}$ mice. A reduction of the autophagic marker LC3B was observed in SN DANs, which was accompanied by elevated levels of mTOR, which inhibits autophagy. This suggests that En1 deficiency also results in an imbalance of protein degradation as observed in PD, further supporting the validity of the mouse model and its relevance for PD. One of the major pathological hallmarks of PD is the aggregation of α-synuclein. Although *En1*$^{+/-}$ mice do not display α-synuclein pathology, induced α-synucleinopathy by injection of pre-formed fibrils is enhanced in mice lacking one allele of *En1 (115)*.

The association with some of the key culprits of PD, like mitochondrial dysfunction, oxidative stress, dysfunctional autophagy, and α-synuclein pathology implies that En1 is an important mediator of DAN health and an interesting protein to investigate in terms of the molecular pathophysiology of PD.

1.4 Wnt signaling

Another pathway that is essential for DAN development is the Wnt signaling pathway. Especially Wnt1 plays a pivotal role in the specification and differentiation of mDAN progenitors (*69, 116*). Wnt1 signals through the evolutionary conserved Wnt/β-catenin pathway that is not only crucial during development but being involved in neuronal death/survival, synapse formation and plasticity, axonal extension, neurogenesis, and regeneration, remains important in the adult brain as well (*117, 118*). Wnt proteins are secretory glycoproteins that induce the signaling cascade by binding to transmembrane receptors of the Frizzled family and the co-receptor LRP5/6. In the absence of Wnt ligands, the glycogen synthase kinase 3β (GSK-3β) and the casein kinase (CK1) are sequestered in a destruction complex and phosphorylate β-catenin, marking it for ubiquitination and degradation in the proteasome (**Figure 4**). Upon binding of Wnt to Frizzled and LRP5/6,

Dishevelled (Dvl) and the destruction complex translocate to the plasma membrane. Through several phosphorylation steps, the GSK-3β activity is inhibited. β-catenin is not targeted for degradation anymore, thus accumulates, translocates to the nucleus where it forms a complex with Lef1/Tcf and induces transcription of Wnt target genes (*117–119*). This is referred to as the canonical Wnt signaling pathway. Wnt can also relay signals independent of β-catenin through the non-canonical pathways, the planar cell polarity (PCP) pathway and the Wnt-Ca^{2+} pathway. Signaling through the Wnt-Ca^{2+} pathway is accompanied by the recruitment of Dvl to the receptors and the activation of heterotrimeric G-proteins. This leads to activation of the phospholipase C, formation of inositol 1,4,5 triphosphate (IP3) and intracellular Ca^{2+} release. Increased Ca^{2+} levels activate Ca^{2+}-sensitive proteins like protein kinase C (PKC) and Ca^{2+}/calmodulin-dependent protein kinase II (CaMKII), which can modify different signaling components, amongst others they can regulate nuclear factor of activated T cells (NFAT) and its target genes (**Figure 4**). In the Wnt-PCP pathway, Dvl activates the small GTPases RhoA, Rac1, and Cdc42. The small GTPases activate the c-Jun N-terminal kinase (JNK), which leads to modifications of the cytoskeleton and activation of transcription via AP1 (*118, 120*) (**Figure 4**). As mentioned above, especially canonical Wnt signaling is crucial in DAN development and thus it is not surprising that Wnt1 has been investigated in the context of PD.

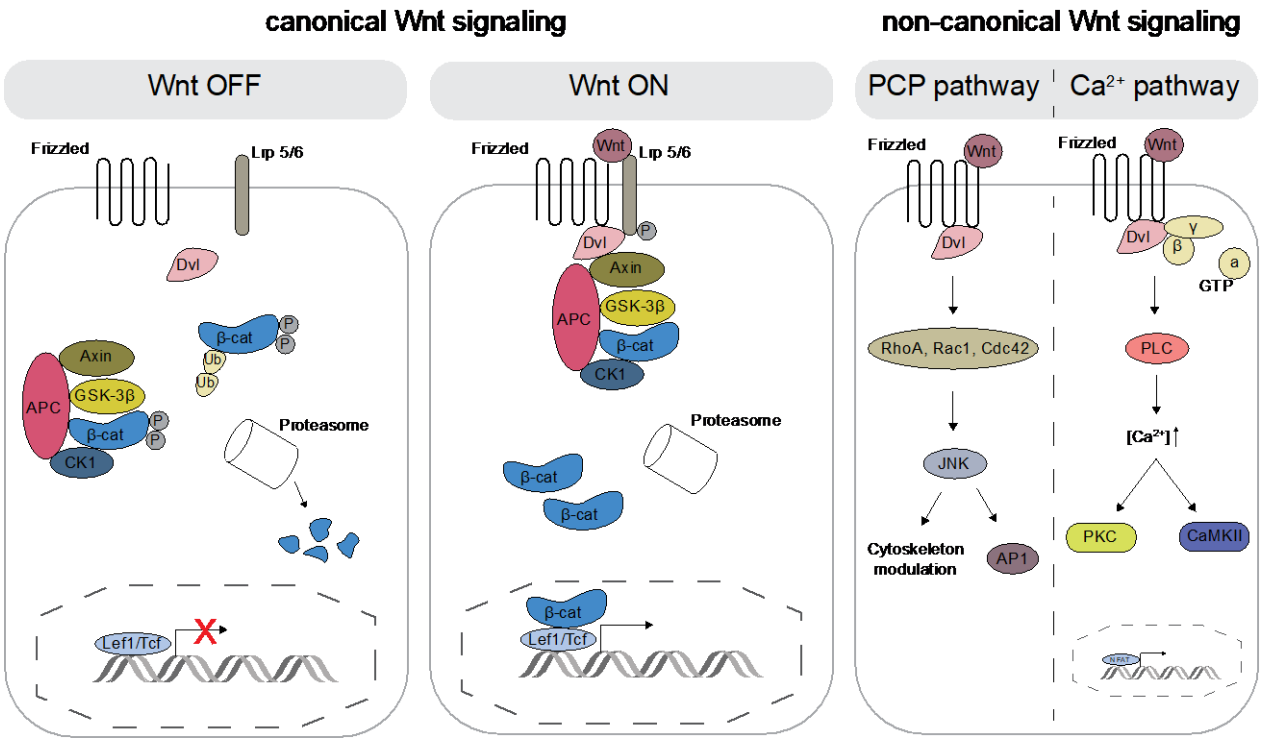

Figure 4: Canonical and non-canonical Wnt signaling pathways. Signaling via the canonical Wnt signaling pathway, prevents the phosphorylation and degradation of β-catenin, which can then induce gene expression of Wnt target genes by binding to Lef1/Tcf. Wnt signaling via the planar cell polarity (PCP) pathway leads to modulation of the cytoskeleton and transcription mediated by JNK. The Wnt-Ca^{2+} pathway leads to an increase of Ca^{2+} in the cell and activation of Ca^{2+} dependent proteins like PKC and CaMKII which regulate transcription of NFAT target genes. Figure adapted from (*117, 118*).

1.4.1 Wnt signaling and PD

There is growing evidence that especially canonical Wnt/β-catenin signaling (in the following referred to as Wnt signaling) is associated with neuronal health. Therefore, it is not surprising that

its dysregulation has been observed in PD patients and rodent models of PD (*117*). Similar to Engrailed, Wnt1 has been attributed a neuroprotective effect.
Initially, Wnt signaling was discovered to be a candidate pathway for neuroprotection as Wnt1 was upregulated in activated astrocytes of the ventral midbrain in response to MPTP treatment (*121*). In recent years, *in vivo* and *in vitro* experiments have shown that Wnt/β-catenin signaling protects DANs from different cytotoxic insults, like 6-OHDA and MPTP (*122*). In addition, the secretion of Wnt1 from astrocytes declines with age, rendering aged astrocytes incapable to protect DANs from degeneration (*123*). These findings strengthen the neuroprotective role of Wnt1, as age is the largest risk factor for PD. Besides the findings in neurotoxic PD models, there is also evidence for the neuroprotective effect of Wnt1 in $En1^{+/-}$ mice, as ectopic Wnt1 expression under the *En1* promotor ($En1^{+/Wnt1}$) could rescue the loss of the DANs (*124*). This confirms the results obtained with the MPTP mouse model and also implies that Wnt1 might act upstream of En1.
The mechanisms that are discussed to be responsible for the neuroprotective effect are amongst others protection from apoptosis (*122, 124*) as well as inflammation (*125*). However, molecular mechanism of Wnt1 neuroprotection have not been fully elucidated so far, but they might be associated with the same pathway En1 is involved in.

1.4.2 Wnt signaling and Engrailed

Like Engrailed, Wnt signaling has a pivotal role in midbrain specification and mDAN development (*69*). Analysis of the *Wnt1* knockout mice, which lack most of the midbrain and rostral parts of the metencephalon already indicated the importance of canonical Wnt signaling (*74*). Interestingly, the phenotype of the *Wnt1* null mice resembles the one observed in *En1* null mice (*79*), which is not surprising as their expression is overlapping at around E8 (*126*). This already implied a connection between *Engrailed* and *Wnt1*. Indeed, it has been shown that the maintenance of *En1* expression is a major role of *Wnt1* in midbrain development *(127)*. The interaction between En1 and Wnt1 is direct via LEF/TCF which bind to the *Engrailed* promotor and also seems to be conserved between species (*128, 129*). This regulation is supported by observations made in a study investigating $En1^{+/Wnt1}$ mice. Compared to $En1^{+/-}$ mice, the *En1* mRNA level was increased when *Wnt1* was expressed under the *En1* promotor. Furthermore, the expression of ectopic Wnt1 in the midbrain could rescue the loss of the DANs by activation of a neuroprotective cascade (*124*).
In addition to *En1* being regulated by Wnt1, there is also evidence that En1 is essential for the repression of *Wnt1* during IsO formation in mouse development (*130*). Thus, En1 and Wnt1 form a feedback loop to regulate their expression. If Wnt1 signaling is active, *En1* expression is induced, which then results in repression of *Wnt1* and subsequently also *En1*.
Interestingly, there is also evidence from chick embryos that En positively regulates the expression of *Wnt1* by suppression of negative regulators (*131*). Taken together, both En1 and Wnt1 are involved in the development of DANs and are crucial for their protection. As far as is currently known, the expression is directly linked with En1 being downstream of Wnt1.

1.5 Cellular energy metabolism

Metabolism is defined by all chemical reactions that are required to maintain life. The reactions can broadly be categorized in catabolic and anabolic processes. In humans, catabolic reactions convert fuels (e.g. carbohydrates or lipids) into intermediates and cellular energy. These are then

used for the synthesis of complex molecules (e.g. glucose, triglyceride, amino acids or DNA) in what is called anabolic reactions. The most important, ubiquitously used energy carrier of cells is ATP, which can be hydrolyzed to adenosine diphosphate (ADP) to provide energy for anabolic processes or to maintain cellular homeostasis (*132*). Although accounting only for 2 % of the total body weight, the brain requires 20 % of an individual's energy expenditure. The brain relies on glucose, which is delivered across the BBB, as the main energy source for neuronal maintenance and neurotransmitter generation (*133*). To generate ATP, glucose is at first degraded in glycolysis followed by the tricarboxylic acid cycle (TCA) and OXPHOS to produce ATP and nicotinamide adenine dinucleotide (NADH)/flavin adenine dinucleotide ($FADH_2$), the latter are subsequently used in OXPHOS for further ATP generation (*132*).

1.5.1 Glycolysis

Glycolysis is a series of chemical reactions that converts one molecule of glucose into two molecules of pyruvate and generates in sum two molecules of ATP in the process. Glycolysis does not require oxygen and is thus the first step in both anaerobic and aerobic cellular metabolism. All reactions take place in the cytosol and can be divided into two phases. Phase 1, the energy-requiring phase, uses two ATP molecules to prepare the glucose for the energy-producing phase 2, which generates 4 molecules of ATP. An overview of the 10 chemical reactions of glycolysis is shown in **Figure 5** [reviewed in (*132, 134*)].

The first step of glycolysis is the irreversible phosphorylation of glucose to glucose-6-phosphate by the enzyme hexokinase. Here, one molecule of ATP is invested to trap glucose inside the cell as glucose-6-phosphate is not able to pass the glucose transporters in the cell membrane and to destabilize the molecule. Following the isomerization of glucose-6-phosohate to fructose-6-phosphate, fructose-6-phosphate is phosphorylated to fructose-1,6-bisphosphate by the phosphofructokinase requiring one molecule of ATP. Fructose-1,6-bisphosphate is then split by aldolase into two three-carbon molecules: dihydroxyacetone phosphate and glyceraldehyde-3-phosphate, which exist in equilibrium and can easily be converted into one another. Only glyceraldehyde-3-phosphate is further processed in the second phase, the energy-producing phase of glycolysis. The two glyceraldehyde-3-phosphate molecules are oxidized to 1,3-bisphosphoglycerate by the glyceraldehyde-3-phosphate dehydrogenase, producing two molecules of NADH. In the following reactions of glycolysis, the two phosphate groups from glyceraldehyde-3-phosphate are transferred to ADP to generate ATP. These reactions are catalyzed by the phosphoglycerate kinase and the pyruvate kinase, leading to the generation of four ATP molecules (*132, 134*).

Glycolysis is a highly regulated metabolic process. The most important control element is the phosphofructokinase (PFK), the rate limiting enzyme of glycolysis. The PFK is an allosteric enzyme that is inhibited by high levels of ATP in the cells, indicating that the cell has a sufficient energy level. In addition, fructose-2,6-bisphosphate is a strong activator of PFK. It is generated by phosphofructo-2-kinase/fructose-2,6-biphosphatase (PFKF3B) when high levels of fructose-6-phosphate indicate the need for an increased rate of glycolysis (**Figure 5**) (*132*). Other enzymes that adapt the glycolysis rate are the hexokinase and pyruvate kinase. Depending on the cellular environment (e.g. oxygen conditions or functional mitochondria), pyruvate can either be reduced to lactate by lactate dehydrogenase regenerating NAD+ and restoring the glycolytic redox balance or pyruvate and NADH can be further metabolized in the TCA or OXPHOS, respectively. The

energy stored in glucose is only partially used in the anaerobic conversion of glucose to lactate. The TCA and OXPHOS which require aerobic conditions and functional mitochondria are more efficient (*132*, *134*). Some cells including neurons metabolize glucose via a pathway diverging from glycolysis at the stage of glucose-6-phosphate, the pentose phosphate pathway (PPP) (*135*, *136*). The PPP is an essential source of nicotinamide adenine dinucleotide phosphate (NADPH) which is required for reductive processes in the cell and regeneration of enzymes that protect cells from ROS. The first reaction is catalyzed by the enzyme glucose-6-phosphate dehydrogenase (G6PD) which is rate-limiting and serves as a regulatory element. The activity is controlled by the NADP+/NAPDH ratio, with low levels of NADP+ inhibiting G6PD. The product after the first oxidative reactions is ribose-5-phosphate which can be used for nucleotide biosynthesis or fed back into glycolysis via enzymatic conversions catalyzed by transaldolase and transketolase (**Figure *5***) (*132*). As neurons, are post-mitotic, the PPP is of minor importance for the nucleotide synthesis. However, neurons have a high energetic burden that results in elevated levels of ROS and thus an increased demand for NADPH (*137*).

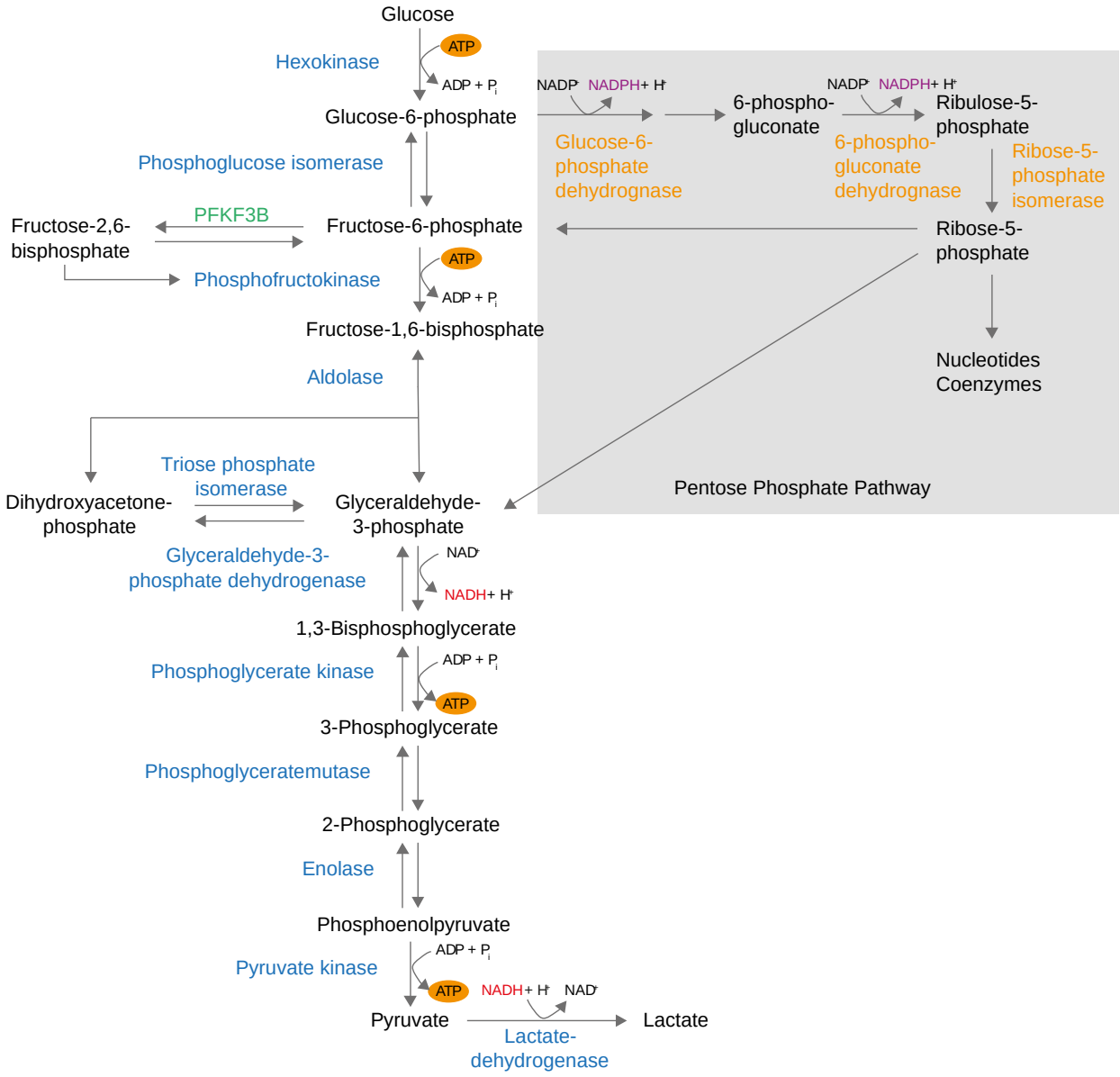

Figure 5: Glycolysis. Glucose is degraded to pyruvate or lactate by the depicted reactions yielding in sum two molecules of ATP and NADH in the process. The pentose phosphate pathway represents an alternative route important for the regeneration of NADPH Figure adapted from (*132, 134*).

1.5.2 Mitochondria

Mitochondria are semi-autonomous, intracellular, membrane-enclosed organelles that are often referred to as the powerhouse of the cell as they are crucial for important metabolic processes including the TCA and OXPHOS. In addition, mitochondria are also involved in other important cellular processes like programmed cell death and Ca^{2+} homeostasis (*138*).
From an evolutionary point of view, it is believed that mitochondria developed from a symbiotic relationship between primordial eukaryotic cells that were unable to use oxygen metabolically and incorporated aerobic bacteria capable of OXPHOS. This also explains why mitochondria contain their own genome as well as transcription and translation system. However, the mitochondrial genome only encodes for 13 OXPHOS proteins whereas the remaining proteins for the respiratory chain are encoded in the nuclear genome (*132, 138*).
Mitochondria consist of two lipid membranes: the outer mitochondrial membrane (OMM) and the inner mitochondrial membrane (IMM). The OMM is permeable for most small molecules and ions, whereas the IMM is impermeable for most ions and polar molecules. Thus, mitochondria have two compartments, the intermembrane space (IMS) and the matrix, which is enclosed by the IMM. All reactions of the TCA take place in the matrix. The respiratory chain complexes are located in the IMM which is densely folded into cristae to increase the surface for OXPHOS (*132, 134, 138*).
Mitochondria are highly dynamic organelles, that undergo constant cycles of fusion and fission and are transported through the cell to locations of high energy demand (*139*). The balance between fission and fusion is crucial for maintaining mitochondrial function. Fusion to large networks optimizes mitochondrial function under conditions of high energy demand by spreading metabolites and enzymes. Fission in contrast, enables mitochondrial trafficking to subcellular locations with high energy demand and mitophagy. Mitophagy is the process of degradation of mitochondria by autophagy in order to remove damaged mitochondria or adjust their number to cellular demands (*140*).
Due to their structure and unique metabolic requirements, neurons do not display a uniform mitochondrial distribution. Synapses or dendritic spines are areas with a high energetic burden and contain more mitochondria than other subcellular locations. Therefore mitochondrial fission and trafficking are especially important in neurons and defects have been implicated in neurodegenerative disease (*138, 139, 141*).

1.5.3 Citric acid cycle and oxidative phosphorylation

The TCA is often described as the center of metabolism. The final oxidation of fuels like carbohydrates, fatty acids, and amino acids occurs in the TCA and its intermediates also serve as valuable components for the biosynthesis of other molecules. The TCA comprises a series of oxidation reactions that result in the final degradation of fuel molecules to carbon dioxide (CO_2). The main function of the TCA is to collect and store the energy-rich electrons as NADH and flavin adenine dinucleotide ($FADH_2$), which are then used to produce ATP during OXPHOS. Thus, the TCA does not require oxygen or produces large amounts of ATP but rather is responsible for the preparatory work for OXPHOS.

During glycolysis, glucose is degraded to two molecules of pyruvate. Pyruvate is then transported into the mitochondrial matrix where it is converted to acetyl-CoA in an irreversible reaction catalyzed by pyruvate dehydrogenase. This reaction also yields two energy-rich electrons which are stored in NADH. The conversion of pyruvate to acetyl-CoA represents the link between glycolysis and the TCA (**Figure 6)**. Acetyl-CoA then enters the TCA in a reaction that combines the two-carbon acetyl group of acetyl-CoA with the four-carbon molecule oxaloacetate to one molecule of six-carbon citrate. Citrate is then isomerized, followed by two decarboxylation reactions to first α-ketoglutarate and succinyl-CoA which are catalyzed by the isocitrate dehydrogenase and the α-ketoglutarate dehydrogenase, respectively. One molecule of NADH is generated in each decarboxylation step. Cleavage of the thioester bond from succinyl-CoA by the succinyl-CoA synthase generates succinate and produces the only molecule of ATP within the TCA. The last part of the TCA comprises reactions to regenerate oxaloacetate yielding one molecule of $FADH_2$ and another NADH. Thus one cycle of the TCA generates a total of four molecules of NADH, one molecule of $FADH_2$ and one molecule of ATP [reviewed in (*132, 134*)].

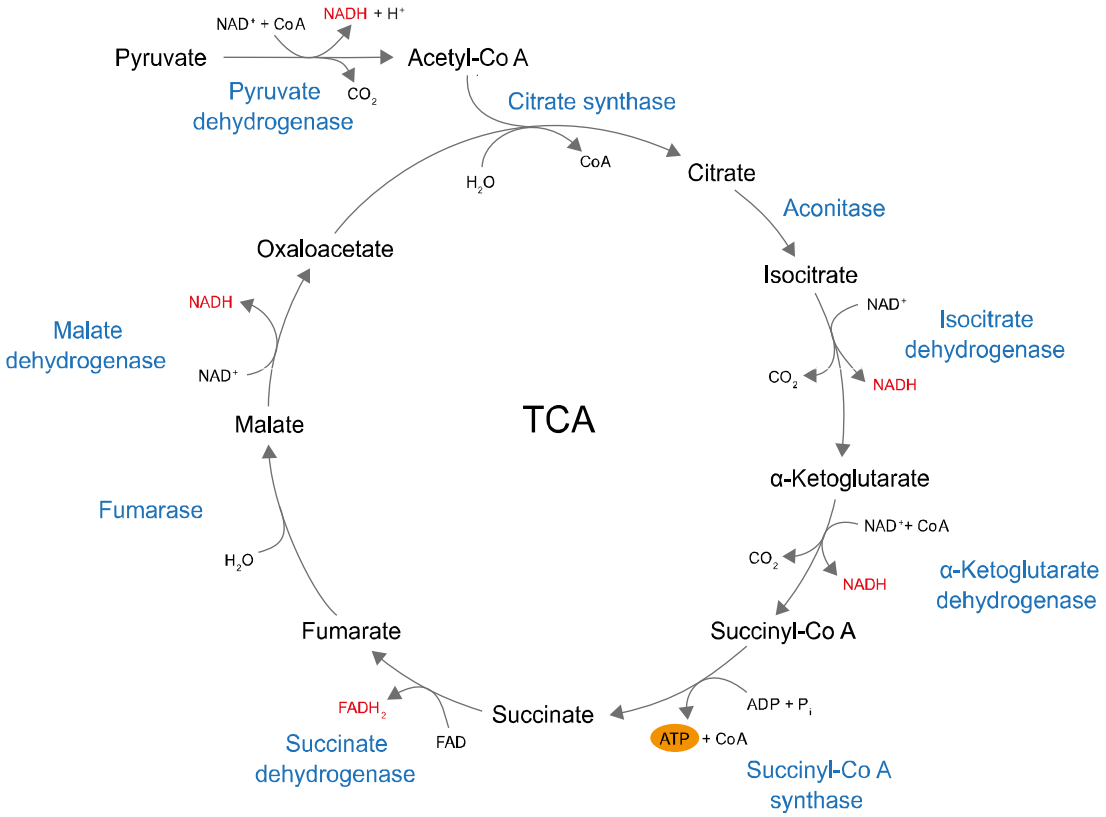

Figure 6*:* Tricarboxylic acid cycle (TCA). Pyruvate is converted to acetyl-CoA and enters the TCA. Passing through the TCA acetyl-CoA is degraded to CO_2 which yields four molecules of NADH (including the conversion of pyruvate to acetyl-CoA), one molecule of $FADH_2$ and one molecule of ATP. Figure adapted from (*132, 134*).

NADH and FADH2 molecules contain electrons with a high transfer potential, which are now in a series of stepwise redox reactions transferred to oxygen (O_2) resulting in the generation of water (H_2O). This process is mediated by four protein complexes located in the IMM which make up the respiratory chain. The redox energy that is released during the transfer of the electrons through the respiratory chain is coupled to the transport of protons from the mitochondrial matrix to the IMS.

The energy stored in the proton gradient over the IMM which is impermeable for ions is used in a final step for the generation of ATP.
All respiratory chain complexes contain electron carriers including iron-sulfur clusters, hemes, flavin, or ubiquinone with increasing electron affinity from complex I to IV. Complex I, also known as NADH-ubiquinone oxidoreductase, is the largest complex of the respiratory chain, that has an L-shaped structure and consists of about 45 subunits (*142*). It oxidizes NADH and transfers the two electrons to ubiquinone, which is reduced to ubiquinol. During this process, four protons are transported across the IMM. The electron carrier ubiquinol has hydrophobic characteristics and diffuses through the IMM to transfer the electrons to complex II. Complex II also known as the succinate dehydrogenase consists of four subunits and is also a component of the TCA. The $FADH_2$ molecule that is generated in complex II directly transfers the electrons to ubiquinone. In contrast to all other respiratory chain complexes, this reaction is not coupled to the translocation of protons. The electrons from ubiquinol are then transferred to cytochrome c in complex III (11 subunits), also known as ubiquinol-cytochrome c oxidoreductase. This is accompanied by the translocation of another four electrons across the IMM. Like ubiquinone, cytochrome c is also mobile and can freely move between the complexes. Complex IV (13 subunits), also referred to as cytochrome c oxidase, accepts the electrons from cytochrome c and reduces the final electron acceptor ½ O_2 to H_2O. Two protons are pumped into the IMS in this final reaction. In addition, both electrons for the generation of H_2O were taken from the matrix contributing also to the proton gradient across the IMM. The transfer of protons across the IMM in the respiratory chain creates an electrochemical proton gradient consisting of a chemical pH gradient and a membrane potential due to the imbalance of positively charged protons. The energy from the electrochemical gradient is used by the ATP synthase, also known as complex V, to generate ATP from ADP and P_i. The ATP synthase spans the IMM and consists of 16 subunits that generate ATP by conformational changes. Therefore, after passing through glycolysis, TCA, and OXPHOS, one molecule of glucose yields in total 30 molecules of ATP with 26 ATP being attributed to OXPHOS [reviewed in (*132*, *134*, *143*)].

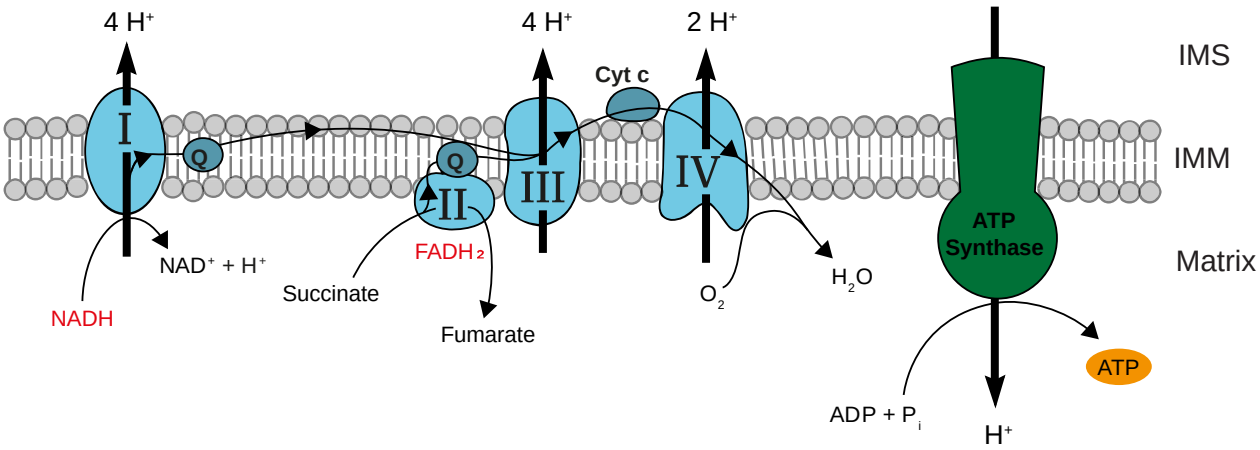

Figure 7: Oxidative phosphorylation. The electron carriers NADH and FADH2 channel the electrons into the respiratory chain where they are transferred in step-wise redox reactions to oxygen. The energy released during these reactions is used to establish a proton gradient over the IMM, which drives the ATP production by the ATP synthase. Cyt c: cytochrome c; IMM: inner mitochondrial membrane; IMS: intermembrane space; Q: ubiquinol. Figure adapted from (*132*).

Despite the highly efficient ATP production, incomplete electron transfer in the respiratory chain is a major source of ROS. Complex III but predominantly complex I are associated with ROS

production even under homeostatic conditions (*144*). Functional impairments of complex I or mutations in genes encoding for subunits of this complex have been associated with an increase in ROS production, which seems to be involved in the pathogenesis of neurodegenerative diseases including PD (*142*).

1.5.4 Mitochondrial function in Parkinson's disease

There is evidence that mitochondrial dysfunction is involved in the molecular pathology of PD. The theory of mitochondria being a central player is appealing as it can at least partially explain the selective vulnerability of the DANs, which have a high energetic burden due to their unique physiology (see also 1.1.4). Thus, especially DANs rely on functional mitochondria and efficient OXPHOS. As mitochondria are associated with the production of ROS, high activity of OXPHOS increases the ROS production and renders the cells vulnerable to additional oxidative stress. Eventually, high oxidative stress levels can result in cell death (*144*, *145*). ROS are species having one or more unpaired electrons like hydroxyl radical or the superoxide anion. Although the cell has a defense system of antioxidant molecules (e.g. glutathione, vitamin E) and enzymes (e.g. superoxide dismutase), ROS can react with and functionally alter proteins, lipids, and DNA, which has deleterious effects on the cell (*145, 146*). As ROS are primarily generated in mitochondria (*144*), these organelles are also particularly vulnerable to be damaged by ROS creating a vicious cycle. Oxidative damage to the respiratory chain proteins might functionally alter them. Furthermore, ROS can react with the DNA, inducing mutations, genomic instability, and non-functional proteins. Especially mitochondrial DNA (mtDNA), which encodes for some subunits of respiratory chain complexes is affected by ROS. In addition, lipids not only make up the plasma membrane but also divide the mitochondrial compartments. The formation of lipid peroxides might jeopardize the membrane integrity and can affect the electrochemical gradient which impairs mitochondrial function (*145, 147*).

Indeed, there is increasing evidence for mitochondrial impairment in PD that could eventually result in the vicious cycle described above. The first hint that mitochondria were involved in PD, came from the accidental exposure of humans to MPTP. MPTP can cross the BBB and is metabolized by astrocytes to the neurotoxin MPP+, an inhibitor of mitochondrial complex I, which is selectively taken up by DANs as it has a high affinity for the dopamine transporter. Patients suffered from parkinsonian-like symptoms afterwards due to the acute degeneration of DANs (*15*). A similar phenotype has been reported for other toxins like rotenone and 6-OHDA that also inhibit complex I and are often used to generate animal models of PD. Studies reporting reduced complex I activity in the SN and cortex of sporadic PD patients further highlights the link between mitochondrial dysfunction and PD (*148, 149*). Complex I might be more severely affected than the other complexes as it contains 7 proteins that are encoded by mtDNA, which showed increased deletions in the SNpc of PD patients (*142, 150*). In addition, high levels of mutations in mtDNA have been associated with reduced activity of complex IV (*150*). One reason for this high level of mtDNA mutations may be the proximity to mitochondrial ROS, which increase as a consequence of age but might also underlie other molecular alterations in PD (*151*).

Finally, monogenic forms of PD provide further evidence for the relevance of mitochondria. *PINK1* and *PRKN*, the most common recessive forms of familial PD (see also 1.1.3.1) are both crucial for the maintenance of mitochondrial homeostasis and quality control. They induce mitophagy of depolarized mitochondria and also regulate mitochondrial biogenesis (*152*). In addition, PINK1

deficiency has been associated with complex I defects (*153*). Mutations in *LRRK2* cause the most common form of autosomal dominant PD and are also associated with defects in mitochondrial dynamics, including mitophagy and trafficking, increased proton leakage and elevated ROS production (*152*).

Taken together evidence from sporadic and familial PD points towards a major role of mitochondrial dysfunction and oxidative stress in the degeneration of DANs in PD.

1.6 Aim of this thesis

En1 is crucial for the development and maintenance of DANs and has been ascribed a neuroprotective function (*94, 101*). Besides, En1 has also been associated with PD (*108, 154*) and in contrast to genetic familial PD animal models, heterozygous *En1* knockout animals suffer from progressive degeneration of dopaminergic neurons and display the well-known motor symptoms (*80, 107*). The DANs in these mice develop but are lost soon thereafter (*105*). Hence, En1 is highly likely linked to signaling pathways that are associated with the survival of these neurons. Identification of these neuroprotective pathways poses a great opportunity to discover molecular processes contributing to PD pathophysiology and the discovery of new therapeutic targets. Although the *En1* knockout has been connected to mitochondrial dysfunction (*94*), it has already been shown that the genetic background is crucial for the development of the *En1* knockout phenotype in mice (*155*). Based on this, species-specific differences are important to investigate. In addition, En1 works as a transcription factor and species-specific differences in target regulation due to genetic sequence variation have been reported for transcription factors (*63, 156*).

Considering the importance of the genetic background and the species-specificity of transcriptional regulation, the aim of this thesis was the translational approach to generate a human *EN1* knockout model and to analyze the molecular pathways that are linked to EN1 and might be underlying pathological processes, including PD.

Therefore, the aims of this thesis were in detail:

1. Generation of homozygous and heterozygous *EN1* knockout hiPSC lines using the CRISPR-Cas9 system.

2. Validation of the *EN1* knockout hiPSCs as a suitable model for PD pathophysiology and determination of species-specific differences by investigation of known *EN1* knockout-associated cellular deficiencies.

3. Uncovering unidentified molecular alterations caused by the *EN1* knockout in the human system using transcriptome analysis and validation of the cellular processes.

Parts of the following chapters were taken from a yet unpublished manuscript (Hembach et al.) submitted to peer-reviewing journals.

2 Results

2.1 Generation of *EN1* knockout human induced pluripotent stem cells (hiPSCs)

In this thesis, a human cellular model was generated to investigate the impact of the *EN1* knockout in the context of PD etiology. For this purpose, the hiPSC line HMGUi001-A (Xm001) was genetically modified at the *EN1* locus.

2.1.1 Targeting strategy and clone selection

EN1 knockout hiPSCs were generated using the clustered regularly interspaced short palindromic repeats (CRISPR)-Cas9 system. The CRISPR-Cas9 system allows the induction of site-specific DNA double-strand breaks. It relies on the endonuclease Cas9 which is guided towards the target locus by a complementary RNA molecule, the guide RNA (gRNA) (*157*). The induced DNA double-strand breaks are often inefficiently repaired by non-homologous end joining (NHEJ) leading to small insertions or deletions (indels) in the targeted region (*158*). The gRNAs were designed to target the N-terminal part of exon 1 aiming towards indels that result in frameshifts and premature termination of translation. Ideally the translation should be terminated before any functional domain of *EN1*. However, as the sequence of *EN1* is highly repetitive and thus difficult to target, the gRNA with the highest cutting efficiency, being located at least 55 bp upstream of an exon-exon boundary to allow for nonsense mediated mRNA decay, was selected (*159*). As animal studies have shown that already the heterozygous knockout of *EN1* can result in severe phenotypes (see 1.3.3) (*80, 107*), the targeting strategy aimed at the generation of homozygous and heterozygous knockouts to assess also the dose-dependent effect of the *EN1* knockout in a human model. Different gRNAs were designed and evaluated for their cutting efficiency in HEK293 cells. Although the use of two gRNAs could enhance the generation of indels (*160*), only the gRNA with the highest cutting efficiency, gRNA 3 (**Figure 8A**) (~30 %, data not shown), was selected for the targeting of hiPSCs, to increase the chance of generating heterozygous clones in addition to homozygous knockouts.
A plasmid encoding the Cas9 endonuclease, the gRNA 3, and a Venus reporter was transfected into hiPSCs (**Figure 8B**). After 48 h, the transfected hiPSCs were isolated by fluorescence activated cell sorting (FACS) and plated on a 10 cm dish at a low density to allow discrimination between cell clones. Individual clones were isolated and screened for indels in the targeted region of *EN1* exon 1. Clones harboring indels leading to a frameshift and premature stop of translation in a single or in both alleles were selected and re-clonalized by serial dilution to ensure single-cell identity of the hiPSCs. In the last step, the single cell identity of the subclones was ensured by subcloning and sequencing of the mRNA. Interestingly, after the first clonalization most clones were still of mixed identity and even after re-clonalization some clones had to be excluded, highlighting the importance of thorough clonalization. From the initially 60 isolated clones, two homozygous *EN1* knockout *(EN1* -/-) clones and one heterozygous *EN1* knockout (*EN1* +/-) clone were verified.

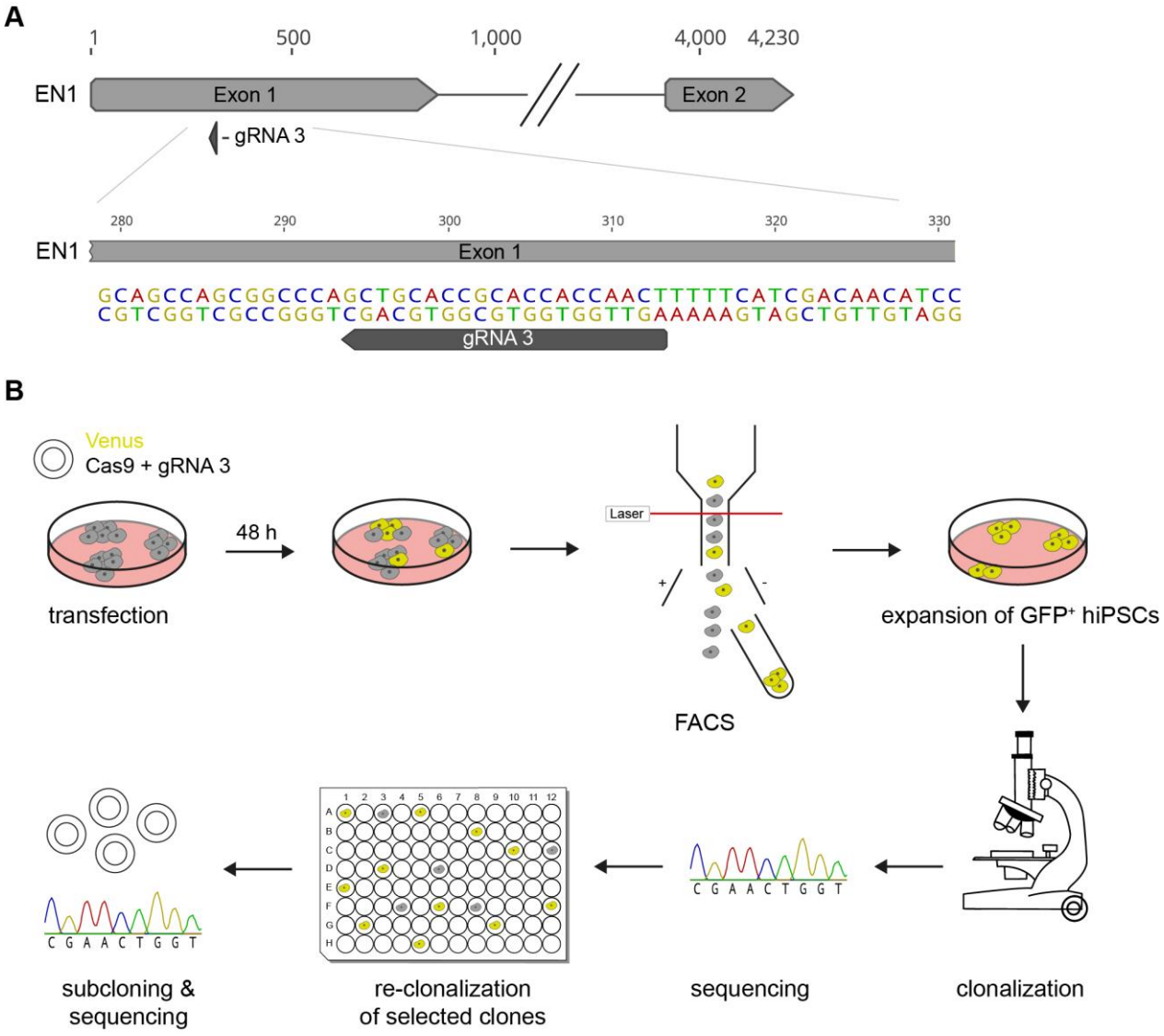

Figure 8: *EN1* Targeting strategy and workflow. (A) Location and sequence of the gRNA used for targeting of *EN1* exon 1. **(B)** Workflow for the generation of the *EN1* knockout hiPSCs and corresponding WT control clones.

The *EN1* -/- clones had indels on both alleles that resulted in a frameshift and two premature stop codons at nucleotide position 432 and 456 from the transcription start in the middle of exon 1. Clone 5 had an insertion of one base pair (bp) on one allele and a one bp insertion combined with a one bp mutation on the other allele. Clone 25 possessed deletions on both alleles, an 11 bp deletion and a 17 bp deletion, respectively (**Figure 9A**). The presence of two different mutations per clone, supported the generation of a biallelic knockout. Clones with the same mutation on both alleles were excluded, due to the possibility of large genomic on-target effects including loss of heterozygosity, which is a frequent event in CRISPR-Cas9 edited hiPSCs and embryos (*161, 162*). The *EN1* +/- clone 35, only exhibited a 17 bp deletion on one allele, whereas the other allele still had the WT sequence. The deletion resulted in a frameshift and premature termination of translation at the same nucleotide position as in the *EN1* -/- clones (**Figure 9B**). To increase the biological replicates and account for hiPSC variability (*163*), two subclones were selected for further experiments, if possible. To have appropriate isogenic controls, WT control clones were

generated in parallel by subjecting untargeted Xm001 hiPSCs to the same two-step clonalization procedure as described above (**Figure 8B**). The *EN1* -/-, *EN1* +/- and WT hiPSC clones that were selected are listed in **Table 4**.

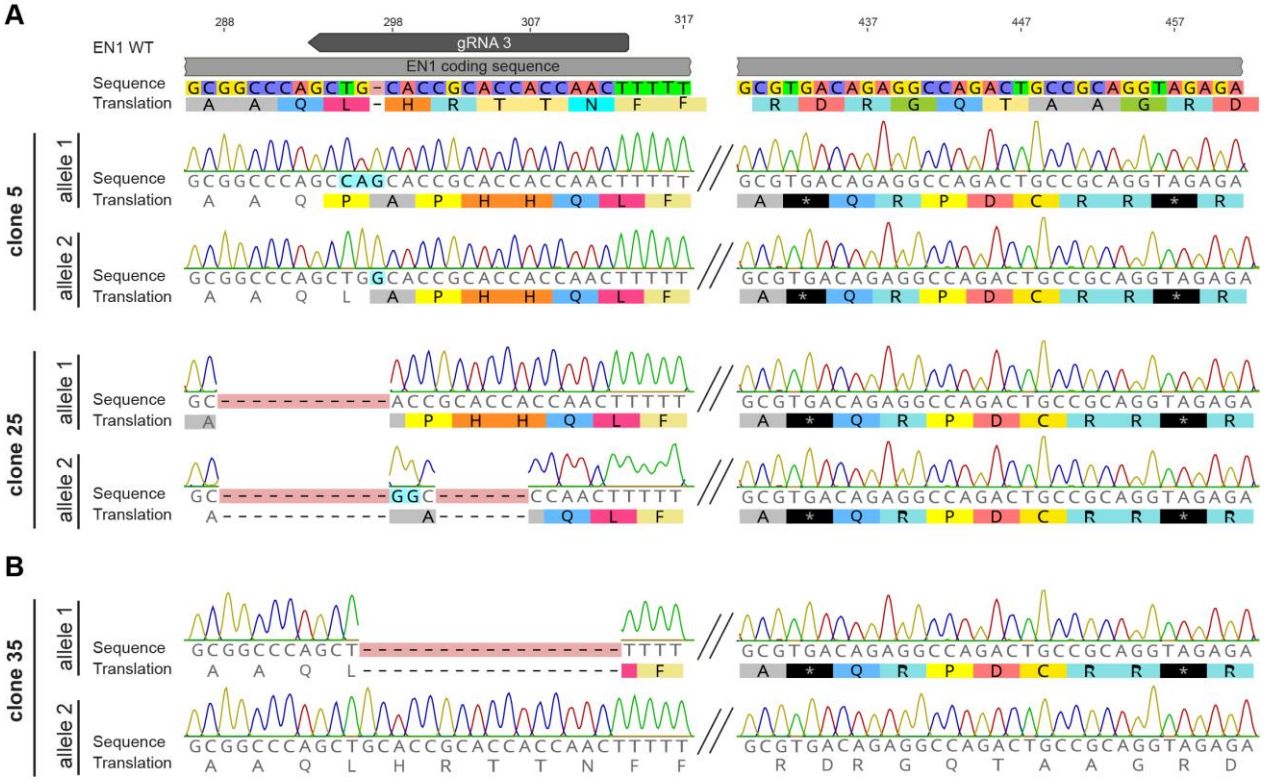

Figure 9: Nucleotide and amino acid sequence of the selected *EN1* -/- and *EN1* +/- clones. Sequences show the CRISPR/Cas9 induced nucleotide alterations after subcloning of the respective mRNA for both alleles as well as the amino acid sequences for *EN1* -/- **(A)** and *EN1* +/- **(B)** clones, respectively. The gRNA target region and the nucleotide positions from the transcription start site are indicated at the top.

Table 4: Overview of the selected *EN1* -/-, *EN1* +/- and WT control clones and subclones. The nucleotide alterations and the effect on protein translation are listed. Shaded clones were excluded after quality control.

Clone	Subclone	Genotype	Mutation	Protein sequence
5	5-6	*EN1* -/-	1 bp insertion 1bp insertion and 1 bp mutation	Frameshift and premature stop codons at nucleotide positions 432 and 456
	5-12	*EN1* -/-	1 bp insertion 1bp insertion and 1 bp mutation	Frameshift and premature stop codons at nucleotide positions 432 and 456
25	25-16	*EN1* -/-	11 bp deletion 17 bp deletion	Frameshift and premature stop codons at nucleotide positions 432 and 456
	25-19	*EN1* -/-	11 bp deletion 17 bp deletion	Frameshift and premature stop codons at nucleotide positions 432 and 456
35	35-10	*EN1* +/-	17 bp deletion WT sequence	Frameshift and premature stop codons at nucleotide positions 432 and 456; WT sequence
	35-11	*EN1* +/-	17 bp deletion WT sequence	Frameshift and premature stop codons at nucleotide positions 432 and 456; WT sequence
WT 4	4-3	WT	none	WT
	4-4	WT	none	WT
	4-5	WT	none	WT
WT 11	11-2	WT	none	WT
WT 15	15-1	WT	none	WT
WT 18	18-3	WT	none	WT

2.1.2 Quality Control

Although the CRISPR-Cas9 system is very specifically guided to the target locus by complementary binding of the gRNA, off-target effects have been reported (*164*). In addition, copy number variations (CNVs) can accumulate during cultivation of hiPSCs, especially when cultivated as single cells (*165*). Therefore, the selected clones were subjected to extensive quality control to ensure genomic integrity and pluripotency. CNV analysis was performed using a HumanCytoSNP-12 v2.1 Bead Chip for *EN1* -/- and *EN1* +/- and an Infinium GSA-24 v3.0 microarray for the WT clones. Except for clone 25-16, no CNVs greater than 100 kb were detected for *EN1* -/- and *EN1* +/- clones (*166, 167*). Clone 25-16 exhibited a duplication of about 5400 kilo bases (kb) on chromosome 2 and a deletion of about 150 kb on chromosome 3 (**Figure 10A left**) (see **Table 21** for exact CNV regions). The region of the deletion does not encode for any genes, however, as the duplication includes a region with important developmental genes like *PAX3* and *EPHA4*, the clone was excluded from further experiments. Both genomic loci that were affected by CNVs were not predicted to be potential off-targets by the CRISPOR tool for the selected target gRNA 3. Furthermore, the other subclone 25-19 was not affected by CNVs in these regions, indicating that the mutations in clone 25-16 occurred during subclone cultivation and were not due to off-target activity of the CRISPR-Cas9 system. In contrast to the *EN1* -/- and *EN1* +/- clones, the WT clones were all affected by CNVs (**Figure 10A right**). Interestingly, all WT clones, except 18-3 showed duplications in the same region of chromosome 14, indicating that the initial clone might have already had the mutation. As the knockout clones, which were generated from the same parental hiPSC cell line (passage ± 1) did not display CNVs on chromosome 14, the difference in CNV profiles might also be explained by the different SNP coverage of the two microarrays that were used for CNV analysis. The genes encoded in this genomic region are olfactory receptor genes, which are of minor importance for the purpose of this thesis. Thus, the clones were not excluded from downstream analyses. Clone 4-5 exhibited an additional deletion on chromosome 16 and clone 18-3 showed duplications on chromosome 7 and 14. However, only few (< 4) or no genes are encoded in these regions and therefore the clones were included. Only clone 11-2 with a large duplication on chromosome 20, that encompassed more than 25 genes including genes involved in apoptosis (*BCL2L1*) and the respiratory chain (*COX4I2*) was excluded from downstream experiments. This particular duplication has already been characterized as it was observed recurrently in hiPSCs. It results in reduced level of apoptosis due to enhanced *BCL2L1* expression. As EN1 is a survival factor and is associated with mitochondrial dysfunction, the exclusion from further experiments can be justified (*168*).

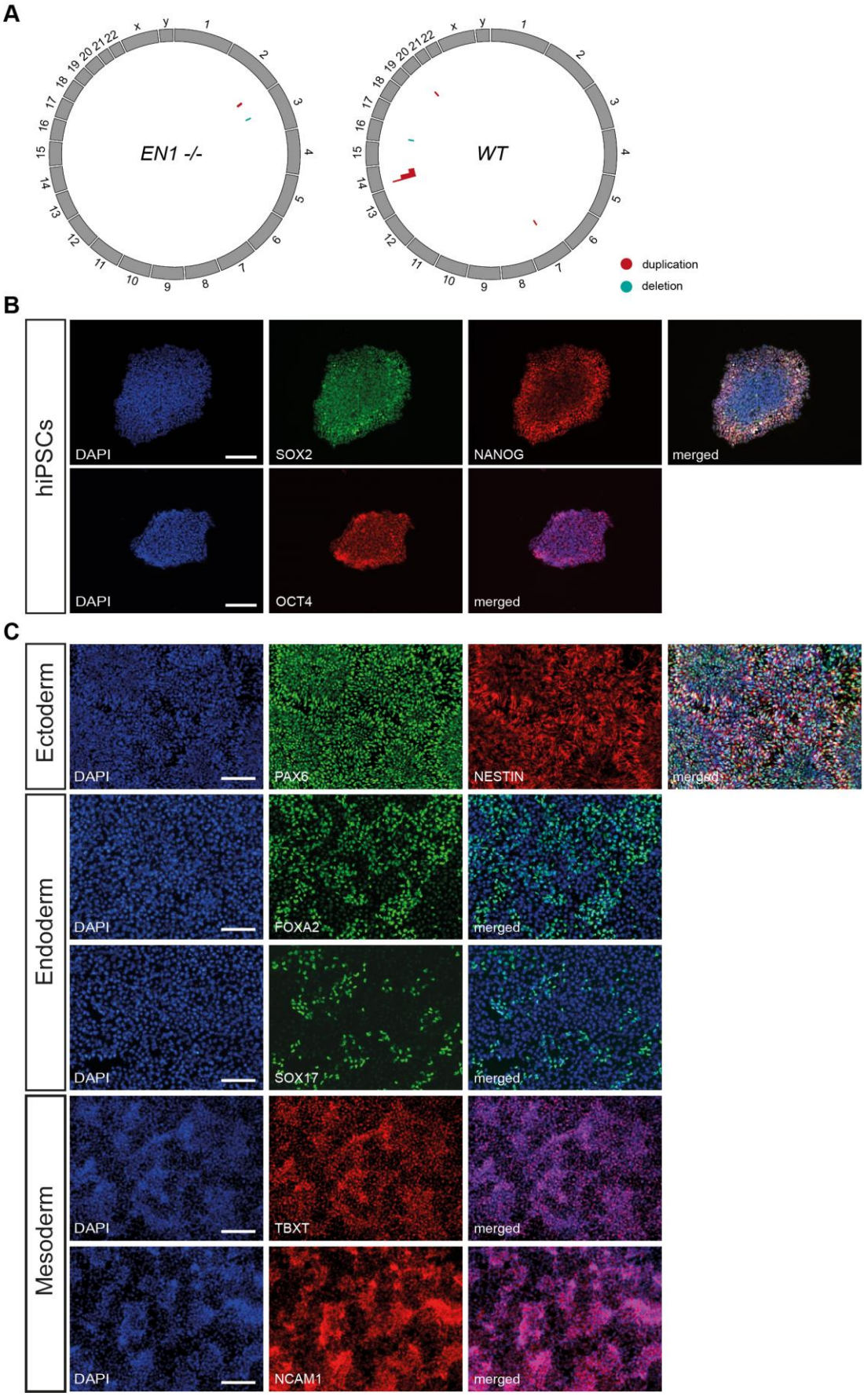
A
EN1 -/-
WT
duplication
deletion
B
hiPSCs
DAPI
SOX2
NANOG
merged
DAPI
OCT4
merged
C
Ectoderm
DAPI
PAX6
NESTIN
merged
Endoderm
DAPI
FOXA2
merged
DAPI
SOX17
merged
Mesoderm
DAPI
TBXT
merged
DAPI
NCAM1
merged

Figure 10: Quality control of generated hiPSCs. (A) Circos plots showing the distribution of somatic CNVs for *EN1* -/- and WT clones. **(B)** Immunofluorescence staining of hiPSCs for the pluripotency markers SOX2, NANOG and OCT4 shown exemplarily for *EN1* -/- clone 25-19. **(C)** Immunofluorescence staining for ectodermal (PAX6, NESTIN), endodermal (FOXA2, SOX17) and mesodermal (TBTX, NCAM1) markers after trilineage differentiation of hiPSCs shown exemplarily for *EN1* -/- clone 5-12. Scale bars: 100 µm.

The pluripotency of the remaining clones was shown by immunostaining for the respective pluripotency markers OCT4, SOX2, and NANOG. (**Figure 10B**). In addition, all clones were differentiated into the three germ layers (**Figure 10**C). The successful differentiation was assessed by immunostaining for the ectodermal markers PAX6 and NESTIN, the endodermal markers FOXA2 and SOX 17, and the mesodermal markers TBXT and NCAM1. All analyzed *EN1* -/-, *EN1* +/- and WT clones were able to differentiate into the different germ layers and thus passed quality control. After quality control, three *EN1* -/- clones, 5-6, 5-12 and 25-19, two *EN1* +/- clones, 35-10 and 35-11, and five WT clones, 4-3, 4-4, 4-5, 15-1 and 18-3 were selected (**Table 4**). As only two *EN1* +/- clones were available, valid quantitative statistical analysis was not possible. Thus, the *EN1* +/- clones were not integrated in the statistical analysis. However, as there was a great effect in $En1^{+/-}$ mice, the clones were analyzed anyhow to get an impression about a possible gene dose-dependent effect of *EN1* in a human model. Observations made in *EN1* +/- clones are therefore shown in a separate chapter (see 2.6).

2.2 Characterization of *EN1* knockout neuronal precursor cells (NPCs)

2.2.1 Differentiation into NPCs

To explore the impact of the *EN1* knockout (*EN1* -/-) in the context of PD etiology, the hiPSC clones were differentiated towards the dopaminergic lineage. In a first step, NPCs mimicking neural epithelial cells capable of differentiating into the neural tube lineage, including DANs as well as neural crest lineage, including peripheral neurons and mesenchymal cells were generated using small molecules (*169*).

Correct NPC identity was assessed by expression of the pluripotency markers SOX2 and SOX1, with SOX1 being also an early marker of the neuroectoderm lineage (*170*) and expression of the neural progenitor markers PAX6 and NESTIN (**Figure 11A**). All selected *EN1* -/- and WT clones (**Table 4**) were stained positive for the respective markers and were thus successfully differentiated into NPCs.

In mice, the expression of *En1* starts around E8 (see 1.3.2). As the small molecule NPCs are able to generate cell types originating from neural tube and neural crest lineages they are believed to be located at the border region of the neural plate (*169*). Thus, developmentally these cells can broadly be staged before neural tube closure which correlates with E8.5 in mice. A developmental stage where *En1* is already expressed. To validate the knockout and the eligibility of NPCs as a cellular model to investigate the molecular pathways associated with the *EN1* knockout, *EN1* expression was analyzed in NPCs. Compared to WT clones, *EN1* -/- clones have significantly reduced mRNA levels (**Figure 11B, Table 22** for statistics) and therefore were used in the following as a robust and easy to handle cellular model to assess the impact of *EN1* knockout on neuronal progenitor cells primed towards midbrain development.

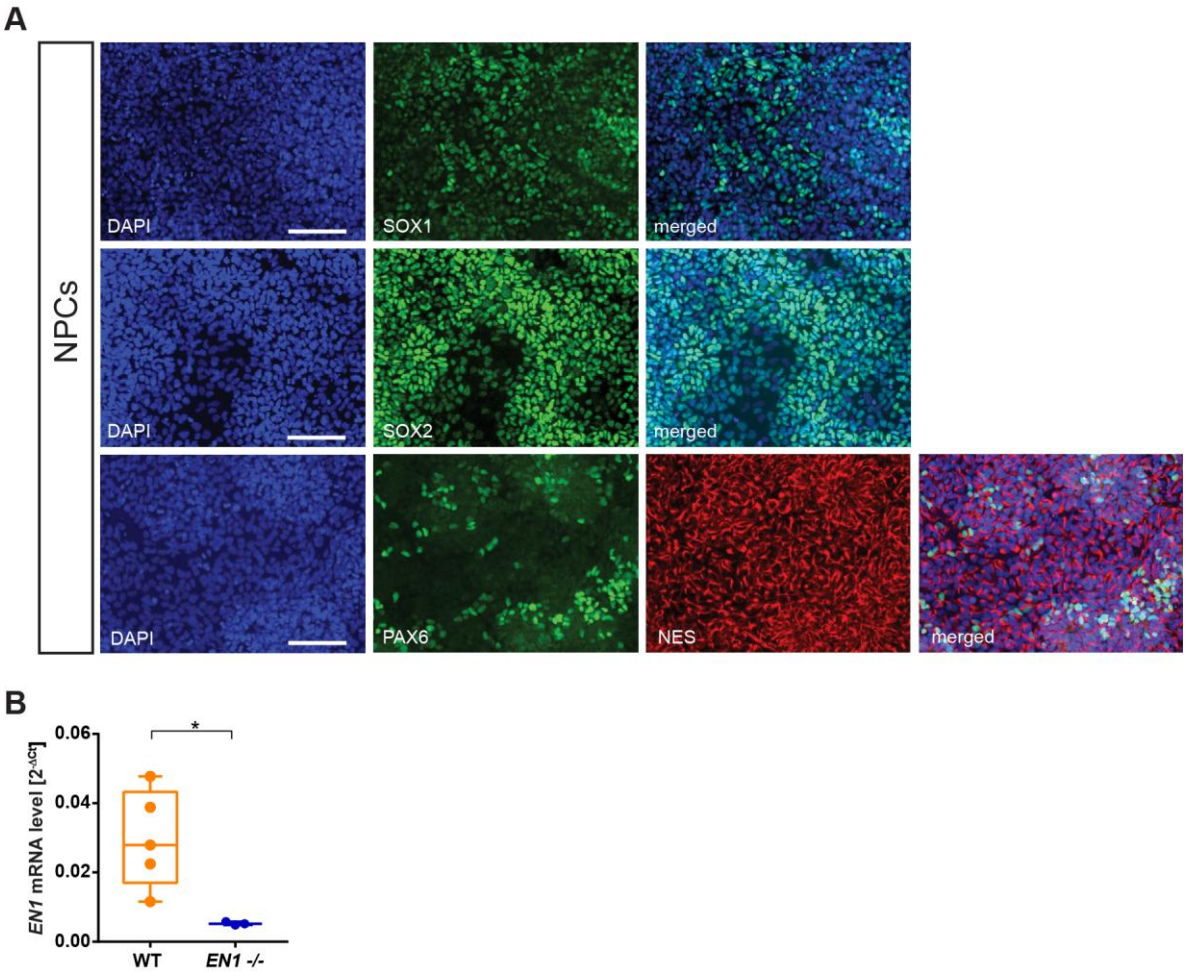

Figure 11: NPC differentiation of *EN1* -/-hiPSCs. (A) Immunofluorescence staining of NPCs for the respective markers SOX1, SOX2, PAX6, and NES is shown exemplarily for *EN1* -/- clone 5-12. Scale bars: 100 µm **(B)** RT-qPCR analysis of *EN1* mRNA expression in NPCs. mRNA levels were normalized to *ACTB*. n = 5 WT and 3 *EN1* -/- clones, in triplicates. Data are depicted as box plots ranging from the 25th to 75th percentiles, showing the median. Whiskers extend from min to max value and each dot represents one clone. P-values were determined by student's t-test or Welch's t-test depending on the standard deviation. Details of statistical analyses are provided in **Table 22**. *, $p < 0.05$.

2.2.2 Transcriptome analysis of *EN1* knockout NPCs

To explore the consequences of the *EN1* knockout in a human model in an unbiased way, transcriptome analysis of *EN1* -/- and WT NPCs was performed. The mRNA from three *EN1* -/-, and five WT clones was isolated in three technical replicates. Libraries were prepared using an Illumina mRNA protocol and pair-end sequencing was performed.

2.2.2.1 Quality control

Dimensionality reduction of the transcriptome data was performed using principal component analysis (PCA). PCA allows to summarize large datasets to increase the interpretability of the results. Variations and similarities between samples and replicates are visualized and outliers can be spotted. PCA of the sequenced clones showed, that clones of the same genotype cluster mostly together and separate along PC1 (**Figure 12A** upper panel), with the exception of one WT clone. Thus, the highest variation of 16.1 % between the clones can be explained by their genotype. In addition, the variation between technical replicates of the same clone is low (**Figure 12A,** lower

panel). As mentioned before, PCA can also be used to identify outliers. The WT clone 18-3 did not cluster with the other WT's and was therefore excluded from further analysis. Exclusion of this clone increased the PC1 score to 18.1 % and improved the clustering of the different genotypes along PC1 **(Figure 12B**). Therefore, PCA showed that the highest variation in the transcriptome data is attributed to the genotype which indicates validity of the transcriptome data for downstream analysis.

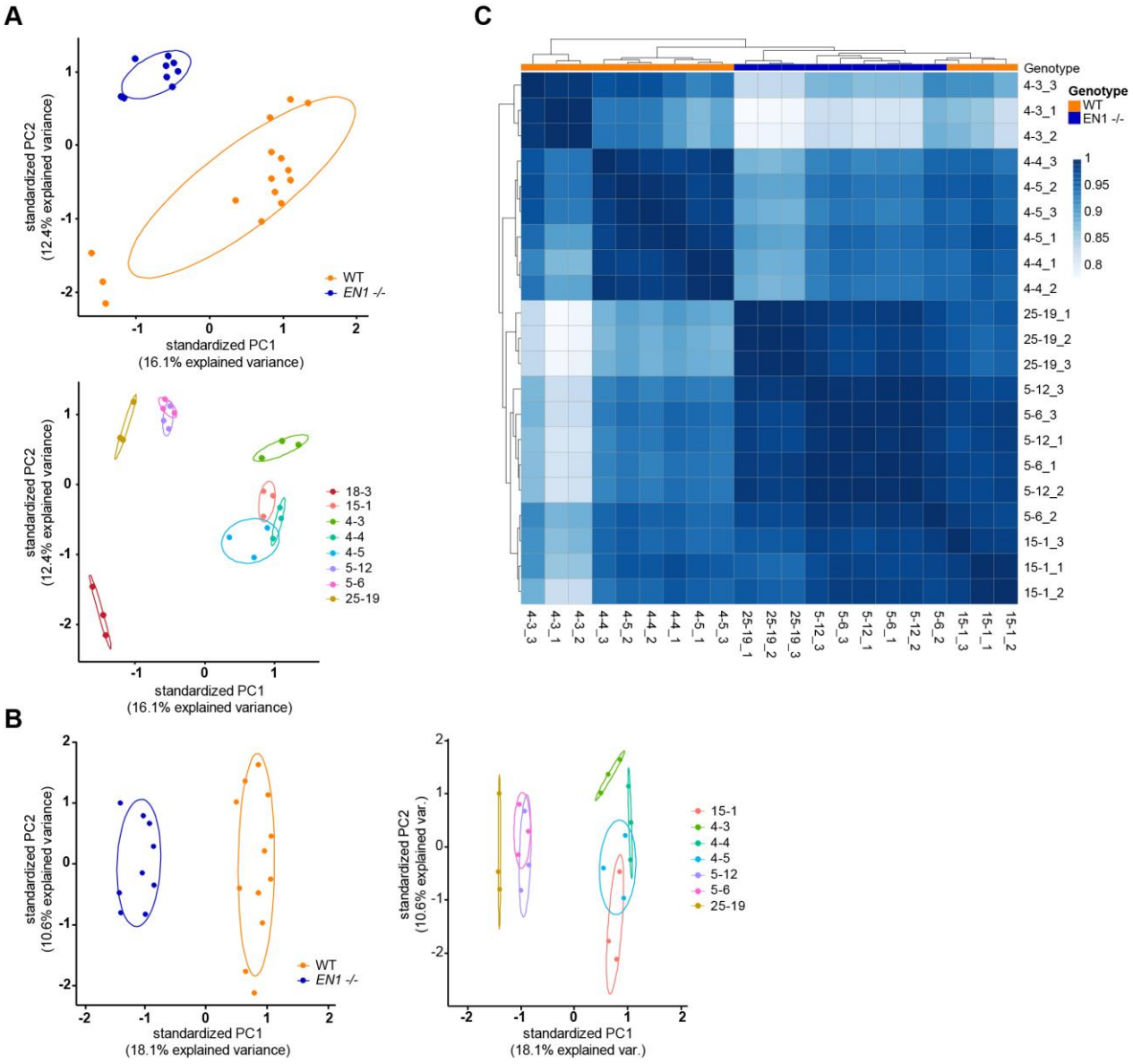

Figure 12: Dimension reduction and quality assessment of transcriptome analysis. (A) Principal component analysis (PCA) of sequenced *EN1* -/- and WT NPCs. PCA plots show distribution of genotype conditions (upper panel) and every sample (lower panel). Probability ellipses depict 0.68 of normal probability. PCA **(B)** and correlation matrix **(C)** after outlier removal. n = 5/4 WT and 3 *EN1* -/- clones, in triplicates. (in collaboration with Sebastian Schmidt)

For further quality control, a correlation analysis of all clones and technical replicates was performed. A correlation heat map shows the correlation between variables which are in this case represented by the different clones. The correlation heatmap illustrated again the similarity between the technical replicates for most of the clones (**Figure *12***C). However, the clones not necessarily

segregated according to their genotype but rather according to their clone. The WT clone 15-1 clusters closer to the knockout clones than the other WT clone. Already between the subclones, there is some variability, for example, the clone 4-3 has a slightly distinct expression profile than the other subclones 4-4 and 4-5. This illustrates a high variability of the different hiPS clones and their subclones. Nevertheless, the highest variance can still be attributed to the genotype as shown in the PCA.

2.2.2.2 Differentially expressed genes in *EN1* knockout NPCs

Quality control assured validity of the transcriptome data as *EN1* -/- and WT NPCs were separated into individual clusters. To determine molecular alterations in the *EN1* knockout, differentially expressed genes (DEGs) were closer analyzed. A total of around 15,000 genes were identified of which 2,476 were significantly dysregulated (p-adjust < 0.05; $\log_2$ fold change > 0.5) between *EN1* -/- NPCs and WT NPCs. A heatmap visualizing the gene expression of all DEGs shows the similarity between clones of the same genotype and highlights the difference between *EN1* -/- clones and WT clones, thus validating DEG analysis (**Figure 13A**). Although the genotype explains the highest variance between the clones, DEGs of subclones are more similar to one another than different primary clones (e.g. *EN1* -/- clone 5 versus (vs) *EN1* -/- clone 25), confirming what has already been observed in the correlation heatmap. Differences in passages can be excluded, however, small genotypic variations (SNPs, CNVs < 100 kb) and slight variations during maintenance might account for the variation between clones (*163*).

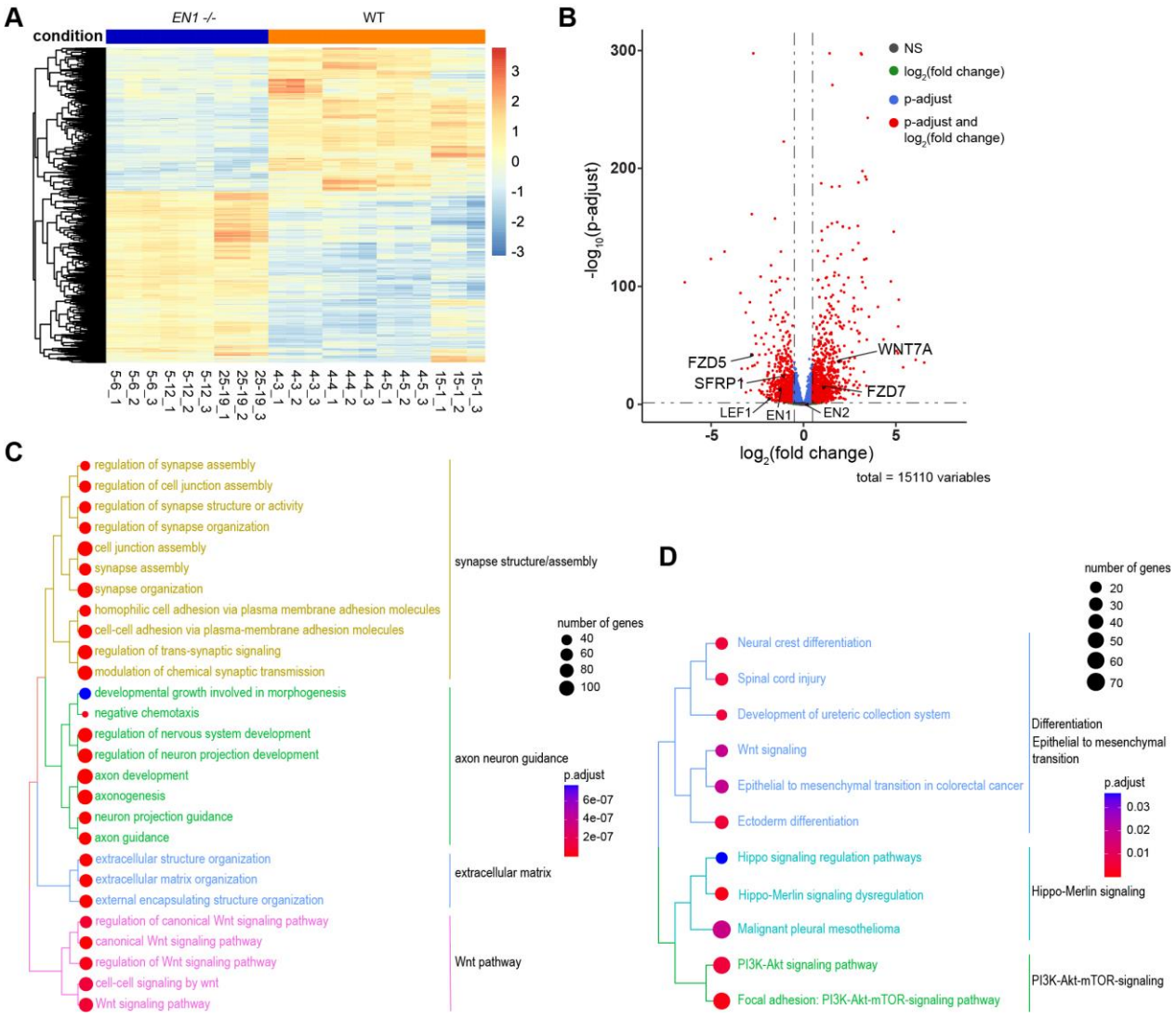

Figure 13: Visualization and pathway enrichment analysis of differentially expressed genes (DEGs) between *EN1* -/- and WT NPCs. (A) Heatmap displaying the DEG expression levels for every sample. Red represents upregulated, and blue represents downregulated genes. **(B)** Volcano plot showing DEGs according to their fold change and significance. Every detected gene is represented by a dot. Lines visualize fold change ($log_2(0.5)$) and significance ($-log_{10}(0.05)$) cut-offs. Selected genes are highlighted. **(C)** Tree plots of the pathway enrichment analysis showing significant WikiPathways **(C)** or GO terms **(D)**. (in collaboration with Sebastian Schmidt)

The volcano plot, which depicts DEGs by their fold change and significance shows that the ratio of up-and downregulated genes is similar (**Figure 13B**). *EN1* expression was significantly downregulated whereas *EN2* expression was unchanged, confirming the knockout. Furthermore, this agrees with the RT-qPCR results, validating the transcriptome (**Figure 11B**; **Figure 17**).
Pathway enrichment analysis was performed to determine the molecular changes in *EN1* -/- NPCs using different databases. The treeplots show that the DEGs were enriched in pathways that can be categorized into synapse structure/assembly, axon guidance, extracellular matrix (ECM), and the Wnt pathway using WikiPathway terms (**Figure 13C**). Gene ontology (GO) terms that came up were associated with differentiation, including also Wnt signaling, Hippo-Merlin signaling, and Pi3K-Akt-mTOR signaling (**Figure 13D**). Some of the pathways match with known functions of EN1. For example, EN1's role in synapse physiology has been shown in murine primary neurons

as well as in drosophila and cockroaches (*171–173*), indicating a conserved function extending also to the human model. Furthermore, axon guidance during development (*95, 174*) but also degeneration of axons in *En1*$^{+/-}$ mice has been described (*109*). The mTOR pathway, the Hippo-Merlin pathway, and the Wnt pathway (see also 1.4.2) have also been associated with En1 in the context of mRNA translation control and regulation of *En1* expression, respectively (*109, 127, 175*). The role in extracellular matrix organization has not been directly linked to EN1. However, the fact that most pathways could be related to established functions of En1 across different organisms suggests a conserved role of En1. Interestingly, the association of En1 with mitochondria and complex I, which is thought to partially mediate its neuroprotective function in *En*1$^{+/-}$ mice (*94*) was not reflected in the transcriptome data.

2.2.3 Validation of mitochondrial and respiratory function in *EN1* knockout NPCs

As the neuroprotective effect of En1 is mainly linked to its connection to mitochondria in mice, the mitochondrial function of the *EN1* knockout NPCs was investigated to validate the respective negative results from the transcriptome analysis of the human model. The degeneration of DANs in *En1*$^{+/-}$ mice has been attributed to increased susceptibility to mitochondrial insults and oxidative stress. Injection of Engrailed in neurotoxic PD models demonstrated its neuroprotective effect, which is amongst others mediated by enhanced translation of two subunits of mitochondrial complex I (*94*) (see 1.3.3). Therefore, mitochondrial integrity and cellular respiration were investigated. At first, the functionality of mitochondria was analyzed using MitoTracker which accumulates specifically in mitochondria with intact membrane potential and hence an active and functional respiratory chain. Mitochondrial functionality was not affected in *EN1* -/- NPCs (**Figure 14A, Table 23** for statistics). To investigate the data in more detail, a distribution analysis was performed, which plots the distribution of fluorescence intensity for single cells per clone. This allows the identification of possible subpopulations. The distribution analysis showed no changes in fluorescence intensity in *EN1* -/- NPCs (**Figure 14B, Table 23** for statistics), suggesting that mitochondria of *EN1* -/- NPCs have the same mitochondrial functionality as WT NPCs.
Although the functional assessment indicated no changes in the *EN1* knockout, the animal models exhibited mitochondrial impairments. As subtle defects might have not been detected in the MitoTracker staining, the integrity of the mitochondria with a focus on the respiratory chain was investigated further. One parameter that can affect mitochondrial functionality is the abundance of respiratory chain complexes. The abundance was analyzed by western blot for labile subunits of each complex. Although EN1 has been described to regulate the expression of two complex I subunits, the relative protein level of complex I or any other respiratory chain complex was not altered in *EN1* -/- NPCs (**Figure 14C**, Western blot is shown exemplarily in **Figure 36**, **Table 23** for statistics). Taken together, the *EN1* knockout displayed no alterations in mitochondrial functionality and in the abundance of respiratory chain complexes.

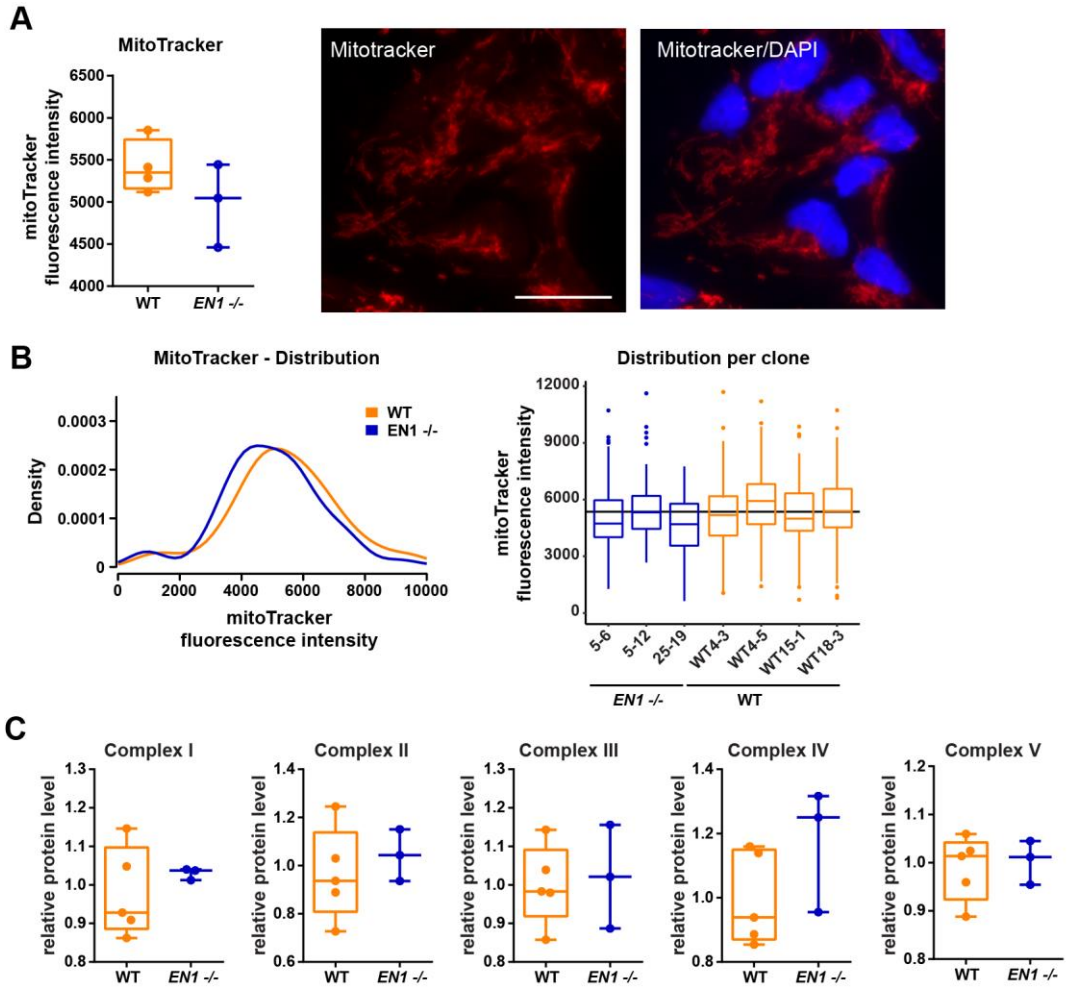

Figure 14: Assessment of mitochondrial quantity and functionality in NPCs. (A) MitoTracker staining to analyze mitochondrial functionality in NPCs. The cytosolic fluorescence intensity was quantified. Staining is shown exemplarily for *EN1* -/- clone 5-6. Scale bar: 20 µm. n = 4 WT and 3 *EN1* -/- clones, in triplicates. **(B)** Density plot showing fluorescence intensity distribution for WT and *EN1* -/- clones combined (left panel) and boxplot showing the distribution for each clone individually (right panel). n = 4 WT and 3 *EN1* -/- clones, in triplicates. **(C)** The quantity of respiratory chain complexes I-V was assessed by western blot using antibodies against NDUFB8 (complex I), SDHB (complex II), UQCRC2 (Complex III), MT-CO2 (complex IV) and ATP5A (complex V). Protein levels were normalized to GAPDH and the average protein level of WT clones. An exemplary western blot is shown in the appendix. n = 5 WT and 3 *EN1* -/- clones, in triplicates. Data are depicted as box plots ranging from the 25th to 75th percentiles, showing the median. Whiskers extend from min to max value and each dot represents one clone (A, C). P values were determined by student's t-test or Welch's t-test depending on the standard deviation (A, C) and Kolmogorov-Smirnov test and linear regression (B). P-values are indicated only if both (Kolmogorov-Smirnov and linear regression) tests resulted in a significance. Details of statistical analyses are provided in **Table 23**.

To further assess the functionality of the cellular respiration, a mitochondrial stress test was performed using a Seahorse XF extracellular flux analyzer. The system simultaneously measures the oxygen consumption rate (OCR) and the extracellular acidification rate (for glycolytic stress tests) in a cellular monolayer. As the mitochondrial ATP synthesis is coupled to oxygen consumption, the OCR can be used to assess mitochondrial respiration. Sequential addition of chemicals that target the integrity of the respiratory chain at various points allows the assessment of parameters like basal respiration, ATP-linked respiration, reserve capacity, proton leak, and maximal respiration (**Figure 15A**).

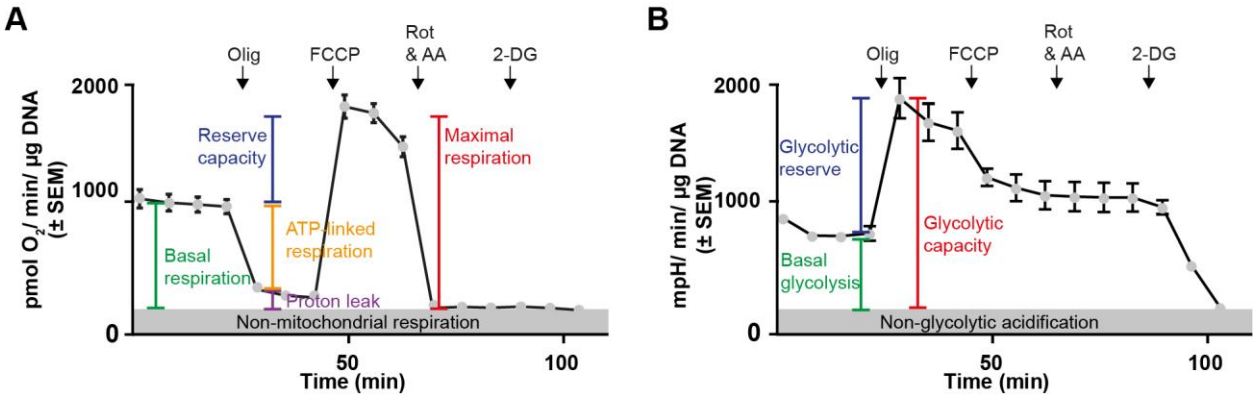

Figure 15: Schematic of the mitochondrial (A) and glycolytic (B) stress test profile and parameters. Cells were incubated in Seahorse XF Assay medium supplemented with 25 mM glucose or 5 mM pyruvate as substrates. The inhibitors of the different respiratory chain complexes Oligomycin (Olig, 1 µg/ml), FCCP (0.5 µM) and Rotenone (Rot, 5µM)/Antimycin A (AA; 2µM) were added at the indicated time points. 2-Deoxyglucose (2-DG, 100 mM) was added at last to determine glycolytic flux.

The basal respiration is the OCR measured under homeostatic conditions. It contains both, the OCR attributed to ATP-linked respiration and the proton leak. The addition of oligomycin (Olig), an ATP-synthase inhibitor shuts down the ATP-linked respiration and determines the OCR that is caused by the proton leak. In a next step, the uncoupling agent FCCP is added to measure the maximal respiration. The proton gradient over the IMM collapses and the respiratory chain works at full capacity to compensate for this. The difference between basal respiration and maximal respiration is thus also referred to as reserve capacity, which the cells can rely on in times of high energy demand. Inhibitors of complex I and III, rotenone (Rot) and antimycin A (AA), respectively are added in the final step to completely shut down the respiratory chain and yield the OCR that is not linked to mitochondrial respiration, which has to be subtracted from all the parameters (**Figure 15A)**.

To detect defects in cellular respiration, a mitochondrial stress test was performed in *EN1* -/- and WT NPCs. The use of different energy substrates allowed the assessment of the contribution of different metabolic processes and the determination of possible bottlenecks. Glucose is metabolized in glycolysis before entering the TCA, whereas pyruvate can directly be fueled into the TCA. Therefore, defects in glycolysis will only become apparent when glucose is used as the substrate whereas the usage of pyruvate allows discrimination between glycolytic and mitochondrial deficits. As the overview of the measurement already suggested, basal OCR, maximal OCR and proton leak were not altered in *EN1* -/- NPCs compared to WT NPCs using either glucose (**Figure 16A, Table 24** for statistics) or pyruvate (**Figure 16B, Table 24** for statistics) as substrates. Thus, the *EN1* knockout did not affect the cellular respiration in human NPCs supporting the MitoTracker results which also did not indicate a difference in mitochondrial functionality between *EN1* -/- NPCs and WT NPCs.

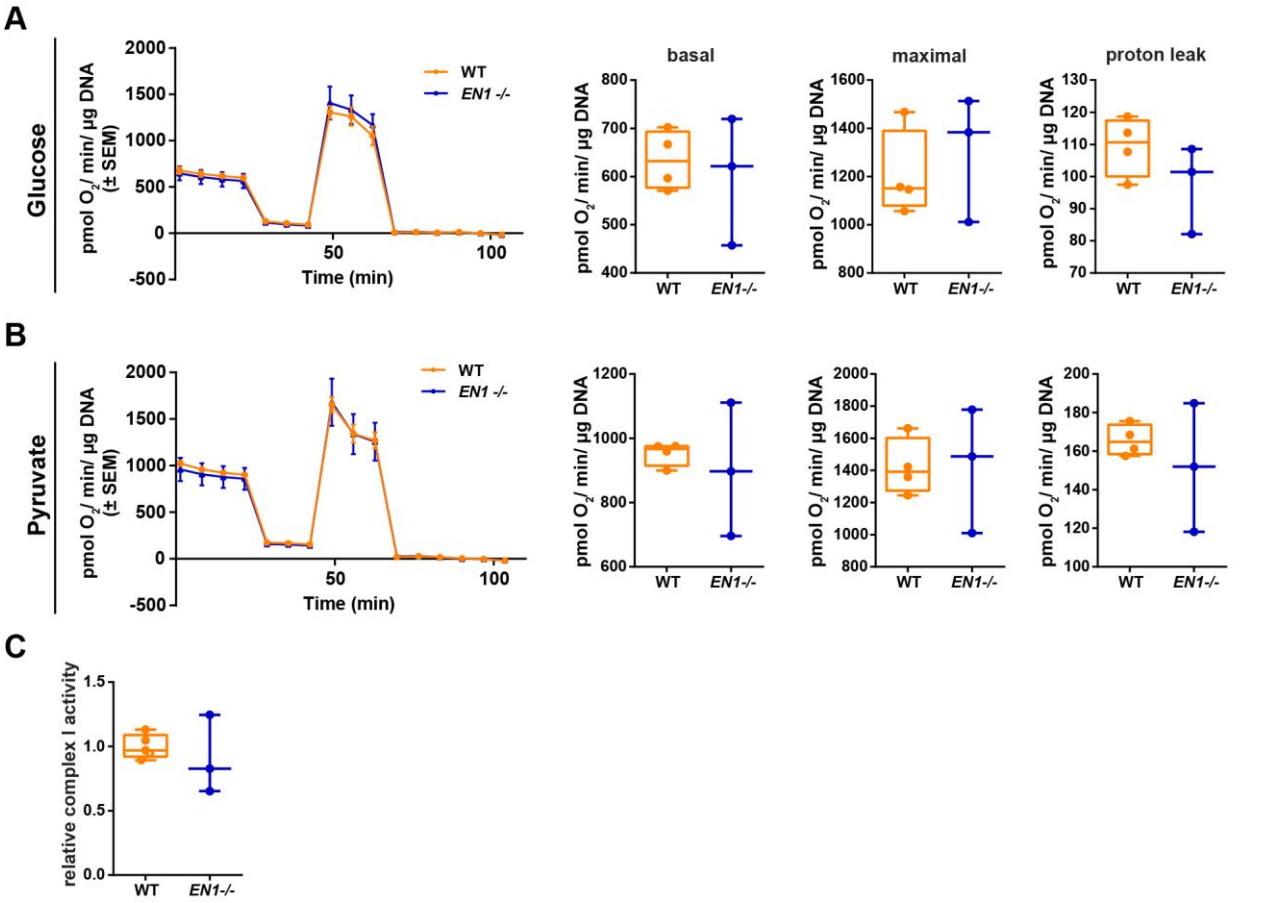

Figure 16: Characterization of mitochondrial respiration in NPCs. The oxygen consumption rate was measured using a Seahorse XFe96 Extracellular Flux Analyzer. The measurement (described in **Figure 15A**) was performed in Seahorse XF assay medium supplemented with either 25 mM glucose **(A)** or 5 mM pyruvate **(B)** as substrates. An overview of the measurement (left panel) and detailed analyses of basal respiration, maximal respiration, and proton leak (right panels) are shown. n = 4 WT and 3 *EN1* -/- clones, in triplicates. **(C)** Quantification of relative complex I activity. Complex I activity was normalized to the average activity of WT clones. n = 5 WT and 3 *EN1* -/- clones, in triplicates. Data are depicted as mean ± standard error of the mean (SEM) and box plots ranging from the 25th to 75th percentiles, showing the median. Whiskers extend from min to max value and each dot represents one clone. P-values were determined by student's t-test or Welch's t-test depending on the standard deviation. Details of statistical analysis are provided in **Table 24** and **Table 25**.

However, EN1 has been specifically linked to the activity of complex I by controlling the translation of two subunits. Subtle effects on a single respiratory chain complex might not have been detected in Seahorse measurement, especially as the OXPHOS is not used to full capacity in NPCs (*176*). Therefore, in a next step the isolated activity of complex I was investigated. Unexpectedly, the *EN1* -/- NPCs showed no alterations in complex I activity (**Figure 16C, Table 25** for statistics), implying that the effect of the knockout does not hinder complex I activity in human NPCs nor the abundance as determined by western blot for the labile subunits. To sum up, the human *EN1* knockout model showed no deficit in mitochondrial function and neither cellular respiration nor the complex I activity were impaired in *EN1* -/- NPCs. These results confirmed and validated the transcriptome analysis, which, in contrast to the observation made in the $En1^{+/-}$ mouse models, revealed no connection between the *EN1* knockout and mitochondrial functionality in this human model.

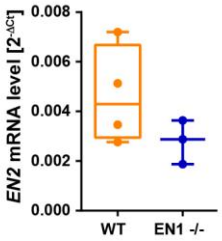

Figure 17: *EN2* expression level. RT-qPCR analysis of *EN2* mRNA expression in NPCs. mRNA levels were normalized to ACTB. n = 5 WT and 3 *EN1* -/- clones, in triplicates. Data are depicted as box plots ranging from the 25th to 75th percentiles, showing the median. Whiskers extend from min to max value and each dot represents one clone. P-values were determined by student's t-test or Welch's t-test depending on the standard deviation. Details of statistical analyses are provided in **Table 22**.

It has been shown that EN1 and EN2 are equivalent in their biochemical function and that they can compensate for each other (*84*) (see 1.31 and 1.3.2). Therefore, a RT-qPCR was performed to analyze the *EN2* expression level in *EN1* -/- and WT NPCs and investigate a possible compensation by EN2. *EN1* -/- NPCs had a comparable *EN2* mRNA expression level as the WT NPCs. (**Figure 17**, **Table 22** for statistics). Hence, a compensation of the *EN1* knockout by increased *EN2* expression can be excluded at least at transcriptome level.

It was unexpected that the *EN1* -/- NPCs did not show any alterations in mitochondrial functions or other pathways that were associated with the heterozygous *En1* knockout in mice, like apoptosis or ROS (see also 1.3.3). Different possibilities can be considered to explain the results. The observations could be attributed to species-specific differences in *EN1* function between mice and humans or it might be a dose-dependent effect and *EN1* expression was too low to capture this. As mentioned before, *En1* expression starts around E8 in mice and NPCs can broadly be staged at E8.5 (*102, 169*). Thus, *EN1* should theoretically be expressed in NPCs, however, the differentiation stage between cells of a single dish can vary supporting the hypothesis that *EN1* expression might have been too low. Although the expression was detected in WT NPCs, the cycle threshold (CT) values in the RT-qPCR were high (> 25) indicating only low expression. In order to make correct assumptions regarding species-specific differences, the cells might need to be triggered to enhance the *EN1* knockout.

One possibility to increase the *EN1* expression is the differentiation of NPCs into DANs. In contrast to the *EN1* expression in NPCs, *En1* has been shown to be and remain stably expressed in adult DANs in mice (*105*) and in DANs derived from NPCs according to the differentiation scheme used in this work (*169*). Furthermore, the deficits in *En1*$^{+/-}$ mice were also shown for matured DANs (*80*). Therefore, the differentiation of NPCs into DANs was used to enhance the effect of the *EN1* knockout in the human model.

2.3 Analysis of mitochondrial and respiratory function in *EN1* knockout DANs

2.3.1 Differentiation of *EN1* knockout hiPSC to DANs

EN1 is essential during development and maintenance of dopaminergic neurons (see also 1.3.2). During the early phase of expression around E8, *EN* is crucial for the correct mid-/hindbrain patterning (*102*) and later on for the maintenance of DANs (*105, 106*). During development, *En1* and *En2* can compensate for each other. In adult DANs however, the maintenance function is relying to a greater extent on *En1* as *En2* is only expressed in a subset of SNpc DANs (*105*).

According to the established function of En1 in mice, it was obvious to analyze the effect of the *EN1* knockout on the ability of cells to differentiate into DANs in the human model. The efficiency of DAN differentiation was estimated by immunostainings for the DAN marker TH after maturation for 42 days. All clones were able to differentiate into RBFOX3+ (also known as NeuN) neurons and TH+ DANs (**Figure 18A**). Interestingly the differentiation efficiency of about 8 % was similar between the *EN1* knockout and the WT. In addition, the percentage of RBFOX3+ neurons in the cultures was constant with 80 - 90 % (**Figure 18B, Table 26** for statistics). This was unexpected, but constant over three independent differentiations.

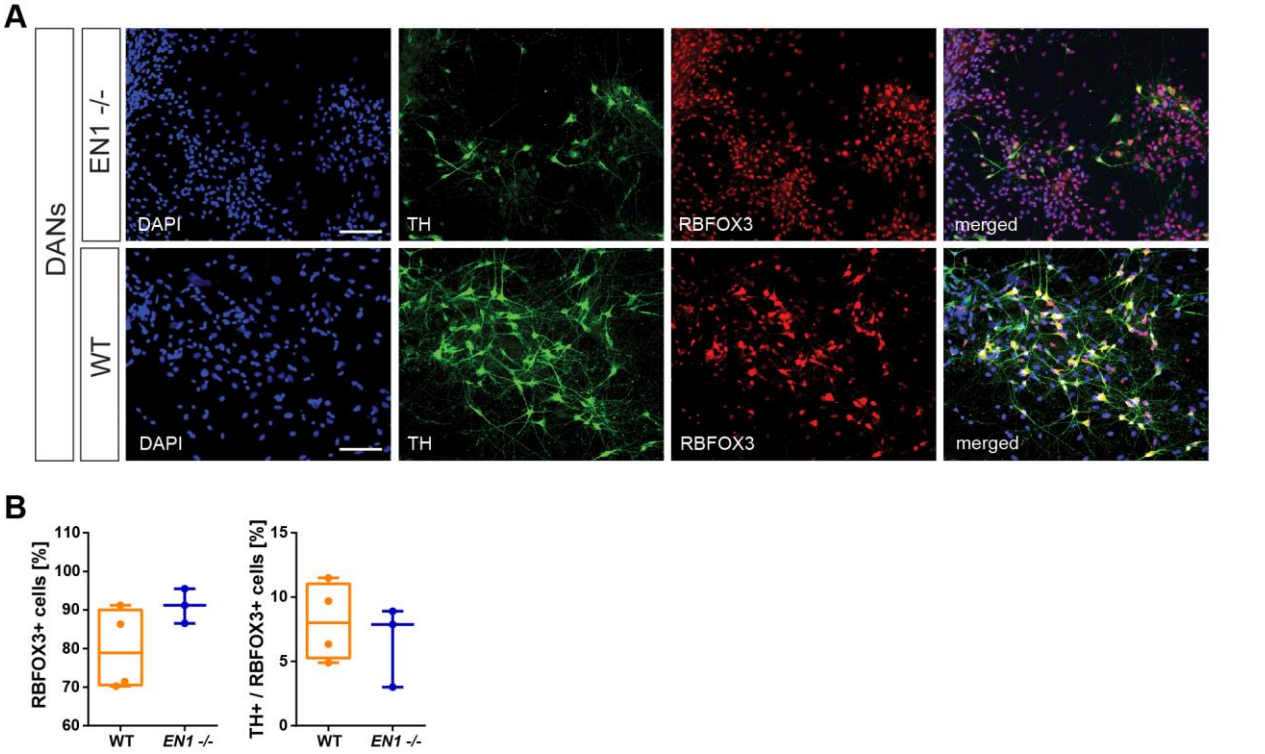

Figure 18: DAN differentiation of *EN1* knockout hiPSCs. (A) Immunofluorescence stainings of DANs for the neuronal marker RBFOX3 and the dopaminergic marker TH, shown exemplarily for *EN1* -/- clone 5-12 and WT clone 4-4. Scale bars: 100 µm **(B)** Quantification of differentiation efficiency. The percentage of neurons (RBFOX3) and DANs (TH) in the culture were quantified by immunostainings. n = 4 WT and 3 *EN1* -/- clones, three independent differentiations. Data are depicted as box plots ranging from the 25th to 75th percentiles, showing the median. Whiskers extend from min to max value and each dot represents one clone. P-values were determined by student's t-test or Welch's t-test depending on the standard deviation. Details of statistical analyses are provided in **Table 26**.

The dose-dependent effect of *Engrailed* has been investigated extensively in mice. In these studies, one allele of *En* was sufficient to ensure normal development of DANs (*174*). *EN2*, which is still intact in *EN1*-/- clones and expressed at a similar level as in WT NPCs (**Figure 17**), might compensate for EN1 regarding specification and survival of DANs during differentiation.

2.3.2 Mitochondrial and respiratory characterization of *EN1* knockout DANs

To investigate if the *EN1* knockout has an effect on mitochondria in DANs, the integrity of mitochondria was investigated using MitoTracker analysis, which accumulates in mitochondria with intact membrane potential. Interestingly, the functionality of mitochondria was not altered in *EN1* -/- DANs, neither in statistical analysis of the average intensity per clone (**Figure 19A, Table 27** for statistics) nor in distribution analysis **(Figure 19B)**. Thus, similar to the NPCs, the

mitochondrial functionality is not compromised upon *EN1* knockout in human DANs. To determine if there are alterations in the abundance of the respiratory chain complexes western blots for labile subunits of each complex were performed. Again, as observed in *EN1* -/- NPCs, the abundance of the EN1-regulated complex I was unchanged in *EN1* -/- DANs. In contrast to what has been observed in NPCs, complex IV was reduced to about 60 % of the WT protein level (**Figure 19C, Table 28** for statistics). Thus, the *EN1* knockout might have a different effect during development and in mature DANs. Although deficits in complex I have been noticed predominantly in connection with the *En1* knockout in mice, impairments of complex IV regarding activity and abundance have also been observed in *SNCA* and *PRKN* PD models, respectively (*177–179*). Therefore, there might be species-specific differences between mice and human, however, still linking EN1 with mitochondrial dysfunction and PD.

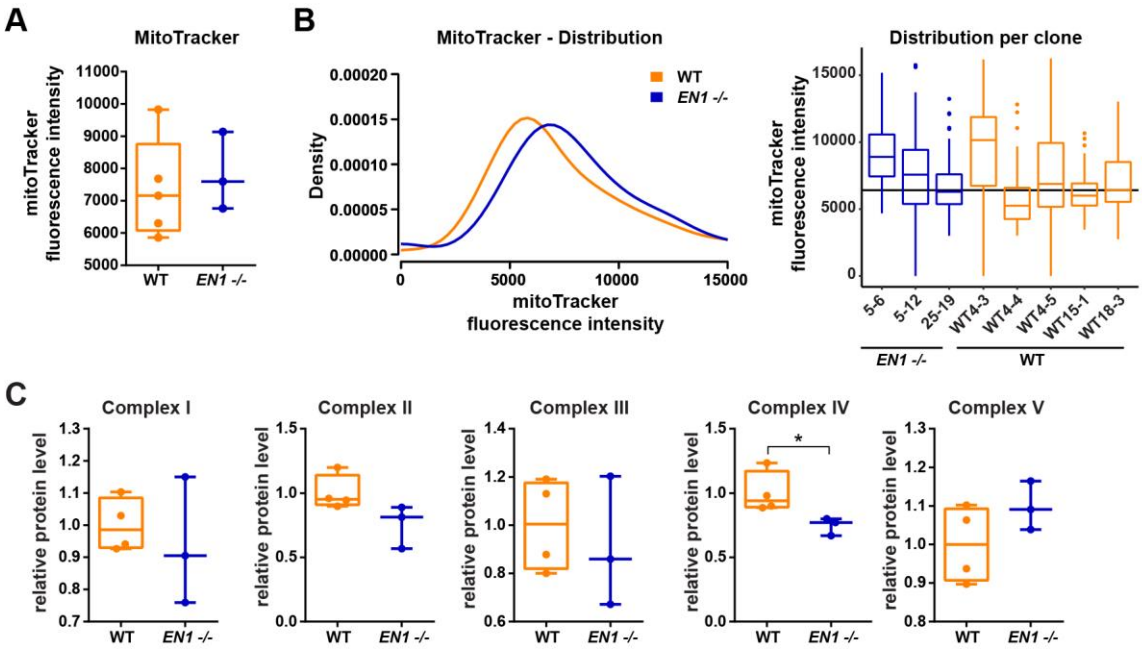

Figure 19: Assessment of mitochondrial quantity and function in DANs. (A) MitoTracker analysis to determine mitochondrial functionality in DANs. The cytosolic fluorescence intensity was quantified. n = 5 WT and 3 *EN1* -/- clones, in triplicates **(B)** Density plot showing fluorescence intensity distribution for WT and *EN1* -/- clones combined (left panel) and boxplot showing the distribution for each individual clone (right panel). n = 5 WT and 3 *EN1* -/- clones, in triplicates. **(C)** The quantity of respiratory chain complexes I-V was assessed by western blot using antibodies against NDUFB8 (complex I), SDHB (complex II), UQCRC2 (Complex III), MT-CO2 (complex IV) and ATP5A (complex V). Protein levels were normalized to GAPDH and the average protein levels of WT clones. An exemplary western blot is shown in the appendix. n = 4 WT and 3 *EN1* -/- clones, in triplicates. Data are depicted as box plots ranging from the 25th to 75th percentiles, showing the median. Whiskers extend from min to max value and each dot represents one clone (A, C). P values were determined by student's t-test or Welch's t-test depending on the standard deviation (A; C) and Kolmogorov-Smirnov test and linear regression (B). P-values are indicated only if both tests (Kolmogorov-Smirnov and linear regression) resulted in a significance. Details of statistical analyses are provided in **Table 27 and Table 28**. *, $p < 0.05$.

Following the assessment of mitochondrial function, *EN1* knockout DANs were investigated for bioenergetic impairments. To assess mitochondrial respiration, a mitochondrial stress test using the Seahorse XF flux analyzer was performed, adding either glucose or pyruvate as substrates. The parameters that can be assessed with the mitochondrial stress test are depicted in **Figure 15A**. At first, glucose was supplemented to the medium. Using glucose as substrate, the basal and maximal OCRs were significantly reduced in *EN1* knockout cells (**Figure 20A, Table 29** for statistics). *EN1* -/- DANs already exhibited a decreased mitochondrial respiration under homeostatic conditions

(basal respiration), which also persists when forced to work with full capacity (maximal respiration) (**Figure 20A, Table 29** for statistics). To determine the bottleneck in the carbohydrate metabolism that is involved in mitochondrial respiration, pyruvate was also added as a substrate. In contrast to what has been observed when relying on glucose as a substrate, WT and *EN1* -/- DANs displayed no difference in basal respiration and maximal respiration when pyruvate was supplemented (**Figure 20B, Table 29** for statistics). This might hint towards a defect upstream of pyruvate, indicating that not the TCA and respiratory chain but rather glycolysis might be affected. The proton leak was not altered between *EN1* -/- and WT DANs when supplied with either glucose or pyruvate (**Figure 20A, B**).

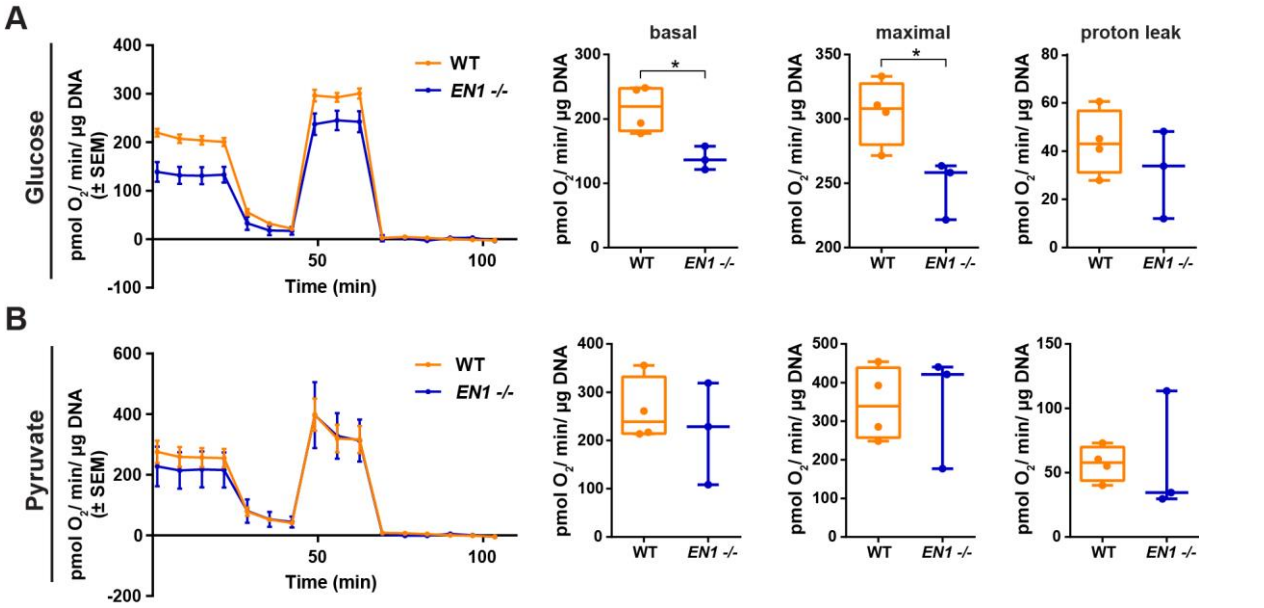

Figure 20: Characterization of mitochondrial respiration in DANs. The oxygen consumption rate was measured using a Seahorse XFe96 Extracellular Flux Analyzer. The measurement (**Figure 15A**) was performed in Seahorse XF assay medium supplemented with either 25 mM glucose **(A)** or 5 mM pyruvate **(B)** as substrates. An overview of the measurement (left panel) and detailed analyses of basal respiration, maximal respiration, and proton leak (right panels) are shown. n = 4 WT and 3 *EN1* -/- clones, in triplicates. Data are depicted as mean ± standard error of the mean (SEM) and box plots ranging from the 25th to 75th percentiles, showing the median. Whiskers extend from min to max value and each dot represents one clone. P-values were determined by student's t-test or Welch's t-test depending on the standard deviation. Details of statistical analysis are provided in **Table 29**. *, $p < 0.05$.

With *En1* being described to be stably expressed in DANs, the effect of the knockout was expected to be more prominent in mature DANs then in NPCs. As already observed in NPCs, mitochondrial function, including membrane potential and quantity of most of the respiratory chain complexes were not altered in *EN1* -/- DANs. Interestingly, enhancing a possible *EN1* knockout by differentiation into DANs resulted in a reduced basal and maximal OCR in the mitochondrial stress test after relying on glucose but not pyruvate as a substrate. Thus, indicating a possible bottleneck in glycolysis, which has not been shown in connection with the *EN1* knockout so far.

2.4 Analysis of *EN1* knockout NPCs after Wnt stimulation

The characterization of *EN1* knockout DANs, showed in contrast to the NPCs a deficit in glycolysis. This might have been an effect from the different differentiation stage or from the higher level of *EN1* and thus a more severe effect of the knockout in DANs. To determine if the phenotype

was caused by a higher *EN1* expression in WTs, the *EN1* expression was stimulated in NPCs. As stated in the literature for different species (*127, 128*) including a human system (*129*), *EN1* expression can be induced by canonical Wnt signaling (in the following only referred to as Wnt signaling). The regulation is direct via the TCF/LEF components of the Wnt pathway (*129*). In addition, the transcriptome data of the *EN1* -/- NPCs identified DEGs in the Wnt signaling pathway which further implied a connection between EN1 and Wnt (**Figure *13*C**). Therefore, to investigate whether the expression level of *EN1* in NPCs has been too low and validate the findings from the DANs, NPCs (*EN1* -/- and WT) were subjected to Wnt stimulation. The GSK-3β inhibitor CHIR99021 which inhibits the phosphorylation and degradation of β-catenin and thus induces the expression of Wnt target genes (including *EN1*) (see also 1.4) was used and added for 48h at a concentration of 3 µM.

A RT-qPCR was performed to assess the *EN1* expression after Wnt stimulation (+CHIR99021). The *EN1* expression level was significantly increased upon stimulation in WT NPCs, whereas the stimulation did not affect *EN1* expression in *EN1* -/- NPCs (**Figure 21, Table 30** for statistics). Exhibiting an *EN1* knockout, *EN1* -/- clones naturally cannot respond to Wnt signaling by increasing the *EN1* expression. After Wnt stimulation (+CHIR99021), the difference between the *EN1* mRNA level in WTs and the *EN1* -/- NPCs is highly significantly reduced (**Figure 21, Table 30** for statistics**)**. Using a two-way ANOVA, there is no significant difference in the *EN1* mRNA level between WT and *EN1* -/- unstimulated NPCs in contrast to what has been shown for unstimulated NPCs using a t-test (**Figure 11B**). The significant difference of *EN1* expression in unstimulated NPCs was masked by the highly significant effect of the stimulation.

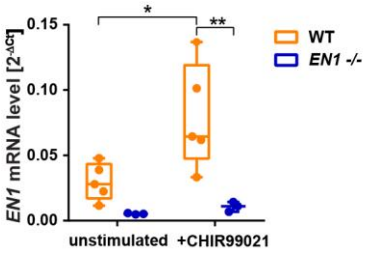

Figure 21: *EN1* expression level in unstimulated and Wnt stimulated NPCs. RT-qPCR analysis of *EN1* mRNA expression in NPCs. mRNA levels were normalized to ACTB. Cells were Wnt stimulated with 3 µM CHIR99021 for 48 h before RNA isolation. n = 5 WT and 3 *EN1* -/- clones, in triplicates. Data are depicted as box plots ranging from the 25th to 75th percentiles, showing the median. Whiskers extend from min to max value and each dot represents one clone. P-values were determined by two-way ANOVA and Sidak post hoc tests. Details of statistical analyses are provided in **Table 30**. *, $p < 0.05$; **, $p < 0.001$.

2.4.1 Transcriptome analysis of Wnt stimulated *EN1* knockout NPCs

The induced expression of *EN1* by stimulation of the Wnt signaling pathway was exploited to enhance the phenotype of the knockout (*129*). The *EN1* expression was increased significantly after Wnt stimulation in the WT clones, whereas in the *EN1* -/- NPCs the expression did not change in response to the stimulation. To assess the consequences of the *EN1* knockout in the enhanced model in an unbiased way, transcriptome analysis was performed of Wnt stimulated *EN1* -/- and WT NPCs. Similar to the unstimulated NPCs, the DEGs between Wnt stimulated *EN1* -/- and WT NPCs were analyzed at first to see if the pathway enrichment analysis confirms the observations made in DANs or reveal other molecular pathways associated with the *EN1* knockout. The effect of the Wnt signaling on WT and *EN1* -/- NPCs, respectively, was investigated subsequently.

2.4.1.1 Quality control

Dimensionality reduction provided an overview of the stimulation effect. PCA of unstimulated and WNT stimulated NPCs showed that the highest variation (PC1) can now be attributed to the stimulation (**Figure 22A**). Similar to the unstimulated NPCs, the clones of the same genotype clustered together (**Figure 22B**). The genotype which was the main component of variance in unstimulated cells explained the variation along PC2, indicating that the Wnt stimulation has a bigger effect on the transcriptome of the NPCs than the genotype. Analogous to unstimulated NPCs, the variation between replicates is also low in Wnt stimulated cells (**Figure 22C**), showing that the transcriptome analysis worked well and DEGs can be attributed to genotype and stimulation effects.

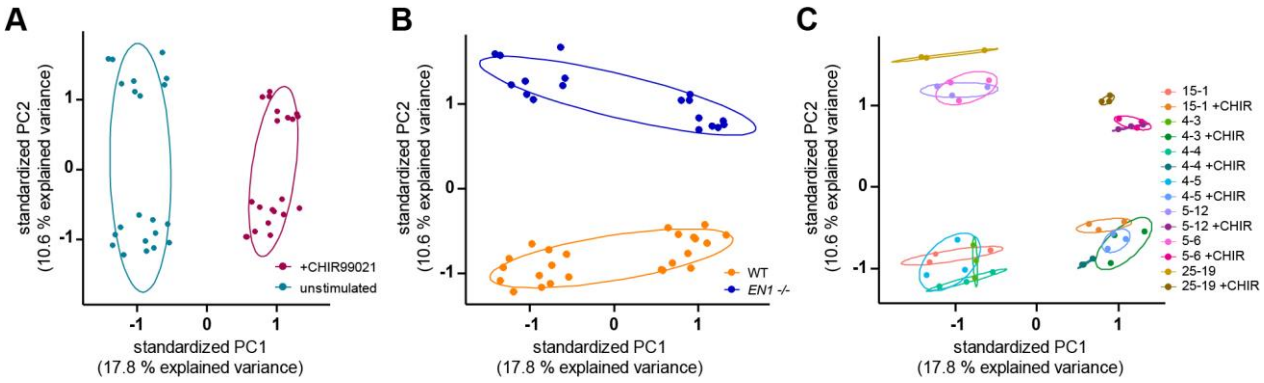

Figure 22: Dimension reduction and quality assessment of transcriptome analysis after Wnt stimulation. PCA of unstimulated and Wnt stimulated (+CHIR99021) *EN1* -/- and WT NPCs. PCA plots show the distribution according to stimulation **(A)**, genotype condition **(B)** and every sample **(C)**. Probability ellipses depict 0.68 of normal probability. n = 4 WT and 3 *EN1* -/- clones, in triplicates. (in collaboration with Sebastian Schmidt)

2.4.1.2 Differentially expressed genes in Wnt stimulated *EN1* knockout NPCs

The transcriptome analysis of Wnt stimulated NPCs identified about 15,000 genes, which is comparable to what was identified in unstimulated NPCs. Using the same thresholds as before (log2 fold change ≥ 0.5 and p-adjust ≤ 0.05), 2061 genes were differentially expressed between Wnt stimulated *EN1* -/- and WT NPCs. This is slightly less than what has been detected in unstimulated NPCs. The heatmap shows that the DEGs correlate with the genotypes, again with a higher variation between the different clones than the subclones (**Figure 23A**). DEGs were divided equally into up- and downregulated genes (**Figure 23B**). The *EN1* mRNA expression level was downregulated, confirming RT-qPCR results (**Figure 21A**) and the knockout (**Figure 23B**). To ensure that the conclusions based on the transcriptome are correct, the mRNA levels of top up- and downregulated DEGs were confirmed by RT-qPCR (**Figure 23C, Table 31** for statistics). Pathway enrichment analysis was performed to investigate the molecular alterations in stimulated *EN1* -/- cells (**Figure 23D, E**). DEGs enriched in pathways associated with axon guidance, ECM, PI3K-Akt-mTOR signaling, and development emerged in the analysis using MSigDB (**Figure 23D**) and WikiPathway (**Figure 23E**) terms. These pathways can be categorized into similar groups as observed for the unstimulated NPCs, indicating that *EN1* plays an important role in these processes that becomes already apparent without enhancing the *EN1* expression level.

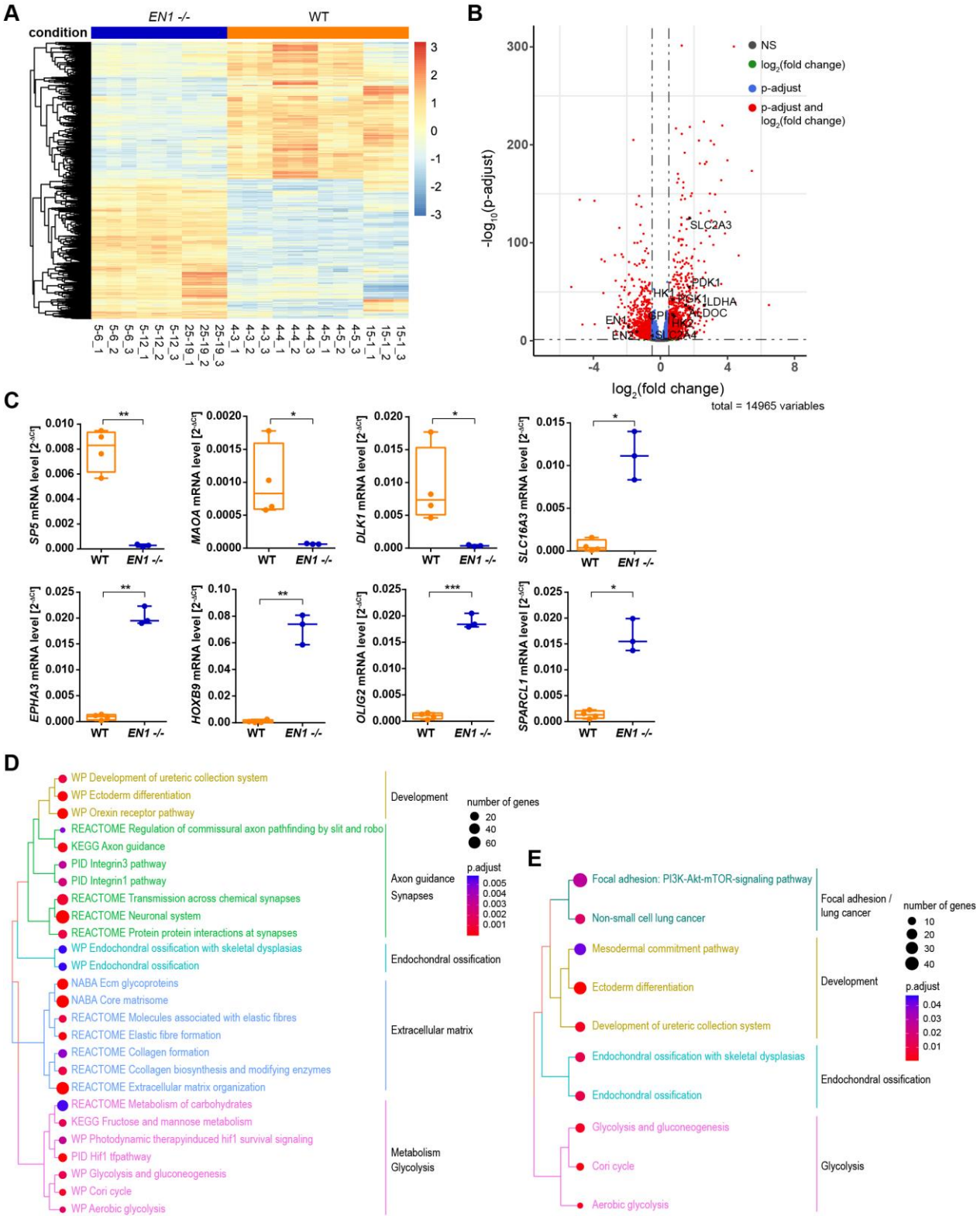

Figure 23: Validation and pathway enrichment analysis of DEGs between Wnt stimulated *EN1* -/- and WT NPCs. (A) Heatmap displaying the DEG expression levels for every sample. Red represents upregulated, and blue represents downregulated genes. **(B)** Volcano plot showing DEGs according to their fold change and significance. Every detected gene is represented by a dot. Lines visualize fold change ($log_2(0.5)$) and significance ($-log_{10}(0.05)$) cut-offs. Selected genes are highlighted **(C)** Validation of top DEGs by RT-qPCR. mRNA levels were normalized to ACTB. Data are depicted as box plots ranging from the 25th to 75th percentiles, showing the median. Whiskers extend from min to max value and each dot represents one clone. n = 4 WT and 3 *EN1*

-/- clones, in triplicates **(D, E)** Tree plots showing significantly enriched pathways using the MSigDB collection **(D)** or solely WikiPathway **(E)** terms. P-values were determined by student's t-test or Welch's t-test depending on the standard deviation. Details of statistical analyses are provided in **Table 31**. *, $p < 0.05$; **, $p < 0.01$; ***, $p < 0.001$. (in collaboration with Sebastian Schmidt)

However, after Wnt stimulation, DEGs that were enriched in pathways associated with metabolic functions appeared. DEGs were summarized in pathways related to the metabolism of carbohydrates and more specifically seem to be classified in glycolysis-associated pathways. This was consistent with the enrichment of terms from three different databases (REACTOME, WikiPathways and KEGG) (**Figure 23D, E)**. Except for the glucose transporter *SLC2A4*, all genes annotated in the WikiPathway 'glycolysis and gluconeogenesis' term were upregulated in Wnt stimulated *EN1* -/- NPCs (**Figure 23B)**. Genes that were upregulated in these pathways are central to carbon metabolism and glycolysis, for example *hexokinase 1* (*HK1)*, *hexokinase 2* (*HK2)*, *phosphoglucose isomerase* (*GPI)* and aldolase C (*ALDOC)*. Upregulation of glycolytic genes might imply a higher glycolytic flux. In contrast, pyruvate dehydrogenase kinase 1 (PDK1*)*, a kinase that inhibits the pyruvate dehydrogenase (PDH*)*, which is responsible for the conversion of pyruvate into acetyl-CoA for carbon transition into the TCA cycle was also upregulated and thus might restrain metabolism through the TCA downstream of glycolysis (*180*).

Unexpectedly, DEGs related to OXPHOS and mitochondria-associated pathways (e.g. ROS and mitophagy) were not enriched in Wnt stimulated *EN1* -/- NPC DEGs. Therefore, even after enhancement of the phenotype by Wnt stimulation, transcriptome analysis does not suggest defects in the respiratory chain but rather upstream of the TCA in glycolysis. This also supports the experimental data from *EN1* -/- DANs, that showed a reduced basal and maximal respiration when glucose was supplied as a substrate.

2.4.1.3 Effect of Wnt stimulation on either WT or *EN1* knockout NPCs

To determine the effect of the Wnt signaling on the transcriptome of *EN1* -/- or WT NPCs and to ensure that the glycolysis associated DEGs can be attributed to a genotype effect, the transcriptome data of unstimulated versus Wnt stimulated NPCs were investigated for both, *EN1* -/- and WT cells. Comparing the gene expression data of unstimulated WT NPCs with Wnt stimulated WT NPCs identified DEGs that were enriched in pathways associated with Wnt signaling. Furthermore, pathways involved in development, differentiation or focal adhesion were identified (**Figure 24A**). As Wnt is essential in all these processes these pathways were not surprising to appear after Wnt stimulation (*181–183*). DEGs of pathways involved in glycolysis, however, were not altered upon Wnt stimulation in WT's, indicating that alterations in glycolysis are not a stimulation but rather a genotype effect.

Next, the pathway enrichment analysis of DEGs from unstimulated versus Wnt stimulated *EN1* -/- NPCs was performed. Many pathways were similar to the pathways detected in the WT's, including for example also differentiation or focal adhesion pathways (**Figure 24A, B**). This indicates that the effect of the Wnt stimulation is at least partially similar between the *EN1* knockout and the WT. Interestingly, also pathways associated with glycolysis were identified when comparing unstimulated and Wnt stimulated *EN1* -/- NPCs **(Figure 24B**), similar to the pathways identified when comparing Wnt stimulated WT with Wnt stimulated *EN1* -/- NPCs (**Figure 23D, E**). Thus, Wnt signaling seems to have an effect on glycolysis in *EN1* -/- cells. However, as the genes were not identified when assessing the effect of Wnt stimulation in WT NPCs, the alterations in genes

associated with glycolysis have to be associated with the *EN1* -/-. The close connection between EN1 and Wnt further supports this assumption.

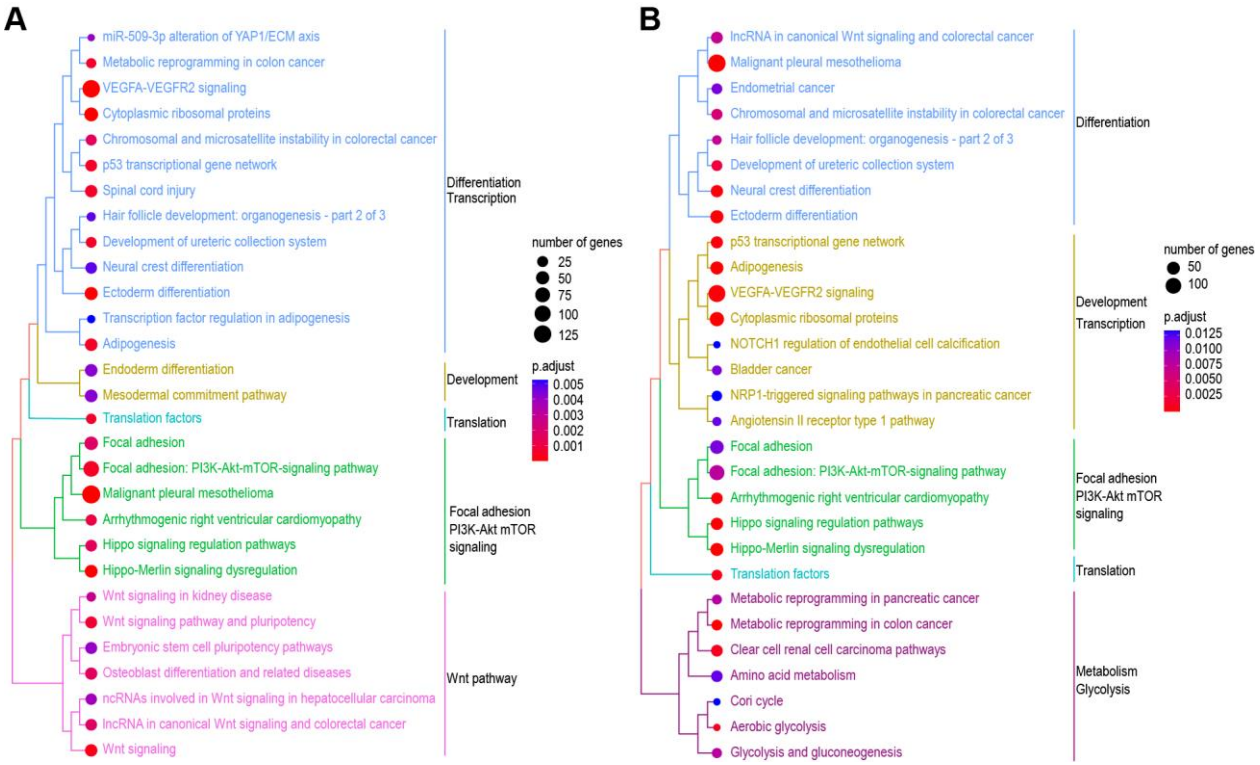

Figure 24: Pathway enrichment analysis of DEGs between unstimulated and Wnt stimulated WT and *EN1* -/- NPCs, respectively. Tree plots showing significantly enriched pathways of DEGs between unstimulated and WNT stimulated WT NPCs **(A)** and unstimulated and WNT stimulated *EN1* -/- NPCs **(B)** using WikiPathway terms. (in collaboration with Sebastian Schmidt)

2.4.2 Validation of glycolytic alterations in Wnt stimulated *EN1* knockout NPCs

To validate the transcriptome results and investigate the hypothesis of alterations in the carbohydrate metabolism in the human Wnt stimulated *EN1* knockout model, a combined glycolytic and mitochondrial stress test was performed using the Seahorse XF extracellular flux analyzer. The parameters that can be assessed with the mitochondrial and glycolytic stress test, respectively are depicted in **Figure 15A, B**. Using glucose as substrate, basal and maximal respiration were significantly reduced in Wnt stimulated *EN1*-/- NPCs. *EN1* -/- NPCs exhibited a decreased OCR already under homeostatic conditions (basal respiration). When forced to work with full capacity (maximal respiration) the difference between Wnt stimulated *EN1* -/- and WT NPCs became even more pronounced (**Figure 25A, Table 32** for statistics). In addition, *EN1* -/- NPCs had a reduced proton leak. Similar to the DANs, the bottleneck in mitochondrial respiration was determined by adding pyruvate as a substrate. Interestingly, despite basal respiration and proton leak being significantly decreased, maximal respiration was not altered, suggesting that reduction in maximal mitochondrial respiration might be due to limitations within glycolysis (**Figure 25B, Table 32** for statistics). Therefore, the results from the mitochondrial stress test of Wnt stimulated *EN1* -/- NPCs also indicated a bottleneck in glycolysis rather than the TCA especially in energy-demanding situations which agrees with the transcriptome data and the results obtained in *EN1* -/- DANs. Comparing the effect of the *EN1* knockout between Wnt stimulated NPCs and DANs, the deficit in the OCR was less pronounced in DANs (compare **Figure 20A, B**

and **Figure 25A, B)**. Especially after using pyruvate as substrate the OCR was unaffected in *EN1* -/- DANs whereas in WNT stimulated NPCs the respiration under homeostatic conditions was compromised. Hence, DANs might not have reached a maturity that requires them to rely on *EN1* as a survival factor or the expression of *EN1* is simply higher after Wnt stimulation than in the DANs, resulting in a more pronounced phenotype. In addition, the differentiation efficiency of only 8 % and high concentrations of differentiation/survival factors (BDNF and GDNF) in the medium might have masked more subtle effects.

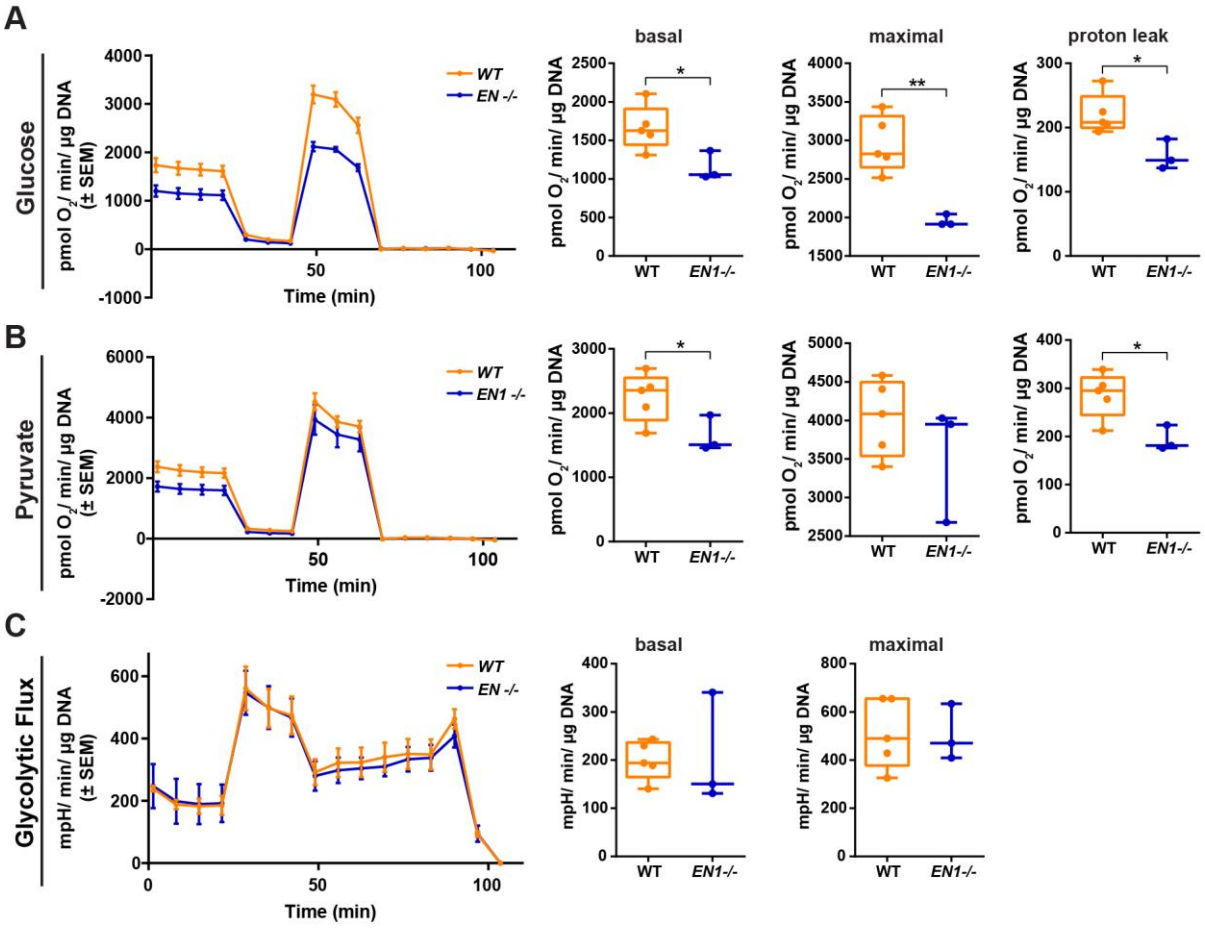

Figure 25: Characterization of mitochondrial respiration and glycolytic flux in Wnt stimulated NPCs. The oxygen consumption rate and extracellular acidification rate were measured in NPC after 48 h of Wnt stimulation with CHIR99021 using a Seahorse XFe96 Extracellular Flux Analyzer. The measurements (**Figure 15**) were performed in Seahorse XF assay medium supplemented with either 25 mM glucose **(A, C)** or 5 mM pyruvate **(B)** as substrates. **(A, B)** An overview of the oxygen consumption rate (left panel) and detailed analyses of basal respiration, maximal respiration, and proton leak (right panels) are shown. **(C)** Overview of the extracellular acidification rate and detailed graphs of basal and maximal glycolytic flux are shown. n = 5 WT and 3 *EN1* -/- clones, in triplicates. Data are depicted as mean ± standard error of the mean (SEM) and box plots ranging from the 25th to 75th percentiles, showing the median. Whiskers extend from min to max value and each dot represents one clone. P-values were determined by student's t-test or Welch's t-test depending on the standard deviation. Details of statistical analysis are provided in **Table 32**. *, $p < 0.05$; **, $p < 0.01$.

In parallel to the oxygen consumption rate, the extracellular acidification rate (ECAR) is measured by the Seahorse XF extracellular flux analyzer, which allows an estimation of the glycolytic flux. During glycolysis, glucose is converted into pyruvate and lactate producing protons in the process (see **Figure 5** for an overview of glycolysis). This results in the acidification of the medium and can therefore be used to assess the glycolytic flux. The glycolytic flux was measured by adding 25

mM glucose as a substrate. Basal glycolytic flux under homeostatic conditions is measured at first, followed by the maximal glycolytic flux (**Figure 15B**). The maximal glycolytic flux, also referred to as glycolytic capacity, is induced by injection of oligomycin which shuts down the mitochondrial ATP-synthase and hence ATP production in mitochondria. To compensate for the energy deficits, the cells increase their glycolytic ATP production. The difference between the basal and the maximal glycolytic flux is called the glycolytic reserve. In a last step, the acidification attributed to non-glycolytic processes was determined by injection of 2-deoxyglucose (2-DG). 2-DG is an allosteric inhibitor of the first enzyme in glycolysis, hexokinase and thus stalls glycolysis completely. The non-glycolytic acidification has to be subtracted from all data to yield the basal and maximal glycolytic flux.
Although the OCR implied a defect in glycolysis, the basal and maximal glycolytic flux measured by the ECAR were not altered in Wnt stimulated *EN1* -/- NPCs (**Figure 25C, Table 32** for statistics). However, the ECAR is very complex to interpret and can only be proportionally linked to the acidification of the medium under the assumption that all lactate is exported out of the cell via the electroneutral lactate/H+ transporter. As not all pyruvate is converted into lactate which is secreted and contributes to medium acidification and lactate can also be oxidized in mitochondria and other metabolic processes, the ECAR provides only a rough overview of the glycolytic rate and only very drastic changes can be detected (*184*). Nevertheless, the results could indicate that metabolic branches relying on glycolysis intermediates are altered upon *EN1* knockout. With most of the DEGs in glycolysis-associated pathways being upregulated a decreased OCR after adding glucose was unexpected **(Figure 23B**).

One reason that could explain the decreased basal and maximal OCR in Wnt stimulated *EN1* -/- NPCs and DANs when cells were relying on glucose while glycolysis-associated genes were upregulated, might be the substrate availability. The insulin regulated glucose transporter SLC2A4 (GLUT4) was the only DEG that was downregulated within the glycolysis-associated pathways in the transcriptome of Wnt stimulated *EN1* -/- NPCs. Therefore, the glucose uptake in Wnt stimulated NPCs was measured to investigate if reduced uptake of glucose underlies the diminished cellular respiration. However, the glucose uptake after Wnt stimulation was not affected in the *EN1* knockouts (**Figure 26, Table 33** for statistics), ruling out a substrate availability problem.

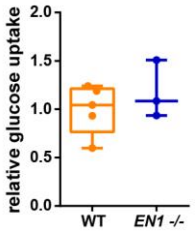

Figure 26: Glucose uptake of Wnt stimulated NPCs. Glucose uptake was measured in NPCs after 48 h of Wnt stimulation with CHIR99021 using a bioluminescent method. Glucose uptake was normalized to the average uptake of WT clones. n = 5 WT and 3 *EN1* -/- clones, in duplicates. Data are depicted as box plots ranging from the 25th to 75th percentiles, showing the median. Whiskers extend from min to max value and each dot represents one clone. P-values were determined by student's t-test or Welch's t-test depending on the standard deviation. Details of statistical analysis are provided in **Table 33**.

To assess the impact of the Wnt stimulation on the respiratory phenotype, the OCR from stimulated NPCs was compared to unstimulated NPCs. Supplying either glucose or pyruvate, the OCR was increased after stimulation of Wnt signaling using the GSK-3β inhibitor CHIR99021 (**Figure 27A,**

B). This can be explained by the function of Wnt to promote cell growth which also requires adaptation and modulation of cellular metabolism (reviewed in (*185*, *186*)).

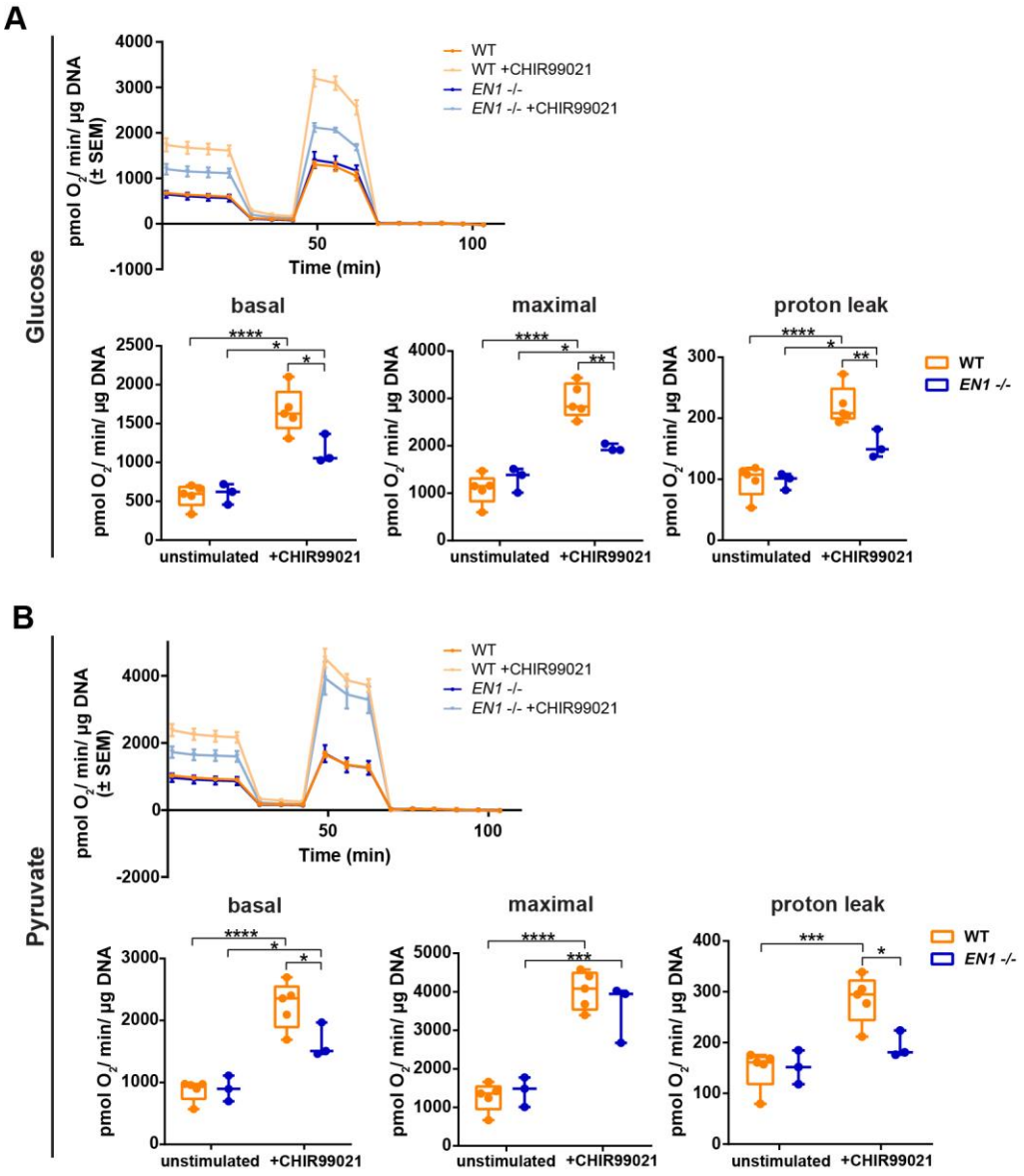

Figure 27: Comparison of mitochondrial respiration between unstimulated and Wnt stimulated NPCs. The oxygen consumption rate was measured in unstimulated and Wnt stimulated (48 h of CHIR99021) NPCs using a Seahorse XFe96 Extracellular Flux Analyzer. The measurement (**Figure 15**) was performed in Seahorse XF assay medium supplemented with either 25 mM glucose **(A)** or 5 mM pyruvate **(B)** as substrates. **(A, B)** An overview of the oxygen consumption rates (upper panel) and detailed analyses of basal respiration, maximal respiration, and proton leak (lower panels) are shown for unstimulated and Wnt stimulated cells. n = 5 WT and 3 *EN1* -/- clones, in triplicates. Data are depicted as mean ± standard error of the mean (SEM) and box plots ranging from the 25th to 75th percentiles, showing the median. Whiskers extend from min to max value and each dot represents one clone. P-values were determined by two-way ANOVA and Sidak post hoc tests. Details of statistical analysis are provided in **Table 34**. *, $p < 0.05$; **, $p < 0.001$; ***, $p < 0.001$; ****, $p \leq 0.0001$.

It has been shown that Wnt signaling supports a shift towards glycolysis and can induce upregulation/activation of key enzymes of glycolysis and the pentose phosphate pathways (PPP) including HK, LDHA, PDK1 and PFK which was neuroprotective in Alzheimer's Disease (*187, 188*). This correlates with observations in the transcriptome analysis. However, the Wnt stimulation

mainly affected the WT clones with the OCR being highly significantly increased in all measured parameters (**Figure 27A, B, Table 34** for statistics). The stimulation also increased the OCR in the *EN1* knockout clones but was less pronounced (**Figure 27A, B, Table 34** for statistics**)**, indicating that the observed deficits in cellular respiration can be attributed to a genotype effect.
Taken together, the mitochondrial and glycolytic stress tests validated the transcriptome data. Analysis of the OCR in the mitochondrial stress test suggested a bottleneck in glycolysis in *EN1* -/-. NPCs, which agrees with the reduced OCR in DANs when relying on glucose as a substrate. As the glycolytic flux as well as the glucose uptake were not altered in *EN1* knockout NPCs, pathways that branch off glycolysis might be affected.

2.4.3 Further assessment of mitochondrial function in Wnt stimulated *EN1* knockout NPCs

The transcriptome data of Wnt stimulated NPCs indicated a metabolic defect in carbohydrate metabolism, which was validated using the Seahorse XF Flux analyzer. The measurement is based on the OCR during OXPHOS. The decreased OCR was more pronounced after supplementing glucose as energy substrate, which implied a glycolytic defect, however, basal respiration was also reduced when supplementing pyruvate. Although not readily detected in the pathway enrichment analysis, these results do not exclude metabolic alterations in the TCA or in the respiratory chain. The connection between EN1 and PD, as well as the neuroprotective effect of EN1 is mainly attributed to reduced mitochondrial vulnerability at least partially mediated by the post-transcriptional regulation of complex I subunits of the respiratory chain in mouse models.

To investigate if the functionality of mitochondria is perturbed, MitoTracker staining was performed in Wnt stimulated NPCs. A trend towards less functional mitochondria was observed for Wnt stimulated *EN1* -/- clones when considering the average fluorescence intensity per clone (**Figure 28A, Table 35** for statistics). Distribution analysis of the data revealed that more *EN1* -/- cells displayed a significantly reduced fluorescence intensity compared to the WT cells (**Figure 28B**). MitoTracker stainings can provide information about two possible scenarios: Changes in the MitoTracker fluorescence can either be attributed to alterations in the number of functional mitochondria per cell or changes in the membrane potential in the same number of mitochondria which would indicate possible defects in the respiratory chain (*189*). As the MitoTracker fluorescence intensity was quantified by measuring the average intensity of all mitochondria per cell (intensity is normalized to all pixels within an area) this allows to draw conclusions about the intensity of the potential and thus the functionality of the respiratory chain. In addition, the total area of mitochondria was unchanged between Wnt stimulated *EN1* knockout and WT NPCs (**Figure 28C**), which further showed that the number of mitochondria is unchanged. To further support these data the ratio between total intensity and total area was increased in WTs compared to *EN1* -/- NPCs (**Figure 28D**). Thus, these data indicate that the changes in fluorescence intensity can be attributed to a reduced membrane potential, rather than decreased functional mitochondrial mass.
Furthermore, changes in the membrane potential and consequentially a reduced proton motive force can explain a reduction in the proton leak that was observed in the mitochondrial stress test for *EN1* -/- NPCs (*190*) (**Figure 25A, B**). Comparing mitochondrial function in unstimulated and Wnt stimulated NPCs, the WNT stimulation had only an effect on WT NPCs, which is concordant with Wnt being upstream of *EN1* (**Figure 28E, Table 35** for statistics) and implies a genotype-related dysfunction.

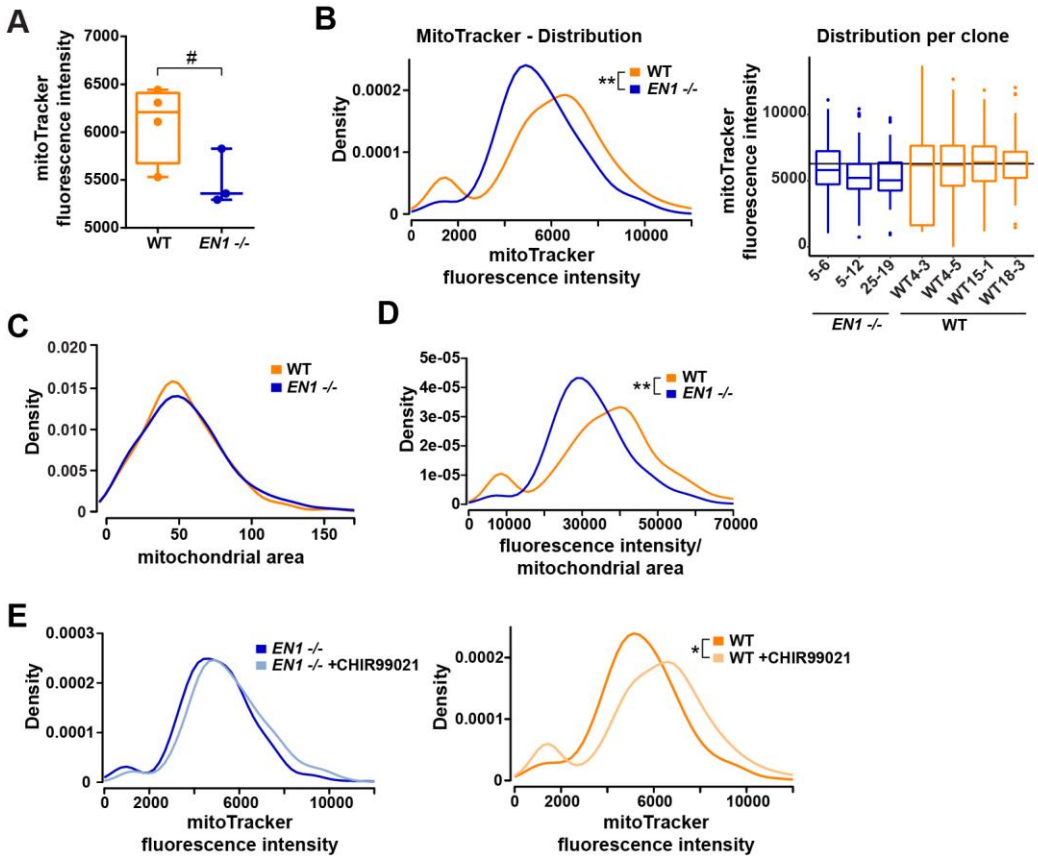

Figure 28: Assessment of mitochondrial functionality in Wnt stimulated NPCs (A) MitoTracker staining to analyze mitochondrial functionality in NPCs. The cytosolic fluorescence intensity was quantified after 48 h of Wnt stimulation with 3 µM CHIR99021. **(B)** Density plot showing fluorescence intensity distribution for WT and *EN1* -/- clones combined (left panel) and boxplot showing the distribution for each individual clone (right panel). **(C, D)** Density plots showing the distribution of the mitochondrial area **(C)** and the ratio of fluorescence intensity and mitochondrial area **(D)** Wnt stimulated *EN1* -/- and WT NPCs. **(E)** Density plots showing fluorescence intensity distribution for unstimulated and Wnt stimulated *EN1* -/- and WT NPCs, respectively. n = 4 WT and 3 *EN1* -/- clones, in triplicates. Data are depicted as box plots ranging from the 25th to 75th percentiles, showing the median. Whiskers extend from min to max value and each dot represents one clone (A). P-values were determined by student's t-test or Welch's t-test depending on the standard deviation (A) and Kolmogorov-Smirnov test and linear regression (B - E). P-values are indicated only if both tests resulted in a significance. Details of statistical analyses are provided in **Table 35**Fehler! Verweisquelle konnte nicht gefunden werden.. #, $p < 0.1$; *, $p < 0.05$; **, $p < 0.001$.

Next, the abundances of the respiratory chain complexes were analyzed by western blot in order to detect any molecular alterations that might underly the reduced mitochondrial membrane potential in the Wnt stimulated *EN1* -/- NPCs. Indeed, Wnt stimulation revealed a decreased abundance of complex I in *EN1* -/- NPCs, while the abundances of the remaining respiratory chain complexes were unchanged. (**Figure 29, Table 36** for statistics). These results match the described En1 function of post-transcriptional regulation of the complex I subunits Ndufs1 and Ndufs3 in mice. A reduced abundance might indicate assembly perturbations that could also be accompanied by functional deficits of complex I. To further investigate the molecular pathways associated with mitochondrial dysfunction in Wnt stimulated *EN1*-/- NPCs, the activity of complex I was analyzed. The assay only measured the NADH-dependent activity of complex I, whereas functions like proton pumping and reduction of ubiquinone were not assessed. As Ndufs1 encodes for a complex I subunit that binds and oxidizes NADH, this is probably the critical function that is compromised upon *En1* knockout (*191*). Surprisingly, complex I activity was not affected by the *EN1* knockout (**Figure 29B, Table 37** for statistics**)**.

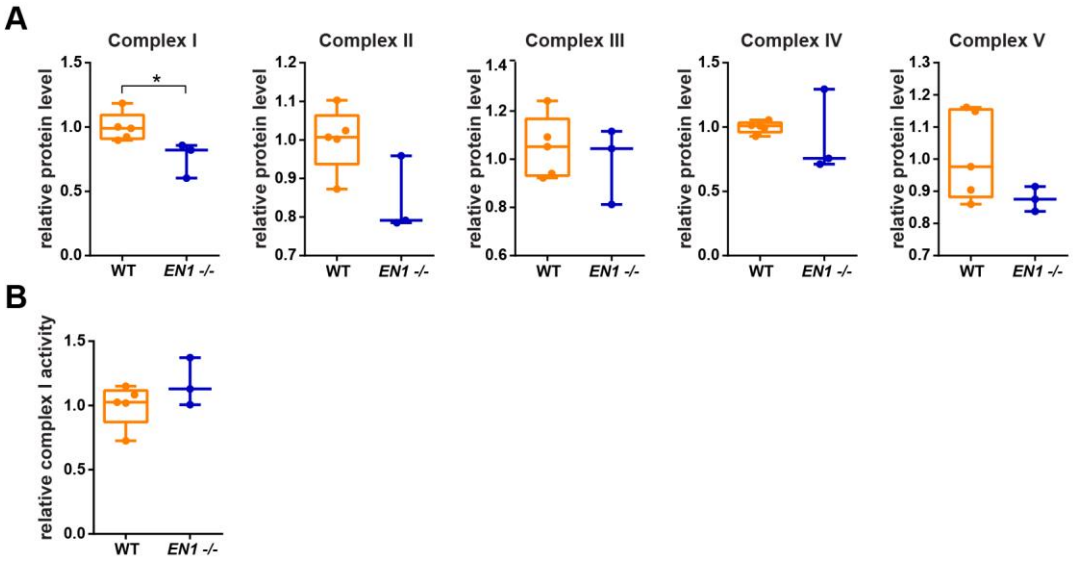

Figure 29: Assessment of respiratory chain composition and function in Wnt stimulated NPCs. (A) The quantity of respiratory chain complexes I-V was assessed by western blot after cells were Wnt stimulated with 3 µM CHIR99021 for 48 h using antibodies against NDUFB8 (complex I), SDHB (complex II), UQCRC2 (Complex III), MT-CO2 (complex IV) and ATP5A (complex V). Protein levels were normalized to ACTB or GAPDH and the average protein levels of WT clones. An exemplary western blot is shown in the appendix. n = 5 WT and 3 *EN1* -/- clones, in triplicates. **(B)** Quantification of relative complex I activity after 48 h of Wnt stimulation with 3 µM CHIR99021. Complex I activity was normalized to the average complex I activity of WT clones. n = 5 WT and 3 *EN1* -/- clones, in triplicates. Data are depicted as box plots ranging from the 25th to 75th percentiles, showing the median. Whiskers extend from min to max value and each dot represents one clone. P-values were determined by student's t-test or Welch's t-test depending on the standard deviation. Details of statistical analyses are provided in **Table 36** and **Table 37**. *, $p < 0.05$.

Therefore, the compromised mitochondrial function in Wnt stimulated *EN1* -/- can most likely be attributed to a reduced abundance of fully functional complex I in a quantitatively unaltered pool of mitochondria. Thus, analyzing the mitochondrial integrity of Wnt stimulated NPCs, suggests respiratory chain complex I associated compromises in *EN1* -/- NPCs in addition to defects in the glycolysis pathway of the carbohydrate metabolism.

2.5 Summary of experimental data

Table 5 summarizes the experimental data from unstimulated *EN1* -/- NPCs and the enhanced knockout in DANs and Wnt stimulated *EN1* -/-. NPCs.

Table 5: Summary of experimental data from *EN1* -/- NPCs, DANs and Wnt stimulated *EN1* -/- NPCs. Data refer to comparison between WT and the *EN1* -/- clones. - = unchanged; n/a = not available.

	***EN1* -/- NPCs**	***EN1* -/- DANs**	**Wnt stimulated *EN1* -/- NPCs**
Mitochondrial function (MitoTracker)	-	-	↓
Complex abundances	-	C IV ↓	C I ↓
Complex I activity	-	n/a	-
Mitochondrial stress test (Seahorse) - glucose	-	Basal OCR Maximal OCR ↓	Basal OCR Maximal OCR Proton leak ↓
Mitochondrial stress test (Seahorse) - pyruvate	-	-	Basal OCR Proton leak ↓

2.6 Observations made in two heterozygous *EN1* knockout clones

Already during the development, the expression of *Engrailed* is crucial for the survival of DANs in a dose-dependent manner, with one allele of *En1* on an *En* null background being sufficient for a normal phenotype during development, whereas DANs are completely absent in *En1* and *En2* double mutants (*105, 106*). Although having no phenotype at birth, heterozygous *En1* knockout mice experience progressive degeneration of DANs starting around 8 weeks after birth (*En2* WT background) (*80*).

Considering the results obtained in mice, it was interesting to also get an impression of the dose-dependency of *EN1* in a human model. Therefore, although not sufficient for a valid statistical analysis due to limited number of clones (n = 2), the *EN1* +/- clones had been analyzed in parallel with the *EN1* -/- clones. As statistical analysis was not feasible, the results were only regarded as observations and need to be validated with a higher number of clones. In order to get a first impression this chapter focuses on the pathways that were altered in *EN1* -/- clones and compare these results with the *EN1* +/- clones.

2.6.1 Observations in *EN1* +/- DANs

In DANs, *EN1* -/- clones showed a reduced basal and maximal respiration after adding glucose as a substrate. Interestingly, the *EN1* +/- DANs exhibited a similar level of reduction in the OCR as the *EN1* -/- DANs in all measured parameters after adding glucose and pyruvate (**Figure 30A, B**). This observation might indicate that already heterozygous *EN1* expression results in alterations in cellular respiration. This partially agrees with the findings in mice, where DANs degenerate eventually and the *En1* level thus seems to be crucial for correct cellular function and survival.

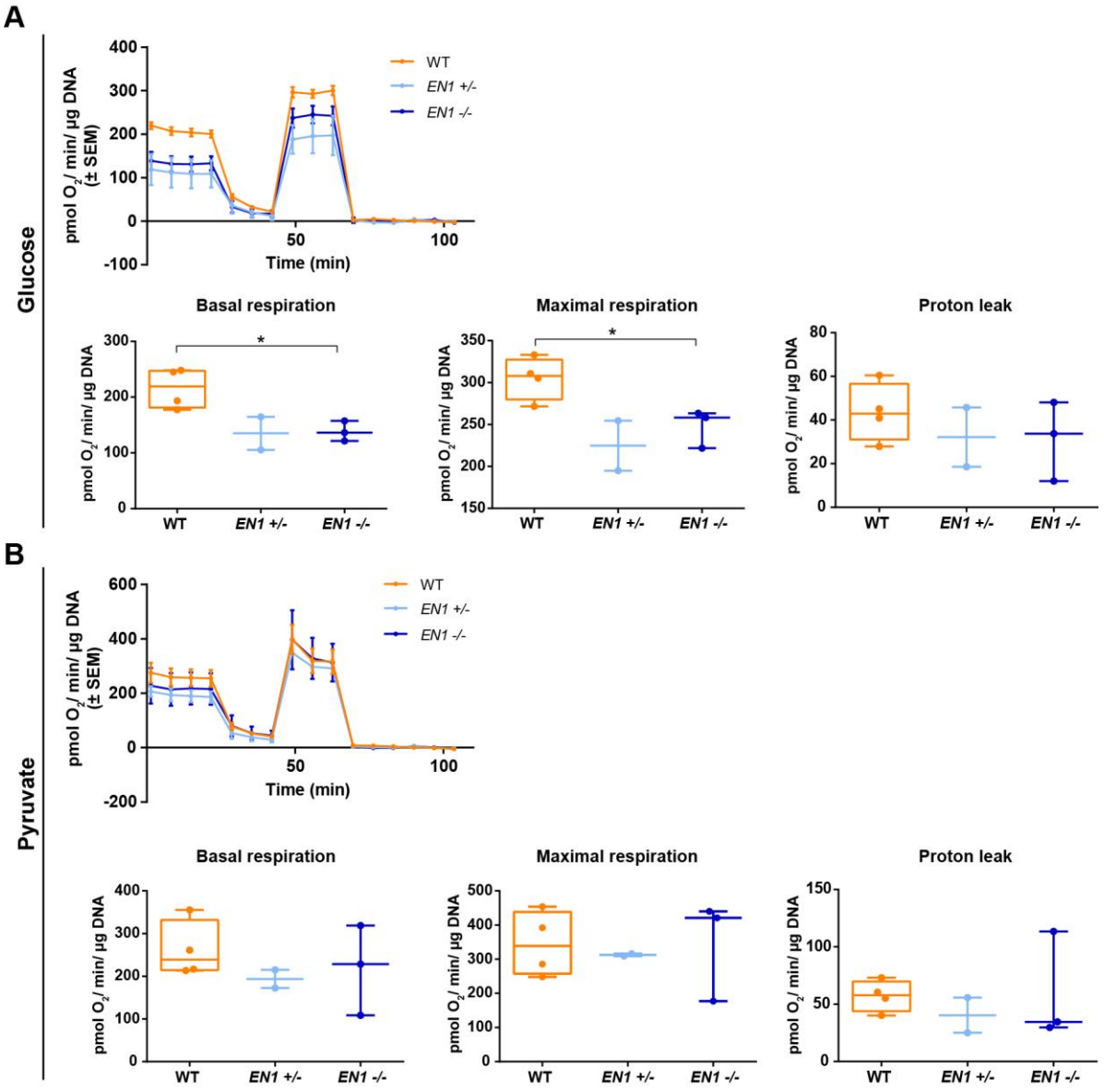

Figure 30: Characterization of mitochondrial respiration in DANs. The oxygen consumption rate was measured using a Seahorse XFe96 Extracellular Flux Analyzer. The measurement (**Figure 15**) was performed in Seahorse XF assay medium supplemented with either 25 mM glucose **(A)** or 5 mM pyruvate **(B)** as substrates. An overview of the measurement (upper panel) and detailed analyses of basal respiration, maximal respiration, and proton leak (lower panels) are shown. n = 4 WT, 2 *EN1* +/- and 3 *EN1* -/- clones, in triplicates. Data are depicted as mean ± standard error of the mean (SEM) and box plots ranging from the 25th to 75th percentiles, showing the median. Whiskers extend from min to max value and each dot represents one clone. P-values were determined by student's t-test or Welch's t-test depending on the standard deviation. *EN1* +/- DANs were not subjected to statistical analysis but are shown for observational purpose. Details of statistical analysis are provided in **Table 29**. *, $p < 0.05$.

Similar to the *EN1* -/- DANs, the *EN1* +/- DANs also showed no alterations in fluorescence intensity and thus membrane potential in the mitoTracker analysis. Again, *EN1* +/- DANs exhibited a comparable membrane potential as the *EN1* -/- clones (**Figure 31A, B**).

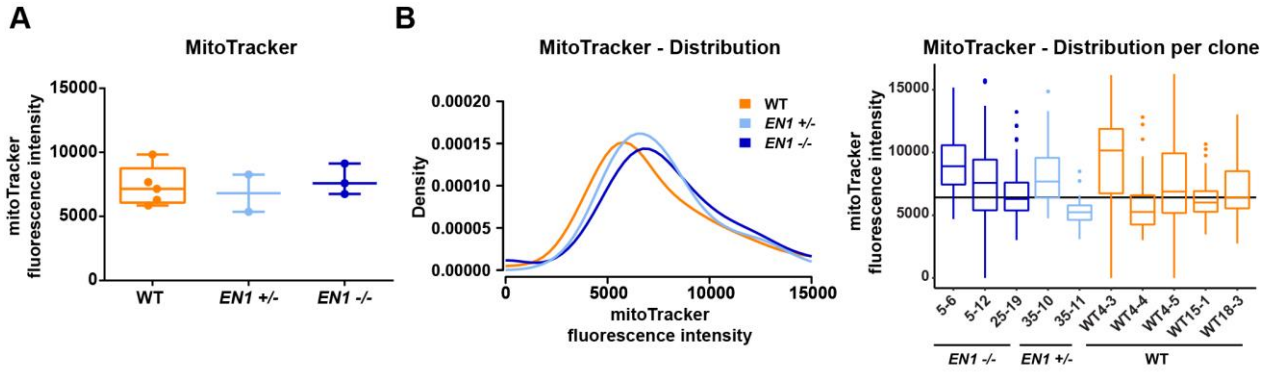

Figure 31: Assessment of mitochondrial function in DANs. (A) MitoTracker analysis to determine mitochondrial functionality in DANs. The cytosolic fluorescence intensity was quantified. n = 5 WT, 2 *EN1* +/- and 3 *EN1* -/- clones, in triplicates **(B)** Density plot showing fluorescence intensity distribution for WT, *EN1* +/- and *EN1* -/- clones combined (left panel) and boxplot showing the distribution for each individual clone (right panel). n = 5 WT, 2 *EN1* +/- and 3 *EN1* -/- clones, in triplicates. Data are depicted as box plots ranging from the 25th to 75th percentiles, showing the median. Whiskers extend from min to max value and each dot represents one clone (A). P values were determined by student's t-test or Welch's t-test depending on the standard deviation (A) and Kolmogorov-Smirnov test and linear regression (B). P-values are indicated only if both tests resulted in a significance. *EN1* +/- DANs were not subjected to statistical analysis but are shown for observational purpose. Details of statistical analyses are provided in **Table 27**.

2.6.2 Observations in *EN1* +/- Wnt stimulated NPCs

The reduced basal and maximal respiration after adding glucose in DANs, was also observed after enhancing the *EN1* knockout by Wnt stimulation. Including the heterozygous *EN1* knockout in the analysis, reduced basal and maximal OCRs and a reduced proton leak compared to the WT NPCs were observed when glucose was supplemented (**Figure 32A**). The decrease was slightly lower as for the *EN1* -/- Wnt stimulated NPCs, so that OCRs of the *EN1* +/- Wnt stimulated NPCs were in between the WT and *EN1* -/- clones. Adding pyruvate as a substrate, the *EN1* +/- clones exhibited similar basal respiration and proton leak as the *EN1* -/- clones. However, the maximal respiration was reduced compared to the WT, whereas the *EN1* -/- clones performed comparable to the WT (**Figure 32B**). The glycolytic flux in *EN1* +/- clones was also comparable with the *EN1* -/- clones after Wnt stimulation (**Figure 32C**).

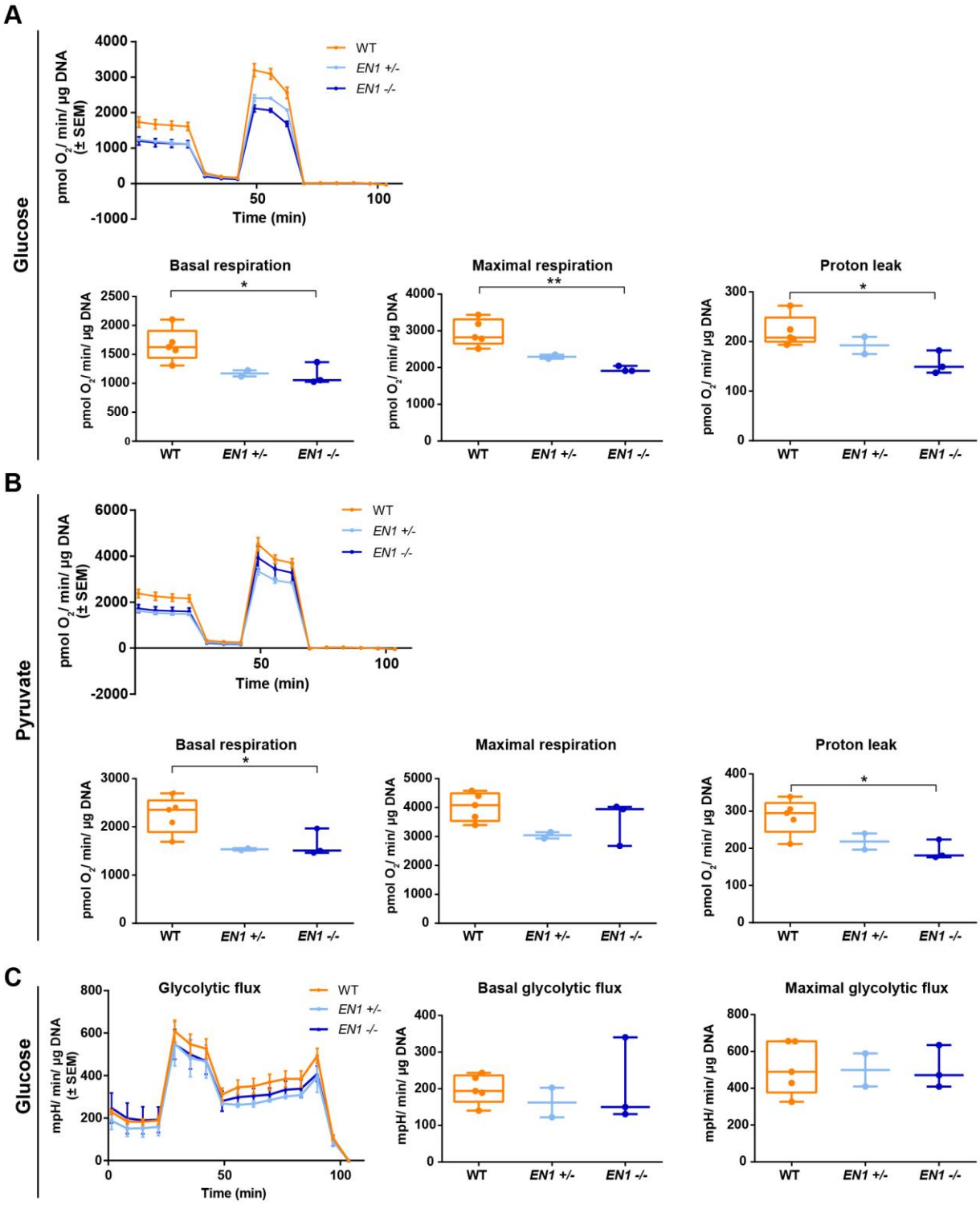

Figure 32: Characterization of mitochondrial respiration and glycolytic flux in Wnt stimulated NPCs. The oxygen consumption rate and extracellular acidification rate were measured in NPC after 48 h of Wnt stimulation with CHIR99021 using a Seahorse XFe96 Extracellular Flux Analyzer. The measurements (**Figure 15**) were performed in Seahorse XF assay medium supplemented with either 25 mM glucose **(A, C)** or 5 mM pyruvate **(B)** as substrates. **(A, B)** An overview of the oxygen consumption rate (upper panel) and detailed analyses of basal respiration, maximal respiration, and proton leak (lower panels) are shown. **(C)** Overview of the extracellular acidification rate and detailed graphs of basal and maximal glycolytic flux are shown. n = 5 WT, 2 *EN1* +/- and 3 *EN1* -/- clones, in triplicates. Data are depicted as mean ± standard error of the mean (SEM) and box plots ranging from the 25th to 75th percentiles, showing the median. Whiskers extend from min to max value and each dot represents one clone. P-values were determined by student's t-test or Welch's t-test depending on the standard deviation. *EN1* +/- DANs were not

subjected to statistical analysis but are shown for observational purpose. Details of statistical analysis are provided in **Table 32**. *, $p < 0.05$; **, $p < 0.01$.

In addition, Wnt stimulated NPCs also exhibited a lower mitochondrial membrane potential and a decrease in complex I abundance. Again, when included in the analysis, *EN1* +/- WNT stimulated NPCs, showed the same phenotype as the *EN1* -/- NPCs. MitoTracker analysis indicated a reduced mitochondrial membrane potential (**Figure 33A, B**) and complex I was also reduced to a similar extend (**Figure 33C**), while complex I activity was unaffected (**Figure 33D**).

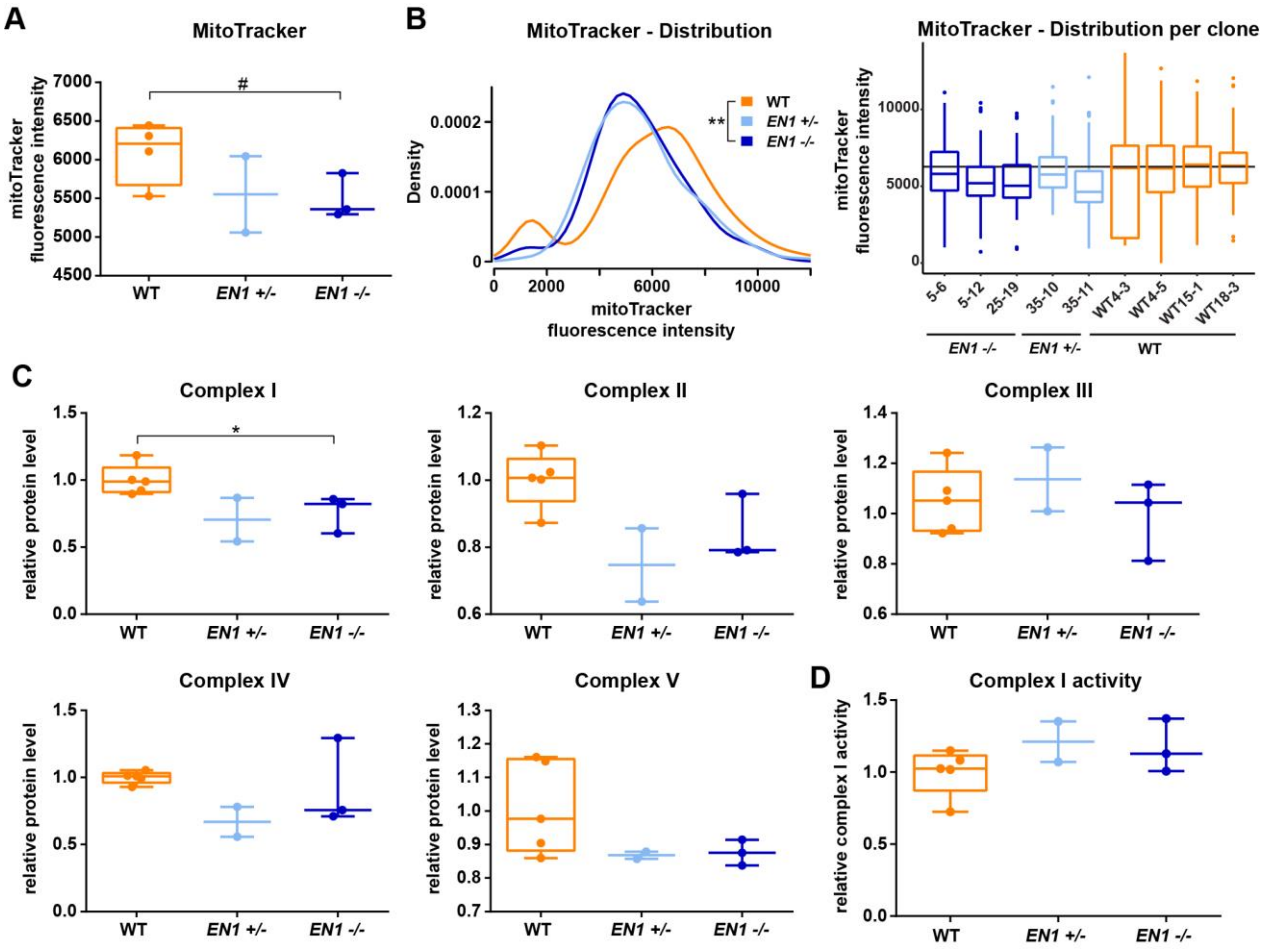

Figure 33: Assessment of mitochondrial quantity and function in Wnt stimulated NPCs. (A) MitoTracker staining to analyze mitochondrial functionality in NPCs. The cytosolic fluorescence intensity was quantified after 48 h of Wnt stimulation with 3 µM CHIR99021. **(B)** Density plot showing fluorescence intensity distribution for WT, *EN1* +/- and *EN1* -/- clones combined (left panel) and boxplot showing the distribution for each individual clone (right panel). **(C)** The quantity of respiratory chain complexes I-V was assessed by western blot after cells were Wnt stimulated with 3 µM CHIR99021 for 48 h using antibodies against NDUFB8 (complex I), SDHB (complex II), UQCRC2 (Complex III), MT-CO2 (complex IV) and ATP5A (complex V). Protein levels were normalized to GAPDH and the average protein levels of WT clones. An exemplary western blot is shown in the appendix. n = 5 WT, 2 *EN1* +/- and 3 *EN1* -/- clones, in triplicates. **(D)** Quantification of relative complex I activity after 48 h of Wnt stimulation with 3 µM CHIR99021. Complex I activity was normalized to the average complex I activity of WT clones. n = 5 WT, 2 *EN1* +/- and 3 *EN1* -/- clones, in triplicates. Data are depicted as box plots ranging from the 25th to 75th percentiles, showing the median. Whiskers extend from min to max value and each dot represents one clone. P-values were determined by student's t-test or Welch's t-test depending on the standard deviation. *EN1* +/- DANs were not subjected to statistical analysis but are shown for observational purpose. Details of statistical analyses are provided in **Table 35, Table 36 and Table 37**. *, $p < 0.05$, **, $p < 0.01$

Considering all the observations made during the analysis of the *EN1* +/- clones, it can be proposed that already one missing allele of *EN1* is sufficient to induce the phenotype in glycolysis which

was observed in DANs and Wnt stimulated NPCs and mitochondrial dysfunction which was only present in Wnt stimulated NPCs. Interestingly, alterations in complex I activity as detected in *En1*$^{+/-}$ mice were not found in *EN1* +/- DANs or WNT stimulated NPCs. This might indicate a difference between human and mice or could also be explained by the maturity of the DANs, as degeneration starts only 8 weeks after birth.

3. Discussion

Animal models carrying mutations in familial or PD-associated genes have been widely used to unravel the molecular mechanisms of PD pathology. Although pathways such as protein aggregation and homeostasis, mitochondrial dysfunction or autophagy have been linked to the pathogenesis of PD (see also 1.1.4), the exact etiology of neurodegeneration is still not clear. This thesis aimed to establish a human knockout model of a gene highly relevant for the survival and maintenance of DANs, namely *Engrailed 1* (*EN1*) (*101*). Uncovering the molecular mechanisms of *EN1* might not just indicate crucial pathways in the pathophysiology of PD but also molecular properties that could be essential for the neuroprotection of DANs, offering new therapeutic possibilities. It further offers the opportunity to uncover possible species-specific differences between mouse and human.

3.1 Successful generation of an hiPSC *EN1* knockout cell line

The knockout was achieved by the introduction of indels into the exon 1 of the *EN1* locus using the CRISPR/Cas9 system. This resulted in premature stop codons and termination of translation at around bp 430 downstream of the transcription start site. Regarding the structure of *EN1*, this refers to a region located shortly behind the EH1 domain (*83*), meaning that the EH1 and the eIF4E binding site were still transcribed. However, as the premature termination occurs more than 50-55 bp upstream of the exon-exon junction in the hiPSCs, the truncated *EN1* mRNA is subjected to nonsense mediated mRNA decay following the 50-55 nucleotide rule (*159, 192*). Once in the cytoplasm, mRNAs are subjected to nonsense-mediated mRNA decay within a minute (*193*). Therefore, translation of the N-terminal part of *EN1* is highly unlikely. Due to missing functional antibodies, validation of the knockout on protein level was unsuccessful using western blot and immunohistochemistry. Nevertheless, the RT-PCR as well as the transcriptome analysis in which the clones were separated according to their genotype proofed the successful *EN1* knockout generation.

Assessing the quality of hiPSCs, CNVs were uncovered in some of the generated clones. Interestingly, besides the *EN1* -/- clone 25-16, only WT clones harbored CNVs. Being localized in the same region, suggested that the CNVs were already present in a precursor cell. However, as WT and knockout clones were derived from the same hiPSC line and had a similar passage (± 1) the results were unexpected. Although it cannot be excluded, it is improbable that the CNVs occurred during the extra passage as somatic mutations are quite stable during passaging when not exposed to selective pressure (*165*). Another possibility is that the resolution of the two microarrays used for the karyotyping of the WT and the knockout (due to limited availability) is responsible for the variation between the clones. The microarrays differed in the number of SNPs located on the affected chromosome 14. The microarray used for karyotyping of the WT clones covered more than double the amount of SNPs (HumanCytoSNP-12 v2.1 Bead Chip (*EN1* -/-): 9513 SNPs and Infinium GSA-24 v3.0 microarray (WTs): 19727 SNPs). Due to the lower resolution of the microarray used for the *EN1* knockout screening, the mutation was probably not discovered. Interestingly, WT clone 18-3 had no CNV in the same region as the other WT, which contradicts the hypothesis of the mutation having been present in the original clone. One can speculate that the pre-existing variations expanded in the other WT's during cultivation, while clone 18-3 was

unaffected (*194*). Especially mutations which are advantageous during the cultivation process (e.g. cancer-associated mutation or anti-apoptotic genes) are often enriched in hiPSCs (*195*). Indeed, WT clone 11-2 harbored a CNV in a region encoding for the anti-apoptotic protein BCL2XL, which has been found in up to 25 % of hiPSCs and has been described as a CNV hotspot (*168, 194*). Having been associated with increased cell survival, this clone was excluded, to reduce the variability of the hiPSCs (*168*). Variation is a major concern in hiPSCs as it can mask biological relevance. It can be attributed to the genetic background, somatic mutations, and non-genetic variation related to culturing procedures or passage numbers (*163, 196*). Approximately 10 % of the somatic mutations in hiPSCs are subclonal, suggesting that there is an intrinsic variability not only in the selected clones but also in their subclones (*165*). Thus, it can be justified, that the subclones can be regarded as individual clones in this study. As only one heterozygous *EN1* knockout clone with two subclones was available in this study, statistical analysis, and eligible interpretation of the data regarding the dose dependency of *EN1* was not possible. Nevertheless, observations are discussed in chapter 3.4. Finally, PCA analysis, which attributed the highest variability of the clones to the genotype presents a confirmation that the variability in the cells is acceptable and the variation can be attributed to the genotype. Therefore, the generation of the human hiPSC *EN1* knockout model was successful. Since *En1* knockout animals, have a knock-in in the *En1* locus which induced a null mutation by deletion of amino acid 1-111 (*84*), the generated hiPSC *EN1* knockout hiPSCs can be used to compare an animal system versus the human system.

3.2 *EN1* knockout NPCs as a model to study PD etiology

Evidence whether genetic variations in the *EN1* locus are associated with susceptibility for PD is conflicting (*14, 108, 154, 197*). Some GWAS studies reported that *EN1* polymorphisms are associated with an increased risk of PD, however, results from larger cohorts could not replicate these findings (*108*). Strikingly, the animal model harboring a heterozygous knockout for *En1*, is one of the few animal models that actually recapitulates the selective progressive neurodegeneration of DANs in the SNpc, which is accompanied by the well-known motor deficits (*80, 107*). However, it has been shown that the genetic background (mouse strain) is crucial for the development of the *En1* knockout phenotype in mice (*155*). Therefore, it was interesting to investigate the *EN1* knockout on a human background. To analyze the effect of an *EN1* knockout in a human cellular model in the context of PD etiology, the knockout hiPSCs were differentiated into NPCs that were primed for the dopaminergic lineage. According to the molecular changes that were discovered in PD (*198*) and what has been published for *En1* in animal models, it was surprising that the transcriptome of the *EN1* knockout NPCs did not indicate alterations in mitochondrial pathways, which was confirmed in validation experiments. Although *EN1* knockout NPCs did not reveal a mitochondrial phenotype, transcriptome analysis revealed DEGs that can be categorized into pathways that are linked to EN1-associated molecular processes. For example, pathways categorized in differentiation like ectodermal and neural crest cell differentiation were dysregulated in *EN1* -/- NPCs. With EN1 being involved in the differentiation of mDANs (*82*) and the positioning of the neural crest/mesoderm border (*199*), it can be explained why the pathways were detected in the transcriptome analysis. Wnt signaling, which directly regulates *EN1* is also among the pathways (*129*). In addition, EN1 has also been connected to synapse physiology (*171–173*), axon guidance (*174, 200, 201*), PI3K-Akt-mTOR signaling (*109, 171*), the Hippo-Merlin

pathway (*175*), and ECM (*202*). Thus, already on NPC level the *EN1* knockout-induced alterations can be acknowledged. It is unlikely that all the pathways are at the bottom of neurodegeneration, however, changes in axon projection or in the ECM for example have been associated with PD or neurodegenerative diseases, respectively. Evidence from post-mortem studies as well as animal models have shown that axon projections and axonal transport of DANs are affected early in PD. Kordower and colleagues found that the axonal projections to the dorsal striatum were virtually absent 4-5 years after diagnosis, whereas the loss of TH-positive neurons in the SNpc was noticeable but minor and a residual population was left even decades after onset (*110*), implying a dying back mechanism of DANs. This has also been observed in genetic animal models (*203, 204*), neurotoxic animal models (*205, 206*), and in *En1* +/- animals (*109*).
Another interesting pathway that has not been discussed very much in connection with PD and has only been related to *En1* in skin tissue are ECM alterations (*202*). Although the ECM plays an important role in the regulation of cellular physiology, it has been often overlooked due to the challenges to study it (*207*). Recently, a glycomics and proteomics study of the pre-frontal cortex of PD brains revealed that ECM proteins were the mostly enriched protein set amongst differentially expressed proteins in PD (*208*). These changes have also been acknowledged in a mouse model of PD (*209*). Furthermore, the ECM components are present in LB's and seem to be involved in the uptake and seeding of α-synuclein (*210, 211*).
Therefore, the transcriptome analysis of the human *EN1* knockout model, revealed pathways that have been associated with EN1 and confirmed the conservation of EN1's role in these pathways in humans. As some of the altered pathways have been associated with PD, this strengthens the relevance of EN1 for the pathophysiology of PD. Although mitochondrial alterations were not observed in unstimulated NPCs, alterations in some of the molecular pathways that were identified in the human *EN1* knockout model might precede the mitochondrial dysfunction and might be interesting to investigate also in murine models of the *En1* knockout.

The discovery that *EN1* -/- NPCs did not exhibit any mitochondrial deficits was surprising and might indicate that *EN1* does not have any effect on mitochondrial function in a human background. However, it is most likely attributed to the fact that *EN1* is expressed only weakly at the developmental stage of NPCs. NPCs approximately present a stage equal to day E8.5 in mice before neural tube closure (*169*). With *EN1* being expressed starting around E8 expression might still be too low (*102*). This is supported by the experimental data that revealed a phenotype of reduced mitochondrial respiration, which can most likely be attributed to alterations in glycolysis (discussed in 3.3) in DANs and Wnt stimulated *EN1* -/- NPCs. However, the analysis of mature *EN1* -/- DANs implied a deficit in glycolysis rather than mitochondrial dysfunction and compromised OXPHOS. This contradicts observations made in the $En1^{+/-}$ animal model (*94*) and observations made in other hiPSC PD models (*212, 213*) and post-mortem material of PD patients (*148, 198*) regarding the molecular culprits of PD. There are different explanations why the *EN1* -/- DANs do not exhibit the mitochondrial dysfunction as detected in the murine model. One hypothesis is that there might be a species-specific difference between mice and humans regarding the function of *EN1*. However, another more likely possibility is that the neurons are not mature enough to recapitulate the full maintenance function of EN1 in mature dopaminergic neurons and thus late-stage PD associated phenotypes. Although DANs differentiated from hiPSCs have been used in a lot of studies to identify the molecular players that are associated with neurodegeneration in PD, including hiPSCs carrying *LRRK2* (*214, 215*), *DJ-1 (216), SNCA (217, 218)* mutations and hiPSCs

derived from sPD patients (*216, 219, 220*), it might be different in the *EN1* knockout model due to the dual function of En1. *En1* is required for the specification of DANs and later for their maintenance starting from E11. However, during the early developmental stages until at least P0 it can be compensated for by *En2* (*84, 105, 106*). As the hiPSCs do not exhibit an *EN2* knockout, a developmental effect is therefore probably compensated for by *EN2*. This is supported by the same DAN differentiation capacity of *EN1* -/- and the WT clones. Although the maintenance function of En1 can be compensated by En2 prenatally, this is not the case in adult DANs, due to their different expression pattern. In contrast to *En1* which is expressed throughout the SNpc and VTA, *En2* is only expressed in a subset of DANs (*105*). Therefore, the DANs that have been differentiated for 42 days starting from NPCs might not be mature enough to uncover the molecular pathways underlying the full maintenance and protective effect of *EN1* in human adult DANs. This actually represents a drawback of the hiPSC models for PD. The investigation of PD pathophysiology requires mature DAN cultures, which are, depending on the protocol, established the earliest after more than 70 days in culture (*221, 222*). According to the differentiation protocol that was employed here, DANs acquired mature electrophysiological properties and formed synaptic contacts already 21 days after initiation of mDAN differentiation. However, cell culture medium containing antioxidants and neurotrophic factors provides great conditions for the cells, which might mask the full extension of the *EN1* knockout phenotype. Thus, in order to recapitulate the neurodegeneration pathology in another study, DANs carrying e.g. the *LRRK2* G2019S mutation had to be challenged using medium without antioxidants or mitochondrial toxins like rotenone (*169*). In addition, modeling of PD as a late-onset disease with age being the highest risk factor, is difficult to achieve in hiPSCs, which have the characteristics of rejuvenated cells and do not age per se (*223*). However, hiPSC-based models can help to unravel the disease mechanism. Therefore, it is intriguing to speculate that the *EN1* -/- DANs capture an early point of *EN1* knockout induced cellular alterations, before even mitochondrial dysfunction becomes apparent. The alterations in glycolysis displayed in DANs could underlie an *EN1*-knockout caused defect that contributes, maybe together with mitochondrial dysfunction, to the degeneration of DANs. Although further validation is required, so far glycolysis deficits have not been associated with *EN1* knockout in the context of PD. It would be interesting to investigate glycolytic processes in $En1^{+/-}$ mice in the phase preceding neuronal degeneration, especially as a reduced glucose metabolism has been detected in PD patients and monkeys (*224–226*).

To determine if the defect in glycolysis in *EN1* -/- DANs was revealed because the *EN1* level increased with differentiation or whether the metabolic changes that are associated with neuronal differentiation (*227, 228*) were responsible for the phenotype, the NPCs were stimulated with Wnt to enhance the *EN1* expression in the precursor cells. Although NPCs are precursor of DANs, studies using hiPSCs from familial PD patients have shown that also progenitor cells can exhibit PD associated phenotypes (*220, 229–231*), which can be accelerated using cellular stressors (*169, 212*) or progerin-induced aging (*232*). Interestingly, NPCs from familial PD and even DANs were often challenged by metabolic or mitochondrial stressors to reveal a phenotype (*169, 229*). Although *EN1* -/- cells were not challenged by mitochondrial stressors, the phenotype was enhanced by Wnt stimulation using the GSK-3β inhibitor CHIR99021. Wnt signaling directly induces *EN1* expression via TCF4 binding to the *EN1* promotor (*128, 129*). Therefore, the WNT stimulation was utilized to enhance the *EN1* expression in WT clones and thus increase the effect of the *EN1* knockout. In addition to inducing *EN1* expression, Wnt signaling can also be regarded

as a stressor for NPCs as Wnt stimulates the metabolism (*233*). Following Wnt stimulation, *EN1* expression increased in WT clones, as expected. Challenging the phenotype by stimulation of Wnt signaling, the transcriptome analysis yielded DEGs that were enriched in almost identical pathways as in the unstimulated NPCs. Genes were also dysregulated in pathways associated with axon guidance, developmental processes and mTOR signaling. All processes EN1 is involved in (*95, 101, 109, 174*). This confirmed that the stimulation did not alter the cellular physiology but primarily enhanced the phenotype of the *EN1* knockout. Interestingly, the transcriptome analysis of the Wnt stimulated *EN1* -/- NPCs now revealed alterations in glycolysis associated pathways, which were validated by a mitochondrial stress test. Confirming the results of *EN1* -/- DANs in Wnt stimulated NPCs showed that the level of *EN1* needed to be enhanced in WT controls to reveal the phenotype associated with the knockout. Throughout the experiments, WT NPCs responded to the Wnt stimulation, e.g., increased the OCR in Seahorse analysis, showed a higher membrane potential, whereas the knockouts were mostly unaffected. As cells were lacking *EN1*, this outcome was expected, at least for cellular mechanisms that are mediated by *EN1*. Interestingly, besides the glycolysis-linked respiratory deficit, Wnt stimulated *EN1* knockout NPCs also showed a reduced mitochondrial membrane potential and alterations of complex I abundance. The induction of *EN1* expression which enhances the effect of the knockout combined with putting the cells in distress is probably exposing the molecular processes, similar to the mitochondrial stressors used in PD hiPSC models. Therefore, the mitochondrial deficits might represent a progression of molecular alterations in the *EN1* knockout hiPSC model which manifests following the glycolytic alterations when cells are in distress. Although complex I activity is not yet affected, the reduced complex I abundance and reduced mitochondrial respiration agree with the increased susceptibility to mitochondrial insults (*111*) and the post-transcriptional regulation of complex I subunit expression (*94*) that has been shown in $En1^{+/-}$ animal models.

Contradicting the experimental evidence of alterations in mitochondrial function, only genes associated with glycolysis related pathways were altered in the transcriptome of WNT stimulated *EN1* -/- cells, whereas OXPHOS- or mitochondria-connected pathways were not detected in our data. However, the transcriptome does not necessarily reflect the proteome of a cell. Especially with EN1 being able to control translation on a post-transcriptional level, which has been shown for the complex I subunits Ndufs1 and Ndufs3, there might be discrepancies (*93*, *94*). Therefore, the transcriptome uncovered interesting pathways that are altered in *EN1* knockout NPCs, regarding its role as transcription factor, but a proteome analysis would allow to gain an even deeper understanding of the molecular changes regarding its additional function as translational regulator.

In summary, transcriptome analysis and experimental evidence proofed that the human *EN1* knockout hiPSC line represents a valuable model to investigate the early molecular mechanisms that may be involved in the pathology of PD.

3.3 Wnt stimulation revealed a bottleneck in glycolysis and mitochondrial deficiency in the human *EN1* knockout model

Genetic alterations, environmental influences, and age are all risk factors for developing PD. The exact molecular mechanism that links these factors to PD has, however, not been determined so

far. A common theory is bioenergetic failure leading to the selective degeneration of highly energy-demanding DANs (*35*). Different reasons can result in failure to meet the energy demand. In the context of PD, mitochondrial dysfunction leading to excessive formation of ROS has been discovered in multiple studies including sPD and familial PD models (*148, 152, 234*). However, besides mitochondrial dysfunction, metabolic alterations including the central carbon metabolism can also directly influence the bioenergetic state of a cell (*226*).

DANs and Wnt stimulated NPCs revealed metabolic alterations in the *EN1* knockout clones. Both differentiation stages showed a reduced basal and maximal OCR when relying on glucose as a substrate. Supplementing pyruvate, however, only resulted in reduced basal mitochondrial respiration in Wnt stimulated NPCs, which was less pronounced than the reduction upon glucose supplementation. This prompted the hypothesis, that the cells suffered from a glycolytic deficit that might precede mitochondrial or TCA-based alteration (discussed in 3.2). A decrease in basal and maximal respiration can have different reasons (*190, 235*).

At first, it can be attributed to inadequate substrate supply. Recent studies have already linked mutations and deletions of the familial PD gene *LRRK2* to defective insulin-stimulated translocation of GLUT4 to the plasma membrane (*236*). *GLUT4* was also the only DEG that was downregulated in the glycolysis associated pathways in the Wnt stimulated *EN1* knockouts. However, the glucose uptake in the *EN1* knockout NPCs was unchanged. Considering that this analysis was not done in a physiological setting, with missing insulin stimulation, one would have to do further investigations *in vivo* to clarify this. Nevertheless, in this human *EN1* knockout model, reduced glucose availability can be ruled out. Secondly, it can be caused by alterations in mitochondrial mass and morphology. While changes in mitochondrial morphology cannot be excluded, the mitochondrial mass was not altered as indicated by MitoTracker staining and quantification of complex V, which can also be used to estimate the mitochondrial quantity. Furthermore, damage to the respiratory chain can also result in reduced basal and maximal respiration. Although complex I activity was not altered in Wnt stimulated NPCs, the abundance was reduced. This can partially explain the deficit in respiration but does not explain the more pronounced deficit after supplementing glucose in comparison to pyruvate. Finally, the reduced activity of a rate-limiting enzyme in the metabolic pathways upstream of mitochondrial respiration can also cause a deficit in OCR.

Although the activity of the rate-limiting enzymes was not investigated, it was surprising that most dysregulated genes involved in glycolysis were upregulated, which would suggest a higher capacity of glycolysis. Every enzyme of glycolysis was affected, except for the pyruvate kinase, which was not altered, and the pyruvate dehydrogenase kinase 1 (PDK1), which was upregulated. PDK1 phosphorylates and inhibits the pyruvate dehydrogenase (PDH) (*237*). Thus it limits the input into the TCA and OXPHOS and high expression has been shown to be responsible for a shift towards a glycolytic metabolism (*238–240*). This might also be attributed to the effect of the Wnt stimulation which supports a shift towards glycolysis and can induce upregulation/activation of key enzymes of glycolysis and the pentose phosphate pathways (PPP) (*187, 188*). The shift towards glycolysis could then be responsible for uncovering the deficits in the *EN1* -/- clones. In addition, the pyruvate kinase is one of the three rate-limiting enzymes in glycolysis and catalyzes the second ATP generating step (*132, 241*). Hence, it might regulate the glycolysis level back to normal which would fit with the unchanged glycolytic flux. The activity of the Pyruvate kinase has been linked to *PRKN* and *PINK1*. One study showed, that the loss of the ubiquitin carboxyl-terminal hydrolase

L1 (UCHL1) results in the destabilization of pyruvate kinase and alleviated the phenotype of PRKN and PINK1 loss of function mutations (*242*). Another study found pyruvate kinase to be a direct target of ubiquitylation by PRKN, which reduces its enzymatic activity (*243*). Both studies imply that inhibition of glycolysis is beneficial in the context of PD. Nevertheless, the role of glycolysis is still highly debated in the field, as a decrease in glucose metabolism has been observed in PD patients and animal models (*224, 225*), and enhancing glycolysis can also be protective (*244*).
Interestingly, Wnt stimulation was necessary on NPC level to reveal the deficit in glycolysis in *EN1* -/- NPCs compared to WT NPCs. Wnt signaling has been shown to induce enhanced glycolysis in neurons by both, mechanisms independent of the transcription of Wnt target genes and by upregulation of rate-limiting enzymes of glycolysis, like hexokinase, phosphofructokinase and pyruvate kinase (*187, 245*). Therefore, the effect of the Wnt stimulation on the cells was investigated in the transcriptome data by comparing unstimulated vs Wnt stimulated cells for both genotypes, WT and *EN1* -/- clones. The effect of the Wnt stimulation in WT clones mostly affected genes that were located in pathways already associated with Wnt, like development, differentiation, or focal adhesion (*181–183*). In contrast to these results, Wnt stimulation in *EN1* -/- NPCs resulted in addition to the pathways identified in WT's in dysregulation of genes located in glycolysis, similar to the comparison of WT with *EN1* -/- NPCs. Therefore, Wnt stimulation seems to unmask the glycolysis dysfunction of the *EN1* knockout NPCs. This can be explained by different scenarios. *EN1* might be protective against the changes the Wnt stimulation induces in the metabolism. As *EN1* is not expressed in *EN1* -/- NPCs the glycolytic metabolism of the cells is reduced. Another possibility is that EN1 might be crucial in conveying the protective effect of the Wnt signaling. There is evidence that impaired Wnt signaling is associated with PD pathogenesis and that Wnt signaling can be neuroprotective in a PD model (*122, 246*). Furthermore, it has been shown for Alzheimer's Disease, that Wnt signaling is protective by enhancing glucose metabolism (*187*). Therefore, the Wnt stimulated *EN1* knockout probably could not convey the effect the Wnt signaling normally has on the cells, thus resulting in impaired glycolysis. This hypothesis is supported by Wnt being able to induce the expression of *En1* and the rescue of dopaminergic degeneration in $En1^{+/Wnt1}$ mice. (*124, 128, 129*)
DANs differentiated from *EN1* -/- hiPSCs also showed a reduced OCR when relying on glucose. In mature/adult DANs, *EN1* is crucial for the survival of these neurons (*80, 105, 106*). The survival effect has been partially attributed to the suppression of the neurotrophin receptor $P75^{NTR}$ and also to the translational control of respiratory chain complex I subunits (*94, 111*). Furthermore, as mentioned above Wnt signaling also has been shown to support regeneration and be protective in an MPTP mouse model and in connection with En1 (*117, 124*). Therefore, it might be possible that similar to the NPCs, the protective function of the Wnt signaling cannot be conveyed in *EN1* -/- DANs resulting in deficient glycolysis. Interestingly, it has been shown that Wnt signaling can be activated by ROS, via the interaction of Dvl and a thioredoxin family protein nucleoredoxin (*247, 248*). As DANs are susceptible to ROS due to their high energy demand resulting from the typical physiological characteristics, like high arborization and pace-maker function (*25, 35*), Wnt signaling is probably active and might be critical for protection via EN1 in DANs.

It was surprising that the glycolysis associated genes were upregulated although the glycolytic respiration was reduced. Besides, the hypothesis of Wnt stimulation being responsible for the enhanced expression, upregulation of the glycolysis associated genes might also be a compensatory mechanism regarding a blockage in a yet unidentified region of the central carbon metabolism. The

transcriptome data does not predicate anything about the protein expression or activity. Protein expression is often controlled by post-transcriptional mechanisms and modifications, including mRNA processing, localization and turnover mediated by RNA binding proteins, small interfering RNAs and microRNAs (*249, 250*). In addition, post-translational modifications can affect the activity and functionality of proteins, which has already been shown for mitochondrial proteins and might also be involved in the pathogenesis of PD (*251, 252*). As EN1 has the ability to regulate translation in a post-transcriptional manner (*94*), a regulation of enzymes involved in glucose metabolism is possible and could also explain the discrepancy between transcriptome data and the experimental data regarding the deficiency in glycolysis in stimulated NPCs and DANs.

It was surprising that the glycolytic flux, estimated by the ECAR, was not altered in Wnt stimulated *EN1* -/- NPCs that displayed a reduced OCR after adding glucose. As the ECAR is believed to mirror mainly the lactate production in the cells, a bottleneck in glycolysis in general is contradictory. Nevertheless, the ECAR is highly complex to interpret, and not only the glycolytic turnover causes acidification of the medium, but also acidification from CO_2 production, intracellular buffering capacities and the diversion of glycolysis intermediates to other biosynthetic pathways can impact the ECAR (*190*).
Another possibility for the proposed bottleneck in glycolysis and constant glycolytic flux is that intermediates of glycolysis are sidetracked to other pathways. Although glucose is considered the main energy substrate of the brain, only 10 % of glucose yield lactate. A great part of glycolysis intermediates are required for the synthesis of carbohydrates for glycoproteins and glycolipids, amino acids or to maintain the antioxidant defense system of the cells (*226, 253*).

In neurons, a considerable amount of glucose is metabolized via the pentose phosphate pathway (PPP) (*135, 136*). In the PPP, glucose-6-phosophate is metabolized to ribose-5-phosphate, producing NADPH in the process, which is crucial for the regeneration of reduced glutathione and the maintenance of the antioxidant status (*254*). Ribose-5-phosphate can subsequently be used for the synthesis of nucleotides or reenter glycolysis (*132*). The PPP is the primary source of NADPH in the cell and reduced enzyme level of the central NADPH producing enzymes glucose-6-phospahte dehydrogenase (G6PD) and 6-phosphogluconate dehydrogenase (6PGD) have been postulated to be an early event in sPD pathogenesis (*255*). Therefore, the failure to retain and increase the antioxidant capacity due to altered glucose metabolism via the PPP might be a driver of PD. This is supported by decreased levels of reduced glutathione in the brain of PD patients (*256, 257*). Furthermore, the overexpression of G6PD rendered mice more resistant to the toxin MPTP (*258*), highlighting the importance of this pathway in response to stressful events. Indeed, a shift towards aerobic glycolysis has been observed upon mitochondrial distress (*259–261*) and in different neurodegenerative diseases (*261, 262*). Since neurons are limited in the upregulation of the classic aerobic glycolysis, because the rate regulating enzyme 6-phosphofructo-2-kinase/fructose-2,6-bisphosphatase-3 (PFKFB3) is constantly degraded, they preferentially metabolize glucose via the PPP (*254, 263*). Although, the genes in the PPP were not dysregulated in the transcriptome analysis, the reduced glycolytic capacity of *EN1* knockout cells might result in reduced flux through the PPP and difficulties in maintaining the cell's redox balance. Hence, the reduced glycolytic metabolism in *EN1* -/- DANs and Wnt stimulated NPCs is possibly accompanied by a compromised antioxidant defense system and could predispose the *EN1* knockout for mitochondrial dysfunction.

Considering the data, one can speculate that a reduced glycolytic capacity can underlie *EN1* knockout-induced neurodegeneration and possibly PD pathogenesis. Various studies have identified glucose hypometabolism in patients already in early stages of PD (*264–266*). During aging, due to genetic mutations, predispositions or environmental influences, neurons are confronted with an increasing burden of oxidative stress. Being unable to increase glycolysis to the extent of healthy neurons, a reduced flux through the PPP diminishes the ability to cope with ROS leading to neurodegeneration. A more comprehensive investigation of the proteome and metabolic flux would be required to confirm this hypothesis. Furthermore, as Wnt stimulation unmasked the glycolysis phenotype, EN1 might be responsible for conveying the protective effect of Wnt signaling that has been described in the literature, i.e enhancing glycolysis in NPCs and DANs.

Besides the proposed glycolytic deficit, experimental evidence from MitoTracker, Seahorse XF, and respiratory chain abundance analyses implied an additional limitation downstream of glycolysis in Wnt stimulated *EN1* knockout NPCs. Adding pyruvate, *EN1* knockout NPCs exhibited a reduced basal mitochondrial respiration. This can be possibly attributed to a reduced abundance of complex I. Being the major entry point for electrons into OXPHOS, complex I is considered the rate-limiting step in respiration (*142*). It was unexpected that the maximal respiration was not altered when the cells relied on pyruvate as a substrate. Interestingly, it has recently been proposed that complex I can be bypassed in muscles under high energetic pressure (*267*). A similar rerouting might occur in *EN1* knockout NPCs, to compensate for deficits in complex I.
Another hypothesis is that the PDK1 limits the input into the TCA by inhibition of the PDH. Again, it is difficult to explain, why a decreased PDH activity would only affect the basal respiration. Recent studies suggested that neurons can undergo a process of metabolic rewiring upon OXPHOS dysfunction. They can promote anaplerotic reactions, including activation of the pyruvate carboxylase and branched-chain amino-acid degradation (*268*). The pyruvate carboxylase, which converts pyruvate into oxaloacetate and thus bypasses the PDH is normally not active in neurons (*269*), at least under homeostatic conditions, but might be activated upon adding an uncoupling reagent like FCCP in the Seahorse measurement, to maintain the neuronal energy and redox state. However, this seems unlikely as one would expect the same compensation when Wnt stimulated *EN1* -/- NPCs were relying on glucose but here the maximal respiration was also decreased.

In conclusion, the metabolic alterations in *EN1* knockout cells suggest that mitochondrial dysfunction and ROS are one of the molecular culprits for PD but bioenergetic failure linked to deficits in glycolysis might be an underestimated pathway regarding neurodegeneration, preceding even the mitochondrial alterations. Neurons rely on glucose in times of high energy demand and can shift their metabolism to glycolysis which has the advantage of a faster ATP production rate (*270*) and possibly maintenance of the redox status via the PPP. This protective mechanism might be mediated by Wnt induced expression of *EN1*. Therefore, glycolysis might provide an interesting target for new therapeutic approaches. However, further validation of this *EN1* knockout model and other PD models are required to pinpoint the affected molecular processes.

3.4 Observations of a dose-dependent effect of *EN1* in a human model

Analyses in mice implied a dose-dependent effect of *EN* during development and also in adult mice (*80, 105*). Therefore, it was interesting to also get an insight into the dose-dependency of *EN1* in a human model. As only two *EN1* +/- clones were available, which was not sufficient for a valid statistical analysis, the results were only regarded as observations, that need to be validated with a higher number of clones.
In DANs the respiratory deficit is only observed upon adding glucose in the *EN1* -/- clones, while the OCR after adding pyruvate as well as the mitochondrial function was unperturbed. *EN1* +/- DANs performed similar as the EN1 -/- cells and only showed a reduced OCR after adding glucose. This implies that even one allele of *EN1* is not sufficient to maintain cellular homeostasis, which agrees with previous findings that one allele of *En1* on an *En* null background is sufficient for a normal phenotype during development (*105, 106*) but maintenance of DANs requires both alleles of *EN1 (80)*. This agrees with the result that *EN1* -/- clones have the same differentiation efficiency into DANs as the WT clones and suggest a dose-dependent effect.
Wnt stimulated *EN1* -/- NPCs also exhibited a reduced glycolytic respiration accompanied by mitochondrial dysfunction and reduced complex I abundance. In NPCs, *EN1* +/- clones performed slightly better than the *EN1* -/- clones in most experiments, however, were also impacted in their functionality. This was surprising considering the differentiation stage, because analyses in mice suggested that one allele of *EN* is sufficient during development (*105, 106*). Agreeing with these data, unstimulated *EN1* -/- and *EN1*+/- (data not shown) NPCs showed no phenotype and behaved as WT clones. Thus, excessive Wnt signaling might have challenged/unbalanced the cells so that one allele of *EN* was not sufficient anymore. In addition to being induced by Wnt signaling, *EN1* also represses Wnt1 inducing a feedback loop which is crucial during development (*130*). Thus, these results imply the importance of the balance in EN1 and WNT1 levels to maintain the feedback loop. If this is not maintained, as in the Wnt stimulated *EN1*-/- and *EN1*+/- cells, both alleles of *EN1* seem to be important to maintain cellular function, including glycolysis and mitochondrial functionality.
The observations made in this thesis therefore partially suggest a gene-dose dependent effect in a human cellular model, with one allele of *EN* being sufficient during development (unstimulated NPCs) but both alleles of *EN1* are required to fulfill EN1's maintenance function in DANs. The results also suggest that the balance between EN1 and Wnt is crucial. Nevertheless, further investigation including an extended pool of heterozygous clones is required to prove the hypothesis.

3.5 Conclusion and outlook

A human hiPSC model was successfully generated in this thesis. The hiPSCs were differentiated towards DANs and represent a valid model to study the molecular processes underlying the *EN1* knockout- and possibly PD-associated neurodegeneration. The data in this work suggested that the phenotype of the *EN1* knockout occurred and progressed upon differentiation to DANs and with stimulation of *EN1* expression. The dysregulated pathways that were discovered in transcriptome analysis, the dose-dependency, and mitochondrial dysfunction in stimulated NPCs suggested a conserved function of En1 across different species. Therefore, the *EN1* knockout hiPSCs represent a valuable model to investigate the selective vulnerability of DANs. The data indicated that a reduced glycolytic capacity, possibly preceding mitochondrial dysfunction might underlie *EN1*

knockout-induced bioenergetic failure. This is the first finding that connects the *EN1* knockout with deficiencies in the carbohydrate metabolism, more specifically in glycolysis. Glycolysis could therefore provide an interesting target for new therapeutic approaches. However, further validation also including *En1*$^{+/-}$ animal models and other PD models is required.

As Wnt stimulation unmasked the *EN1* -/- phenotype in NPCs, it can be proposed that EN1 is crucial in mediating the protective effect of the Wnt signaling in DANs.

To pinpoint the alterations in the central carbon metabolism, further analysis regarding the enzymatic functions of rate-limiting enzymes in aerobic glycolysis and the PPP are crucial. Furthermore, a proteome analysis could support the interpretation of transcriptome data and add information regarding the effect of post-transcriptional regulation of translation by EN1. Finally, a prolonged cultivation of DANs would be interesting to uncover further *EN1* associated neuroprotective mechanisms. Alternatively, mitochondrial or cellular stressors can be used to reveal additional effects of the *EN1* knockout in DANs, in an environment resembling late-stage PD. **Figure *34*** depicts and summarizes the findings of this work.

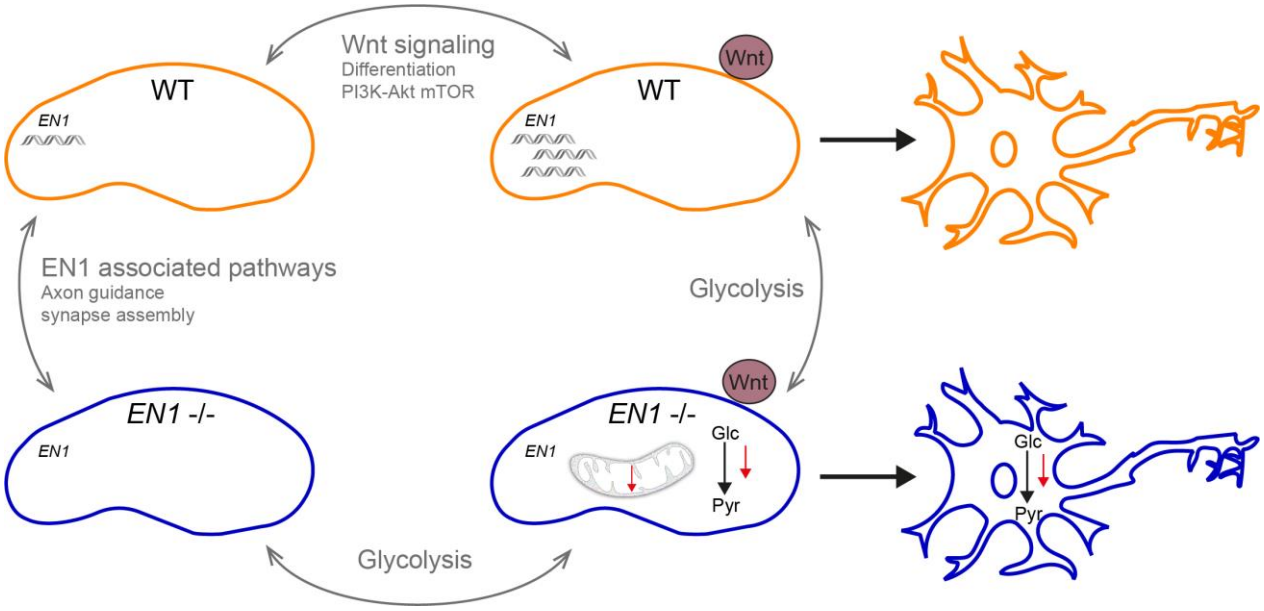

Figure 34: Graphical summary. Summary of the transcriptome and experimental data from NPCs, Wnt stimulated NPCs, and DANs. Transcriptome results are depicted in grey. Experimentally validated alterations are shown in the respective cells and refer to the comparison between WT and the *EN1* -/- clones of the respective differentiation stage/stimulation.

4. Material and Methods

4.1. Material

Table 6: Chemicals.

Chemicals	Catalogue number	Supplier
2-Deoxy-D-glucose GRADE II	D8375-25G	Sigma-Aldrich
2-Mercaptoethanol	31350010	Thermo Fisher Scientific
Acetic acid	W200603	Sigma-Aldrich
Agar	05040	Sigma-Aldrich
Agarose	870055	Biozym
Antimycin A	A8674-50MG	Sigma-Aldrich
Ascorbic acid 2-phosphate	A8960-5G	Sigma-Aldrich
Bovine Serum Album (BSA)	A7906-500G	Sigma-Aldrich
Carbonyl cyanide 4-(trifluoromethoxy)phenylhydrazone (FCCP)	C2920-10MG	Sigma-Aldrich
CHIR99021	4423/10	Tocris Bioscience
cOmplete Mini, EDTA-free	11836170001	Roche Diagnostics
DAPI-Solution	62248	Thermo Fisher Scientific
Dimethyl sulfoxide, >=99.5 %	D5879-100ML	Sigma-Aldrich
Dorsomorphin dihydrochloride	3093/10	Tocris Bioscience
Ethanol, absolute	1009832500	Merck Millipore
Ethidium bromide	2218.2	Carl Roth
Ethylenediaminetetraacetic acid (EDTA)	EDS-1KG	Sigma-Aldrich
Formalin, 10 %	F5554	Sigma-Aldrich
Gentamycinsulfat BioChemica	A1492,0005	AppliChem
Glucose	15023021	Thermo Fisher Scientific
Methanol	1.06009.2500	Merck Millipore
Milk powder	70166-500G	Sigma-Aldrich
N^6,2′-O-Dibutyryladenosine 3′,5′-cyclic monophosphate sodium salt (dbcAMP)	D0627-1G	Sigma-Aldrich
Oligomycin	O4876-5MG	Sigma-Aldrich
Proteinase K	A3830	AppliChem
Purmorphamine	4551	Tocris Bioscience
Pyruvic acid	P5280-25G	Sigma-Aldrich
Rotenone	R8875-1G	Sigma-Aldrich
Sodium chloride (NaCl)	106404	Merck Millipore
Sodium deoxycholate	D6750	Sigma-Aldrich
Sodium dodecyl sulfate (SDS)	L3771	Sigma-Aldrich
StemMACS SB431542	130-106-275	Miltenyi Biotec
Tris (Trizma-Base)	93352	Sigma-Aldrich
Triton X-100	T9284	Sigma-Aldrich
Trizma hydrochloride	T3253	Sigma-Aldrich
Tryptone	T7293	Sigma-Aldrich
Tween 20	P1379	Sigma-Aldrich
Water for molecular biology	H20MB0506	Millipore
Y-27632 dihydrochloride	ALX-270333-M005	Enzo Life Sciences
Yeast extract	Y1625	Sigma-Aldrich

Table 7: Consumables.

Consumables	Catalogue number	Supplier
10x Tris/Glycine Buffer for Western Blots	1610734	Bio-Rad
20x XT MOPS Running Buffer	1610788	Bio-Rad
35 µm cell strainer	352235	Corning
Clarity Max Western ECL Substrate	1705062	BioRad
Aqua-Poly/Mount	18606-20	Polysciences Inc.
Cell scraper	83.183	Sarstedt
Cover slips 14 mm Ø	6206579	Wagner und Munz
Criterion XT Bis-Tris Gel, 4-12 %, 18-well, 30 µl	3450124	Bio-Rad
Immobilon – P Membranes	IPVH00010	Merck Millipore
Microplate 96/F-PP wh/bl	30601700	Neolab
Multi-well plate, 24 well	353047	Corning
Multi-well plate, 6 well	353046	Corning
Multi-well plate, 96 well	353072	Corning
Neubauer improved cell counting chamber	PK361	Carl Roth
Nunc™ Cell Culture/Petri Dishes 100x15mm	150350	Thermo Fisher Scientific
NuPAGE™ LDS Sample Buffer (4X)	NP0007	Novex
Protein Marker VI	A8889	AppliChem
SafeSeal SurPhob Filtertips, 1250 µl, sterile	VT0270	Biozym
Seahorse XFe96 FluxPak	102416100	Agilent Technologies
Sterile filter 0.2 µM	INTG156608	VWR, Germany
SuperFrost Plus Glass Slides	4951PLUS4	Thermo Fisher Scientific
Whatman cellulose chromatography papers	WHA3030672	Sigma-Aldrich
XF96 cell culture microplates	101085004	Agilent Technologies

Table 8: Cell culture media and supplements.

Cell culture media and supplements	Catalogue number	Supplier
Advanced Dulbecco's Modified Eagle Medium	12491023	Thermo Fisher Scientific
B-27 Supplement (50x), minus vitamin A-10 mL	12587010	Thermo Fisher Scientific
CloneR™	05888	STEMCELL Technologies
CryoStor(R) cell cryopreservation media, CS10	C2874100ML	Sigma-Aldrich
DMEM/F-12, GlutaMAX Supplement-10x 500 ml	31331093	Thermo Fisher Scientific
Essential 8™ Flex Medium	A2858501	Thermo Fisher Scientific
Fetal bovine serum	P30-1402	PAN-Biotech
GlutaMax	35050061	Thermo Fisher Scientific
Human BDNF, research grade	130-093-811	Miltenyi Biotec
Human FGF-8b, premium grade	130-095-741	Miltenyi Biotec
Human GDNF, research grade	130-096-291	Miltenyi Biotec
Human TGF-β3, research grade	130-094-008	Miltenyi Biotec
Knockout DMEM-500 ml	10829018	Thermo Fisher Scientific
KnockOut Serum Replacement-500 ml	10828028	Thermo Fisher Scientific
L-Glutamine	5030024	Thermo Fisher Scientific
N2 supplement 5 ml	17502048	Thermo Fisher Scientific
Neurobasal Medium-500 ml	21103049	Thermo Fisher Scientific
Non-essential amino acids	11140035	Thermo Fisher Scientific
Opti-MEM Reduced Serum Medium	31985062	Thermo Fisher Scientific
Penicillin-Streptomycin (10.000 U/ml)	15140122	Thermo Fisher Scientific

Phosphate buffered saline, no calcium, no magnesium	14190169	Thermo Fisher Scientific
Seahorse XF base medium, 500 ml	103334-100	Agilent Technologies
Seahorse XF Calibrant Solution	100840000	Agilent Technologies
Trypsin 0,25 % EDTA 100 ml	25200056	Thermo Fisher Scientific
X-tremeGENE HP DNA Transfection Reagent	6366236001	Sigma-Aldrich

Table 9: Coatings and passaging solutions.

Coatings and passaging solutions	Catalogue number	Supplier
Accutase	A6964-500ML	Sigma-Aldrich
Collagenase, Type IV, powder	17104019	Thermo Fisher Scientific
Geltrex	A1413302	Thermo Fisher Scientific
Laminin Mouse Protein, Natural	23017015	Thermo Fisher Scientific
Poly-L-ornithine hydrobromide	P3655	Sigma-Aldrich
StemMACS Passaging Solution XF	130-104-688	Miltenyi Biotec

Table 10: Kits.

Kits	Catalogue number	Supplier
Complex I enzymatic activity microplate assay kit	ab109721	Abcam
Glucose Uptake-Glo™ Assay	J1341	Promega
HumanCytoSNP-12 v2.1 BeadChip Kit	WG-320-2101	Illumina
Infinium Global Screening Array-24 v3.0 Kit	20030770	Illumina
Lipofectamine Stem Transfection Reagent	STEM00001	Thermo Fisher Scientific
Maxima H Minus Double-Stranded cDNA Synthesis Kit	K2561	Thermo Fisher Scientific
Monarch PCR & DNA Cleanup Kit	T1030	New England Biolabs
Monarch DNA Gel Extraction Kit	T1020	New England Biolabs
MitoTracker Orange CMTMRos	M7510	Thermo Fisher Scientific
Pierce BCA Protein Assay Kit	23225	Thermo Fisher Scientific
QIAamp DNA Mini Kit	51306	Qiagen
QIAGEN Plasmid Maxi Kit	12162	Qiagen
QIAprep Spin Miniprep Kit	27104	Qiagen
Quant-iT PicoGreen dsDNA Assay Kit	P11496	Thermo Fisher Scientific
RNeasy Plus Mini Ki	74134	Qiagen
STEMdiff™ Trilineage Differentiation Kit	05230	STEMCELL Technologies
SuperScript VILO cDNA Synthesis Kit	11754050	Thermo Fisher Scientific
TaqMan™ Fast Advanced Master-Mix	4444556	Thermo Fisher Scientific
TaqMan™ Universal PCR Master Mix, no AmpErase™ UNG	4324018	Thermo Fisher Scientific
TOPO™ TA Cloning™ Kit for Sequencing, without competent cells	450030	Thermo Fisher Scientific

Table 11: RT-qPCR probes.

RT-qPCR probe	Catalogue number	Supplier
ACTB (Hs99999903_m1)	4331182	Thermo Fisher Scientific

DLK1 (Hs00171584_m1)	4331182	Thermo Fisher Scientific
EN1 (Hs00154977_m1)	4331182	Thermo Fisher Scientific
EN2 (Hs00171321_m1)	4331182	Thermo Fisher Scientific
EPHA3 (Hs00739092_m1)	4331182	Thermo Fisher Scientific
HOXB9 (Hs00256886_m1)	4331182	Thermo Fisher Scientific
MAOA (Hs00165140_m1)	4331182	Thermo Fisher Scientific
OLIG2 (Hs00377820_m1)	4331182	Thermo Fisher Scientific
SLC16A3 (Hs00358829_m1)	4331182	Thermo Fisher Scientific
SP5 (Hs01370227_mH)	4331182	Thermo Fisher Scientific
SPARCL1 (Hs00949886_m1)	4331182	Thermo Fisher Scientific

Table 12: Antibodies.

Antibodies	Dilution	Catalogue number	Supplier
ACTB	1:1000	ABO145-200	OriGene
ATP5A	1:20000	ab14748	Abcam
Complex II - Subunit 30	1:500	459230	Thermo Fisher Scientific
donkey-anti-goat IgG Alexa 488	1:500	A11055	Thermo Fisher Scientific
donkey-anti-goat IgG Alexa 594	1:500	A11058	Thermo Fisher Scientific
donkey-anti-mouse IgG Alexa 488	1:500	A21202	Thermo Fisher Scientific
donkey-anti-mouse IgG Alexa 594	1:500	A21203	Thermo Fisher Scientific
donkey-anti-rabbit IgG Alexa 488	1:500	A21206	Thermo Fisher Scientific
donkey-anti-rabbit IgG Alexa 594	1:500	A21207	Thermo Fisher Scientific
FOXA2	1:200	AF2400	R&D
GAPDH (coupled to HRP)	1:10000	GTX627408	GeneTex
goat-anti-mouse IgG peroxidase	1:10000	115-035-003	Dianova
MTCO2	1:500	ab110258	Abcam
NANOG	1:200	AF1997	R&D Systems
NDUFB8	1:1000	459210	Novex
NCAM1	1:200	ab7813	Abcam
NESTIN	1:250	MA1-110	Thermo Fisher Scientific
PAX6	1:200	19013	BioLegend
POU5F1	1:500	2840S	Cell Signaling
rabbit-anti-goat IgG peroxidase	1.10000	305-035-003	Dianova
RBFOX3	1:800	ab104224	Abcam
SOX1	1:500	Ab87775	Abcam
SOX2	1:200	2748	Cell Signaling
SOX17	1:200	AF1924	R&D
TBXT	1:1000	ab209665	Abcam
TH	1:600	P40101	PelFreez
UQCRC2	1:2500	ab14745	Abcam

Table 13: Enzymes.

Description	Catalogue number	Supplier
BbsI	R0539	New England Biolabs
T4 DNA Ligase	M0202	New England Biolabs
OneTaq® Hot Start 2X Master Mix with GC Buffer	M0485	New England Biolabs

Table 14: Primer.

Description	Sequence (5' -> 3')	Annealing Temp.	Extension time
hEN1_Exon1_fwd	CTCACAGACCCATAATCCTG	51°C	120 sec
hEN1_Exon1_rev	TTGGCTGAGCCCATAAGTAG		
hEN1_cDNA_fwd	TATGGAAGAACAGCAGCCGG	54°C	80 sec
hEN1_cDNA_rev	CCTACTCGCTCTCGTCTTTGT		
M13-RP (GATC)	CAGGAAACAGCTATGACC		
hEn1_Exon1_seq	CTTCGCTGAGGCTTCGCCTG		

Table 15: guide RNAs.

Description	Sequence (5' -> 3') without PAM
gRNA_EN1_1	AGCCTCAGTCCGGGCGCCAG
gRNA_EN1_2	AACATCCTGAGGCCGGACTT
gRNA_EN1_3	AGTTGGTGGTGCGGTGCAGC
gRNA_EN1_4	TGCGCCCCGGACGCGAACTG
gRNA_EN1_5	GTGGGCCACAGTTCGCGTCC
gRNA_EN1_6	AGGCTCAGGCTGAGGCCGCC

Table 16: **DNA Plasmids.**

Description	Supplier
E298 pU6-(BbsI)sgRNA_CAG-Cas9-venus-bpA	Available at IDO
BCL-XL	Available at IDO
pCR™4-TOPO™	Thermo Fisher Scientific (included in kit)

Table 17: Media / buffer composition.

Media / Buffer	Composition
Blocking buffer (Immunocytochemistry)	1 % (w/v) BSA 0.3 % (v/v) Triton X-100 in PBS
Agar plates	10 g Tryptone 5 g Yeast extract 10 g NaCl 15 g Agar Add water to 1 l
Blocking buffer (Western Blot)	5 % (w/v) skim milk powder in TBS-T
HEK293 growth medium	Advanced DMEM 1xGlutamax 10 % fetal bovine serum

Knockout serum replacement medium	80 % (v/v) KnockOut DMEM 20 % (v/v) Knockout serum replacement 10 µM SB431542 0.5 µM purmorphamine 1 µM dorsomorphin 3 µM CHIR99021 4.44 nM FGF-8b 1 % (v/v) non-essential amino acids 1 % (v/v) L-glutamine 150 µM ascorbic acid 2-phosphate 0.02 % (v/v) β-mercaptoethanol
DAN differentiation medium	50 % (v/v) DMEM/F12-GlutaMAX 50 % (v/v) Neurobasal 1 % (v/v) B27 (minus vitamin A) 0.5 % (v/v) N2 200 µM ascorbic acid 2-phosphate 1 µM purmorphamine 4.44 nM FGF-8b
DAN maturation medium 1	50 % (v/v) DMEM/F12-GlutaMAX 50 % (v/v) Neurobasal 1 % (v/v) B27 (minus vitamin A) 0.5 % (v/v) N2 200 µM ascorbic acid 2-phosphate 0.5 µM purmorphamine 500 µM dbcAMP 10 ng/ml BDNF 10 ng/ml GDNF 1 ng/ml TGF-3ß
DAN maturation medium 2	50 % (v/v) DMEM/F12-GlutaMAX 50 % (v/v) Neurobasal 1 % (v/v) B27 (minus vitamin A) 0.5 % (v/v) N2 200 µM ascorbic acid 2-phosphate 500 µM dbcAMP 10 ng/ml BDNF 10 ng/ml GDNF 1 ng/ml TGF-3ß
LB medium	10 g Tryptone 5 g Yeast extract 10 g NaCl Add water to 1 l Adjust to pH 7
Neuronal precursor maintenance medium	50 % (v/v) DMEM/F12-GlutaMAX 50 % (v/v) Neurobasal 1 % (v/v) B27 (minus vitamin A) 0.5 % (v/v) N2 10 µM SB431542 1 µM dorsomorphin 4.44 nM FGF-8b 150 µM ascorbic acid 2-phosphate 0.02 % (v/v) β-mercaptoethanol

Neuronal precursor medium	50 % (v/v) DMEM/F12-GlutaMAX 50 % (v/v) Neurobasal 1 % (v/v) B27 (minus vitamin A) 0.5 % (v/v) N2 10 µM SB431542 0.5 µM purmorphamine 1 µM dorsomorphin 3 µM CHIR99021 4.44 nM FGF-8b 150 µM ascorbic acid 2-phosphate 0.02 % (v/v) β-mercaptoethanol
PBS	171 mM NaCl 3,4 mM KCl 10 mM Na2HPO4 1,8 mM KH2PO4 in H_2O Adjust to pH 7.4
radioimmunoprecipitation assay (RIPA) buffer	50 mM Tris-HCL 150 mM NaCl 1 % (v/v) Triton X-100 0.5 % (w/v) Sodium-Deoxycholate 0.1 % (w/v) SDS 3 mM EDTA in H_2O
TAE buffer	40 mM Tris 20 mM Acetic acid 1 mM EDTA
10 x TBS pH8	100 mM Tris 1.4 M NaCl In H_2O Adjust to pH 8 with HCl
1x TBS-T	10 % (v/v) 10x TBS 0.1 % (v/v) Tween20 In H_2O
1x Tris/Glycine transfer buffer	10 % (v/v) 10x Tris/Glycine Buffer 20 % (v/v) Methanol In H_2O
1x XT MOPS running buffer	5 % (v/v) 20x MOPS Buffer In H_2O

Table 18: Cell lines.

Description	Information
HMGUi001-A	generated at Helmholtz Center Munich at the Institute of Diabetes and Regeneration Research (IDR)
EN1 homozygous knockout	generated at Helmholtz Center Munich (IDG) as part of this thesis

EN1 heterozygous knockout	generated at Helmholtz Center Munich (IDG) as part of this thesis

Table 19: Devices.

Devices	Supplier
Axiocam 506 mono	Zeiss
AxioCam HRc camera	Zeiss
Axio Imager.M2 microscope	Zeiss
Axiovert 200 microscope	Zeiss
Biological Safety Cabinet, Herasafe	Thermo Fisher Scientific
Cellinsight NXT platform	Thermo Fisher Scientific
Criterion Blotter	Bio-Rad
Criterion Vertical Electrophoresis Cell	Bio-Rad
Fusion Sl Gel Chemiluminescence Documentation System	PEQLAB
Gel-Documentation System E.A.S.Y. Win32	Herolab
iScan system	Illumina
Milli-Q Integral Water Purification System	Merck Millipore
Mr. Frosty™ Freezing Container	Thermo Fisher Scientific
NanoDrop Spectrophotometer ND-1000	Peqlab
Orbital Shaker (7-0030)	Neolab
QuantStudio 7 Flex	Thermo Fisher Scientific
Seahorse XF96 Analyzer	Agilent Technologies
SpectraMax M5	Molecular Devices

4.2. Ethical compliance

Work with human hiPSCs, including skin biopsy, isolation and characterization of dermal fibroblasts were performed according to protocols approved by the Ethics Committee of the Medical Faculty of the Eberhard Karls University, Tübingen (approval number: 130/2018BO2). The design of the study followed the principles of the Declaration of Helsinki. All participants or legal guardians gave written informed consent prior to the study. All related experiments and methods were performed in accordance with relevant guidelines and regulations. The HMGUi001-A hiPSC line was generated and characterized by Xianming Wang (*271*). The CRISPR-Cas9 induced *EN1* knockout lines and respective controls were established and characterized as described in this work.

4.3 Molecular Methods

4.3.1 Polymerase chain reaction (PCR)

PCR was performed with the polymerase and primer named in the respective paragraphs. If not indicated otherwise, cycling was performed according to manufacturer's instructions and the reaction volume was 25 µl. Primers, annealing temperatures and extension times are listed in **Table 13.**

4.3.2 Cloning

Digest of DNA Fragments
For cloning purposes, 1 µg of DNA fragments or plasmids were digested with the selected restriction enzyme according to the manufacturer's instructions.

Double-stranded cDNA synthesis for cloning
Double-stranded cDNA for cloning was transcribed from RNA with the Maxima H Minus Double-Stranded cDNA Synthesis Kit according to the manufacturer's instructions, using the provided oligo(dT)$_{18}$ primer and 5 µg of RNA.

Agarose gel electrophoresis
To control the size of amplified DNA products following a PCR or to control fragments after a restriction digest, DNA was separated by agarose gel electrophoresis. Agarose was boiled in 1x TAE buffer in the microwave until completely dissolved and ethidium bromide was added at a concentration of 0.05 %. Depending on the size of the fragments, different agarose concentrations were used. Normally 1% gels were casted. When the gel was dry, 1 x TAE running buffer was added and the DNA samples mixed with loading dye were loaded. Gel electrophoresis was performed at 120 V. The E.A.S.Y Win32 Gel-Documentation system was used to acquire pictures. If fragments were used for cloning, either gel bands were excised with a scalpel and purified using the Monarch DNA Gel Extraction Kit or only a small portion was loaded on the gel to control for size and the remaining PCR was purified using the Monarch PCR & DNA Cleanup Kit.

Ligation of DNA fragments
Ligation of DNA fragments was performed using T4 DNA Ligase according to the manufacturer's instructions. If not indicated otherwise, 50 ng of vector were used, and inserts were supplied at a molar ratio of 1:3.

Transformation of bacteria
Plasmids were transformed into chemically competent DH5α bacteria for amplification. Bacteria were thawed on ice and 3 µl of plasmid were added to 50 µl of DH5α. After 30 minutes (min) of incubation on ice, a heat shock at 42°C for 45 sec was performed. Bacteria were cooled on ice for 2 min before LB medium was added and bacteria were incubated at 37°C and 180 rpm for 1 hour (h). Bacteria were then harvested by centrifugation and plated on LB agar plates containing ampicillin at a concentration of 50 µg/ml as selection marker. Plates were incubated overnight at 37°C and single colonies were picked the next day for further analysis.

Plasmid DNA preparation
Plasmids were isolated from bacteria using the QIAprep Spin Miniprep Kit or the QIAGEN Plasmid Maxi Kit. To screen for correct clones, 3 ml of LB medium containing ampicillin (50 µg/ml) were inoculated with a single colony and incubated at 37°C and 180 rpm overnight. The Miniprep kit was used to isolate the plasmids. For the Maxiprep, 100 ml LB medium containing ampicillin were inoculated with 1 ml Miniprep culture. Plasmid concentrations were determined at the NanoDrop.

4.3.3 Isolation of genomic DNA

Genomic DNA was isolated using the QIAamp DNA Mini Kit according to the manufacturer's instructions following the protocol for cultured cells. Briefly, cells (iPSCs, NPCs) were detached

using a cell scraper and harvested by centrifugation for 5 min at 300 x g. In the last step, the genomic DNA was eluted in 80 µl H_2O.

4.3.4 Protein isolation and quantification

For protein isolation, RIPA buffer was supplemented with protease inhibitors right before use. The cells were washed with PBS once and lysed directly in the well by adding 200 µl RIPA buffer and collecting the material using a cell scraper. Cells were incubated on ice for 10 min and cell debris was removed by centrifugation at maximal speed (21000 g) and 4 °C for 15 min. The supernatant was stored in aliquots at -80°C. The protein concentration was determined using the Pierce BCA assay according to the manufacturer's instructions.

4.3.5 Immunoblot

Protein levels were compared by immunoblot using the CriterionTM Cell System from Biorad. Proteins were thawed on ice and diluted to the desired concentration (5 µg / 20 µl) with RIPA buffer. NuPAGE^{TM} LDS-sample buffer was supplemented with 2 µl 2-mercaptoethanol / 50 µl sample buffer and added at a 1x concentration (6.6 µl). Samples were heated for 5 min to 60°C and 25 µl sample and 5 µl protein marker were loaded on a Criterion XT 4-12% Bis-Tris Gel. Proteins were separated at 180 V for 75 min in 1x XT MOPS running buffer using a Criterion Vertical Electrophoresis Cell from BioRad. Following electrophoresis, the proteins were blotted on a PVDF membrane. The blotting sandwich was prepared as followed: sponge, blotting paper, gel, methanol-activated membrane, blotting paper, sponge. All the components were soaked in 1x Tris/Glycine buffer, and the transfer was performed in 1x Tris/Glycine for 2 h at 60 V at 4°C. The membrane was then blocked with 5 % milk in TBS-T for 75 min at room temperature (RT). Primary antibodies were diluted in 5 % milk in TBS-T and the membrane was incubated with the primary antibody in a 50 ml falcon overnight at 4°C at 20 rpm. The membrane was washed three times for 15 min with TBS-T rotating at 15 rpm. The secondary antibody coupled to a peroxidase was then diluted in 5 % milk in TBS-T and incubated with the membrane for 1 h at RT. After the incubation, the membrane was washed again three times for 5 min with TBS-T and proteins were detected using Clarity Max ECL detection substrate and visualized using a Fusion SL Gel chemiluminescence documentation system. Protein levels were quantified using Image Lab.

4.3.6 RNA isolation and cDNA synthesis

RNA was isolated using the RNeasy Plus Mini Kit (Qiagen) according to the manufacturer's instructions. Concentration and purity were determined with the NanoDrop, and samples were stored at -80°C. 1 µg of RNA was reverse transcribed to cDNA using the VILO cDNA Synthesis kit. cDNA was stored at -20°C.

4.3.7 Quantitative real-time PCR

Gene expression was analyzed by quantitative real-time PCR (RT-qPCR) in 384-well format. A total amount of 25 ng cDNA (2.78 ng/µl) per well was supplied and amplified using TaqMan universal PCR MM no Ung or TaqMan Fast Advanced Master-Mix and gene specific TaqMan probes on a QuantStudio 7 Flex Real-Time PCR system. The difference in gene expression was assessed using the comparative Ct method. The mean Ct value of technical replicates was calculated and normalized to ACTB. The mRNA level was depicted using the Delta Ct method.

4.4 Cell culture

All cell culture experiments were performed under sterile conditions.

4.4.1 Cultivation of human cell lines

HEK293 cells were cultivated in growth medium (Advanced DMEM supplemented with GlutaMAX and 10% FCS) at 37°C and 5 % CO_2. When cells reached a confluency of about 90% cells were passaged. Cells were washed with PBS and detached by incubation with 0.25% Trypsin/EDTA for 5 min in the incubator. The reaction was stopped by adding growth medium and cells were centrifuged for 5 min at 200 g. The supernatant was removed, cells were resuspended in fresh growth medium and seeded at the desired dilution. Medium was changed every second day.

4.4.2 Cultivation of undifferentiated human induced pluripotent stem cells

Human induced pluripotent stem cells (hiPSCs) were cultivated in Essential 8 (E8) Flex Medium under feeder-free conditions on Geltrex-coated plates at 37°C, 5 % CO_2 and 21% O_2. Geltrex was diluted 1:50 in DMEM/F12-GlutaMAX and coating was incubated for at least 1 h in the incubator. When cells reached a confluency of 70%, colonies were detached by adding StemMACS Passaging Solution XF and incubation for 5 min at 37°C. The Passaging solution was aspirated, and colonies were chopped in 1 ml E8 Flex Medium using a 1000 µl pipette tip. hiPSCs were diluted and seeded at the desired density on fresh Geltrex-coated plates.

4.4.3 Differentiation and cultivation of human neuronal precursor cells

hiPSCs were differentiated into small molecule neuronal progenitor cells (NPCs) via an embryoid body stage according to the protocol described by Reinhardt et al. (*169*) with minor adaptations. When hiPSCs reached a confluency of approximately 70%, cells were washed with PBS and colonies were detached using collagenase type IV (2 mg/ml) and incubation for 40-60 min at 37°C, 5% CO_2, 21%O_2. The detached colonies were transferred into a 15 ml falcon tube containing 1 ml E8 Flex Medium. Colonies were allowed to sediment for 3-5 minutes; the supernatant was removed, and the colonies were resuspended in KnockOut-Serum Replacement Medium (KSR-Medium). The colonies were transferred to a non-coated 6-well plate and incubated at 37°C, 5% CO_2, 21%O_2 on a shaker at 80 rpm. Medium was changed every day for two days. On day 3, the EBs were changed to neuronal precursor medium and maintained in this medium for 4 days on a shaker at 80 rpm at 37°C, 5% CO_2, 21%O_2 with daily medium changes. The EBs were transferred to neuronal precursor maintenance medium at day 6 and seeded on Geltrex-coated plates the following day. NPCs were allowed to expand for 3-4 days in neuronal precursor maintenance medium at 37°C, 5% CO_2, 21%O_2. Medium was changed daily. When NPCs were confluent, usually after 10-11 days, cells were detached using accutase and incubation for 10 min at 37°C, 5% CO_2, 21%O_2. Using a 1000 µl pipette tip, cells were harvested and transferred into a falcon tube containing 5 ml neuronal precursor maintenance medium to stop the reaction. The cells were pelleted by centrifugation for 5 min at 200 g, resuspended in fresh neuronal precursor maintenance medium and seeded on Geltrex-coated plates. From this point on, NPCs were cultivated at 37°C, 5% CO_2, 21%O_2 and passaged at 80 % confluency using accutase. Medium was changed daily.

4.4.4 Differentiation of human dopaminergic neurons

NPCs were differentiated into dopaminergic neurons according to the protocol described by Reinhardt et al. (*169*). NPCs were cultivated for 8 days in dopaminergic neuron (DAN) differentiation medium with daily medium change. The medium was then changed to DAN maturation medium 1 and the cells were seeded on poly-L-ornithine and laminin coated plates on day 9 using accutase. NPCs were washed with PBS and separated into single cells with accutase at 37°C, 5% CO_2, 21%O_2 for 10 min. Cells were diluted in DAN maturation medium 1 and centrifuged for 5 min at 200 g. The cells were counted, and a defined number of cells was seeded on the coated plates. For the coating, poly-L-ornithine was diluted in PBS to a concentration of 15 µg/ml and plates were incubated at 37°C, 5% CO_2, 21%O_2 overnight. Poly-L-ornithine was removed the next day, plates were washed 3 times with PBS and 10 µg/ml laminin diluted in PBS was added. Plates were incubated for at least 4 h at 37°C, 5% CO_2, 21%O_2. One day after the re-seed, the medium was changed to DAN maturation medium 2 and medium was then changed every 3-5 days. DANs were differentiated for at least 42 days starting from initiation.

4.4.5 Trilineage differentiation

EN1 knockout hiPSCs were differentiated into the three germ layers using the STEMdiff Trilineage Differentiation Kit according to manufacturer's instructions. Differentiation was performed on 24-well plates and cells were seeded at the recommended density in E8 Flex Medium. Cells were fixed at day 5 (mesoderm and endoderm) or 7 (ectoderm) and stained for lineage specific markers. SOX17 and FOXA2 were used as endodermal markers, TBXT and NCAM as mesodermal markers and PAX6 and NESTIN as ectodermal markers.

4.4.6 Transfection of cells

HEK293 cells were transfected using X-tremeGENE HP DNA transfection reagent in a 24-well format. Cells were seeded the day before transfection with $5x10^4$ cells per well. DNA (500 ng/well) was diluted in Opti-MEM and X-tremeGENE HP DNA transfection reagent was added at a ratio of 3:1 to DNA. After 15 min of incubation at RT, the solution was added to the cells in a dropwise manner. Medium was replaced the following day and DNA was isolated 48 h after transfection.

4.5 Generation of *EN1* knockout hiPSC clones

4.5.1 Design, generation, and efficiency test of gRNA constructs

Guide RNAs (gRNAs) targeting the beginning of Exon 1 of the human *EN1* gene were designed using the online tool CRISPOR (http://crispor.tefor.net/). Six gRNAs in the desired region with a high specificity score were selected (**Table *15***) and cloned into the E298 pU6-(BbsI)sgRNA_CAG-Cas9-venus-bpA plasmid. Sense and anti-sense oligonucleotides containing the respective gRNA sequence and appropriate overhangs for ligation with the vector were dissolved to a concentration of 100 µM in H_2O. Sense and anti-sense oligo were annealed by heating an equal amount of each oligo in 100 µl Tris-EDTA (TE) buffer to 99°C for 5 min and letting the mixture cool down to RT slowly. Next, 1 µg of the E298 pU6-(BbsI)sgRNA_CAG-Cas9-venus-bpA plasmid was digested using the restriction enzyme BbsI according to the manufacturer's instructions to create sticky ends for ligation with the annealed oligonucleotide. After gel purification of the digested vector, 50 ng of vector were ligated with 4 µl of annealed oligonucleotides using the T4 DNA ligase and

transformed into DH5α bacteria. Correct plasmids were identified by sequencing (for more detailed information see 4.3.2).

The cutting efficiency of the gRNAs was determined by transfecting HEK293 cells with the different gRNAs. Genomic DNA was isolated after 48 h and the target region of the gRNAs was amplified by PCR using the One Taq Polymerase and the primer hEN1_Exon1_fwd and hEN1_Exon1_rev. PCR products were sequenced using hEN1_Exon1_rev and hEN1_Exon1_seq primers (**Table *14***).The cutting efficiency was determined based on the sequencing results using the Interference of CRISPR Edits (ICE) CRISPR analysis tool from Synthego (https://ice.synthego.com/#/).

4.5.2 Transfection and sorting

The hiPSC line HMGUi001-A was cultured as described in 4.4.2 in E8 Flex Medium and cultivated on Geltrex-coated plates. The cells were transfected with a plasmid encoding a gRNA targeting Exon 1 of *EN1* and the Cas9 protein fused to a Venus reporter for sorting and a plasmid encoding the anti-apoptotic protein BCL-XL. One day prior to transfection, the hiPSCs (passage (P) 28) were seeded. Cells were washed with PBS and detached using accutase for 10 min at 37°C to achieve a single cell solution. hiPSCs were counted using a Neubauer chamber and 4 x 10^5 cells per 6-well were seeded in E8 Flex Medium containing 10 µM ROCK inhibitor Y27632. After 24 h, the cells were transfected using Lipofectamine Stem Transfection Reagent. ROCK inhibitor Y27632 was removed 4 h before the transfection and 2.5 µg DNA was transfected (1.25 µg of each plasmid). The DNA was diluted in 100 µl Opti-MEM Reduced Serum Medium, followed by 5 min of incubation at RT. The Lipofectamine Stem Transfection Reagent (5 µl) was diluted in the same amount of Opti-MEM and incubated for 5 min at RT. The DNA was then added to the Lipofectamine followed by 20 min of incubation at RT. The Lipofectamine/DNA particles were then added to the cells in a dropwise manner. Medium was changed the next day and cells were sorted 48 h after transfection for Venus positive cells. For the sorting, the cells were detached using accutase, resuspended in E8 Flex medium containing 10 µM ROCK inhibitor Y27632 and put through a cell strainer before proceeding to the fluorescent activated cell sorting (FACS). The sorted hiPSCs were plated at a low density (approximately 2000 cells) on a 10 cm dish in E8 Flex Medium containing 10 µM ROCK inhibitor Y27632 and antibiotics (Penicillin/Streptomycin 1:100). After two days, the medium was changed to E8 Flex containing CloneR supplement (1:10) to increase single cell survival. When cells started to form colonies, 4 days after sorting, the medium was changed to E8 Flex. Colonies were then manually picked, chopped 2-3 times with the 1000 µl pipette tip and replated on a 24-well plate once they reached a sufficient size. To increase survival, the cells were cultured in E8 containing 10 µM ROCK inhibitor Y27632 for 1 day. The colonies were characterized by sequencing on the targeted region of the *EN1* locus. To generate corresponding wildtype (WT) control clones, HMGUi001-A cells were seeded at a low density to allow picking of single clones and processed similar to the manipulated cells.

4.5.3 Re-clonalization

To ensure single cell clonality, selected clones containing the desired knockout were clonalized again. WT clones were also re-clonalized to avoid any bias resulting from differences in handling. When colonies reached a sufficient size, hiPSCs were detached using accutase (see 4.4.3). After centrifugation, the cells were resuspended in E8 Flex Medium containing CloneR (1:10) and passed

through a cell strainer. The cell number was determined using the Neubauer Chamber and diluted to a concentration of 0.8 cells per 100 µl in E8 Flex medium containing CloneR. The cells were plated on a Geltrex coated 96-well plate using 100 µl per well. A medium change was performed after 2 days and after 4 days medium was changed back to E8 Flex without CloneR. Once colonies had a sufficient size, the hiPSCs were transferred to a coated 24-well plate using passaging solution (see 4.4.2). The clones were expanded for further characterization by subcloning of the *EN1* cDNA. RNA was isolated, transcribed into cDNA and *EN1* cDNA was amplified by PCR using the One Taq polymerase and the hEN1_cDNA_fwd and hEN1_cDNA_rev primer pair. The PCR product was cloned into the pCR4-TOPO vector using the TOPO™ TA Cloning™ Kit for Sequencing according to the manufacturer's instructions. The plasmid was transformed into bacteria and the plasmid was isolated from at least 5 single colonies per cell clone and sequenced using the M13-RP primer provided by GATC.

4.6 Cell-based assays

4.6.1 MitoTracker staining

NPCs and DANS were maintained at 37°C, 5% CO_2, 21%O_2, on Geltrex- or poly-L-ornithine/laminin-coated 96-well plates in neuronal precursor maintenance medium or DAN maturation medium 2, respectively. Cells were cultivated in 100 µl of the respective medium per well. The same amount of prewarmed medium supplemented with 200 nM MitoTracker Orange CMTMRos was added per well and cells were incubated for 20 min at 37°C, 5% CO_2, 21%O_2. Afterwards, cells were washed with PBS twice and fixed with 10 % formalin for 15 min at RT. Fixed cells were washed three times with PBS and DAPI staining was performed as described in 4.7. In case of CHIR99021 stimulation, neuronal precursor maintenance medium was supplemented with 3 µM CHIR99021 for 48 h before the MitoTracker staining. The Medium was changed daily.

4.6.2 Respiratory and glycolytic flux analysis

Respiratory and glycolytic flux analysis was performed for NPCs and DANs.
NPCs were maintained in neuronal precursor maintenance medium on Geltrex-coated plates at 37°C, 5% CO_2, 21%O_2. NPCs were passaged at 80 % confluency. The cell number was determined and 70.000 cells per well were seeded on Geltrex-coated XF96 cell culture microplates in neuronal precursor maintenance medium containing 10 µM ROCK inhibitor Y27632. Cells were incubated for 72 h before Seahorse measurement. After 24 h, medium was changed to neuronal precursor maintenance medium without ROCK inhibitor Y27632. Medium was changed daily. At least 6 replicates per cell clone were seeded. For the CHIR99021 stimulation, NPCs were seeded in neuronal precursor maintenance medium containing 10 µM ROCK inhibitor Y27632. After 24 h, ROCK inhibitor Y27632 was removed and 3 µM CHIR99021 was added for 48 h with daily medium change.

At day 9 of the DAN differentiation, DANs were passaged according to the protocol as described in 4.4.4. The cell number was determined and DANs were seeded in two different densities (2000 and 3000 cells per well) on poly-L-ornithine/laminin-coated XF96 cell culture microplates. Cells were allowed to mature until day 42 of the differentiation (33 days after seeding) with medium changes every 2-5 days. At least 6 replicates per cell clone were seeded for each density.

The respiratory analysis was performed using a Seahorse XF96 Analyzer, which allows real-time metabolic flux analysis. All measurements and dilutions were performed in XF Assay medium. Prior to the Seahorse analysis, the cells were washed once with 180 µl XF Assay medium and incubated for 1 h at 37 °C, 0 % CO2, 21 % O_2 with 180 µl XF Assay medium supplemented either with 25 mM glucose or 5 mM pyruvate. At least three replicates per substrate and cell clone were measured. The XFe96 Sensor Cartridges were hydrated with 200 µl H_2O per well overnight and 200 µl calibrant for at least 1 h at 37 °C, 0 % CO2, 21 % O_2. The ports were loaded from A to D with oligomycin, FCCP, rotenone with antimycin A and 2-deoxyglucose (Table 20).

Table 20: Compound concentrations for Seahorse XF Analysis. Stocks were prepared in DMSO.

Compound	Stock concentration	Port	Port concentration	Assay concentration
Oligomycin	1 mg/ml	A	10 µg/ml	1 µg/ml
FCCP	2.5 mM	B	5 µM	0.5 µM
Rotenone	2.5 mM	C	50 µM	5 µM
Antimycin A	2.5 mM	C	20 µM	2 µM
2-deoxyglucose	1 M	D	1 M	100 mM

After equilibration of the cartridge in the Seahorse XF96 Analyzer, the cell plate was loaded, and analysis was performed. Basal respiration was assessed with four measurement points (mix for 1 min, 2 min time delay, measure for 3 min). The ports were then injected one after the other followed by three measurement points after each injection. The plate was sealed and stored at -20°C immediately after the Seahorse run was completed for quantification of DNA content. All data were normalized to DNA content, either quantified from the analyzed plate (same plate) (DANs) or a copy plate (NPCs), which was seeded and treated the same way as the analyzed plate. For the copy plate procedure, the medium was aspirated, and the copy plate was also stored at -20°C immediately after the run. The DNA content was quantified using the Quant-iT PicoGreen dsDNA Assay Kit. For copy plate analysis, cells were lysed in 60 µl RIPA buffer (**Table *17***) per well for 20 min on ice. In case the DNA was quantified from the same plate, 10 µl Proteinase K were added per well and cells were lysed at 37°C for 1 h. The plates were then centrifuged for 30 min or 5 min at 3000 g, respectively and the supernatant was used for DNA quantification. The Quant-iT PicoGreen dsDNA Assay was performed according to manufacturer's instructions using Lambda DNA standards to calculate the DNA concentrations by linear regression. For statistical analysis, the mean OCR values for basal and maximal mitochondrial respiration as well as for the proton leak were calculated for each clone. Basal mitochondrial respiration is represented by the four measuring points prior to injection of port A. Proton leak is measured after injection of port A and before injection of port B and maximal mitochondrial respiration is calculated from the three measuring points after injection of port B and before injection of port C. The OCR caused by non-mitochondrial respiration (last 4 measuring points) was subtracted from each value.
Basal glycolytic flux and glycolytic capacity were calculated from the mean ECAR values for each clone at the four measurements points before injection of port A and the three measurements after injection of port A and before injection of port B, respectively. The last measuring point represents the non-glycolytic acidification and was subtracted from all values.

4.6.3 Analysis of complex I activity

Complex I activity was analyzed using the Complex I Enzyme Activity Assay Kit according to the manufacturer's instructions. Protein was isolated freshly, and the concentration was determined by BCA assay according to manufacturer's instructions. The concentration of all samples was adjusted to 1250 µg/ml. Kinetics were measured every 30 sec for 30 min on a SpectraMax M5 microplate reader. The relative complex I activity is shown in relation to the average complex I activity of WT clones.

4.6.4 Glucose uptake assay

As described above, NPCs were maintained in neuronal precursor maintenance medium on Geltrex-coated plates at 37°C, 5% CO_2, 21%O_2 and were passaged at 80 % confluency. Cells were seeded at 70.000 cells per well on a Geltrex-coated 96-well plate in neuronal precursor maintenance medium with ROCK inhibitor Y27632. After 24 h ROCK inhibitor was removed, and cells were stimulated for 48 h with CHIR99021 with daily medium change before the glucose uptake was measured. The Glucose Uptake-Glo Assay (Promega) was used to determine the glucose uptake according to the manufacturer's instructions. The cells were incubated with 2-deoxyglucose for 10 minutes and detection reagent was added for 1 h before luminescence measurement with an integration time of 0.5 seconds. The glucose uptake was normalized to the DNA content using the copy plate procedure (see 4.6.2 for details). Data are depicted as relative glucose uptake normalized to the average uptake of the WT clones.

4.7 Immunocytochemistry and imaging of human cells

Cells (hiPSCs, NPCs, DANs) were cultivated on coated glass coverslips or 96-well plates for immunocytochemistry. Cells were washed with PBS (except for DANs) and fixed with 10 % formalin for 15 min at RT. To remove the formalin, the cells were washed three times with PBS. Afterwards, the cells were permeabilized and blocked in PBS containing 1 % Bovine Serum Albumin (BSA) and 0.3 % Triton-X-100 for 15 min. Primary antibodies (**Table *12***) were diluted in 1% BSA and 0.3 % Triton-X-100 as listed in **Table 17** and cells were incubated overnight at 4°C. After three washing steps with PBS, the corresponding secondary antibodies, diluted in 1 % BSA and 0.3 % Triton-X-100 were added to the cells and incubated for 1 h at RT in the dark. Next, the cells were washed twice with PBS and nuclei were stained by adding DAPI-solution (100 ng/ml in PBS) for 5 min at RT. Cells were again washed with PBS and mounted on glass slides using Aqua-Poly/Mount. Once slides were dry, they were stored at 4 °C protected from light. Fluorescent images were acquired using the Axio Imager.M2 microscope (Zeiss) with a 20x or 40x objective. Images were analyzed using the Cellinsight NXT platform or ImageJ (ImageJ 1.48v).

4.8 Image (intensity) quantification

The Cellinsight NXT platform with a 20x 0.4 NA objective (field size 454.51 by 454.51 µm) was used to acquire images for fluorescence intensity quantification and HCS Studio 2.0 was used for analysis. The configurations were adjusted for every antibody and chromophore. DAPI staining was performed to label all nuclei and assessed in channel 1. A mask was created in channel 1 using the image analysis segmentation algorithm to determine all viable cells as valid objects based on their nuclear size and shape. This mask was then used to identify the desired markers (e.g. MitoTracker intensity) of all valid objects in channel 2 using a fixed exposure time

(RingSpotAvgIntenCh2). As cytoplasmic markers were analyzed, a ring mask (width 15) around the nucleus was used for quantification of the intensity. In DANs, channel 2 was used to filter for TH positive neurons using a ring mask with a width of 6 and a threshold for the average spot intensity. The MitoTracker intensity of the valid objects from channel 2 was measured in channel 3 using a ring width of 7. The average fluorescence intensity per cell clone was quantified. In addition, a distribution analysis was performed with 140 NPCs and 50 DANs per clone. The *sm.density.compare* function which applies a bootstrap hypothesis test of equal distribution was used to generate and compare distribution plots (R package "sm: Smoothing Methods for Nonparametric Regression and Density Estimation" version 2.2-5.6, R version 4.1.2). The *ks.test* function was used to apply a two-sample Kolmogorov Smirnov test.

The differentiation efficiency was also quantified using the Cellinsight NXT platform. The neuronal identity (RBFOX3/NeuN) was analyzed in channel 2 using a nuclear marker. Cells that passed the average intensity cut off (circle) were screened for the dopaminergic marker TH in channel 3 using a ring mask with a width of 6 to detect the cytoplasmic marker.

4.9 CNV analysis

Clones were assessed at passage 42 to passage 45. Genomic DNA was isolated from EN1 -/-, EN1 +/- and WT hiPSC clones using the QIAamp DNA Mini Kit according to the manufacturer's instructions following the protocol for cultured cells. DNA concentrations were determined using the Quant-iT PicoGreen dsDNA Assay Kit as described in the Infinium HTS Assay Protocol Guide (Illumina). Genomic integrity was analyzed using the HumanCytoSNP-12 BeadChip (knockouts) (Illumina) and the Infinium Global Screening Array-24 v3.0 Kit (WT's) (Illumina). The assay was performed at the genome analysis center of the Helmholtz Center Munich. Downstream analysis including clustering, quality control and SNP calling was performed using Genome Studio 2.0 (Illumina) as described by Guo et al. (2014) (*272*). Copy number variations (CNV) for each cell clone were determined using the B-allele frequency (BAF) and $\log_2$ R ratios with the cnvPartition v3.2.1 plug in (Illumina). cnvPartition v3.2.1 was run with default settings and a confidence threshold of 50. CNVs greater than 100 kb were considered.

4.10 Transcriptome analysis

4.10.1 Library preparation and sequencing

Gene expression profiling was performed at the stage of hNPCs. All 5 WT lines and the 3 *EN1* ko lines were used. hNPCs were seeded at a density of 1,000,000 cells per well on Geltrex coated 6-well plates containing neural precursor maintenance medium supplemented with 10 µM ROCK inhibitor Y27632. In total, 6 replicates per cell line were prepared and incubated at 37 °C, 7% CO_2, 21% O_2. The next day, medium was changed to neural precursor maintenance medium for 3 replicates and to neuronal precursor maintenance medium supplemented with 3 µM CHIR99021 for the other 3 replicates. After 48h, the RNA was isolated using the RNeasy Plus Mini Kit according to the manufacturer's instructions. RNA libraries for RNA-seq were prepared using the TruSeq Stranded mRNA kit (Illumina) following manufacturer's protocols. In total, 48 libraries were prepared. Libraries were pooled and paired-end sequencing (100bp per read) was performed

on a NovaSeq 6000 (Illumina) with an estimated read depth of 30,000,000 reads per sample. Sequencing was performed in the genome analysis center of Helmholtz Munich.

4.10.2 Bioinformatic analysis

RNA-seq data were analyzed using a local Galaxy v 22.05 instance. The quality of sequencing reads stored in FASTQ files was assessed using FastQC v0.72. Paired-end reads were trimmed, and short reads (<20 bp) were removed using Trimmomatic v0.38.1. RNA STAR Aligner v2.7.8a was used to align sequence reads to the human reference genome GRCh38. Alignment summary statistics were reported using samtools idxstats v2.0.3. Alignment quality was further assessed using RSeQC v1.1 and its provided annotation BED files for the human reference genome GRCh38. The number of reads mapped to each gene was extracted from the STAR aligner BAM output file using featureCounts v1.6.4 and gene annotations (release 32) obtained from GENCODE. Gene counts were converted to a matrix using Count matrix v0.0.3. Output results from FastQC, Trimmomatic, STAR aligner, samtools idxstats, featureCounts, and RSeQC were aggregated using MultiQC v1.9.

Further analysis was performed using R v4.1.0 as described by (*273*). In brief, PCA was performed using the prcomp function and visualized using the package ggbiplot v0.55 with probability ellipses (0.68 of normal probability). The Pearson correlation between samples was calculated using the cor function within R, and correlations were plotted in a heatmap using the pheatmap function of the R package pheatmap v1.0.12. Agglomerative hierarchical clustering by the hclust function (method = "complete") was applied to group samples.

Hypothesis testing was performed using the package DESeq2 and the design formula design = ~clone.n + clone.n:replicate + condition with condition being either WT or *EN1* -/-, clone.n being a unique number per cell line per condition, and replicate indicating the different replicates per cell line (1, 2, or 3). For assessing the stimulation effect, the design formula design = ~clone.n + clone.n:replicate + stimulation with stimulation being either unstimulated or CHIR99021 stimulated. The p-values were adjusted for multiple testing within DESeq2 by Benjamini and Hochberg (*274*). Genes with a p-adjust-value (q-value) < 0.05 were considered significantly altered in EN1 -/- NPCs.

Volcano plot and heatmap

Based on the complete set of differentially expressed genes (DEGs) a volcano plot and heatmap was produced. For the volcano plot, log2(fold change) was plotted versus the -log10(p-adjust-value) on the x and y-axis, respectively. The Volcano plot was generated using the EnhancedVolcano function of the R package EnhancedVolcano v1.12.0 with p-adjust cutoff = 0.05 and fold change cutoff = 0.5. The heatmap was generated by using the heatmap.2 function within the gplots v3.1.1 package. Agglomerative hierarchical clustering by the hclust function (method = "complete") was applied to group samples or genes. Log2(fold changes) of DEGs were scaled and represented as z-score.

Pathway enrichment analysis

DEGs were investigated for enrichment in GO, KEGG and WikiPathway (WP) terms using the enrichGO, enrichKEGG, or enrichWP function of the R package clusterProfiler v4.2.2 (one-sided hypergeometric test). Enrichment of Reactome terms was assessed using the enrichPathway

function of the R package ReactomePA v1.38.0 (one-sided1 hypergeometric test). p-values were adjusted for multiple testing by Benjamini and Hochberg (*274*). Enrichment maps were generated using the treeplot function of clusterProfiler v4.2.2.

4.11 Statistics and reproducibility

Sample size was not predetermined by statistical methods. If not indicated otherwise, statistical analysis was performed using GraphPad Prism 6 with mean values of three biological replicates for n = 3 EN1 -/-, n = 2 EN1 +/- and n= 5 WT clones. Two group comparison was performed to compare EN1 -/- or EN1 +/- with WT cell clones using unpaired, two-tailed t-test in case of normal distribution and similar standard deviation. A Welch t-test was applied if standard deviation was not similar. In case of non-Gaussian distribution, a two-tailed Man-Whitney-U test was applied. For comparison multiple groups (stimulation and genotype) a two-way ANOVA with Sidak or Tukey's post-hoc test was performed. Boxplots are displayed with the box extending from the 25^{th} to 75^{th} percentile showing the median and whiskers ranging from min to max value with all data points shown.

Distribution plots for MitoTracker analysis were performed using R version 4.1.0.The plots were generated and compared using the sm.density.compare function, applying a bootstrap hypothesis test for equal distribution (R package "sm: Smoothing Methods for Nonparametric Regression and Density Estimation" version 2.2-5.681). In addition, a two-sample Kolmogorov-Smirnov test was performed using the ks.test function in R and a linear mixed effects model (lm) was fit using the lmer function (R package "lme4" Version 1.1-31). Here, unique cells were included but nested within clones (formula: fluorescence intensity ~ genotype + 1 |genotype:clones; REML = FALSE). P-values for the linear mixed effects model were calculated using the Anova function (R package "car" Version 3.0-10)

P-values ≤ 0.05 were considered significant. All statistical details and data are listed in the Appendix.

5. References

1. *Ageing and health* (30.06.2022) (available at https://www.who.int/news-room/fact-sheets/detail/ageing-and-health).
2. *The top 10 causes of death* (30.06.2022) (available at https://www.who.int/news-room/fact-sheets/detail/the-top-10-causes-of-death).
3. W. Poewe *et al.*, Parkinson disease. *Nature reviews. Disease primers*. **3**, 17013 (2017), doi:10.1038/nrdp.2017.13.
4. S. Ovallath, P. Deepa, The history of parkinsonism: descriptions in ancient Indian medical literature. *Movement disorders : official journal of the Movement Disorder Society*. **28**, 566–568 (2013), doi:10.1002/mds.25420.
5. J. Parkinson, An essay on the shaking palsy. 1817. *The Journal of neuropsychiatry and clinical neurosciences*. **14**, 223-36; discussion 222 (2002), doi:10.1176/jnp.14.2.223.
6. A. Reeve, E. Simcox, D. Turnbull, Ageing and Parkinson's disease: Why is advancing age the biggest risk factor?☆. *Ageing Research Reviews*. **14**, 19–30 (2014), doi:10.1016/j.arr.2014.01.004.
7. L. V. Kalia, A. E. Lang, Parkinson's disease. *The Lancet*. **386**, 896–912 (2015), doi:10.1016/S0140-6736(14)61393-3.
8. C. A. Haaxma *et al.*, Gender differences in Parkinson's disease. *Journal of neurology, neurosurgery, and psychiatry*. **78**, 819–824 (2007), doi:10.1136/jnnp.2006.103788.
9. R. B. Postuma *et al.*, Identifying prodromal Parkinson's disease: pre-motor disorders in Parkinson's disease. *Movement disorders : official journal of the Movement Disorder Society*. **27**, 617–626 (2012), doi:10.1002/mds.24996.
10. M. A. Hely, W. G. J. Reid, M. A. Adena, G. M. Halliday, J. G. L. Morris, The Sydney multicenter study of Parkinson's disease: the inevitability of dementia at 20 years. *Movement disorders : official journal of the Movement Disorder Society*. **23**, 837–844 (2008), doi:10.1002/mds.21956.
11. B. Pinter *et al.*, Mortality in Parkinson's disease: a 38-year follow-up study. *Movement disorders : official journal of the Movement Disorder Society*. **30**, 266–269 (2015), doi:10.1002/mds.26060.
12. H. Deng, P. Wang, J. Jankovic, The genetics of Parkinson disease. *Ageing Research Reviews*. **42**, 72–85 (2018), doi:10.1016/j.arr.2017.12.007.
13. J. A. Obeso *et al.*, Past, present, and future of Parkinson's disease: A special essay on the 200th Anniversary of the Shaking Palsy. *Movement disorders : official journal of the Movement Disorder Society*. **32**, 1264–1310 (2017), doi:10.1002/mds.27115.
14. M. A. Nalls *et al.*, Identification of novel risk loci, causal insights, and heritable risk for Parkinson's disease: a meta-analysis of genome-wide association studies. *The Lancet Neurology*. **18**, 1091–1102 (2019), doi:10.1016/S1474-4422(19)30320-5.
15. J. W. Langston, P. Ballard, J. W. Tetrud, I. Irwin, Chronic Parkinsonism in humans due to a product of meperidine-analog synthesis. *Science (New York, N.Y.)*. **219**, 979–980 (1983), doi:10.1126/science.6823561.
16. S. Wen, T. Aki, K. Unuma, K. Uemura, Chemically Induced Models of Parkinson's Disease: History and Perspectives for the Involvement of Ferroptosis. *Frontiers in cellular neuroscience*. **14**, 581191 (2020), doi:10.3389/fncel.2020.581191.
17. A. Priyadarshi, S. A. Khuder, E. A. Schaub, S. S. Priyadarshi, Environmental risk factors and Parkinson's disease: a metaanalysis. *Environmental research*. **86**, 122–127 (2001), doi:10.1006/enrs.2001.4264.
18. C. Marras, C. G. Canning, S. M. Goldman, Environment, lifestyle, and Parkinson's disease: Implications for prevention in the next decade. *Movement disorders : official journal of the Movement Disorder Society*. **34**, 801–811 (2019), doi:10.1002/mds.27720.
19. B. Ritz *et al.*, Pooled analysis of tobacco use and risk of Parkinson disease. *Archives of neurology*. **64**, 990–997 (2007), doi:10.1001/archneur.64.7.990.
20. N. Palacios *et al.*, Caffeine and risk of Parkinson's disease in a large cohort of men and women. *Movement disorders : official journal of the Movement Disorder Society*. **27**, 1276–1282 (2012), doi:10.1002/mds.25076.
21. E. L. Thacker *et al.*, Recreational physical activity and risk of Parkinson's disease. *Movement disorders : official journal of the Movement Disorder Society*. **23**, 69–74 (2008), doi:10.1002/mds.21772.

22. C. Klein, A. Westenberger, Genetics of Parkinson's disease. *Cold Spring Harbor Perspectives in Medicine*. **2**, a008888 (2012), doi:10.1101/cshperspect.a008888.
23. C. B. Lücking *et al.*, Association between early-onset Parkinson's disease and mutations in the parkin gene. *The New England journal of medicine*. **342**, 1560–1567 (2000), doi:10.1056/NEJM200005253422103.
24. L. Cook Shukla *et al.*, *GeneReviews®, Parkinson Disease Overview* (Seattle (WA), 1993).
25. N. Giguère, S. Burke Nanni, L.-E. Trudeau, On Cell Loss and Selective Vulnerability of Neuronal Populations in Parkinson's Disease. *Frontiers in neurology*. **9**, 455 (2018), doi:10.3389/fneur.2018.00455.
26. J. L. Lanciego, N. Luquin, J. A. Obeso, Functional neuroanatomy of the basal ganglia. *Cold Spring Harbor Perspectives in Medicine*. **2**, a009621 (2012), doi:10.1101/cshperspect.a009621.
27. M. M. McGregor, A. B. Nelson, Circuit Mechanisms of Parkinson's Disease. *Neuron*. **101**, 1042–1056 (2019), doi:10.1016/j.neuron.2019.03.004.
28. A. A. Kühn *et al.*, High-frequency stimulation of the subthalamic nucleus suppresses oscillatory beta activity in patients with Parkinson's disease in parallel with improvement in motor performance. *The Journal of neuroscience : the official journal of the Society for Neuroscience*. **28**, 6165–6173 (2008), doi:10.1523/JNEUROSCI.0282-08.2008.
29. W. S. Kim, K. Kågedal, G. M. Halliday, Alpha-synuclein biology in Lewy body diseases. *Alzheimer's research & therapy*. **6**, 73 (2014), doi:10.1186/s13195-014-0073-2.
30. H. Braak *et al.*, Staging of brain pathology related to sporadic Parkinson's disease. *Neurobiology of aging*. **24**, 197–211 (2003), doi:10.1016/s0197-4580(02)00065-9.
31. E. Angot *et al.*, Alpha-synuclein cell-to-cell transfer and seeding in grafted dopaminergic neurons in vivo. *PloS one*. **7**, e39465 (2012), doi:10.1371/journal.pone.0039465.
32. P. Brundin, R. Melki, R. Kopito, Prion-like transmission of protein aggregates in neurodegenerative diseases. *Nature reviews. Molecular cell biology*. **11**, 301–307 (2010), doi:10.1038/nrm2873.
33. K. Vekrellis, M. Xilouri, E. Emmanouilidou, H. J. Rideout, L. Stefanis, Pathological roles of α-synuclein in neurological disorders. *The Lancet Neurology*. **10**, 1015–1025 (2011), doi:10.1016/S1474-4422(11)70213-7.
34. L. V. Kalia *et al.*, Clinical correlations with Lewy body pathology in LRRK2-related Parkinson disease. *JAMA neurology*. **72**, 100–105 (2015), doi:10.1001/jamaneurol.2014.2704.
35. D. J. Surmeier, J. A. Obeso, G. M. Halliday, Selective neuronal vulnerability in Parkinson disease. *Nature reviews. Neuroscience*. **18**, 101–113 (2017), doi:10.1038/nrn.2016.178.
36. M. S. Moehle, A. B. West, M1 and M2 immune activation in Parkinson's Disease: Foe and ally? *Neuroscience*. **302**, 59–73 (2015), doi:10.1016/j.neuroscience.2014.11.018.
37. E. C. Hirsch, S. Hunot, Neuroinflammation in Parkinson's disease: a target for neuroprotection? *The Lancet Neurology*. **8**, 382–397 (2009), doi:10.1016/S1474-4422(09)70062-6.
38. R. M. Ransohoff, How neuroinflammation contributes to neurodegeneration. *Science (New York, N.Y.)*. **353**, 777–783 (2016), doi:10.1126/science.aag2590.
39. H.-M. Gao *et al.*, Neuroinflammation and oxidation/nitration of alpha-synuclein linked to dopaminergic neurodegeneration. *The Journal of neuroscience : the official journal of the Society for Neuroscience*. **28**, 7687–7698 (2008), doi:10.1523/JNEUROSCI.0143-07.2008.
40. S. George, P. Brundin, Immunotherapy in Parkinson's Disease: Micromanaging Alpha-Synuclein Aggregation. *Journal of Parkinson's disease*. **5**, 413–424 (2015), doi:10.3233/JPD-150630.
41. J. P. Bolam, E. K. Pissadaki, Living on the edge with too many mouths to feed: why dopamine neurons die. *Movement disorders : official journal of the Movement Disorder Society*. **27**, 1478–1483 (2012), doi:10.1002/mds.25135.
42. J. N. Guzman *et al.*, Oxidant stress evoked by pacemaking in dopaminergic neurons is attenuated by DJ-1. *Nature*. **468**, 696–700 (2010), doi:10.1038/nature09536.
43. J. Sanchez-Padilla *et al.*, Mitochondrial oxidant stress in locus coeruleus is regulated by activity and nitric oxide synthase. *Nature neuroscience*. **17**, 832–840 (2014), doi:10.1038/nn.3717.
44. P. Muñoz, S. Huenchuguala, I. Paris, J. Segura-Aguilar, Dopamine oxidation and autophagy. *Parkinson's disease*. **2012**, 920953 (2012), doi:10.1155/2012/920953.
45. B. G. Trist, D. J. Hare, K. L. Double, Oxidative stress in the aging substantia nigra and the etiology of Parkinson's disease. *Aging Cell*. **18**, e13031 (2019), doi:10.1111/acel.13031.

46. B. Bilgic, A. Pfefferbaum, T. Rohlfing, E. V. Sullivan, E. Adalsteinsson, MRI estimates of brain iron concentration in normal aging using quantitative susceptibility mapping. *NeuroImage*. **59**, 2625–2635 (2012), doi:10.1016/j.neuroimage.2011.08.077.
47. O. Scudamore, T. Ciossek, Increased Oxidative Stress Exacerbates α-Synuclein Aggregation In Vivo. *Journal of neuropathology and experimental neurology*. **77**, 443–453 (2018), doi:10.1093/jnen/nly024.
48. A. K. Reeve *et al.*, Aggregated α-synuclein and complex I deficiency: exploration of their relationship in differentiated neurons. *Cell death & disease*. **6**, e1820 (2015), doi:10.1038/cddis.2015.166.
49. T. B. Stoker, J. C. Greenland, Eds., *Parkinson's disease, Pathogenesis and clinical aspects* (Codon Publications, Brisbane, Australia, December 2018).
50. F. Blandini, M.-T. Armentero, Animal models of Parkinson's disease. *The FEBS journal*. **279**, 1156–1166 (2012), doi:10.1111/j.1742-4658.2012.08491.x.
51. W. J. Nicklas, S. K. Youngster, M. Kindt, R. E. Heikkila, IV. MPTP, MPP+ and mitochondrial function. *Life Sciences*. **40**, 721–729 (1987), doi:10.1016/0024-3205(87)90299-2.
52. A. Schober, Classic toxin-induced animal models of Parkinson's disease: 6-OHDA and MPTP. *Cell and tissue research*. **318**, 215–224 (2004), doi:10.1007/s00441-004-0938-y.
53. G. Palmer, D. J. Horgan, H. Tisdale, T. P. Singer, H. Beinert, Studies on the respiratory chain-linked reduced nicotinamide adenine dinucleotide dehydrogenase. XIV. Location of the sites of inhibition of rotenone, barbiturates, and piericidin by means of electron paramagnetic resonance spectroscopy. *The Journal of biological chemistry*. **243**, 844–847 (1968).
54. R. Betarbet *et al.*, Chronic systemic pesticide exposure reproduces features of Parkinson's disease. *Nature neuroscience*. **3**, 1301–1306 (2000), doi:10.1038/81834.
55. A. B. Manning-Bog *et al.*, The herbicide paraquat causes up-regulation and aggregation of alpha-synuclein in mice: paraquat and alpha-synuclein. *The Journal of biological chemistry*. **277**, 1641–1644 (2002), doi:10.1074/jbc.C100560200.
56. S. J. Chia, E.-K. Tan, Y.-X. Chao, Historical Perspective: Models of Parkinson's Disease. *International journal of molecular sciences*. **21** (2020), doi:10.3390/ijms21072464.
57. S. M. Fleming, P.-O. Fernagut, M.-F. Chesselet, Genetic Mouse Models of Parkinsonism: Strengths and Limitations. *NeuroRx*. **2**, 495–503 (2005).
58. E. Masliah *et al.*, Dopaminergic loss and inclusion body formation in alpha-synuclein mice: implications for neurodegenerative disorders. *Science (New York, N.Y.)*. **287**, 1265–1269 (2000), doi:10.1126/science.287.5456.1265.
59. M. Decressac, B. Mattsson, M. Lundblad, P. Weikop, A. Björklund, Progressive neurodegenerative and behavioural changes induced by AAV-mediated overexpression of α-synuclein in midbrain dopamine neurons. *Neurobiology of disease*. **45**, 939–953 (2012), doi:10.1016/j.nbd.2011.12.013.
60. K. C. Luk *et al.*, Pathological α-synuclein transmission initiates Parkinson-like neurodegeneration in nontransgenic mice. *Science (New York, N.Y.)*. **338**, 949–953 (2012), doi:10.1126/science.1227157.
61. D. Ramonet *et al.*, Dopaminergic Neuronal Loss, Reduced Neurite Complexity and Autophagic Abnormalities in Transgenic Mice Expressing G2019S Mutant LRRK2. *PloS one*. **6** (2011), doi:10.1371/journal.pone.0018568.
62. S. P. Javier Blesa, Parkinson’s disease: animal models and dopaminergic cell vulnerability. *Frontiers in Neuroanatomy*. **8** (2014), doi:10.3389/fnana.2014.00155.
63. J. A. Potashkin, S. R. Blume, N. K. Runkle, Limitations of animal models of Parkinson's disease. *Parkinson's disease*. **2011**, 658083 (2010), doi:10.4061/2011/658083.
64. R. P. Zinzen, E. E. M. Furlong, Divergence in cis-regulatory networks: taking the 'species' out of cross-species analysis. *Genome biology*. **9**, 240 (2008), doi:10.1186/gb-2008-9-11-240.
65. B. H. Falkenburger, T. Saridaki, E. Dinter, Cellular models for Parkinson's disease. *Journal of neurochemistry*. **139 Suppl 1**, 121–130 (2016), doi:10.1111/jnc.13618.
66. B. H. Falkenburger, J. B. Schulz, Limitations of cellular models in Parkinson's disease research. *Journal of neural transmission. Supplementum*, 261–268 (2006), doi:10.1007/978-3-211-45295-0_40.
67. K. Takahashi, S. Yamanaka, Induction of pluripotent stem cells from mouse embryonic and adult fibroblast cultures by defined factors. *Cell*. **126**, 663–676 (2006), doi:10.1016/j.cell.2006.07.024.
68. K. Simmnacher, J. Lanfer, T. Rizo, J. Kaindl, B. Winner, Modeling Cell-Cell Interactions in Parkinson's Disease Using Human Stem Cell-Based Models. *Frontiers in cellular neuroscience*. **13**, 571 (2019), doi:10.3389/fncel.2019.00571.

69. E. Arenas, M. Denham, J. C. Villaescusa, How to make a midbrain dopaminergic neuron. *Development (Cambridge, England)*. **142**, 1918–1936 (2015), doi:10.1242/dev.097394.
70. K. Takaoka, M. Yamamoto, H. Hamada, Origin of body axes in the mouse embryo. *Current opinion in genetics & development*. **17**, 344–350 (2007), doi:10.1016/j.gde.2007.06.001.
71. V. Broccoli, E. Boncinelli, W. Wurst, The caudal limit of Otx2 expression positions the isthmic organizer. *Nature*. **401**, 164–168 (1999), doi:10.1038/43670.
72. W. Wurst, L. Bally-Cuif, Neural plate patterning: upstream and downstream of the isthmic organizer. *Nature reviews. Neuroscience*. **2**, 99–108 (2001), doi:10.1038/35053516.
73. C. L. Chi, S. Martinez, W. Wurst, G. R. Martin, The isthmic organizer signal FGF8 is required for cell survival in the prospective midbrain and cerebellum. *Development (Cambridge, England)*. **130**, 2633–2644 (2003), doi:10.1242/dev.00487.
74. A. P. McMahon, A. Bradley, The Wnt-1 (int-1) proto-oncogene is required for development of a large region of the mouse brain. *Cell*. **62**, 1073–1085 (1990), doi:10.1016/0092-8674(90)90385-R.
75. E. Andersson *et al.*, Identification of intrinsic determinants of midbrain dopamine neurons. *Cell*. **124**, 393–405 (2006), doi:10.1016/j.cell.2005.10.037.
76. M. P. Smidt *et al.*, A second independent pathway for development of mesencephalic dopaminergic neurons requires Lmx1b. *Nature neuroscience*. **3**, 337–341 (2000), doi:10.1038/73902.
77. N. Prakash *et al.*, A Wnt1-regulated genetic network controls the identity and fate of midbrain-dopaminergic progenitors in vivo. *Development (Cambridge, England)*. **133**, 89–98 (2006), doi:10.1242/dev.02181.
78. R. H. Zetterström *et al.*, Dopamine neuron agenesis in Nurr1-deficient mice. *Science (New York, N.Y.)*. **276**, 248–250 (1997), doi:10.1126/science.276.5310.248.
79. W. Wurst, A. B. Auerbach, A. L. Joyner, Multiple developmental defects in Engrailed-1 mutant mice: an early mid-hindbrain deletion and patterning defects in forelimbs and sternum. *Development (Cambridge, England)*. **120**, 2065–2075 (1994), doi:10.1242/dev.120.7.2065.
80. L. Sonnier *et al.*, Progressive Loss of Dopaminergic Neurons in the Ventral Midbrain of Adult Mice Heterozygote for Engrailed1. *The Journal of Neuroscience*. **27**, 1063–1071 (2007), doi:10.1523/JNEUROSCI.4583-06.2007.
81. C. Jiang *et al.*, Age-dependent dopaminergic dysfunction in Nurr1 knockout mice. *Experimental neurology*. **191**, 154–162 (2005), doi:10.1016/j.expneurol.2004.08.035.
82. H. H. Simon, S. Thuret, L. Alberi, Midbrain dopaminergic neurons: control of their cell fate by the engrailed transcription factors. *Cell and tissue research*. **318**, 53–61 (2004), doi:10.1007/s00441-004-0973-8.
83. C. Logan *et al.*, Cloning and sequence comparison of the mouse, human, and chicken engrailed genes reveal potential functional domains and regulatory regions. *Dev. Genet.* **13**, 345–358 (1992), doi:10.1002/dvg.1020130505.
84. M. Hanks, W. Wurst, L. Anson-Cartwright, A. B. Auerbach, A. L. Joyner, Rescue of the En-1 mutant phenotype by replacement of En-1 with En-2. *Science (New York, N.Y.)*. **269**, 679–682 (1995), doi:10.1126/science.7624797.
85. C. R. Kissinger, B. Liu, E. Martin-Blanco, T. B. Kornberg, C. O. Pabo, Crystal structure of an engrailed homeodomain-DNA complex at 2.8 Å resolution: A framework for understanding homeodomain-DNA interactions. *Cell*. **63**, 579–590 (1990), doi:10.1016/0092-8674(90)90453-L.
86. J. B. Jaynes, P. H. O'Farrell, Activation and repression of transcription by homoeodomain-containing proteins that bind a common site. *Nature*. **336**, 744–749 (1988), doi:10.1038/336744a0.
87. K. Han, M. S. Levine, J. L. Manley, Synergistic activation and repression of transcription by Drosophila homeobox proteins. *Cell*. **56**, 573–583 (1989), doi:10.1016/0092-8674(89)90580-1.
88. Y. Ohkuma, M. Horikoshi, R. G. Roeder, C. Desplan, Engrailed, a homeodomain protein, can repress in vitro transcription by competition with the TATA box-binding protein transcription factor IID. *Proceedings of the National Academy of Sciences of the United States of America*. **87**, 2289–2293 (1990), doi:10.1073/pnas.87.6.2289.
89. E. N. Tolkunova, M. Fujioka, M. Kobayashi, D. Deka, J. B. Jaynes, Two distinct types of repression domain in engrailed: one interacts with the groucho corepressor and is preferentially active on integrated target genes. *Molecular and cellular biology*. **18**, 2804–2814 (1998), doi:10.1128/MCB.18.5.2804.
90. M. A. van Dijk, C. Murre, extradenticle Raises the DNA binding specificity of homeotic selector gene products. *Cell*. **78**, 617–624 (1994), doi:10.1016/0092-8674(94)90526-6.
91. M. Kobayashi *et al.*, Engrailed cooperates with extradenticle and homothorax to repress target genes in Drosophila. *Development (Cambridge, England)*. **130**, 741–751 (2003), doi:10.1242/dev.00289.

92. N. Serrano, F. Maschat, Molecular mechanism of polyhomeotic activation by Engrailed. *The EMBO journal*. **17**, 3704–3713 (1998), doi:10.1093/emboj/17.13.3704.
93. I. Brunet *et al.*, The transcription factor Engrailed-2 guides retinal axons. *Nature*. **438**, 94–98 (2005), doi:10.1038/nature04110.
94. D. Alvarez-Fischer *et al.*, Engrailed protects mouse midbrain dopaminergic neurons against mitochondrial complex I insults. *Nature neuroscience*. **14**, 1260–1266 (2011), doi:10.1038/nn.2916.
95. S. Nédélec *et al.*, Emx2 homeodomain transcription factor interacts with eukaryotic translation initiation factor 4E (eIF4E) in the axons of olfactory sensory neurons. *Proceedings of the National Academy of Sciences of the United States of America*. **101**, 10815–10820 (2004), doi:10.1073/pnas.0403824101.
96. A. Joliot *et al.*, Identification of a signal sequence necessary for the unconventional secretion of Engrailed homeoprotein. *Current Biology*. **8**, 856–863 (1998), doi:10.1016/S0960-9822(07)00346-6.
97. A. Joliot *et al.*, Association of Engrailed homeoproteins with vesicles presenting caveolae-like properties. *Development (Cambridge, England)*. **124**, 1865–1875 (1997), doi:10.1242/dev.124.10.1865.
98. A. Maizel, O. Bensaude, A. Prochiantz, A. Joliot, A short region of its homeodomain is necessary for engrailed nuclear export and secretion. *Development (Cambridge, England)*. **126**, 3183–3190 (1999), doi:10.1242/dev.126.14.3183.
99. D. Derossi, A. H. Joliot, G. Chassaing, A. Prochiantz, The third helix of the Antennapedia homeodomain translocates through biological membranes. *Journal of Biological Chemistry*. **269**, 10444–10450 (1994), doi:10.1016/S0021-9258(17)34080-2.
100. R. Morgan, Engrailed: complexity and economy of a multi-functional transcription factor. *FEBS letters*. **580**, 2531–2533 (2006), doi:10.1016/j.febslet.2006.04.053.
101. K. N. Alavian *et al.*, The lifelong maintenance of mesencephalic dopaminergic neurons by Nurr1 and engrailed. *Journal of biomedical science*. **21**, 27 (2014), doi:10.1186/1423-0127-21-27.
102. A. Liu, A. L. Joyner, EN and GBX2 play essential roles downstream of FGF8 in patterning the mouse mid/hindbrain region. *Development (Cambridge, England)*. **128**, 181–191 (2001), doi:10.1242/dev.128.2.181.
103. A. L. Joyner, K. Herrup, B. A. Auerbach, C. A. Davis, J. Rossant, Subtle cerebellar phenotype in mice homozygous for a targeted deletion of the En-2 homeobox. *Science (New York, N.Y.)*. **251**, 1239–1243 (1991), doi:10.1126/science.1672471.
104. A. P. McMahon, A. L. Joyner, A. Bradley, J. A. McMahon, The midbrain-hindbrain phenotype of Wnt-1−Wnt-1− mice results from stepwise deletion of engrailed-expressing cells by 9.5 days postcoitum. *Cell*. **69**, 581–595 (1992), doi:10.1016/0092-8674(92)90222-X.
105. H. H. Simon, H. Saueressig, W. Wurst, M. D. Goulding, D. D. O'Leary, Fate of midbrain dopaminergic neurons controlled by the engrailed genes. *J Neurosci*. **21**, 3126–3134 (2001).
106. L. Albéri, P. Sgadò, H. H. Simon, Engrailed genes are cell-autonomously required to prevent apoptosis in mesencephalic dopaminergic neurons. *Development (Cambridge, England)*. **131**, 3229–3236 (2004), doi:10.1242/dev.01128.
107. P. Sgadò *et al.*, Slow progressive degeneration of nigral dopaminergic neurons in postnatal Engrailed mutant mice. *Proceedings of the National Academy of Sciences of the United States of America*. **103**, 15242–15247 (2006), doi:10.1073/pnas.0602116103.
108. D. Haubenberger *et al.*, Association of transcription factor polymorphisms PITX3 and EN1 with Parkinson's disease. *Neurobiology of aging*. **32**, 302–307 (2011), doi:10.1016/j.neurobiolaging.2009.02.015.
109. U. Nordströma *et al.*, Progressive nigrostriatal terminal dysfunction and degeneration in the engrailed1 heterozygous mouse model of Parkinson's disease. *Neurobiology of disease*. **73**, 70–82 (2015), doi:10.1016/j.nbd.2014.09.012.
110. J. H. Kordower *et al.*, Disease duration and the integrity of the nigrostriatal system in Parkinson's disease. *Brain : a journal of neurology*. **136**, 2419–2431 (2013), doi:10.1093/brain/awt192.
111. K. N. Alavian, P. Sgadò, L. Alberi, S. Subramaniam, H. H. Simon, Elevated P75NTR expression causes death of engrailed-deficient midbrain dopaminergic neurons by Erk1/2 suppression. *Neural Development*. **4**, 11 (2009), doi:10.1186/1749-8104-4-11.
112. H. Rekaik *et al.*, Engrailed Homeoprotein Protects Mesencephalic Dopaminergic Neurons from Oxidative Stress. *Cell reports*. **13**, 242–250 (2015), doi:10.1016/j.celrep.2015.08.076.

113. C. Malagelada, Z. H. Jin, V. Jackson-Lewis, S. Przedborski, L. A. Greene, Rapamycin protects against neuron death in in vitro and in vivo models of Parkinson's disease. *J Neurosci*. **30**, 1166–1175 (2010), doi:10.1523/JNEUROSCI.3944-09.2010.
114. C. Vives-Bauza, S. Przedborski, Mitophagy: the latest problem for Parkinson's disease. *Trends in molecular medicine*. **17**, 158–165 (2011), doi:10.1016/j.molmed.2010.11.002.
115. D. Chatterjee *et al.*, Loss of One Engrailed1 Allele Enhances Induced α-Synucleinopathy. *Journal of Parkinson's disease*. **9**, 315–326 (2019), doi:10.3233/JPD-191590.
116. W. Wurst, N. Prakash, Wnt1-regulated genetic networks in midbrain dopaminergic neuron development. *Journal of molecular cell biology*. **6**, 34–41 (2014), doi:10.1093/jmcb/mjt046.
117. B. Marchetti, Wnt/β-Catenin Signaling Pathway Governs a Full Program for Dopaminergic Neuron Survival, Neurorescue and Regeneration in the MPTP Mouse Model of Parkinson's Disease. *International journal of molecular sciences*. **19** (2018), doi:10.3390/ijms19123743.
118. N. C. Inestrosa, E. Arenas, Emerging roles of Wnts in the adult nervous system. *Nature reviews. Neuroscience*. **11**, 77–86 (2010), doi:10.1038/nrn2755.
119. R. Nusse, H. Clevers, Wnt/β-Catenin Signaling, Disease, and Emerging Therapeutic Modalities. *Cell*. **169**, 985–999 (2017), doi:10.1016/j.cell.2017.05.016.
120. E. Arenas, Wnt signaling in midbrain dopaminergic neuron development and regenerative medicine for Parkinson's disease. *Journal of molecular cell biology*. **6**, 42–53 (2014), doi:10.1093/jmcb/mju001.
121. F. L'Episcopo *et al.*, Reactive astrocytes and Wnt/β-catenin signaling link nigrostriatal injury to repair in 1-methyl-4-phenyl-1,2,3,6-tetrahydropyridine model of Parkinson's disease. *Neurobiology of disease*. **41**, 508–527 (2011), doi:10.1016/j.nbd.2010.10.023.
122. F. L'episcopo *et al.*, A Wnt1 regulated Frizzled-1/β-Catenin signaling pathway as a candidate regulatory circuit controlling mesencephalic dopaminergic neuron-astrocyte crosstalk: Therapeutical relevance for neuron survival and neuroprotection. *Molecular neurodegeneration*. **6**, 49 (2011), doi:10.1186/1750-1326-6-49.
123. F. L'episcopo *et al.*, Wnt/β-catenin signaling is required to rescue midbrain dopaminergic progenitors and promote neurorepair in ageing mouse model of Parkinson's disease. *Stem cells (Dayton, Ohio)*. **32**, 2147–2163 (2014), doi:10.1002/stem.1708.
124. J. Zhang *et al.*, A WNT1-regulated developmental gene cascade prevents dopaminergic neurodegeneration in adult En1(+/-) mice. *Neurobiology of disease*. **82**, 32–45 (2015), doi:10.1016/j.nbd.2015.05.015.
125. F. L'episcopo *et al.*, Microglia Polarization, Gene-Environment Interactions and Wnt/β-Catenin Signaling: Emerging Roles of Glia-Neuron and Glia-Stem/Neuroprogenitor Crosstalk for Dopaminergic Neurorestoration in Aged Parkinsonian Brain. *Frontiers in aging neuroscience*. **10**, 12 (2018), doi:10.3389/fnagi.2018.00012.
126. C. A. Davis, A. L. Joyner, Expression patterns of the homeo box-containing genes En-1 and En-2 and the proto-oncogene int-1 diverge during mouse development. *Genes & development*. **2**, 1736–1744 (1988), doi:10.1101/gad.2.12b.1736.
127. P. S. Danielian, A. P. McMahon, Engrailed-1 as a target of the Wnt-1 signalling pathway in vertebrate midbrain development. *Nature*. **383**, 332–334 (1996), doi:10.1038/383332a0.
128. L. McGrew, K.-I. Takemaru, R. Bates, R. T. Moon, Direct regulation of the Xenopus engrailed-2 promoter by the Wnt signaling pathway, and a molecular screen for Wnt-responsive genes, confirm a role for Wnt signaling during neural patterning in Xenopus. *Mechanisms of development*. **87**, 21–32 (1999), doi:10.1016/s0925-4773(99)00136-7.
129. J. Y. Kim *et al.*, Wnt signal activation induces midbrain specification through direct binding of the beta-catenin/TCF4 complex to the EN1 promoter in human pluripotent stem cells. *Exp Mol Med*. **50**, 1–13 (2018), doi:10.1038/s12276-018-0044-y.
130. W. M. Kouwenhoven, J. V. Veenvliet, J. A. van Hooft, L. P. van der Heide, M. P. Smidt, Engrailed 1 shapes the dopaminergic and serotonergic landscape through proper isthmic organizer maintenance and function. *Biology open*. **5**, 279–288 (2016), doi:10.1242/bio.015032.
131. I. Araki, H. Nakamura, Engrailed defines the position of dorsal di-mesencephalic boundary by repressing diencephalic fate. *Development (Cambridge, England)*. **126**, 5127–5135 (1999), doi:10.1242/dev.126.22.5127.
132. J. M. Berg, J. L. Tymoczko, L. Stryer, *Stryer Biochemie* (Springer Berlin Heidelberg; Imprint; Springer Spektrum, Berlin, Heidelberg, ed. 7, 2013).
133. S. Camandola, M. P. Mattson, Brain metabolism in health, aging, and neurodegeneration. *The EMBO journal*. **36**, 1474–1492 (2017), doi:10.15252/embj.201695810.

134. G. Löffler, P. C. Heinrich, P. E. Petrides, Eds., *Biochemie und Pathobiochemie* (Springer Medizin Verlag Heidelberg, Berlin, Heidelberg, ed. 8, 2007).
135. E. M. F. Brekke, A. B. Walls, A. Schousboe, H. S. Waagepetersen, U. Sonnewald, Quantitative importance of the pentose phosphate pathway determined by incorporation of 13C from 2-13C- and 3-13Cglucose into TCA cycle intermediates and neurotransmitter amino acids in functionally intact neurons. *Journal of Cerebral Blood Flow & Metabolism*. **32**, 1788–1799 (2012), doi:10.1038/jcbfm.2012.85.
136. P. Rodriguez-Rodriguez, E. Fernandez, J. P. Bolaños, Underestimation of the pentose-phosphate pathway in intact primary neurons as revealed by metabolic flux analysis. *Journal of Cerebral Blood Flow & Metabolism*. **33**, 1843–1845 (2013), doi:10.1038/jcbfm.2013.168.
137. J. P. Bolaños, A. Almeida, The pentose-phosphate pathway in neuronal survival against nitrosative stress. *IUBMB life*. **62**, 14–18 (2010), doi:10.1002/iub.280.
138. C. Perier, M. Vila, Mitochondrial biology and Parkinson's disease. *Cold Spring Harbor Perspectives in Medicine*. **2**, a009332 (2012), doi:10.1101/cshperspect.a009332.
139. D. Safiulina, A. Kaasik, Energetic and dynamic: how mitochondria meet neuronal energy demands. *PLoS biology*. **11**, e1001755 (2013), doi:10.1371/journal.pbio.1001755.
140. B. Westermann, Bioenergetic role of mitochondrial fusion and fission. *Biochimica et biophysica acta*. **1817**, 1833–1838 (2012), doi:10.1016/j.bbabio.2012.02.033.
141. Z.-H. Sheng, Q. Cai, Mitochondrial transport in neurons: impact on synaptic homeostasis and neurodegeneration. *Nature reviews. Neuroscience*. **13**, 77–93 (2012), doi:10.1038/nrn3156.
142. L. K. Sharma, J. Lu, Y. Bai, Mitochondrial respiratory complex I: structure, function and implication in human diseases. *Current medicinal chemistry*. **16**, 1266–1277 (2009), doi:10.2174/092986709787846578.
143. B. Alberts *et al.*, Eds., *Molecular Biology of the Cell. 4th edition* (Garland Science, 2002).
144. M. P. Murphy, How mitochondria produce reactive oxygen species. *The Biochemical journal*. **417**, 1–13 (2009), doi:10.1042/BJ20081386.
145. A. Singh, R. Kukreti, L. Saso, S. Kukreti, Oxidative Stress: A Key Modulator in Neurodegenerative Diseases. *Molecules*. **24** (2019), doi:10.3390/molecules24081583.
146. B. Halliwell, Reactive species and antioxidants. Redox biology is a fundamental theme of aerobic life. *Plant physiology*. **141**, 312–322 (2006), doi:10.1104/pp.106.077073.
147. C. A. Juan, J. M. La Pérez de Lastra, F. J. Plou, E. Pérez-Lebeña, The Chemistry of Reactive Oxygen Species (ROS) Revisited: Outlining Their Role in Biological Macromolecules (DNA, Lipids and Proteins) and Induced Pathologies. *International journal of molecular sciences*. **22** (2021), doi:10.3390/ijms22094642.
148. A. Schapira *et al.*, MITOCHONDRIAL COMPLEX I DEFICIENCY IN PARKINSON'S DISEASE. *The Lancet*. **333**, 1269 (1989), doi:10.1016/S0140-6736(89)92366-0.
149. W. D. Parker, J. K. Parks, R. H. Swerdlow, Complex I deficiency in Parkinson's disease frontal cortex. *Brain research*. **1189**, 215–218 (2008), doi:10.1016/j.brainres.2007.10.061.
150. A. Bender *et al.*, High levels of mitochondrial DNA deletions in substantia nigra neurons in aging and Parkinson disease. *Nature genetics*. **38**, 515–517 (2006), doi:10.1038/ng1769.
151. A. B. Salmon, A. Richardson, V. I. Pérez, Update on the oxidative stress theory of aging: does oxidative stress play a role in aging or healthy aging? *Free radical biology & medicine*. **48**, 642–655 (2010), doi:10.1016/j.freeradbiomed.2009.12.015.
152. J.-S. Park, R. L. Davis, C. M. Sue, Mitochondrial Dysfunction in Parkinson's Disease: New Mechanistic Insights and Therapeutic Perspectives. *Current Neurology and Neuroscience Reports*. **18**, 21 (2018), doi:10.1007/s11910-018-0829-3.
153. T. Amo, S. Saiki, T. Sawayama, S. Sato, N. Hattori, Detailed analysis of mitochondrial respiratory chain defects caused by loss of PINK1. *Neuroscience letters*. **580**, 37–40 (2014), doi:10.1016/j.neulet.2014.07.045.
154. J. Fuchs *et al.*, The transcription factor PITX3 is associated with sporadic Parkinson's disease. *Neurobiology of aging*. **30**, 731–738 (2009), doi:10.1016/j.neurobiolaging.2007.08.014.
155. H. Rekaik, F.-X. Blaudin de Thé, A. Prochiantz, J. Fuchs, R. L. Joshi, Dissecting the role of Engrailed in adult dopaminergic neurons--Insights into Parkinson disease pathogenesis. *FEBS letters*. **589**, 3786–3794 (2015), doi:10.1016/j.febslet.2015.10.002.
156. M. D. Wilson *et al.*, Species-specific transcription in mice carrying human chromosome 21. *Science (New York, N.Y.)*. **322**, 434–438 (2008), doi:10.1126/science.1160930.

157. J. A. Doudna, E. Charpentier, Genome editing. The new frontier of genome engineering with CRISPR-Cas9. *Science (New York, N.Y.)*. **346**, 1258096 (2014), doi:10.1126/science.1258096.
158. B. M. Stinson, J. J. Loparo, Repair of DNA Double-Strand Breaks by the Nonhomologous End Joining Pathway. *Annual review of biochemistry*. **90**, 137–164 (2021), doi:10.1146/annurev-biochem-080320-110356.
159. E. Nagy, L. E. Maquat, A rule for termination-codon position within intron-containing genes: when nonsense affects RNA abundance. *Trends in Biochemical Sciences*. **23**, 198–199 (1998), doi:10.1016/S0968-0004(98)01208-0.
160. S. Acosta, L. Fiore, I. A. Carota, G. Oliver, Use of two gRNAs for CRISPR/Cas9 improves bi-allelic homologous recombination efficiency in mouse embryonic stem cells. *Genesis (New York, N.Y. : 2000)*. **56**, e23212 (2018), doi:10.1002/dvg.23212.
161. D. Simkin *et al.*, Homozygous might be hemizygous: CRISPR/Cas9 editing in iPSCs results in detrimental on-target defects that escape standard quality controls. *Stem Cell Reports*. **17**, 993–1008 (2022), doi:10.1016/j.stemcr.2022.02.008.
162. G. Alanis-Lobato *et al.*, Frequent loss of heterozygosity in CRISPR-Cas9-edited early human embryos. *Proceedings of the National Academy of Sciences of the United States of America*. **118** (2021), doi:10.1073/pnas.2004832117.
163. V. Volpato, C. Webber, Addressing variability in iPSC-derived models of human disease: guidelines to promote reproducibility. *Disease models & mechanisms*. **13** (2020), doi:10.1242/dmm.042317.
164. I. Höijer *et al.*, CRISPR-Cas9 induces large structural variants at on-target and off-target sites in vivo that segregate across generations. *Nature communications*. **13**, 627 (2022), doi:10.1038/s41467-022-28244-5.
165. M. D'Antonio *et al.*, Insights into the Mutational Burden of Human Induced Pluripotent Stem Cells from an Integrative Multi-Omics Approach. *Cell reports*. **24**, 883–894 (2018), doi:10.1016/j.celrep.2018.06.091.
166. P.-J. Viailly *et al.*, Improving high-resolution copy number variation analysis from next generation sequencing using unique molecular identifiers. *BMC Bioinformatics*. **22**, 1–15 (2021), doi:10.1186/s12859-021-04060-4.
167. *HumanCytoSNP-12 BeadChip | Scalable, high-resolution cytogenetic array* (08/24/2022 09:26:11) (available at https://emea.illumina.com/products/by-type/clinical-research-products/human-cytosnp-12.html).
168. H. T. Nguyen *et al.*, Gain of 20q11.21 in human embryonic stem cells improves cell survival by increased expression of Bcl-xL. *Molecular human reproduction*. **20**, 168–177 (2014), doi:10.1093/molehr/gat077.
169. P. Reinhardt *et al.*, Derivation and expansion using only small molecules of human neural progenitors for neurodegenerative disease modeling. *PloS one*. **8**, e59252 (2013), doi:10.1371/journal.pone.0059252.
170. M. Venere *et al.*, Sox1 marks an activated neural stem/progenitor cell in the hippocampus. *Development (Cambridge, England)*. **139**, 3938–3949 (2012), doi:10.1242/dev.081133.
171. A. A. Di Nardo *et al.*, Dendritic localization and activity-dependent translation of Engrailed1 transcription factor. *Molecular and cellular neurosciences*. **35**, 230–236 (2007), doi:10.1016/j.mcn.2007.02.015.
172. A. Pézier, S. H. Jezzini, B. Marie, J. M. Blagburn, Engrailed alters the specificity of synaptic connections of Drosophila auditory neurons with the giant fiber. *J Neurosci*. **34**, 11691–11704 (2014), doi:10.1523/JNEUROSCI.1939-14.2014.
173. B. Marie, J. P. Bacon, J. M. Blagburn, Double-stranded RNA interference shows that Engrailed controls the synaptic specificity of identified sensory neurons. *Current Biology*. **10**, 289–292 (2000), doi:10.1016/S0960-9822(00)00361-4.
174. H. Saueressig, J. Burrill, M. Goulding, Engrailed-1 and netrin-1 regulate axon pathfinding by association interneurons that project to motor neurons. *Development (Cambridge, England)*. **126**, 4201–4212 (1999), doi:10.1242/dev.126.19.4201.
175. J. C. D. Bairzin, M. Emmons-Bell, I. K. Hariharan, The Hippo pathway coactivator Yorkie can reprogram cell fates and create compartment-boundary-like interactions at clone margins. *Science advances*. **6** (2020), doi:10.1126/sciadv.abe8159.
176. T. Namba, J. Nardelli, P. Gressens, W. B. Huttner, Metabolic Regulation of Neocortical Expansion in Development and Evolution. *Neuron*. **109**, 408–419 (2021), doi:10.1016/j.neuron.2020.11.014.
177. L. J. Martin *et al.*, Parkinson's disease alpha-synuclein transgenic mice develop neuronal mitochondrial degeneration and cell death. *The Journal of neuroscience : the official journal of the Society for Neuroscience*. **26**, 41–50 (2006), doi:10.1523/JNEUROSCI.4308-05.2006.

178. J. J. Palacino *et al.*, Mitochondrial dysfunction and oxidative damage in parkin-deficient mice. *The Journal of biological chemistry*. **279**, 18614–18622 (2004), doi:10.1074/jbc.M401135200.
179. S. R. Subramaniam, M.-F. Chesselet, Mitochondrial dysfunction and oxidative stress in Parkinson's disease. *Progress in neurobiology*. **0**, 17–32 (2013), doi:10.1016/j.pneurobio.2013.04.004.
180. J. Kim, I. Tchernyshyov, G. L. Semenza, C. V. Dang, HIF-1-mediated expression of pyruvate dehydrogenase kinase: a metabolic switch required for cellular adaptation to hypoxia. *Cell metabolism*. **3**, 177–185 (2006), doi:10.1016/j.cmet.2006.02.002.
181. Z. Steinhart, S. Angers, Wnt signaling in development and tissue homeostasis. *Development (Cambridge, England)*. **145** (2018), doi:10.1242/dev.146589.
182. C. Christodoulides, C. Lagathu, J. K. Sethi, A. Vidal-Puig, Adipogenesis and WNT signalling. *Trends in endocrinology and metabolism: TEM*. **20**, 16–24 (2009), doi:10.1016/j.tem.2008.09.002.
183. E. P. M. Timmermans-Sprang, A. Gracanin, J. A. Mol, High basal Wnt signaling is further induced by PI3K/mTor inhibition but sensitive to cSRC inhibition in mammary carcinoma cell lines with HER2/3 overexpression. *BMC cancer*. **15**, 545 (2015), doi:10.1186/s12885-015-1544-y.
184. C. A. Schmidt, K. H. Fisher-Wellman, P. D. Neufer, From OCR and ECAR to energy: Perspectives on the design and interpretation of bioenergetics studies. *The Journal of biological chemistry*. **297**, 101140 (2021), doi:10.1016/j.jbc.2021.101140.
185. J. K. Sethi, A. Vidal-Puig, Wnt signalling and the control of cellular metabolism. *The Biochemical journal*. **427**, 1–17 (2010), doi:10.1042/BJ20091866.
186. F. Abou Azar, G. E. Lim, Metabolic Contributions of Wnt Signaling: More Than Controlling Flight. *Frontiers in cell and developmental biology*. **9**, 709823 (2021), doi:10.3389/fcell.2021.709823.
187. P. Cisternas *et al.*, Wnt-induced activation of glucose metabolism mediates the in vivo neuroprotective roles of Wnt signaling in Alzheimer disease. *Journal of neurochemistry*. **149**, 54–72 (2019), doi:10.1111/jnc.14608.
188. Y. Lecarpentier, O. Schussler, J.-L. Hébert, A. Vallée, Multiple Targets of the Canonical WNT/β-Catenin Signaling in Cancers. *Frontiers in Oncology*. **9** (2019), doi:10.3389/fonc.2019.01248.
189. B. Xiao, X. Deng, W. Zhou, E.-K. Tan, Flow Cytometry-Based Assessment of Mitophagy Using MitoTracker. *Frontiers in cellular neuroscience*. **10**, 76 (2016), doi:10.3389/fncel.2016.00076.
190. A. S. Divakaruni, A. Paradyse, D. A. Ferrick, A. N. Murphy, M. Jastroch, Analysis and interpretation of microplate-based oxygen consumption and pH data. *Methods in enzymology*. **547**, 309–354 (2014), doi:10.1016/B978-0-12-801415-8.00016-3.
191. Y. Ni *et al.*, Mutations in NDUFS1 Cause Metabolic Reprogramming and Disruption of the Electron Transfer. *Cells*. **8** (2019), doi:10.3390/cells8101149.
192. S. Lykke-Andersen, T. H. Jensen, Nonsense-mediated mRNA decay: an intricate machinery that shapes transcriptomes. *Nature reviews. Molecular cell biology*. **16**, 665–677 (2015), doi:10.1038/nrm4063.
193. T. Trcek, H. Sato, R. H. Singer, L. E. Maquat, Temporal and spatial characterization of nonsense-mediated mRNA decay. *Genes & development*. **27**, 541–551 (2013), doi:10.1101/gad.209635.112.
194. M. Yoshihara, Y. Hayashizaki, Y. Murakawa, Genomic Instability of iPSCs: Challenges Towards Their Clinical Applications. *Stem Cell Rev and Rep*. **13**, 7–16 (2017), doi:10.1007/s12015-016-9680-6.
195. F. T. Merkle *et al.*, Human pluripotent stem cells recurrently acquire and expand dominant negative P53 mutations. *Nature*. **545**, 229–233 (2017), doi:10.1038/nature22312.
196. V. Volpato *et al.*, Reproducibility of Molecular Phenotypes after Long-Term Differentiation to Human iPSC-Derived Neurons: A Multi-Site Omics Study. *Stem Cell Reports*. **11**, 897–911 (2018), doi:10.1016/j.stemcr.2018.08.013.
197. C. Blauwendraat *et al.*, Parkinson's disease age at onset genome-wide association study: Defining heritability, genetic loci, and α-synuclein mechanisms. *Movement disorders : official journal of the Movement Disorder Society*. **34**, 866–875 (2019), doi:10.1002/mds.27659.
198. D. Toulorge, A. H. V. Schapira, R. Hajj, Molecular changes in the postmortem parkinsonian brain. *Journal of neurochemistry*. **139 Suppl 1**, 27–58 (2016), doi:10.1111/jnc.13696.
199. R. A. Deckelbaum *et al.*, Regulation of cranial morphogenesis and cell fate at the neural crest-mesoderm boundary by engrailed 1. *Development (Cambridge, England)*. **139**, 1346–1358 (2012), doi:10.1242/dev.076729.
200. A. Wizenmann *et al.*, Extracellular Engrailed participates in the topographic guidance of retinal axons in vivo. *Neuron*. **64**, 355–366 (2009), doi:10.1016/j.neuron.2009.09.018.

201. J. Fuchs *et al.,* Engrailed signaling in axon guidance and neuron survival. *The European journal of neuroscience*. **35**, 1837–1845 (2012), doi:10.1111/j.1460-9568.2012.08139.x.
202. S. Mascharak *et al.,* Abstract 189. *Plastic and Reconstructive Surgery - Global Open*. **8**, 128–129 (2020), doi:10.1097/01.GOX.0000667812.57122.ac.
203. P. Tagliaferro *et al.,* An early axonopathy in a hLRRK2(R1441G) transgenic model of Parkinson disease. *Neurobiology of disease*. **82**, 359–371 (2015), doi:10.1016/j.nbd.2015.07.009.
204. C. Y. Chung, J. B. Koprich, H. Siddiqi, O. Isacson, Dynamic changes in presynaptic and axonal transport proteins combined with striatal neuroinflammation precede dopaminergic neuronal loss in a rat model of AAV alpha-synucleinopathy. *J Neurosci*. **29**, 3365–3373 (2009), doi:10.1523/JNEUROSCI.5427-08.2009.
205. W. Meissner *et al.,* Time-Course of Nigrostriatal Degeneration in a Progressive MPTP-Lesioned Macaque Model of Parkinson's Disease. *Molecular neurobiology*. **28**, 209–218 (2003), doi:10.1385/MN:28:3:209.
206. X. Lu, J. S. Kim-Han, S. Harmon, S. E. Sakiyama-Elbert, K. L. O'Malley, The Parkinsonian mimetic, 6-OHDA, impairs axonal transport in dopaminergic axons. *Molecular neurodegeneration*. **9**, 17 (2014), doi:10.1186/1750-1326-9-17.
207. A. D. Levy, M. H. Omar, A. J. Koleske, Extracellular matrix control of dendritic spine and synapse structure and plasticity in adulthood. *Frontiers in Neuroanatomy*. **8**, 116 (2014), doi:10.3389/fnana.2014.00116.
208. R. Raghunathan, J. D. Hogan, A. Labadorf, R. H. Myers, J. Zaia, A glycomics and proteomics study of aging and Parkinson's disease in human brain. *Sci Rep*. **10**, 12804 (2020), doi:10.1038/s41598-020-69480-3.
209. A. Freitas *et al.,* Characterization of the Striatal Extracellular Matrix in a Mouse Model of Parkinson's Disease. *Antioxidants*. **10** (2021), doi:10.3390/antiox10071095.
210. S. Lehri-Boufala *et al.,* New roles of glycosaminoglycans in α-synuclein aggregation in a cellular model of Parkinson disease. *PloS one*. **10**, e0116641 (2015), doi:10.1371/journal.pone.0116641.
211. E. Ihse *et al.,* Cellular internalization of alpha-synuclein aggregates by cell surface heparan sulfate depends on aggregate conformation and cell type. *Sci Rep*. **7**, 9008 (2017), doi:10.1038/s41598-017-08720-5.
212. S. D. Ryan *et al.,* Isogenic human iPSC Parkinson's model shows nitrosative stress-induced dysfunction in MEF2-PGC1α transcription. *Cell*. **155**, 1351–1364 (2013), doi:10.1016/j.cell.2013.11.009.
213. M. Trombetta-Lima, A. M. Sabogal-Guáqueta, A. M. Dolga, Mitochondrial dysfunction in neurodegenerative diseases: A focus on iPSC-derived neuronal models. *Cell calcium*. **94**, 102362 (2021), doi:10.1016/j.ceca.2021.102362.
214. G.-H. Liu *et al.,* Progressive degeneration of human neural stem cells caused by pathogenic LRRK2. *Nature*. **491**, 603–607 (2012), doi:10.1038/nature11557.
215. P. Reinhardt *et al.,* Genetic correction of a LRRK2 mutation in human iPSCs links parkinsonian neurodegeneration to ERK-dependent changes in gene expression. *Cell stem cell*. **12**, 354–367 (2013), doi:10.1016/j.stem.2013.01.008.
216. L. F. Burbulla *et al.,* Dopamine oxidation mediates mitochondrial and lysosomal dysfunction in Parkinson's disease. *Science (New York, N.Y.)*. **357**, 1255–1261 (2017), doi:10.1126/science.aam9080.
217. B. Byers *et al.,* SNCA triplication Parkinson's patient's iPSC-derived DA neurons accumulate α-synuclein and are susceptible to oxidative stress. *PloS one*. **6**, e26159 (2011), doi:10.1371/journal.pone.0026159.
218. G. Kouroupi *et al.,* Defective synaptic connectivity and axonal neuropathology in a human iPSC-based model of familial Parkinson's disease. *Proceedings of the National Academy of Sciences of the United States of America*. **114**, E3679-E3688 (2017), doi:10.1073/pnas.1617259114.
219. J. Krauskopf *et al.,* Transcriptomics analysis of human iPSC-derived dopaminergic neurons reveals a novel model for sporadic Parkinson's disease. *Molecular psychiatry* (2022), doi:10.1038/s41380-022-01663-y.
220. S. Schmidt *et al.,* Primary cilia and SHH signaling impairments in human and mouse models of Parkinson's disease. *Nat Commun*. **13**, 1–25 (2022), doi:10.1038/s41467-022-32229-9.
221. E. M. Hartfield *et al.,* Physiological characterisation of human iPS-derived dopaminergic neurons. *PloS one*. **9**, e87388 (2014), doi:10.1371/journal.pone.0087388.
222. L. M. Heger, R. M. Wise, J. T. Hees, A. B. Harbauer, L. F. Burbulla, Mitochondrial Phenotypes in Parkinson's Diseases-A Focus on Human iPSC-Derived Dopaminergic Neurons. *Cells*. **10** (2021), doi:10.3390/cells10123436.
223. J. Mertens, D. Reid, S. Lau, Y. Kim, F. H. Gage, Aging in a Dish: iPSC-Derived and Directly Induced Neurons for Studying Brain Aging and Age-Related Neurodegenerative Diseases. *Annual review of genetics*. **52**, 271–293 (2018), doi:10.1146/annurev-genet-120417-031534.

224. J. L. Eberling, B. C. Richardson, B. R. Reed, N. Wolfe, W. J. Jagust, Cortical glucose metabolism in Parkinson's disease without dementia. *Neurobiology of aging*. **15**, 329–335 (1994), doi:10.1016/0197-4580(94)90028-0.
225. E. Palombo *et al.*, Local cerebral glucose utilization in monkeys with hemiparkinsonism induced by intracarotid infusion of the neurotoxin MPTP. *J Neurosci*. **10**, 860–869 (1990), doi:10.1523/JNEUROSCI.10-03-00860.1990.
226. A. Anandhan *et al.*, Metabolic Dysfunction in Parkinson's Disease: Bioenergetics, Redox Homeostasis and Central Carbon Metabolism. *Brain research bulletin*. **133**, 12–30 (2017), doi:10.1016/j.brainresbull.2017.03.009.
227. X. Zheng *et al.*, Metabolic reprogramming during neuronal differentiation from aerobic glycolysis to neuronal oxidative phosphorylation. *eLife*. **5** (2016), doi:10.7554/eLife.13374.
228. C. Maffezzini, J. Calvo-Garrido, A. Wredenberg, C. Freyer, Metabolic regulation of neurodifferentiation in the adult brain. *Cellular and Molecular Life Sciences*. **77**, 2483–2496 (2020), doi:10.1007/s00018-019-03430-9.
229. A. Flierl *et al.*, Higher vulnerability and stress sensitivity of neuronal precursor cells carrying an alpha-synuclein gene triplication. *PloS one*. **9**, e112413 (2014), doi:10.1371/journal.pone.0112413.
230. V. Vasquez *et al.*, Chromatin-Bound Oxidized α-Synuclein Causes Strand Breaks in Neuronal Genomes in in vitro Models of Parkinson's Disease. *Journal of Alzheimer's disease : JAD*. **60**, S133-S150 (2017), doi:10.3233/JAD-170342.
231. J. Walter *et al.*, Neural Stem Cells of Parkinson's Disease Patients Exhibit Aberrant Mitochondrial Morphology and Functionality. *Stem Cell Reports*. **12**, 878–889 (2019), doi:10.1016/j.stemcr.2019.03.004.
232. J. D. Miller *et al.*, Human iPSC-based modeling of late-onset disease via progerin-induced aging. *Cell stem cell*. **13**, 691–705 (2013), doi:10.1016/j.stem.2013.11.006.
233. S. B. Arredondo, D. Valenzuela-Bezanilla, M. D. Mardones, L. Varela-Nallar, Role of Wnt Signaling in Adult Hippocampal Neurogenesis in Health and Disease. *Frontiers in cell and developmental biology*. **8**, 860 (2020), doi:10.3389/fcell.2020.00860.
234. S. Avazzadeh, J. M. Baena, C. Keighron, Y. Feller-Sanchez, L. R. Quinlan, Modelling Parkinson's Disease: iPSCs towards Better Understanding of Human Pathology. *Brain Sciences*. **11** (2021), doi:10.3390/brainsci11030373.
235. M. D. Brand, D. G. Nicholls, Assessing mitochondrial dysfunction in cells. *Biochemical Journal*. **435**, 297–312 (2011), doi:10.1042/BJ20110162.
236. N. Funk *et al.*, The Parkinson's disease-linked Leucine-rich repeat kinase 2 (LRRK2) is required for insulin-stimulated translocation of GLUT4. *Sci Rep*. **9**, 4515 (2019), doi:10.1038/s41598-019-40808-y.
237. M. E. Watts, R. Pocock, C. Claudianos, Brain Energy and Oxygen Metabolism: Emerging Role in Normal Function and Disease. *Frontiers in molecular neuroscience*. **11**, 216 (2018), doi:10.3389/fnmol.2018.00216.
238. A. Erdem *et al.*, The Glycolytic Gatekeeper PDK1 defines different metabolic states between genetically distinct subtypes of human acute myeloid leukemia. *Nat Commun*. **13**, 1105 (2022), doi:10.1038/s41467-022-28737-3.
239. F. Peng *et al.*, Glycolysis gatekeeper PDK1 reprograms breast cancer stem cells under hypoxia. *Oncogene*. **37**, 1062–1074 (2018), doi:10.1038/onc.2017.368.
240. X. Deng *et al.*, Pyruvate dehydrogenase kinase 1 interferes with glucose metabolism reprogramming and mitochondrial quality control to aggravate stress damage in cancer. *Journal of Cancer*. **11**, 962–973 (2020), doi:10.7150/jca.34330.
241. S. M. Bell *et al.*, Peripheral Glycolysis in Neurodegenerative Diseases. *International journal of molecular sciences*. **21** (2020), doi:10.3390/ijms21238924.
242. S. J. Ham *et al.*, Loss of UCHL1 rescues the defects related to Parkinson's disease by suppressing glycolysis. *Science advances*. **7** (2021), doi:10.1126/sciadv.abg4574.
243. K. Liu *et al.*, Parkin Regulates the Activity of Pyruvate Kinase M2. *The Journal of biological chemistry*. **291**, 10307–10317 (2016), doi:10.1074/jbc.M115.703066.
244. R. Cai *et al.*, Enhancing glycolysis attenuates Parkinson's disease progression in models and clinical databases. *The Journal of clinical investigation*. **129**, 4539–4549 (2019), doi:10.1172/JCI129987.
245. P. Cisternas, P. Salazar, C. Silva-Álvarez, L. F. Barros, N. C. Inestrosa, Activation of Wnt Signaling in Cortical Neurons Enhances Glucose Utilization through Glycolysis. *The Journal of biological chemistry*. **291**, 25950–25964 (2016), doi:10.1074/jbc.M116.735373.

246. F. Stephano *et al.,* Impaired Wnt signaling in dopamine containing neurons is associated with pathogenesis in a rotenone triggered Drosophila Parkinson's disease model. *Sci Rep*. **8**, 2372 (2018), doi:10.1038/s41598-018-20836-w.
247. Y. Funato, T. Michiue, M. Asashima, H. Miki, The thioredoxin-related redox-regulating protein nucleoredoxin inhibits Wnt-beta-catenin signalling through dishevelled. *Nature cell biology*. **8**, 501–508 (2006), doi:10.1038/ncb1405.
248. T. Rharass *et al.,* Ca2+-mediated mitochondrial reactive oxygen species metabolism augments Wnt/β-catenin pathway activation to facilitate cell differentiation. *The Journal of biological chemistry*. **289**, 27937–27951 (2014), doi:10.1074/jbc.M114.573519.
249. J. Mata, S. Marguerat, J. Bähler, Post-transcriptional control of gene expression: a genome-wide perspective. *Trends in Biochemical Sciences*. **30**, 506–514 (2005), doi:10.1016/j.tibs.2005.07.005.
250. J. Blackinton *et al.,* Post-transcriptional regulation of mRNA associated with DJ-1 in sporadic Parkinson disease. *Neuroscience letters*. **452**, 8–11 (2009), doi:10.1016/j.neulet.2008.12.053.
251. A. R. Stram, R. M. Payne, Post-translational modifications in mitochondria: protein signaling in the powerhouse. *Cellular and molecular life sciences : CMLS*. **73**, 4063–4073 (2016), doi:10.1007/s00018-016-2280-4.
252. S. Schmidt, D. M. Vogt Weisenhorn, W. Wurst, Chapter 5 - "Parkinson's disease - A role of non-enzymatic posttranslational modifications in disease onset and progression?". *Molecular aspects of medicine*. **86**, 101096 (2022), doi:10.1016/j.mam.2022.101096.
253. P. Mergenthaler, U. Lindauer, G. A. Dienel, A. Meisel, Sugar for the brain: the role of glucose in physiological and pathological brain function. *Trends in neurosciences*. **36**, 587–597 (2013), doi:10.1016/j.tins.2013.07.001.
254. A. Herrero-Mendez *et al.,* The bioenergetic and antioxidant status of neurons is controlled by continuous degradation of a key glycolytic enzyme by APC/C-Cdh1. *Nature cell biology*. **11**, 747–752 (2009), doi:10.1038/ncb1881.
255. L. Dunn *et al.,* Dysregulation of glucose metabolism is an early event in sporadic Parkinson's disease. *Neurobiology of aging*. **35**, 1111–1115 (2014), doi:10.1016/j.neurobiolaging.2013.11.001.
256. T. L. Perry, D. V. Godin, S. Hansen, Parkinson's disease: A disorder due to nigral glutathione deficiency? *Neuroscience letters*. **33**, 305–310 (1982), doi:10.1016/0304-3940(82)90390-1.
257. E. Sofic, K. W. Lange, K. Jellinger, P. Riederer, Reduced and oxidized glutathione in the substantia nigra of patients with Parkinson's disease. *Neuroscience letters*. **142**, 128–130 (1992), doi:10.1016/0304-3940(92)90355-b.
258. R. Mejías *et al.,* Neuroprotection by transgenic expression of glucose-6-phosphate dehydrogenase in dopaminergic nigrostriatal neurons of mice. *J Neurosci.* **26**, 4500–4508 (2006), doi:10.1523/JNEUROSCI.0122-06.2006.
259. A. D. Chaudhuri, S. Kabaria, D. C. Choi, M. M. Mouradian, E. Junn, MicroRNA-7 Promotes Glycolysis to Protect against 1-Methyl-4-phenylpyridinium-induced Cell Death. *The Journal of biological chemistry*. **290**, 12425–12434 (2015), doi:10.1074/jbc.M114.625962.
260. A. M. Smith *et al.,* Mitochondrial dysfunction and increased glycolysis in prodromal and early Parkinson's blood cells. *Movement disorders : official journal of the Movement Disorder Society*. **33**, 1580–1590 (2018), doi:10.1002/mds.104.
261. B. L. Tang, Glucose, glycolysis, and neurodegenerative diseases. *Journal Cellular Physiology*. **235**, 7653–7662 (2020), doi:10.1002/jcp.29682.
262. G. N. Valbuena *et al.,* Metabolomic Analysis Reveals Increased Aerobic Glycolysis and Amino Acid Deficit in a Cellular Model of Amyotrophic Lateral Sclerosis. *Molecular neurobiology*. **53**, 2222–2240 (2016), doi:10.1007/s12035-015-9165-7.
263. R. Requejo-Aguilar, J. P. Bolaños, Mitochondrial control of cell bioenergetics in Parkinson's disease. *Free radical biology & medicine*. **100**, 123–137 (2016), doi:10.1016/j.freeradbiomed.2016.04.012.
264. P. Borghammer *et al.,* Cortical hypometabolism and hypoperfusion in Parkinson's disease is extensive: probably even at early disease stages. *Brain Struct Funct.* **214**, 303–317 (2010), doi:10.1007/s00429-010-0246-0.
265. F. Albrecht, T. Ballarini, J. Neumann, M. L. Schroeter, FDG-PET hypometabolism is more sensitive than MRI atrophy in Parkinson's disease: A whole-brain multimodal imaging meta-analysis. *NeuroImage. Clinical*. **21**, 101594 (2019), doi:10.1016/j.nicl.2018.11.004.

266. Y. Zilberter, M. Zilberter, The vicious circle of hypometabolism in neurodegenerative diseases: Ways and mechanisms of metabolic correction. *Journal of neuroscience research*. **95**, 2217–2235 (2017), doi:10.1002/jnr.24064.
267. A. Nilsson, E. Björnson, M. Flockhart, F. J. Larsen, J. Nielsen, Complex I is bypassed during high intensity exercise. *Nature communications*. **10**, 5072 (2019), doi:10.1038/s41467-019-12934-8.
268. E. Motori *et al.*, Neuronal metabolic rewiring promotes resilience to neurodegeneration caused by mitochondrial dysfunction. *Science advances*. **6**, eaba8271 (2020), doi:10.1126/sciadv.aba8271.
269. L. Hertz, R. Dringen, A. Schousboe, S. R. Robinson, Astrocytes: glutamate producers for neurons. *Journal of neuroscience research*. **57**, 417–428 (1999).
270. C. M. Díaz-García, G. Yellen, Neurons rely on glucose rather than astrocytic lactate during stimulation. *Journal of neuroscience research*. **97**, 883–889 (2019), doi:10.1002/jnr.24374.
271. X. Wang *et al.*, Genome-wide analysis of PDX1 target genes in human pancreatic progenitors. *Molecular metabolism*. **9**, 57–68 (2018), doi:10.1016/j.molmet.2018.01.011.
272. Y. Guo *et al.*, Illumina human exome genotyping array clustering and quality control. *Nature protocols*. **9**, 2643–2662 (2014), doi:10.1038/nprot.2014.174.
273. S. Schmidt *et al.*, Molecular mechanisms underlying a reversible state of hypometabolism in sporadic Parkinson's disease. *in Revision*.
274. Y. Benjamini, Y. Hochberg, Controlling the False Discovery Rate: A Practical and Powerful Approach to Multiple Testing. *Journal of the Royal Statistical Society: Series B (Methodological)*. **57**, 289–300 (1995), doi:10.1111/j.2517-6161.1995.tb02031.x.

6. Appendix

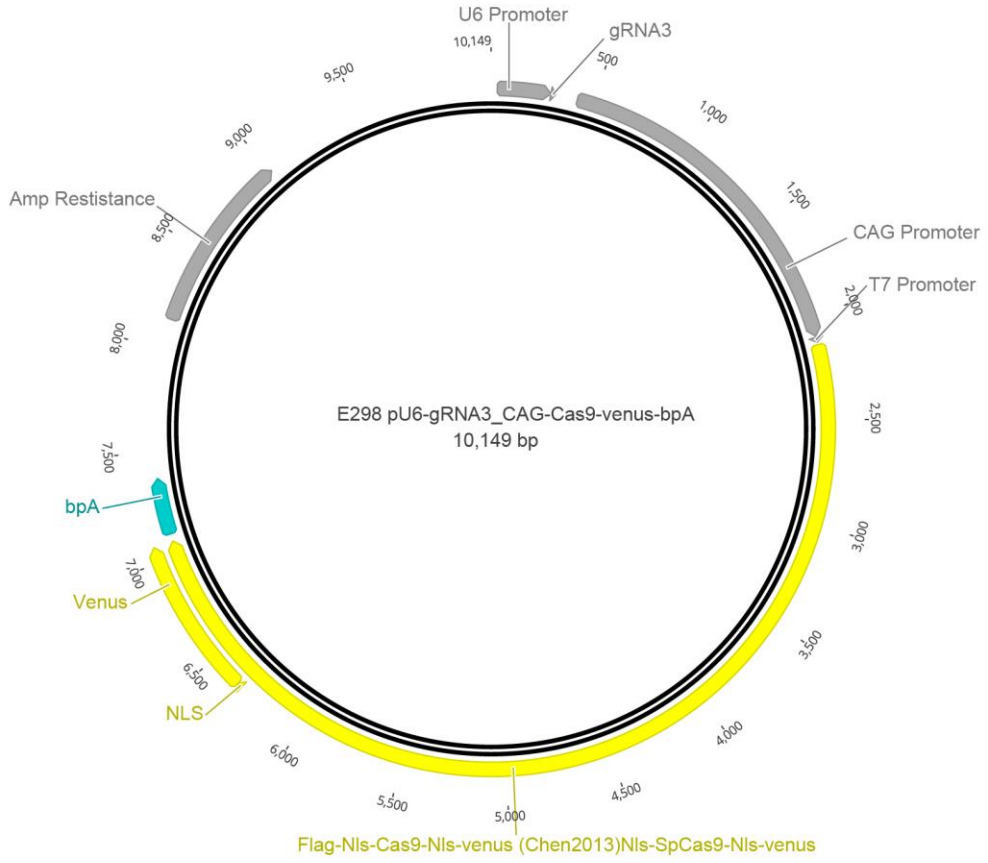

Figure 35: Plasmid map of E298 pU6-gRNA3_CAG-Cas9-venus-bpA. The plasmid contains a gRNA for targeting the EN1 locus and the Cas9 exonuclease fused to a venus reporter.

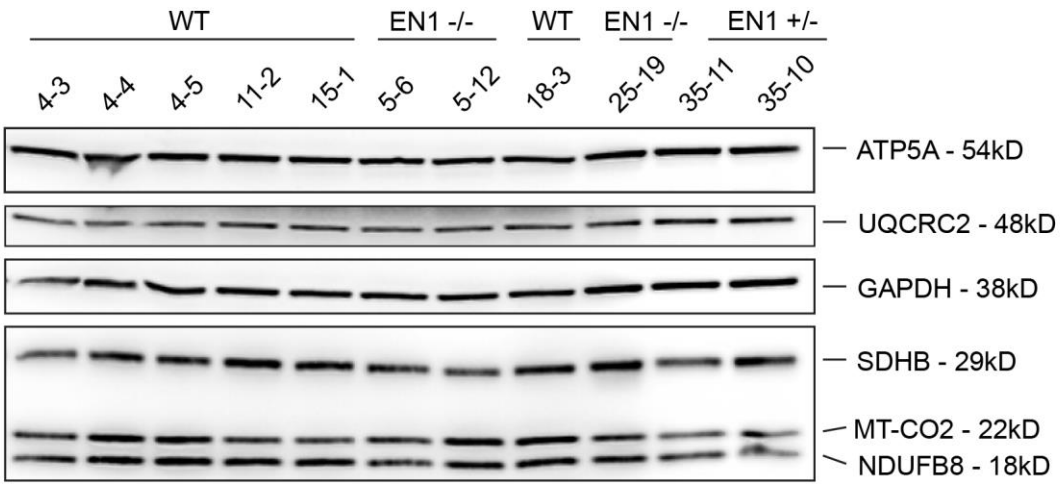

Figure 36: Western blot of complex I - V abundance analysis in NPCs. Western blot of CHIR99021 stimulated NPCs is shown exemplary. Antibodies against NDUFB8 (complex I), SDHB (complex II), UQCRC2 (Complex III), MT-CO2 (complex IV) and ATP5A (complex V) were used. Protein levels were normalized to ACTB or GAPDH and the average protein levels of WT clones.

Table 21: Chromosomal position and size of CNVs. All CNVs greater than 100 kb are listed. CNVs were detected using the HumanCytoSNP-12 v2.1 (clone 25-16) or the Infinium GSA-24 v3.0 bead chip (remaining clones that are listed). Related to **Figure 10**.

Clone	Copy number	Chromosome	Start	End	Size [bases]
25-16	3	2	220395337	225833056	5437719
25-16	0	3	80815597	80963053	147456
4-3	3	14	20220501	20416363	195862
4-4	3	14	20220501	20416363	195862
4-5	3	14	20239764	20410565	170801
4-5	1	16	28627333	28837515	210182
11-2	3	14	20220501	20397969	177468
11-2	3	20	29811475	31471313	1659838
15-1	3	14	20220501	20416363	195862
18-3	3	7	62079261	62447367	368106
18-3	3	14	63596906	63779111	182205
18-3	3	14	65972641	66407339	434698

Table 22: Statistical analysis of RT-qPCR of *EN1* and *EN2* mRNA level. Comparison of genotypes in unstimulated NPCs. Data are shown as mean ± standard deviation. n = 5 WT and 3 *EN1* -/- clones, in triplicates. Related to **Figure 11** and **Figure 17**.

Experiment	Genotypes	Statistical test	p-value	Average WT [$2^{-\Delta Ct}$]	Average *EN1* -/- [$2^{-\Delta Ct}$]
EN1 level	WT vs. *EN1* -/-	Welch's t-test	0.0177	0.02971 ± 0.01409	0.005255 ± 0.0004878
EN2 level	WT vs. *EN1* -/-	Welch's t-test	0.1669	0.004639 ± 0.001973	0.002798 ± 0.0008812

Table 23: Statistical analysis of western blot and MitoTracker. Comparison of genotypes in unstimulated NPCs. Data are shown as mean ± standard deviation. Western blot: n = 5 WT and 3 *EN1* -/- clones, in triplicates. MitoTracker: n = 4 WT and 3 *EN1* -/- clones, in triplicates. FI: fluorescence intensity; ks: Kolmogorov-Smirnov. Related to **Figure 14**.

Experiment	Parameter	Genotypes	Statistical test	p-value	Average WT [relative protein level/FI]	Average *EN1* -/- [relative protein level/FI]
Western Blot	Complex I	WT vs. *EN1* -/-	Welch's t-test	0.3834	0.9787 ± 0.1159	1.03 ± 0.01528
	Complex II	WT vs. *EN1* -/-	Welch's t-test	0.49	0.9656 ± 0.1911	1.043 ± 0.1074
	Complex III	WT vs. *EN1* -/-	t-test	0.8118	1 ± 0.1035	1.021 ± 0.1347
	Complex IV	WT vs. *EN1* -/-	Welch's t-test	0.249	0.9955 ± 0.1438	1.174 ± 0.1922
	Complex V	WT vs. *EN1* -/-	t-test	0.7536	0.9891 ± 0.06693	1.253 ± 0.07863
MitoTracker		WT vs. *EN1* -/-	Welch's t-test	0.2699	5418 ± 313.4	4984 ± 494.4
MitoTracker	Distribution analysis	WT vs. *EN1* -/-	ks test	0.0002894		
		WT vs. *EN1* -/-	'nested' ANOVA	0.08958		

Table 24: Statistical analysis of Seahorse XF measurement. Comparison of genotypes in unstimulated NPCs. Data are shown as mean ± standard deviation. n = 4 WT and 3 *EN1* -/- clones, in triplicates. Related to **Figure 16**.

Seahorse measurement		Genotypes	Statistical test	p-value	Average WT [pmol O_2/min /µg DNA]	Average *EN1* -/- [pmol O_2/min /µg DNA]
OCR, Glucose	basal respiration	WT vs. *EN1* -/-	Welch's t-test	0.7069	634.1 ± 61	599.6 ± 132.4
	proton leak	WT vs. *EN1* -/-	t-test	0.2176	109.4 ± 9.109	97.36 ± 13.68
	maximal respiration	WT vs. *EN1* -/-	Welch's t-test	0.6184	1207 ± 179.6	1303 ± 260.2
OCR, Pyruvate	basal respiration	WT vs. *EN1* -/-	Welch's t-test	0.7132	952.3 ±36	901 ±207.3
	proton leak	WT vs. *EN1* -/-	Welch's t-test	0.544	165.7 ± 7.985	151.6 ± 33.32
	maximal respiration	WT vs. *EN1* -/-	Welch's t-test	0.9924	1422 ± 175.6	1425 ± 387.3

Table 25: Statistical analysis of complex I activity measurement. Comparison of genotypes in unstimulated NPCs. Data are shown as mean ± standard deviation. n = 5 WT and 3 *EN1* -/- clones, in triplicates. Related to **Figure 16**.

Experiment	Genotypes	Statistical test	p-value	Average WT [relative complex I activity]	Average *EN1* -/- [relative complex I activity]
Complex I activity	WT vs. *EN1* -/-	Welch's t-test	0.6654	0.998 ± 0.09235	0.9086 ± 0.305

Table 26: Statistical analysis of DAN differentiation efficiency. Comparison of genotypes. Data are shown as mean ± standard deviation. n = 4 WT, 2 *EN1* +/- and 3 *EN1* -/- clones, in triplicates. Related to **Figure 18**.

Experiment	Parameter	Genotypes	Statistical test	p-value	Average WT [%]	Average *EN1* -/- [%]
Differentiation DANs	RBFOX3+ cells	WT vs. *EN1* -/-	Welch's t-test	0.1233	79.81 ± 10.54	91.08 ± 4.482
	TH+/RBFOX3+ cells	WT vs. *EN1* -/-	t-test	0.5479	8.105 ± 3.017	6.594 ± 3.154

Table 27: Statistical analysis of MitoTracker. Comparison of genotypes in DANs. Data are shown as mean ± standard deviation. n = 5 WT and 3 *EN1* -/- clones, in triplicates. FI: fluorescence intensity; ks: Kolmogorov-Smirnov. Related to **Figure 19** and **Figure 31**.

Experiment	Parameter	Genotypes	Statistical test	p-value	Average WT [FI]	Average *EN1* -/- [FI]
MitoTracker	Density analysis	WT vs. *EN1* -/-	Welch's t-test	0.6523	7363 ± 1550	7831 ± 1205
MitoTracker		WT vs. *EN1* -/-	ks test	0.009249		
		WT vs. *EN1* -/-	'nested' ANOVA	0.608		

Table 28: Statistical analysis of western blot. Comparison of genotypes in DANs. Data are shown as mean ± standard deviation. Western blot: n = 4 WT and 3 *EN1* -/- clones, in triplicates. Related to **Figure 19**.

Experiment	Parameter	Genotypes	Statistical test	p-value	Average WT [relative protein level]	Average *EN1* -/- [relative protein level]
Western Blot	Complex I	WT vs. *EN1* -/-	Welch's t-test	0.6505	1 ± 0.08223	0.9381 ± 0.1973
	Complex II	WT vs. *EN1* -/-	t-test	0.0857	1 ± 0.1359	0.7562 ± 0.1676
	Complex III	WT vs. *EN1* -/-	t-test	0.6285	1 ± 0.1902	0.9114 ± 0.2693
	Complex IV	WT vs. *EN1* -/-	Welch's t-test	0.0454	1 ± 0.1621	0.7468 ± 0.06945

	Complex V	WT vs. *EN1* -/-	t-test	0.1955	1 ± 0.0982	1.098 ± 0.06312

Table 29: Statistical analysis of Seahorse XF measurement. Comparison of genotypes in DANs. Data are shown as mean ± standard deviation. n = 4 WT and 3 *EN1* -/- clones, in triplicates. Related to **Figure 20** and **Figure 30**.

Seahorse measurement		Genotypes	Statistical test	p-value	Average WT [pmol O_2/min /µg DNA]	Average *EN1* -/- [pmol O_2/min /µg DNA]
OCR, Glucose	basal respiration	WT vs. *EN1* -/-	Welch's t-test	0.0157	216 ± 35.9	138.3 ± 18.15
	proton leak	WT vs. *EN1* -/-	t-test	0.3474	43.59 ± 13.44	31.32 ± 18.16
	maximal respiration	WT vs. *EN1* -/-	t-test	0.0276	305.1 ± 25.43	247.8 ± 22.76
OCR, Pyruvate	basal respiration	WT vs. *EN1* -/-	Welch's t-test	0.5762	261.8 ± 66.17	218.7 ± 105.5
	proton leak	WT vs. *EN1* -/-	Welch's t-test	0.9483	57.2 ± 13.58	59.22 ± 47
	maximal respiration	WT vs. *EN1* -/-	Welch's t-test	0.9909	344.9 ± 94.86	346.1 ± 146.7

Table 30: Statistical analysis of RT-qPCR of *EN1* mRNA level in NPCs after Wnt stimulation. Comparison of stimulation and genotype using two-way ANOVA and Sidak post-hoc tests. n = 5 WT and 3 *EN1* -/- clones, in triplicates. unstim: unstimulated; stim = Wnt stimulated with CHIR99021. Related to **Figure 21**.

Experiment	Stimulation, F (DFn, DFd); P-value	Genotype, F (DFn, DFd); P-value	P-value *EN1* -/-; unstim vs. stim;	P-value WT; unstim vs. stim;	P-value unstim; WT vs. *EN1* -/-	P-value stim; WT vs. *EN1* -/-
EN1 level	F (1, 12) = 4,741; P = 0.0501	F (1, 12) = 13,48; P = 0.0032	0.9556	0.0151	0.3573	0.0048

Table 31: Validation of top DEGs from transcriptome. Comparison of genotypes in Wnt stimulated NPCs. Data are shown as mean ± standard deviation. n = 4 WT and 3 EN1 -/- clones, in triplicates. Related to **Figure 23**.

Experiment	Genotypes	Statistical test	p-value	Average WT [$2^{-\Delta Ct}$]	Average *EN1* -/- [$2^{-\Delta Ct}$]
DLK1 level	WT vs. *EN1* -/-	t-test	0.049	0.009255 ± 0.005805	0.00037 ± 0.0001253
SP5 level	WT vs. *EN1* -/-	Welch's t-test	0.0028	0.007933 ± 0.001699	0.0002767 ± 0.0001106
MAOA level	WT vs. *EN1* -/-	Welch's t-test	0.0426	0.001005 ± 0.0005545	0.00006333 ± 0.000005774
HOXB9 level	WT vs. *EN1* -/-	Welch's t-test	0.0083	0.0009775 ± 0.001083	0.07099 ± 0.01133
EPHA3 level	WT vs. *EN1* -/-	Welch's t-test	0.0017	0.000875 ± 0.0005256	0.02025 ± 0.001781
OLIG2 level	WT vs. *EN1* -/-	Welch's t-test	0.0006	0.001035 ± 0.0005687	0.01893 ± 0.001363
SPARCL1 level	WT vs. *EN1* -/-	Welch's t-test	0.0119	0.001338 ± 0.0007475	0.01636 ± 0.003176
SLC16A3 level	WT vs. *EN1* -/-	Welch's t-test	0.0194	0.0005925 ± 0.0006842	0.01116 ± 0.002825

Table 32: Statistical analysis of Seahorse XF measurement. Comparison of genotypes in Wnt stimulated NPCs. Data are shown as mean ± standard deviation. n = 5 WT and 3 *EN1* -/- clones, in triplicates. Related to **Figure 25** and **Figure 32**.

Seahorse measurement		Genotypes	Statistical test	p-value	Average WT [pmol O_2/min /µg DNA]	Average *EN1* -/- [pmol O_2/min /µg DNA]
OCR, Glucose	basal respiration	WT vs. *EN1* -/-	Welch's t-test	0.0229	1666 ± 286.7	1150 ± 188.1

	proton leak	WT vs. *EN1* -/-	t-test	0.021	220.8 ± 30.84	156.1 ± 23.33
	maximal respiration	WT vs. *EN1* -/-	Welch's t-test	0.0027	2951 ± 362.3	1956 ± 75.53
OCR, Pyruvate	basal respiration	WT vs. *EN1* -/-	Welch's t-test	0.0459	2248 ± 377.4	1646 ± 280.8
	proton leak	WT vs. *EN1* -/-	Welch's t-test	0.0119	285.7 ± 46.95	193.5 ± 26.23
	maximal respiration	WT vs. *EN1* -/-	Welch's t-test	0.3989	4031 ± 492.4	3552 ± 757.5
ECAR, Glucose	basal	WT vs. *EN1* -/-	Welch's t-test	0.9173	199.3 ± 40.29	207.3 ± 115.9
	maximal	WT vs. *EN1* -/-	t-test	0.9519	510.9 ± 144	504.7 ± 116.3

Table 33: Statistical analysis of glucose uptake. Comparison of genotypes in Wnt stimulated NPCs. Data are shown as mean ± standard deviation. n = 5 WT and 3 *EN1* -/- clones, in duplicates. Related to **Figure 26**.

Experiment	Genotypes	Statistical test	p-value	Average WT [relative glucose uptake]	Average *EN1* -/- [relative glucose uptake]
Glucose uptake	WT vs. *EN1* -/-	t-test	0.4073	1 ± 0.2553	1.176 ± 0.297

Table 34: Statistical analysis of Seahorse XF measurement. Comparison of stimulation and genotype using two-way ANOVA and Sidak post-hoc tests. n = 5 WT and 3 EN1 -/- clones, in triplicates. unstim: unstimulated; stim = Wnt stimulated with CHIR99021. Related to **Figure 27**.

Seahorse measurement		Stimulation, F (DFn, DFd); P-value	Genotype, F (DFn, DFd); P-value	P-value *EN1* -/-; unstim vs. stim;	P-value WT; unstim vs. stim;	P-value unstim; WT vs. *EN1* -/-	P-value stim; WT vs. *EN1* -/-
OCR, Glucose	basal respiration	F (1, 12) = 58.65; P < 0.0001	F (1, 12) = 5222; P = 0.0413	0.0139	< 0.0001	0.9832	0.0105
	proton leak	F (1, 12) = 46.20; P < 0.0001	F (1, 12) = 6.033; P = 0.0302	0.0327	< 0.0001	0.9988	0.01
	maximal respiration	F (1, 12) = 67.01; P < 0.0001	F (1, 12) = 6.376; P = 0.0267	0.0393	< 0.0001	0.5605	0.0013
OCR, Pyruvate	basal respiration	F (1, 12) = 54.00; P < 0.0001	F (1, 12) = 4.011; P = 0.0683	0.0134	< 0.0001	0.9907	0.0239
	proton leak	F (1, 12) = 19.46; P = 0.0008	F (1, 12) = 4.790; P = 0.0491	0.3859	0.0003	0.9923	0.015
	maximal respiration	F (1, 12) = 90.65; P < 0.0001	F (1, 12) = 0.4038; P = 0.5371	0.0004	< 0.0001	0.898	0.378

Table 35: Statistical analysis of MitoTracker. Comparison of genotypes in Wnt stimulated NPCs and comparison of stimulation for both genotypes. Data are shown as mean ± standard deviation. n = 4 WT and 3 *EN1* -/- clones, in triplicates. FI: fluorescence intensity; ks: Kolmogorov-Smirnov; unstim: unstimulated; stim = Wnt stimulated with CHIR99021. Related to **Figure 28** and **Figure 33**.

Experiment	Parameter	Genotypes	Statistical test	p-value	Average WT [FI, area, ratio]	Average *EN1* -/- [FI, area, ratio]
MitoTracker	FI	WT vs. *EN1* -/-	Welch's t-test	0.0691	6097 ± 402.3	5493 ± 290.2
MitoTracker - distribution analysis	FI	WT vs. *EN1* -/-	ks test	9.837e-10		
		WT vs. *EN1* -/-	'nested' ANOVA	0.00963		
MitoTracker - distribution analysis	Mitochondrial area	WT vs. *EN1* -/-	ks test	0.4134		
		WT vs. *EN1* -/-	'nested' ANOVA	0.6475		

MitoTracker - distribution analysis	FI/mitochondrial area	WT vs. *EN1* -/-	ks test	3.16E-14
		WT vs. *EN1* -/-	'nested' ANOVA	0.007536
MitoTracker – distribution analysis	FI	WT unstim vs. *stim*	ks test	9.746e-13
		WT unstim vs. *stim*	'nested' ANOVA	0.00208
		EN1 -/- unstim vs. *stim*	ks test	0.001144
		EN1 -/- unstim vs. *stim*	'nested' ANOVA	0.05952

Table 36: Statistical analysis of western blot. Comparison of genotypes in Wnt stimulated NPCs. Data are shown as mean ± standard deviation. n = 5 WT and 3 EN1 -/- clones, in triplicates. Related to **Figure 29** and **Figure 33**.

Experiment	Parameter	Genotypes	Statistical test	p-value	Average WT [relative protein level]	Average *EN1* -/- [relative protein level]
Western Blot	Complex I	WT vs. *EN1* -/-	t test	0.0362	0.9993 ± 0.1125	0.7608 ± 0.138
	Complex II	WT vs. *EN1* -/-	t test	0.0513	1.002 ± 0.0828	0.8451 ± 0.09839
	Complex III	WT vs. *EN1* -/-	t test	0.5805	1.05 ± 0.1292	0.9902 ± 0.1584
	Complex IV	WT vs. *EN1* -/-	Welch's t-test	0.7165	0.9995 ± 0.04552	0.9208 ± 0.3248
	Complex V	WT vs. *EN1* -/-	Welch's t-test	0.0979	1.01 ± 0.1386	0.8758 ± 0.0384

Table 37: Statistical analysis of complex I activity measurement. Comparison of genotypes in Wnt stimulated NPCs. Data are shown as mean ± standard deviation. n = 5 WT and 3 *EN1* -/- clones, in triplicates. Related to **Figure 29** and **Figure 33**.

Experiment	Genotypes	Statistical test	p-value	Average WT [relative complex I activity]	Average *EN1* -/- [relative complex I activity]
Complex I activity	WT vs. *EN1* -/-	Welch's t-test	0.2244	1 ± 0.1626	1.169 ± 0.186

List of Figures

List of Tables

Acronyms

6-OHDA	6-hydroxydopamine
6PGD	6-phosphogluconate dehydrogenase
ADP	adenosine diphosphate
ALNS	astrocyte-neuron lactate shuttle
ATP	adenosine triphosphate
BAF	B-allele frequency
BBB	blood-brain barrier
bp	Base pairs
Ca^{2+}	calcium
CaMKII	Ca^{2+}/calmodulin-dependent protein kinase II
CK1	casein kinase
CNVs	copy number variations
CO_2	carbon dioxide.
CRISPR	clustered regularly interspaced short palindromic repeats
CT	Cycle threshold
DAN	Dopaminergic neuron
DEGs	Differentially expressed genes
Dvl	Dishevelled
E	embryonic day
ECAR	Extracellular acidification rate
ECM	extracellular matrix
EDTA	ethylenediaminetetraacetic acid
e.g.	for example/exempli gratia
EH	Engrailed homology
eIF4E	eukaryotic translation initiation factor 4E
EN1	Engrailed 1
EN2	Engrailed 2
$FADH_2$	flavin adenine dinucleotide
FP	floor plate
fPD	familial Parkinson's disease
G6PD	glucose-6-phospahte dehydrogenase
GABA	γ-aminobutyric acid
gRNA	Guide RNA
GPi	globus pallidus internus
GPe	globus pallidus externus
GSK-3β	glycogen synthase kinase 3β
GWAS	genome wide association study
H	Hour
hiPSCs	Human induced pluripotent stem cells
H_2O	Water
IMM	inner mitochondrial membrane
IMS	intermembrane space
IP3	inositol 1,4,5 triphosphate
IsO	isthmic organizer

kb	Kilo bases
JNK	c-Jun N-terminal kinase
ko	Knock out
LB	Lewy body
LUHMES	Lund human mesencephalic
mDAN	Midbrain dopaminergic neuron
mFP	midbrain FP
Min	minute
MHB	mid-hindbrain boundary
MPTP	1-methyl-4-phenyl-1,2,3,6-tetrahydropyridine
MPP+	1-methyl-4-phenylpyridinium
MSN	medium spiny neuron
mtDNA	mitochondrial DNA
mTOR	mammalian target of rapamycin
NaCl	Sodium chloride
$NADH/NAD^+$	nicotinamide adenine dinucleotide
Ndufs1	NADH:Ubiquinone oxidoreductase core subunit S1
Ndufs3	NADH:Ubiquinone oxidoreductase core subunit S3
NFAT	nuclear factor of activated T cells
NHEJ	non-homologous end joining
NPC	Neuronal precursor cell
O_2	oxygen
OCR	Oxygen consumption rate
OMM	outer mitochondrial membrane
OXPHOS	oxidative phosphorylation
P (in hiPSCs)	passage
P (in mice)	postnatal day
PCA	Principal component analysis
PCP	planar cell polarity
PD	Parkinson’s disease
PCR	Polymerase chain reaction
PKC	protein kinase C
PPP	pentose phosphate pathway
ROS	reactive oxygen species
RT	Room temperature
RIPA	radioimmunoprecipitation assay buffer
SN	Substantia nigra
SNpc	Substantia nigra pars compacta
sPD	sporadic Parkinson’s disease
STN	subthalamic nucleus
TCA	tricarboxylic acid cycle
TE	Tris-EDTA
TH	tyrosine hydroxylase
TFIID	transcription factor II D
VTA	ventral tegmental area
WT	wildtype
2-DG	2-deoxyglucose

Acknowledgements

Als Erstes möchte ich mich bei Prof. Wolfgang Wurst und Dr. Daniela Vogt Weisenhorn für die Möglichkeit bedanken, meine Doktorarbeit am IDG zu absolvieren. Vielen Dank für die gute Betreuung, eure Unterstützung und die hilfreichen fachlichen Diskussionen.

Besonderes möchte ich mich auch bei Daniela für Ihre Unterstützung und die vielen guten und auch nicht immer fachlichen Gespräche bedanken.

Außerdem möchte ich mich auch herzlich bei meinem „zweiten“ Betreuer Florian bedanken, der immer ein offenes Ohr hatte und sich die Zeit genommen hat mir zu weiterzuhelfen.

Danke auch an mein Thesis Committee, Prof. Jovica Ninkovic und Prof. Magdalena Götz für den Input während der jährlichen Treffen.

Ein besonderes Dankeschön auch an die AG Vogt Weisenhorn für die Unterstützung und die schöne Zeit während der letzten Jahre. Vielen Dank an Tanja Orschmann für Ihre große Hilfe und Unterstützung in der Zellkultur. Vielen Dank an Susanne Badeke für die tatkräftige Unterstützung mit Stainings und diversen Genotypisierungen. Vielen Dank an Anja Folchert für die Einführung in die Mausarbeit und die Hilfe bei den Zuchten. Vor allem auch einen großen Dank an Annerose Kurz-Drexler, für diverse Western Blots und dass du für fast jedes Problem eine Lösung wusstest und immer gute Laune verbreitest hast. Neben eurer fachlichen Unterstützung möchte ich mich auch für den tollen Zusammenhalt bedanken und an unseren Hüttenausflug, die Weihnachtsfeiern den Besuch der Rocky Horror Picture Show oder auch mittagliche Grillevents werde ich immer gerne zurückdenken.

Vielen Dank an meine PhD Kollegen, Kristina, Bianca und Sebi, die mittlerweile zu Freunden geworden sind, für die schöne und lustige Zeit, für eure Unterstützung, wenn es mal nicht so lief und dass wir mit sehr viel Galgenhumor meistens doch noch ein Licht am Ende des Tunnels gefunden haben.

Ein großer Dank gilt auch meinen Freunden auf die ich mich immer verlassen konnte, in schwierigen Phasen. Insbesondere, vielen Dank an Julia, Corinna, Rebecca und Jana, die immer wussten wovon ich rede und mich damit aufgemuntert haben, dass es auch anderswo nicht besser läuft. Vielen Dank an meine Rotaract Mädels für die schönen Wochenenden, die eine willkommene Abwechslung während des PhD Alltags waren. Vielen Dank an die „schrecklichen sieben“, die mich auch aus der Ferne immer unterstützt haben. Ein besonderer Dank an Corinna, die zusammen mit mir das München Abenteuer begonnen hat und die immer ein offenes Ohr für mich hatte. Unsere Mädels Abende, mit Risotto, Schokokuchen und einem Film haben mich immer aufgemuntert.

Ein besonderer Dank auch an meinen „erst Kollegen, dann Freund Sebi“. Du hast mich am Anfang fachlich sehr unterstütz und nachher dann auch in allen anderen Höhen und Tiefen. Vielen Dank, dass du mich verstanden hast, wusstest wie du mich aufmuntern kannst und immer für mich da warst. Ich bin sehr froh dich zu haben.

Zuletzt möchte ich mich bei meiner Familie bedanken. Ihr wart und seid eine große Stütze für mich. Vielen Dank an die Hembachs, meine Tante Anke und natürlich an meinen Eltern Achim und Claudia und meinen Bruder Nils. Ihr habt mich in allen meinen Vorhaben unterstützt und mir sehr viel ermöglicht. Vielen Dank für alles!